Modeling Size-Controlled Assembly of Polymeric Nanoparticles in Interdigital Micromixers

Dissertation

zur Erlangung des Grades „Doktor der Naturwissenschaften“ am Fachbereich Physik, Mathematik und Informatik der Johannes Gutenberg-Universität in Mainz

vorgelegt von Simon Keßler, geboren in Oberwesel.
Angefertigt am Fraunhofer ICT-IMM.

JOHANNES GUTENBERG UNIVERSITÄT MAINZ

Fraunhofer ICT – IMM

Mainz, 18. Mai 2017

Abstract

We apply mean field continuum theories to model the assembly of particles in the co-solvent method – to which we refer as size-controlled assembly – with the objective to explain nanoparticle size dependencies on solvent mixing speeds.

Our investigation starts at considering a Cahn-Hilliard equation with a Flory-Huggins-de Gennes free energy functional restricted to homopolymers. Upon modeling solvent mixing by a time dependent interaction parameter, structure formation during spinodal decomposition is analyzed. The qualitative agreement of our simulated data to both recently published Molecular Dynamics simulations and experiments indicates that size-controlled assembly can, on principle, be described by relaxation dynamics within a mean field approximation, and suggests a response of molecular organization to solvent mixing in the very early stages of phase separation to eventually determine final particle sizes. In contrast to Molecular Dynamics simulations, the Cahn-Hilliard model is able to simulate realistic mixing times and enables a perturbation approximation. The perturbation approximation does not only give an analytical interpretation to the underlying physical mechanism of size-control as a competition between molecular repulsion and interfacial tension of diffuse interfaces, but also yields a general theoretical scaling behavior $R \propto s^{-1/6}$ (R is a mean particle radius and s a solvent mixing speed) that is reflected in experiments and Molecular Dynamics simulations. After introducing the notion of effective two-component models, we combine the computational efficiency of models based on time dependent interaction parameters with a more realistic description of solvent mixing by relative chemical potentials of solvents. This novel description is then shown to agree with incompressible three-component dynamics in dilute solutions that correspond to experimental conditions.

Size-controlled assembly of amphiphilic diblock-copolymers is studied by inserting time dependent interaction parameters into an External Potential Dynamics model with a free energy functional from the Self Consistent Field Theory. A satisfactory analysis of particle size distributions requires the development of a new numerical integration scheme to deal with stiffness instabilities at high compressive moduli, which accelerates simulations by a factor of up to 100. Subsequent simulations indicate that neither the fundamental qualitative characteristics of particle size dependencies on mixing speeds nor the physical mechanism behind the size-control are significantly affected by copolymer architecture. Experimentally observed transitions of particle morphologies are also reproduced qualitatively. To conclude, an effective two-component model with a revised description of solvent mixing for copolymers is proposed. Based on the findings in the present work, we consider it a suitable starting point for quantitative studies of size-controlled copolymer assembly.

Zusammenfassung

In dieser Arbeit wird die Cosolvent-Methode zur Nanopartikelherstellung unter Verwendung von mean field-Theorien modelliert. Ziel ist es, eine Erklärung für die Partikelgrößenabhängigkeit von Lösungsmittel-Mischgeschwindigkeiten zu finden.

Um Aggregatbildung während einer spinodalen Entmischung zu untersuchen, wird eine Cahn-Hilliard-Gleichung mit einem Flory-Huggins-de Gennes freien Energiefunktional für Homopolymere verwendet. Die Lösungsmittelmischung wird dabei durch einen zeitlich wachsenden Flory-Huggins-Wechselwirkungsparameter modelliert. Die qualitative Übereinstimmung simulierter Aggregatgrößen mit veröffentlichten Molekulardynamik-Simulationen und experimentellen Daten deutet darauf hin, dass die Cosolvent-Methode als Relaxationsprozess aufgefasst werden kann und dass die finale Partikelgröße durch den Einfluss der Lösungsmittelmischung auf die Aggregation einzelner Polymerketten schon zu Beginn der Phasentrennung festgelegt wird. Im Gegensatz zur Molekulardynamik ermöglicht die Cahn-Hilliard-Gleichung die Simulation realistischer Mischzeiten. Sie erlaubt zusätzlich eine analytisch lösbare Näherung im Rahmen einer Störungstheorie. Diese Näherung zeigt nicht nur, dass die Abhängigkeit der Partikelgröße R von Mischgeschwindigkeiten s durch eine Synergie von zeitlich wachsender Repulsion chemischer Komponenten und der Spannung diffuser Oberflächen verursacht wird, sondern sie liefert auch ein Skalengesetz $R \propto s^{-1/6}$, das sowohl in den Ergebnissen der Molekulardynamik-Simulationen auftritt als auch in experimentellen Daten widergespiegelt wird. Um die Recheneffizienz von zeitabhängigen Wechselwirkungsparametern mit realistischeren Implementierungen für Lösungsmittelmischung zu kombinieren, wird ein neues effektives Zweikomponentenmodell konstruiert, bei dem die Lösungsmittelverteilungen über chemische Potentiale bestimmt werden. Dieses neue Modell ist konsistent mit konventioneller Dreikomponentendynamik in verdünnten, inkompressiblen Polymerlösungen, welche in der Cosolvent-Methode verwendet werden.

Die Assemblierung von amphiphilen Diblock-Copolymeren wird mit einem freien Energiefunktional aus der Selbstkonsistenten Feldtheorie in Kombination mit External Potential Dynamics untersucht. Eine zufriedenstellende Auswertung erfordert die Entwicklung eines neuen numerischen Integrators, um Steifigkeitsinstabilitäten bei hohen Kompressionsmoduli zu unterdrücken. Dieser Integrator erlaubt bis zu 100 mal kürzere Rechenzeiten. Darauffolgende Simulationen zeigen, dass sich Charakteristika von Partikelgrößenabhängigkeiten direkt von Homo- auf Copolymerlösungen übertragen, was impliziert, dass die Charakteristika nicht signifikant von der Polymerarchitektur beeinflusst werden. Experimentell beobachtete Einflüsse von Mischgeschwindigkeiten auf Partikelmorphologien werden ebenfalls reproduziert. Zum Schluss wird ein effektives Zweikomponentenmodell für Copolymerlösungen vorgeschlagen, das ausgehend von den Ergebnissen der vorliegenden Arbeit als Startpunkt für zukünftige, potentiell quantitative Simulationsmethoden in Frage kommen könnte.

Parts of this thesis have been published in

S. Keßler, F. Schmid, K. Drese. Modeling Size Controlled Nanoparticle Precipitation with the Co-solvency Method by Spinodal Decomposition, *Soft Matter*, 12, 7231 – 7240 (2016),

S. Keßler, K. Drese, F. Schmid. Simulating Copolymeric Nanoparticle Assembly in the Co-solvent Method: How Mixing Rates Control Final Particle Sizes and Morphologies, *Polymer*, 126, 9 – 18 (2017).

Table of contents

Chapter 1

Introduction

Size-controlled assembly of nanoparticles is a branch of nanotechnology. According to the US National Nanotechnology Initiative (NNI) "*nanotechnology is the understanding and control of matter at dimensions of roughly 1 and 100 nanometers (nm) [...]*" [1] and in this general context nanoparticles are simply molecule aggregates with spatial extensions on scales of 1 to 100 nm. Size-controlled assembly refers to a technique to manufacture nanoparticles of a specific size.

Nanoparticles have attracted growing interest during the last decades because the preceding technological advancement that allowed to visualize and manipulate nanoscale structures revealed their great potential in different applications. Depending on the chemical composition of a nanoparticle these applications include mesoscopic models for atomic systems [2, 3], optoelectronic devices [4], nanoreactors, or models for biological cells [5, 6]. Their probably most prominent application, however, is found in the field of drug delivery where they serve as transport vehicles for medication, called drug delivery systems [7, 8, 9]. The purpose of such transport vehicles is to overcome, for instance, deficiencies in the traditional treatment of diseases like cancer. One major deficiency is the lack of control over the in vivo biodistribution of commonly applied toxic low molecular weight substances and their large volume of distribution. To ensure an adequate concentration at localized tumors, an effective treatment thus requires administrating excessive amounts of medication, which may provoke severe side effects as those toxic substances inexorably corrode healthy tissue. In particular cells with high cell division rates, such as hair roots and stomach lining, are affected. Besides shielding highly susceptible substances from rapid depletion, nanoparticulate transport vehicles allow for a selective cancer treatment, e.g. by passive targeting of tumors based on the Enhanced Permeability and Retention (EPR) effect [10]. The term 'EPR effect' subsumes two distinctive traits that distinguish diseased from healthy tissue: an enhanced cell spacing of vascular endothelial cells due to faster growth and an enhanced retention time of irrupted substances caused by an impeded lymphatic drainage. The enhanced permeability of the endothelium can be exploited to achieve a targeted substance accumulation in tumors by encapsulating low molecular weight medication into nanoparticles as sketched in figure 1.1. The accumulation is further intensified by the reduced lymphatic drainage, and capsules may be loaded with iron molecules during fabrication to enable a release of medication by excitation via magnetic fields.

Since nanocapsules need to be large enough to prevent penetration into healthy tissue while still being small enough to guarantee accumulation in a tumor, passive targeting via the EPR effect is an illustrative example for the significance of nanoparticle size. The endothelial cell

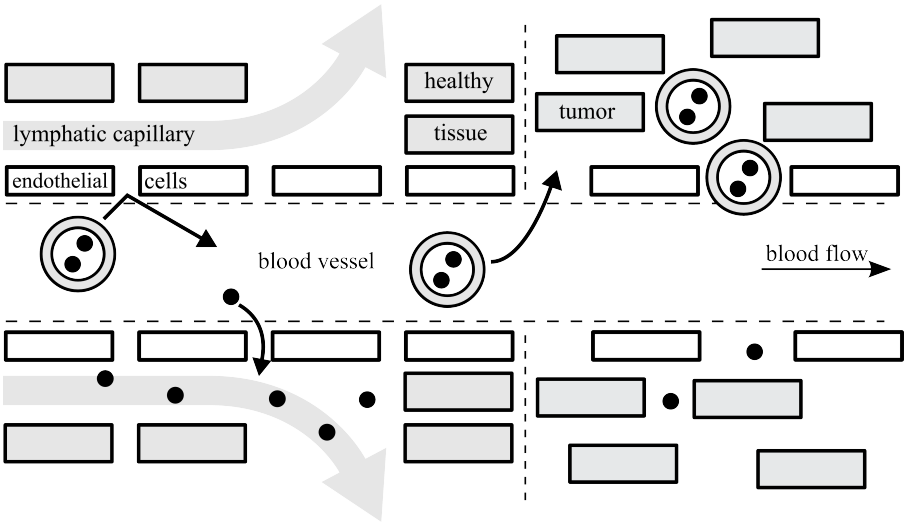

Figure 1.1: *Schematic of passive tumor targeting based on the EPR effect. Solid black dots represent molecules of a toxic low molecular weight substance and circular discs symbolize vesicular nanoparticles. The schematic shows a small section of a blood vessel surrounded by healthy tissue on the left and a tumor on the right. Cells are represented by rectangles and the white ones highlight vascular endothelial cells. The sketch is conceptually divided into two parts, which are separated by an imaginary horizontal line along the center of the blood vessel. The lower part paints the distribution of low molecular weight substances in traditional cancer therapy and the upper one the distribution of nanocapsules: medication encapsulated by nanoparticles specifically accumulates in the tumor due to larger cell spacing compared to healthy tissue, while most of its non-encapsulated counterpart penetrates into the latter, which reduces the efficacy of a therapy and causes side effects. The principle schematic was taken from Bleul [11] and adapted.*

spacing in infested blood vessels may range from 200 nm to 1.2 μm depending on the tumor [12] and the vascular endothelium in healthy tissue is permeable to substances of less than approximately 10 nm in diameter [13]. So if only cell spacing in blood vessels had to be considered, particles with any arbitrary diameter inside a window of approximately 20 to 200 nm should selectively accumulate in tumors only. What eventually makes the definite size of drug delivery systems inside that window a particularly critical property is its intricate impact on their removal from the bloodstream by filtration organs or the immune system. This removal is problematic because an effective therapy necessarily requires large amounts of nanocapsules to reach an infested section of a blood vessel after intravenous injection and therefore, a sufficiently high retention time in the cardiovascular system is mandatory. A general statement about the role of filtration organs is very difficult because it depends on the chemical properties of a nanoparticle and the biological species under consideration, but the human liver, for example, tends to extract particles smaller than approximately 107 nm in diameter as this value is typical for the spacing of fenestrae [14]. In rats, zinc oxide nanoparticles of 70 nm in diameter are found to be removed more slowly by excretion kinetics than 20 nm particles [15], and silver particles with diameters of approximately 40, 160, and 240 nm are observed to be rapidly removed from the blood and to accumulate with size specific preference in the liver or the spleen [16]. The reason why nanoparticle size may also trigger unwanted opsonization and an accompanied removal by the immune system [17] is

because the size is a critical determinant of the protein corona in blood [18]. As such, it indirectly affects the biological identity of a nanoparticle.

The biological identity depends, of course, on the chemical composition of the nanoparticle surface as well. Since a favored adsorption of opsonins is observed for charged particles or particles with rough and strongly hydrophobic surfaces, (biocompatible) hydrophilic groups such as polyethyleneglycol (PEG) – otherwise known as polyethyleneoxide (PEO) – may be grafted onto the molecular constituents of the particles to complicate opsonization [19]. The constituents of hitherto developed commercial drug delivery systems are mainly amphiphilic lipids, some of them PEO-protected, or hydrophobic therapeutic molecules that are directly linked to PEO [11, 20]. Because of an enhanced stability, increased modification possibilities, and easier synthesis, (amphiphilic) diblock-copolymers render promising candidates with extended tunability to replace these constituents in order to form multifunctional drug delivery systems [8, 11, 21, 22, 23]. Increasing the tunability of nanocapsules naturally extends their scope of application as very specific surface qualities are necessary, for instance, to enable nanoparticles a harmless passage of the blood-brain barrier in order to potentially treat brain tumors or Alzheimer's disease [24, 25, 26].

The above-mentioned complex and sensitive size-dependence of their biological fate demands multifunctional drug delivery systems to be manufactured by a method that allows for a precise and reliable customization of their size. Manufacturing methods for polymeric nanoparticle populations are the polymerization of monomers [27, 28, 29, 30], emulsification in combination with solvent stripping [31, 32, 33], and nanoprecipitation [6, 30, 34], also known as the co-solvent method. The first two methods suffer from certain disadvantages as polymerization cannot guarantee purity of fabricated particles and emulsification might result in large polydispersities [34], so the latter proves most convenient. Although it was recently reported by Nikoubashman et al. [35] that the co-solvent method also allows to fabricate stable nanoparticles built from homopolymers, we describe the method by only referring to the more commonly utilized diblock-copolymers for the sake of convenience in the following. The setup for homopolymers is completely analogous. To produce vesicular nanocapsules like the ones that are sketched in figure 1.1 with the co-solvent method, a co-solvent is mixed into a homogeneous solution of an amphiphilic diblock-copolymer and a good solvent for both blocks. The addition of co-solvent – commonly a selective solvent which is unfavorable for one block – eventually induces particle growth by triggering precipitation of the polymer. The solvent mixing continues during particle growth and in case the co-solvent method is implemented as a batch process where the selective solvent is injected drop by drop into a petri dish that contains the polymer solution [36, 37], the mean size of manufactured nanoparticles can be decreased by increasing the injection rate [36] (the solution is gently stirred during the injection). Another implementation of the co-solvent method is sketched in figure 1.2. Here, solvent mixing is performed by continuous flow micro fluidic mixing devices, the so called *micromixers*. In this continuous implementation mean particle sizes are reported to decrease with an increasing flow rate v or the Reynolds number [22, 23, 35]. They also depend on the temperature T and the mean polymer concentration c in the initial solution.

To our knowledge, the most comprehensive experimental study about particle size dependencies on macroscopic parameters of the co-solvent method was done by Thiermann et al. [22, 23] who also showed that symmetric flow conditions, i.e. equal flow rates v of both initial solution and selective solvent in figure 1.2, enable a size-control with high fidelity. The corre-

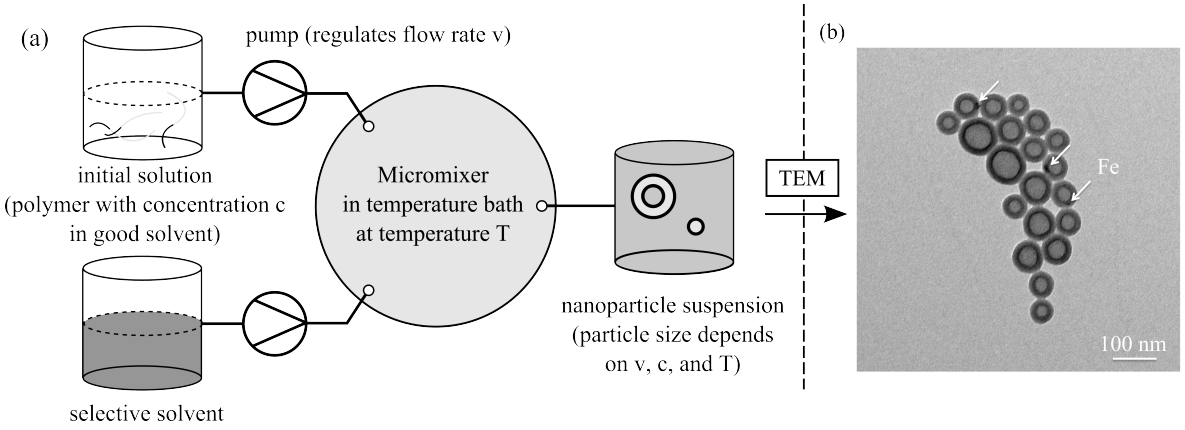

Figure 1.2: *The continuous implementation of the co-solvent method and a snapshot of fabricated nanoparticles. (a) shows a sketch of the experimental setup [22]. Here, a solution of an amphiphilic diblock-copolymer and a good solvent for both blocks (the initial solution) is mixed with a selective solvent inside a continuous flow micromixer. Since the selective solvent is unfavorable for one block (in this case the grey one), solvent mixing induces particle formation. The initial solution often contains a premixed amount of selective solvent that is not yet sufficient to trigger polymer precipitation. (b) is a Transmission Electron Microscopy (TEM) image of fabricated* $PEO_{160} - PB_{60} - COOH$ *vesicles that are loaded with iron particles (indicated by white arrows). The TEM image corresponds to figure 4.19 from Thiermann [22].*

sponding compilation of experimentally determined particle sizes in figure 1.3 confirms that the co-solvent method is suited to tweak diameters within the aforementioned preferential window for drug delivery systems of approximately 20 to 200 nm in diameter. Particle radii as functions of flow rates show a scaling behavior $R_{DLS} \propto v^{\alpha}$, where the mean value of α over all measurements reads $\bar{\alpha} \approx -0.158$ with a standard deviation $\sigma_{\alpha} = 0.058$. Increasing either the polymer concentration c (figure 1.3 (c)) or the temperature T (figure 1.3 (d)) mainly shifts the scaling law upwards. The utilized polymers are amphiphilic diblock-copolymers made of polybutadiene (PB, hydrophobic) and polyethyleneoxide (PEO, hydrophilic), the good solvent is tetrahydrofuran (THF), and the selective one is water. The micromixer approach has several advantages over the batch process as it generally achieves higher reproducibility of nanoparticle sizes, larger throughput, and narrower size distributions without additional steps like membrane extrusion [23]. These advantages render it a promising approach for potential commercial production and are the main reason why all the experimental data in figure 1.3 except for figure 1.3 (e) stem from micromixer implementations. The flow rate dependence of particle sizes is a particularly appealing characteristic of the continuous implementation, because flow rates are easily and accurately adjustable with High Performance Liquid Chromatography pumps. Unlike controlling particle sizes by temperature variations, controlling them by flow rates does not require waiting for a thermal equilibrium of a temperature bath, either, and unlike variations of c, flow rate variations do not demand the preparation of multiple different initial solutions.

Since varying injection rates and flow rates generate different particle sizes but do not affect any macroscopic state variable of a fabricated particle suspension at $t \to \infty$ (the maximum amount of selective solvent is identical for any injection rate or flow rate), the

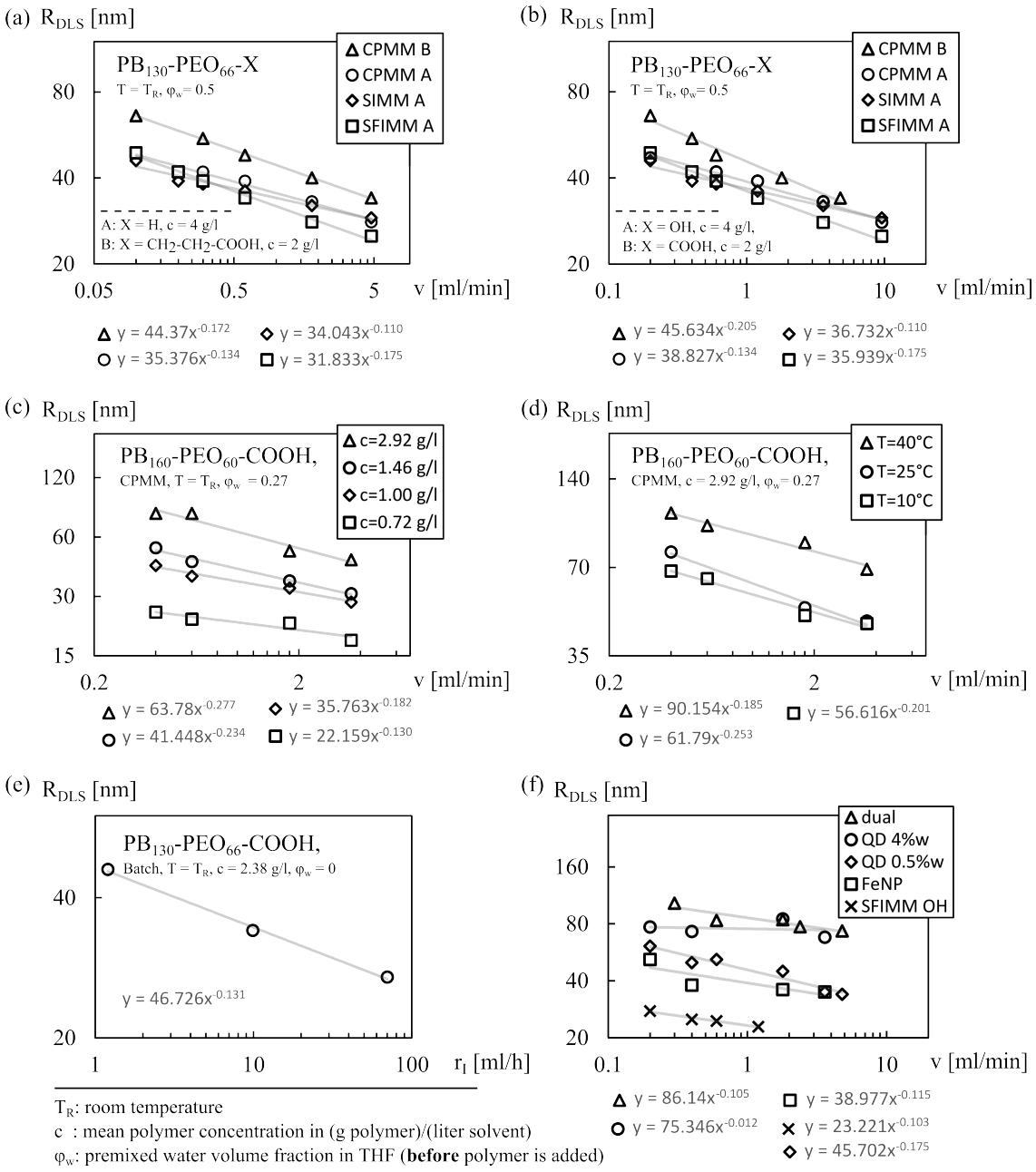

Figure 1.3: *Compilation of experimental data for the co-solvent method from Thiermann et al. [22, 23] and Mueller [36]. (a) shows the flow rate dependence of mean particle radii R_{DLS} in different micromixers (CPMM, SIMM, and SFIMM are type designations) for symmetric flow conditions [23]. A and B label different end groups X attached to the utilized amphiphilic diblock-copolymer $PB_{130} - PEO_{66} - X$ as listed beneath the dashed line inside the diagram, and the equations directly below the diagram belong to the grey trend lines. (b) depicts exactly the same for slightly different end groups [22]. (c) and (d) illustrate the impact of mean polymer concentration and temperature variations for the polymer $PB_{160} - PEO_{60} - COOH$ in the CPMM [22]. (e) shows R_{DLS} in dependence on the water injection rate r_I from a batch implementation [36], and (f) summarizes all remaining measurements for symmetric flow conditions found in [22] to complete the compilation. 'Dual', 'QD' (quantum dots), and 'FeNP' (iron nanoparticles) denote different loadings of the produced nanoparticles. R_{DLS} was measured by Dynamic Light Scattering and error bars (typically about 5 nm or below) are omitted for the sake of clarity.*

size-control is clearly a non-equilibrium phenomenon. Typical mixing times of solvents in micromixers lie between milliseconds and seconds. The difficulty to experimentally access non-equilibrium processes on a nanometer scale during such short time spans suggests that computer simulations are suitable tools to develop a thorough understanding of the co-solvent method. However, although the co-solvent method has been applied in experiments for years, there are hardly any simulation attempts or modeling approaches. To our knowledge, there are no detailed theoretical or experimental studies about physical mechanisms that cause one of its most appealing aspects, namely the control over particle sizes by variations of flow rates, either. Thus, the fundamental 'working principle' of the co-solvent method is still unclear. Concrete questions that arise from this ambiguity are, for instance:

- What causes the approximate scaling behavior $R_{DLS} \propto v^{\alpha}$ in figure 1.3? Is this behavior only specific to the chemical components used by references [22, 23, 36] or is it more general? How can it be broken?
- Taking into account that the polydispersity of nanoparticle populations is also important for their applications, is it theoretically possible to control the polydispersity with the co-solvent method independently of their mean size?
- Assuming one wants to develop simulation tools that enable accurate predictions about particle sizes in the future, which theoretical descriptions can be used as starting points? Which physical mechanisms need to be included? And how could a computationally efficient implementation of these mechanisms look like?

In the present work we model the co-solvent method with the objective to explain characteristics of the experimental results in figure 1.3 and thereby to answer, inter alia, the questions listed above.

In order to clarify the classification of the present work into the general literature on assembly of nanoparticles, it is expedient to establish a clear terminological demarcation between *spontaneous self-assembly* and *controlled assembly*. *Spontaneous self-assembly* refers to particle formation in the absence of external fields at fixed thermodynamic variables of state, i.e. if there is no further extrinsic interference after specification of the initial state. The formation of differently large particles in one single bad solvent at distinct fixed concentrations c or temperatures T, for instance, would count as spontaneous self-assembly. Inspired by the particle size dependence on injection rates in the batch implementation of the co-solvent method (cp. figure 1.3 (e)), we are going to call a particle growth process during solvent mixing *size-controlled assembly (of nanoparticles)*. From a theoretical perspective we define solvent mixing as a controlled temporal change of the state variables 'particle numbers' in an arbitrary fixed volume at temperature T. It will eventually turn out that, loosely speaking, size-controlled assembly may be understood as a synonym for the co-solvent method regardless of a batch or continuous implementation, but in a more strict context we use the term 'co-solvent method' to denote the experimental realization with all its facets while 'size-controlled assembly' implies a simplified abstraction of the latter. This abstraction concerns the translation of complicated real mixing processes into temporally changing state variables of partial volumes inside a mixer geometry as well as the neglection of hydrodynamic effects like flow shearing in micro channels. In the present work controlled assembly is just an abbreviation for size-controlled assembly.

PART I

FUNDAMENTALS

Preliminary Remark

Chapters 2 and 3 recapitulate the established theories that form the basis of the present work. We are going to model the co-solvent method by coupling solvent mixing into a theory that is commonly used to describe spontaneous self-assembly. As a preparation, chapter 2 therefore outlines eligible mathematical descriptions for spontaneous self-assembly in lipid or polymer solutions and gives an overview over the current state of the related literature. The literature overview points out respective length and time scales that have been accessed in various simulations, since these accessible scales are going to be crucial when we eventually choose a specific theory as a framework to describe the co-solvent method in the present work. Expressions for solvent mixing are derived in chapter 3 by presenting analytical descriptions for mixing processes in micromixers. The corresponding discussion focuses on the effect of flow rates v on solvent mixing, which turns out to be very similar to the effect of injection rates r_I in the batch implementation. This analogy between v and r_I is essential to explain the experimental data in figure 1.3.

Chapter 4 conceptually connects particle growth to flow rates on a basic qualitative level in consideration of chapters 2 and 3. This connection eventually motivates describing the continuous implementation of the co-solvent method by size-controlled assembly and leads to a more general formulation of the rather specific task to explain the flow rate dependencies from figure 1.3. The more general formulation is used to classify the current work with respect to the available theoretical literature about size-controlled assembly in order to complement the overview over the experimental literature we gave in chapter 1. To our current knowledge, the available theoretical literature about size-control with the co-solvent method is limited to the two recent publications by Nikoubashman et al. [35] and Spaeth et al. [38]. Based on references [35] and [38], the objectives of the present work are then stated more precisely from a theoretical perspective.

Chapter 2

Descriptions of self-assembly on different length and time scales

Since the (spontaneous) self-assembly of molecules is driven by intermolecular interactions, it is a many-body problem. On nano- to micrometer scales, many-body problems can be described by particle models or continuum theories [39]. In contrast to particle models where polymer chains are explicitly represented by a combination of several individual particles, continuum theories only describe coarse grained density fields that do not capture molecular details like chain conformations. This reduced complexity makes continuum models typically less accurate than particle models but also computationally less expensive. Thus, accuracy is sacrificed in order to speed up simulations or to access time scales that go beyond the scope of particle models. In section 2.1 we briefly discuss particle models by introducing Classical Molecular Dynamics, Brownian Dynamics, and Dissipative Particle Dynamics. Section 2.2 deals with the continuum theories. At this point it is mentioned in advance that our modeling approaches will be based on continuum theories. For this reason, we are going to discuss them in much more detail than the particle models. Particle models are mainly introduced for two reasons: to sketch the connection of continuum field theories (that also correspond to phenomenological thermodynamic approaches) to microscopic dynamics and because Nikoubashman et al. [35] apply Classical Molecular Dynamics while Spaeth et al. [38] use Dissipative Particle Dynamics.

2.1 Particle models

2.1.1 Molecular Dynamics

Molecular Dynamics constitutes the most accurate particle model. It can directly be derived from the Schrödinger equation in the limit of classical nuclear motion within a micro canonical ensemble [40]. The corresponding set of equations coincides with Newton's equations of motion,

$$M_I \frac{d^2}{dt^2} \vec{R}_I(t) = -\nabla_{\vec{R}_I} V(\vec{R}_1(t), \vec{R}_2(t), \vec{R}_3(t), ...). \tag{2.1}$$

M_I is the mass of a nucleus I, $\vec{R}_I$ its position, $\nabla_{\vec{R}_I}$ the gradient with respect to $\vec{R}_I$, and V an interaction potential. The choice of the interaction potential specifies subcategories of Molecular Dynamics. Ehrenfest Molecular Dynamics [40], Born-Oppenheimer Molecular Dynamics [41], and Car-Parinello Molecular Dynamics [42] represent so called *ab initio* methods, meaning they require only natural constants as input parameters. Here, the electronic

wave function is contained in V and has to be calculated from a separate equation. Ab initio methods are way too expensive to study length and time scales that are relevant to spontaneous self-assembly. We do not know of any publication that studies self-assembly of polymers or lipids with an ab initio method.

To avoid the calculation of electronic wave functions and to reduce computational costs significantly, V may be expanded in terms of many-body contributions according to

$$V(\vec{R}_1, \vec{R}_2, \vec{R}_3, ...) \approx \sum_I v_1(\vec{R}_I) + \sum_{I<J} v_2(\vec{R}_I, \vec{R}_J) + \sum_{I<J<K} v_3(\vec{R}_I, \vec{R}_J, \vec{R}_K) + ... \ . \tag{2.2}$$

The contributions v_i usually incorporate several empiric parameters and consequently, the combination of equations 2.1 and 2.2 is no ab initio method in general. As it involves no quantum mechanics either, this set of equations is called *Classical Molecular Dynamics*. It can be generalized to canonical or isothermal-isobaric ensembles by introducing thermostats [43] or barostats [44]. In case no external fields are applied, one has $v_1 \equiv 0$, and very often only v_2 is different from zero. Finding a suitable function v_i and the determination of its empirical parameters are highly non-trivial tasks and depend on the chemical components under consideration [45]. Particles in a Classical Molecular Dynamics simulation do not necessarily need to be nuclei of single atoms but may also constitute coarse grained particles, i.e. groups of several atoms, which requires an adaptation of force fields. A systematic procedure for such an adaptation is Essential Dynamics Coarse Graining [46]. Lennard-Jones potentials are frequently used to describe non-bonded van der Waals attractions between different particles while spring potentials often represent covalent bonds, which connect monomers of a polymer chain.

(Coarse grained) Classical Molecular Dynamics has been used in a variety of publications to study spontaneous self-assembly of lipid bilayers, micelles, and vesicles [47, 48, 49, 50, 51, 52, 53], to investigate bilayer or vesicle fusion [54, 55], and to analyze basic properties or the structure of bilayers [56, 57, 58, 59]. Typical simulated time spans in all these studies lie below 50 microseconds in simulations boxes with edge lengths of less than 100 nanometers.

2.1.2 Dissipative Particle, Langevin, and Brownian Dynamics

If the level of coarse graining becomes so high that microscopic interactions need to be described by empirical dissipative and random forces in order to capture essential dynamical features, one arrives at *Dissipative Particle Dynamics* or *Langevin Dynamics*. Both share a general form of the Hamiltonian equations,

$$\frac{d}{dt}\vec{r}_i = \frac{\vec{p}_i}{m_i} \quad \text{and} \quad \frac{d}{dt}\vec{p}_i = \vec{F}_i + \vec{F}_i^D + \vec{F}_i^R, \tag{2.3}$$

where $\vec{F}_i$ is a conservative force acting on particle i, $\vec{F}_i^D$ a dissipative force, and $\vec{F}_i^R$ a random force. The only difference between Dissipative Particle Dynamics and Langevin Dynamics are the expressions for $\vec{F}_i^D$ and $\vec{F}_i^R$ [60]: in Langevin Dynamics they obey the relations

$$\vec{F}_i^D = -\gamma \frac{d}{dt}\vec{r}_i = -\gamma \frac{\vec{p}_i}{m_i}, \quad \left\langle \vec{F}_i^R \right\rangle = 0, \quad \left\langle F_{i\mu}^R(t) F_{j\nu}^R(t') \right\rangle = 2\gamma k_B T \delta_{ij} \delta_{\mu\nu} \delta(t - t'), \tag{2.4}$$

where γ is a friction coefficient and $F_{i\mu}^R$ the μ-th component of $\vec{F}_i^R$, while in Dissipative Particle Dynamics they are defined by

$$\vec{F}_i^D = \sum_{j \neq i} \vec{F}_{ij}^D \text{ with } \vec{F}_{ij}^D = -\gamma \omega^D(|\vec{r}_{ij}|)(\vec{e}_{ij} \cdot \vec{v}_{ij})\vec{e}_{ij}$$

$$\vec{F}_i^R = \sum_{j \neq i} \vec{F}_{ij}^R \text{ with } \vec{F}_{ij}^R = \sigma \omega^R(|\vec{r}_{ij}|)\Theta_{ij}\vec{e}_{ij}, \tag{2.5}$$

where $\vec{r}_{ij} = \vec{r}_i - \vec{r}_j$, $\vec{e}_{ij} = {}^{\vec{r}_{ij}}/_{|\vec{r}_{ij}|}$, and $\vec{v}_{ij} = \vec{v}_i - \vec{v}_j$. Θ_{ij} is a random variable with zero mean and

$$\langle \Theta_{ij}(t)\Theta_{kl}(t') \rangle = (\delta_{ij}\delta_{jl} + \delta_{il}\delta_{jk})\delta(t - t').$$

ω^D and ω^R are weighting functions with $\omega^D = (\omega^R)^2$ to fulfill the fluctuation dissipation theorem. Usually it is

$$\omega^D(r) = \begin{cases} 1 - {}^r/_{r_c} & r \leq r_c \\ 0 & r > r_c \end{cases} \tag{2.6}$$

with a model dependent cutoff radius r_c. The random force conserves momentum in Dissipative Particle Dynamics, but not in Langevin Dynamics. As a consequence, Langevin Dynamics does not correctly capture hydrodynamic effects. This is why Dissipative Particle Dynamics is usually used as an explicit solvent model, and Langevin Dynamics as an implicit one – the lost or gained momentum of particles is said to be transferred to a solvent that is not modeled explicitly. Brownian Dynamics is sometimes considered to be the over-damped version of Langevin Dynamics where the inertial term ${}^{d\vec{p}_i}/_{dt}$ in equation 2.3 is neglected, while some authors use it as a synonym for Langevin Dynamics. As both Dissipative Particle Dynamics and Langevin Dynamics can be derived from classical Molecular Dynamics, there is a systematic way to determine conservative force fields from microscopic interaction potentials [61].

Originally, Dissipative Particle Dynamics was introduced with a conservative force $\vec{F}_i = \sum_{j \neq i} a_{ij}\omega^D(|\vec{r_{ij}}|)\vec{e}_{ij}$ to study hydrodynamics [62]. But with suitable adaptions of $\vec{F}_i$ it succeeds at simulating spontaneous self-assembly of vesicles or membranes [63, 64, 65, 66, 67], phase separation on membranes [68], nanoparticle targeting to a vascular surface [69], or at analyzing equilibrium structures of amphiphilic membranes [70] and their fusion with vesicles [71]. Dissipative Particle Dynamics enables an extension of length and time scales to several 100 nanometers and several 100 microseconds. Studies of spontaneous self-assembly with Langevin Dynamics are performed with similar maximum (simulated) length and time scales [72, 73, 74]. In all references cited above, individual particles are collections of multiple monomers but still represent beads of a polymer chain, i.e. chain conformations are resolved on a coarse grained level.

2.2 Continuum field theories

2.2.1 Dynamical master equation and kinetic coupling

Kawasaki and Sekimoto [75] first derived the master equation describing the temporal evolution of an α-monomer density field ρ_α, which does not resolve degrees of freedom related to molecular details like chain conformation of polymers, from Brownian Dynamics by appli-

cation of a local equilibrium approximation (assuming equilibrium statistics of chain conformations at fixed density fields) to the generalized Smoluchowksi equation [76]. The master equation is valid in canonical ensembles and reads

$$\frac{\partial \rho_\alpha}{\partial t}(\vec{r},t) = -\sum_{\gamma=1}^{\mathcal{A}} \int M_{\alpha\gamma}[\{\rho(\cdot,t)\}](\vec{r},\vec{r}\,') \frac{\delta \mathcal{F}[\{\rho(\cdot,t)\}]}{\delta \rho_\gamma(\vec{r}\,')}\, d\vec{r}\,' + \eta_\alpha(\vec{r},t) \quad \forall \alpha \in \mathcal{A} \tag{2.7}$$

with a kinetic coefficient matrix $M(\vec{r},\vec{r}\,')$ and a free energy $\mathcal{F}$, which are both functionals of the set $\{\rho(\cdot,t)\} = \{\rho_\alpha(\cdot,t)\}_{\alpha\in\mathcal{A}}$ at fixed time t. Spatial integration is performed over the system volume, $\mathcal{A}$ is the number of monomer species, $\frac{\delta\mathcal{F}[\{\rho(\cdot,t)\}]}{\delta\rho_\gamma}$ the variational derivative of $\mathcal{F}$ evaluated at $\{\rho(\cdot,t)\}$, and η_α a random noise satisfying the fluctuation dissipation theorem

$$\langle \eta_\alpha(\vec{r},t)\rangle = 0 \text{ and } \langle \eta_\alpha(\vec{r},t)\eta_\gamma(\vec{r}\,',t')\rangle = 2k_BTM_{\alpha\gamma}[\{\rho(\cdot,t)\}](\vec{r},\vec{r}\,')\delta(t-t'). \tag{2.8}$$

The free energy functional $\mathcal{F}$ is connected to the partition function Z (an equilibrium quantity!) through

$$Z = \left[\prod_{\alpha=1}^{\mathcal{A}} \int \mathcal{D}\rho_\alpha\right] e^{-\beta\mathcal{F}[\rho_1,\rho_2,...,\rho_{\mathcal{A}}]}, \tag{2.9}$$

where $\beta = 1/k_BT$ is the Boltzmann factor and $\int \mathcal{D}\rho_\alpha$ the path integral with respect to ρ_α. If polymer blends containing n_j identical chains of type $j = 1,...,J$ are considered, and a polymer type is defined by a specific sequence of N_j monomers with potentially $\mathcal{A}$ different species, the kinetic coefficient $M_{\alpha\gamma}$ can be expressed as

$$M_{\alpha\gamma}[\{\rho\}](\vec{r},\vec{r}\,') = \left\langle \sum_{j,j'=1}^{J} \sum_{i_j=1}^{n_j} \sum_{p_{j'}=1}^{n_{j'}} \sum_{s_j=1}^{N_j} \sum_{q_{j'}=1}^{N_{j'}} \frac{\partial\hat{\rho}_\alpha}{\partial \vec{R}^{(j)}_{i_j s_j}}(\vec{r}) \cdot C^{(\alpha\gamma)}_{(j,i_j,s_j),(j',p_{j'},q_{j'})} \frac{\partial\hat{\rho}_\gamma}{\partial \vec{R}^{(j')}_{p_{j'}q_{j'}}}(\vec{r}\,') \right\rangle_{\{\rho\}}.$$

$\hat{\rho}_\alpha(\vec{r}) = \sum_{j=1}^{J}\sum_{i_j=1}^{n_j}\sum_{s_j=1}^{N_j} \delta^{(j)}_{\alpha s_j}\delta(\vec{r}-\vec{R}^{(j)}_{i_j,s_j})$ is the microscopic density of α-monomers, $\vec{R}^{(j)}_{is}$ the position of the s-th monomer in chain i from type j, and

$$\delta^{(j)}_{\alpha s} = \begin{cases} 1 & \text{if an } \alpha\text{-monomer is placed at position } s \text{ in type } j \text{ polymers} \\ 0 & \text{else} \end{cases}$$

specifies the polymer architecture. $C^{(\alpha\gamma)}_{(j,i_j,s_j)(j',p_{j'},q_{j'})} \in \mathbb{R}^{3\times3}$ is a matrix block from the microscopic translational mobility matrix [75, 76] in the Smoluchowksi equation. It connects the velocity of an α-monomer at position $\vec{R}^{(j)}_{i_j s_j}$ to a force acting on a γ-monomer at $\vec{R}^{(j')}_{p_{j'}q_{j'}}$ [76]. $\langle\cdot\rangle_{\{\rho\}}$ denotes the statistical ensemble average under the constraint of fixed density fields,

$$\langle h\rangle_{\{\rho\}} = \frac{1}{\int p(\Gamma)\delta[\{\rho\}-\kappa\{\hat{\rho}(\Gamma)\}]d\Gamma} \int h(\Gamma)\delta[\{\rho\}-\kappa\{\hat{\rho}(\Gamma)\}]p(\Gamma)d\Gamma,$$

where h is a scalar function, Γ a vector in the phase space containing all monomer coordinates $\vec{R}^{(j)}_{is}$, p its probability (Boltzmann distribution), and κ an appropriate smoothing operator that can be neglected in the argument of $\langle\cdot\rangle_{\{\rho\}}$ while keeping ρ_α in $\{\rho\} = \{\rho_\alpha\}_{\alpha\in\mathcal{A}}$ smooth. Such an operator could, for instance, just replace delta functions $\delta(\vec{r}-\vec{R}^{(j)}_{is})$ in $\hat{\rho}$ by $\vec{R}^{(j)}_{is}$-centered normal distributions $\delta_\epsilon(\vec{r}-\vec{R}^{(j)}_{is}) = \frac{1}{\epsilon\sqrt{2\pi}}\exp\left[-(\vec{r}-\vec{R}^{(j)}_{is})^2/2\epsilon^2\right]$ with a sufficiently low

ϵ. Insertion of microscopic densities into the mobility coefficient yields

$$M_{\alpha\gamma}[\{\rho\}](\vec{r},\vec{r}\,')$$

$$= \left\langle \sum_{j\in J_\alpha} \sum_{j'\in J_\gamma} \sum_{i_j=1}^{n_j} \sum_{p_{j'}=1}^{n_{j'}} \sum_{s_j=1}^{N_j} \sum_{q_{j'}=1}^{N_{j'}} \delta^{(j)}_{\alpha s_j} \frac{\partial\delta(\vec{r}-\vec{R}^{(j)}_{i_j s_j})}{\partial\vec{R}^{(j)}_{i_j s_j}} \cdot C^{(\alpha\gamma)}_{(j,i_j,s_j),(j',p_{j'},q_{j'})} \delta^{(j')}_{\gamma q_{j'}} \frac{\partial\delta(\vec{r}\,'-\vec{R}^{(j')}_{p_{j'}q_{j'}})}{\partial\vec{R}^{(j')}_{p_{j'}q_{j'}}} \right\rangle_{\{\rho\}},$$

where J_α is the set of polymer types that contain monomers of species α. The explicit and closed representation of equation 2.7 varies with specification of $C^{(\alpha\gamma)}$, $\mathcal{F}$, and the construction rule for ρ_α from microscopic densities.

A particular choice of $C^{(\alpha\gamma)}_{(j,i_j,s_j),(j',p_{j'},q_{j'})} \in \mathbb{R}^{3\times3}$ determines the kinetic coupling model. If different coordinate directions are decoupled, it can be written as

$$C^{(\alpha\gamma)}_{(j,i_j,s_j),(j',p_{j'},q_{j'})} = \Lambda^{(\alpha\gamma)}_{(j,i_j,s_j),(j',p_{j'},q_{j'})}\underline{1}, \tag{2.10}$$

where $\underline{1}$ is the $\mathbb{R}^{3\times3}$ unity matrix and $\Lambda^{(\alpha\gamma)}_{(j,i_j,s_j),(j',p_{j'},q_{j'})} \in \mathbb{R}$ specifies coupling possibilities of monomers.

If kinetic coupling of beads is completely ignored, it is $\Lambda^{(\alpha\gamma)}_{(j,i_j,s_j),(j',p_{j'},q_{j'})} = \beta D_\alpha \delta_{jj'}\delta_{i_j p_{j'}}\delta_{s_j q_{j'}}$ with the diffusion coefficient of separated α-monomers D_α. This leads to

$$M_{\alpha\gamma}[\{\rho(\cdot,t)\}](\vec{r},\vec{r}\,') = -\beta D_\alpha \delta_{\alpha\gamma} \nabla_{\vec{r}} \cdot \rho_\alpha(\vec{r},t) \nabla_{\vec{r}}\delta(\vec{r}-\vec{r}\,'), \tag{2.11}$$

which is referred to as a local coupling model. In this case equation 2.7 reduces to

$$\frac{\partial\rho_\alpha}{\partial t}(\vec{r},t) = \beta D_\alpha \nabla_{\vec{r}} \cdot \left[\rho_\alpha(\vec{r},t)\nabla_{\vec{r}} \frac{\delta\mathcal{F}[\{\rho(\cdot,t)\}]}{\delta\rho_\alpha(\vec{r})}\right] + \eta_\alpha(\vec{r},t). \tag{2.12}$$

The reason why entries $M_{\alpha\gamma}$ of the mobility matrix can be expressed as differential operators is that they contain integrals over derivatives of delta functions in the form of microscopic densities and because $\int \nabla\delta(\vec{r}-\vec{r}_0)\mu(\vec{r})d\vec{r} = -\nabla\mu(\vec{r}_0)$ and $\int \nabla\delta(\vec{r}-\vec{r}_0)\cdot\vec{v}(\vec{r})\,d\vec{r} = -\nabla\cdot\vec{v}(\vec{r}_0)$ for arbitrary differentiable functions μ and $\vec{v}$. There are also different ways to derive equation 2.12 directly from Brownian Dynamics or the corresponding Fokker-Planck equation without a circuitous route via the master equation [77]. In this case the local equilibrium assumption is coupled to two-body density distribution functions [78]. The noise term η_α depends on the construction rule of ρ_α from microscopic densities [77]: if ρ_α is constructed by statistically averaging microscopic densities, the noise term vanishes and $\eta_\alpha \equiv 0$; if ρ_α is a coarse grained density obtained by temporal convolution with a smoothing kernel instead of averaging, η_α satisfies

$$\eta_\alpha(\vec{r},t) = \nabla_{\vec{r}} \cdot \left[\sqrt{\beta D_\alpha \rho_\alpha(\vec{r},t)}\sqrt{\frac{\tau_0}{\tau}}\vec{\xi}_\alpha(\vec{r},t)\right] \text{ with}$$

$$\langle\xi_{\alpha n}(\vec{r},t)\rangle = 0 \text{ and } \langle\xi_{\alpha n}(\vec{r},t)\xi_{\gamma m}(\vec{r}\,',t')\rangle = 2k_B T\delta_{\alpha\gamma}\delta_{nm}\delta(\vec{r}-\vec{r}\,')\delta(t-t'), \tag{2.13}$$

where $\xi_{\alpha n}$ is the n-th component of the random variable $\vec{\xi}_\alpha$, τ the coarse grained time scale, and τ_0 the time scale of microscopic dynamics. The functional form of the noise term in equation 2.13 is consistent with equation 2.8 [79]. Equation 2.12 can also be obtained phenomenologically by expressing fluxes in a continuity equation through $J_\alpha = \rho_\alpha v_\alpha = \rho_\alpha \beta D_\alpha \nabla\mu_\alpha$ with thermodynamic driving forces $\nabla\mu_\alpha = \nabla\frac{\delta F}{\delta\rho_\alpha}$ and the mobility βD_α [80]. In literature, local

coupling models have been applied to study spontaneous self-assembly [81, 82, 83] and to investigate microphase separation in copolymer melts [80, 84, 85].

Coupling all beads within single polymer chains by setting $\Lambda^{(\alpha\gamma)}_{(j,i_j,s_j),(j',p_{j'},q_{j'})} = \beta D_j \delta_{jj'} \delta_{i_j p_{j'}}$ leads to the non-local mobility coefficient

$$
\begin{aligned}
&M_{\alpha\gamma}[\{\rho(\cdot,t)\}](\vec{r},\vec{r}\,') \\
&= -\sum_{j\in J_\alpha\cap J_\gamma} \beta D_j \nabla_{\vec{r}} \cdot \sum_{i_j=1}^{n_j} \left\langle \left(\sum_{s_j=1}^{N_j} \delta^{(j)}_{\alpha s_j} \delta(\vec{r} - \vec{R}^{(j)}_{i_j s_j}) \right) \left(\sum_{q_j=1}^{N_j} \delta^{(j)}_{\gamma q_j} \delta(\vec{r}\,' - \vec{R}^{(j)}_{i_j q_j}) \right) \right\rangle_{\{\rho\}} \nabla_{\vec{r}\,'} \\
&= -\sum_{j\in J_\alpha\cap J_\gamma} \beta D_j \nabla_{\vec{r}} \cdot \sum_{i_j=1}^{n_j} \left\langle \hat{\rho}^{(c,j)}_{\alpha i_j}(\vec{r}) \hat{\rho}^{(c,j)}_{\gamma i_j}(\vec{r}\,') \right\rangle_{\{\rho\}} \nabla_{\vec{r}\,'} =: -\sum_{j\in J_\alpha\cap J_\gamma} \beta D_j \nabla_{\vec{r}} \cdot P^{(j)}_{\alpha\gamma}(\vec{r},\vec{r}\,') \nabla_{\vec{r}\,'}.
\end{aligned}
\tag{2.14}
$$

$\hat{\rho}^{(c,j)}_{\alpha i} = \sum_{s=1}^{N_j} \delta^{(j)}_{\alpha s} \delta(\vec{r} - \vec{R}^{(j)}_{is})$ is the density of α-monomers in a single polymer chain i of type j, D_j the center of mass diffusion coefficient of type j chains, and $P^{(j)}_{\alpha\gamma}(\vec{r},\vec{r}\,')$ the sum over corresponding two-body correlators. Note that in the local coupling model Λ is proportional to a *monomer* diffusion coefficient that is independent of the chain length N, and in the non-local coupling model Λ is proportional to the diffusion coefficient of complete *chains* [86]. If all chains of type j possess equal statistics, it is

$$
P^{(j)}_{\alpha\gamma}(\vec{r},\vec{r}\,') = \sum_{i_j=1}^{n_j} \left\langle \hat{\rho}^{(c,j)}_{\alpha i_j}(\vec{r}) \hat{\rho}^{(c,j)}_{\gamma i_j}(\vec{r}\,') \right\rangle_{\{\rho\}} = n_j \left\langle \hat{\rho}^{(c,j)}_{\alpha 1}(\vec{r}) \hat{\rho}^{(c,j)}_{\gamma 1}(\vec{r}\,') \right\rangle_{\{\rho\}}. \tag{2.15}
$$

Since the argument of $\langle \cdot \rangle_{\{\rho\}}$ contains only monomer positions in a single polymer chain $i_j = 1$ and since the statistics of single polymer chains become less affected by prescribed density constraints with increasing particle number in a system under consideration, the correlators for decoupled polymer chains in the macroscopic limit can be approximated by

$$
P^{(j)}_{\alpha\gamma}(\vec{r},\vec{r}\,') = n_j \left\langle \rho^{(c,j)}_{\alpha 1}(\vec{r}) \rho^{(c,j)}_{\gamma 1}(\vec{r}\,') \right\rangle_c, \tag{2.16}
$$

where $\langle \cdot \rangle_c$ is the statistical average for a single chain in equilibrium. In a copolymer melt with only one polymer type of arbitrary architecture the sum over j in equation 2.14 collapses and equation 2.7 becomes

$$
\frac{\partial \rho_\alpha}{\partial t}(\vec{r},t) = \beta D \sum_{\gamma=1}^{\mathcal{A}} \nabla_{\vec{r}} \cdot \int P_{\alpha\gamma}(\vec{r},\vec{r}\,') \nabla_{\vec{r}\,'} \frac{\delta \mathcal{F}[\{\rho(\cdot,t)\}]}{\delta \rho_\gamma(\vec{r}\,')} \, d\vec{r}\,' + \eta_\alpha(\vec{r},t). \tag{2.17}
$$

The diffusion coefficient of respective chains is $D = {}^{D_0}/_N$ with a bead diffusion coefficient D_0 and the chain length N. Upon calculation of $M_{\alpha\gamma}$, the noise term η_α is specified by equation 2.8. An alternative deviation of equation 2.17 from microscopic dynamics can be found in the appendix of reference [86]. In case an AB-diblock-copolymer solution is considered, where $j = 1$ denotes the polymer and $j = 2, ..., J$ with $J = \mathcal{A} - 1$ solvents consisting of $N_j = 1$ monomer from species S_j, it is

$$
\delta^{(1)}_{As} = \begin{cases} 1, & 1 \le s \le s' \\ 0, & s' < s < N_1 \end{cases}, \; \delta^{(1)}_{Bs} = \begin{cases} 0, & 1 \le s \le s' \\ 1, & s' < s < N_1 \end{cases}, \text{ and } \delta^{(1)}_{S_j s} = 0 \, \forall \, s \in [1, N_1] \tag{2.18}
$$

as well as

$$\delta^{(i)}_{S_j 1} = \begin{cases} 1 & i = j \\ 0 & i \neq j \end{cases} \text{ and } \delta^{(j)}_{A1} = \delta^{(j)}_{B1} = 0 \text{ for } i, j > 1 \tag{2.19}$$

in equation 2.14. The associated set of dynamical equations reads

$$\frac{\partial \rho_\alpha}{\partial t}(\vec{r}, t) = \beta \sum_{\gamma \in \{A,B\}} D_1 \nabla_{\vec{r}} \cdot \int P^{(1)}_{\alpha\gamma}(\vec{r}, \vec{r}\,') \nabla_{\vec{r}\,'} \frac{\delta \mathcal{F}[\{\rho(\cdot, t)\}]}{\delta \rho_\gamma(\vec{r}\,')} \, d\vec{r}\,' + \eta_\alpha(\vec{r}, t) \text{ for } \alpha \in \{A, B\}$$

$$\frac{\partial \rho_{S_j}}{\partial t}(\vec{r}, t) = \beta D_j \nabla_{\vec{r}} \cdot \int P^{(j)}_{S_j S_j}(\vec{r}, \vec{r}\,') \nabla_{\vec{r}\,'} \frac{\delta \mathcal{F}[\{\rho(\cdot, t)\}]}{\delta \rho_{S_j}(\vec{r}\,')} \, d\vec{r}\,' + \eta_{S_j}(\vec{r}, t) \text{ for } j = 2, 3, ..., J. \tag{2.20}$$

Because pair correlators $P_{\alpha\gamma}$ are zero for $(\alpha, \gamma) = (A, S_j), (B, S_j), (S_i, S_j)$ and corresponding permutations with $i \neq j$, equations 2.20 may be written in accordance to 2.17 as

$$\frac{\partial \rho_\alpha}{\partial t}(\vec{r}, t) = \beta \sum_{\gamma \in \mathcal{C}} D_{j(\gamma)} \nabla_{\vec{r}} \cdot \int P^{(j(\gamma))}_{\alpha\gamma}(\vec{r}, \vec{r}\,') \nabla_{\vec{r}\,'} \frac{\delta \mathcal{F}[\{\rho(\cdot, t)\}]}{\delta \rho_\gamma(\vec{r}\,')} \, d\vec{r}\,' + \eta_\alpha(\vec{r}, t) \, \forall \, \alpha \in \mathcal{C}, \tag{2.21}$$

where

$$\mathcal{C} = \{A, B, S_2, ..., S_J\} \text{ and } j(\gamma) = \begin{cases} 1, & \gamma \in \{A, B\} \\ j, & \gamma = S_j \end{cases} . \tag{2.22}$$

$D_{j(\gamma)}$ is the diffusion coefficient of the sole polymer type that contains the γ-monomers. Nonlocal coupling models are applied to analyze structure formation in copolymer melts [86, 87], and to study spontaneous self-assembly [88, 89]. Simulated time spans in these studies range to ≈ 0.75 seconds in simulation boxes with side lengths of several hundred nanometers. Continuum descriptions therefore allow to simulate much larger times scales than particle models, where simulated time spans are typically shorter than several 100 microseconds as discussed in section 2.1.

2.2.2 Self Consistent Field Theory (SCF)

Performing calculations with dynamic field theories requires the specification of a free energy functional $\mathcal{F}$ in the master equation 2.7. $\mathcal{F}$ can be obtained by rewriting partition functions in conformity with equation 2.9. Such path integral representations typically constitute intermediate results of equilibrium field theories. The most prominent representatives of these theories are the Density Functional Theory and the Self Consistent Field Theory. Both are based on introducing a set of external potentials $\{\omega\}$, but differ in the way the potentials are handled. In Density Functional Theory they are considered to depend on densities and a bijective functional $\{\rho\}[\{\omega\}]$ is inverted with certain approximations in order to express free energies or partition functions in terms of densities only. Equilibrium properties are subsequently calculated by minimization with respect to $\{\rho\}$. In Self Consistent Field Theory $\{\omega\}$ is regarded as a set of independent variables that is eventually determined by an extremization procedure, which allows to investigate equilibrium states without the necessity to perform a functional inversion. The two approaches are interrelated [90] and the current subsection restricts to the Self Consistent Field Theory because it is applied at some point in the present work. The recapitulation follows the review articles [91] and [92].

In doing so, a canonical ensemble with n_j identical polymer molecules of type $j \in \{1, ..., J\}$

is considered, each consisting of N_j monomers with potentially different species $\alpha \in \{1, ..., \mathcal{A}\}$, just like in subsection 2.2.1. This time the polymers are continuous Gaussian chains, and the i-th chain of type j is parameterized by a function $\vec{R}_i^{(j)}(s)$ with $s \in [0, N_j]$. The consideration of a continuum limit proves convenient in the current section but discrete chains would reproduce analogous results. The microscopic density of α-monomers in a system with continuous chains is defined as

$$\hat{\rho}_\alpha(\vec{r}) = \sum_{j=1}^{J} \sum_{i_j=1}^{n_j} \int_0^{N_j} \delta(\vec{r} - \vec{R}_{i_j}^{(j)}(s)) \gamma_{\alpha,j}(s)\, ds, \tag{2.23}$$

where $\gamma_{\alpha,j}(s)$ specifies the architecture of a polymer chain similar to $\delta_{\alpha s}^{(j)}$: $\gamma_{\alpha,j}(s)$ is 1 if a monomer of species α is placed at position s in a chain of type j or zero otherwise. The corresponding partition function reads

$$Z = \prod_{j=1}^{J} \left[\frac{1}{n_j! V^{n_j}} \prod_{i_j=1}^{n_j} \int \mathcal{D}\vec{R}_{i_j}^{(j)}\, P_j[\vec{R}_{i_j}^{(j)}; N_j] \right] e^{-\beta U[\{\hat{\rho}\}]}. \tag{2.24}$$

U is a functional that contains monomer interactions and depends on the set of microscopic densities $\{\hat{\rho}\} = \{\hat{\rho}_1, \hat{\rho}_2, ..., \hat{\rho}_\mathcal{A}\}$. $P_j[\vec{R}; s']$ is proportional to the probability density that a segment of length s' in a single Gaussian polymer chain of type j takes the conformation $\vec{R}$. It is defined by

$$P_j[\vec{R}; s'] = \mathcal{N}_j(s') e^{-\sum_{\alpha=1}^{\mathcal{A}} \frac{3}{2b_\alpha^2} \int_0^{s'} \left| \frac{d\vec{R}}{ds}(s) \right|^2 \gamma_{\alpha,j}(s)\, ds} \tag{2.25}$$

with the normalization constant

$$\mathcal{N}_j \coloneqq \mathcal{N}_j(s') = V \left(\int \mathcal{D}\vec{R}\, e^{-\sum_{\alpha=1}^{\mathcal{A}} \frac{3}{2b_\alpha^2} \int_0^{s'} \left| \frac{d\vec{R}}{ds}(s) \right|^2 \gamma_{\alpha,j}(s)\, ds} \right)^{-1} \tag{2.26}$$

and the Kuhn length b_α associated to a particular monomer species. Path integrals operate on anything to their right, including $e^{-\beta U[\{\hat{\rho}\}]}$ in equation 2.24. This exponential expression often contains mathematically complicated coupling terms among polymer chains that make a direct evaluation of Z impossible. To develop a convenient description, individual chains can be decoupled by introducing potential fields ω_α in order to substitute microscopic densities $\hat{\rho}_\alpha$ by $\vec{R}_i^{(j)}$-independent field variables ρ_α via the relation

$$f[\{\hat{\rho}\}] = \prod_{\alpha=1}^{\mathcal{A}} \int \mathcal{D}\rho_\alpha\, \delta[\rho_\alpha - \hat{\rho}_\alpha] f[\{\rho\}] = \prod_{\alpha=1}^{\mathcal{A}} \int \mathcal{D}\rho_\alpha \int_{i\infty} \mathcal{D}\omega_\alpha\, e^{\int \omega_\alpha(\vec{r})(\rho_\alpha(\vec{r}) - \hat{\rho}_\alpha(\vec{r}))\, d\vec{r}} f[\{\rho\}]$$

with $\{\rho\} = \{\rho_1, \rho_2, ..., \rho_\mathcal{A}\}$ and $f[\{\hat{\rho}\}] = \exp(-\beta U[\{\hat{\rho}\}])$. The integral subscript $i\infty$ indicates that every ω_α is integrated along the imaginary axis. Employing the above relation in equation 2.24 immediately leads to

$$Z = \left[\prod_{\alpha=1}^{\mathcal{A}} \int \mathcal{D}\rho_\alpha \int_{i\infty} \mathcal{D}\omega_\alpha \right] \prod_{j=1}^{J} \left[\frac{1}{n_j! V^{n_j}} \prod_{i_j=1}^{n_j} \int \mathcal{D}\vec{R}_{i_j}^{(j)}\, P_j[\vec{R}_{i_j}^{(j)}; N_j] \right] e^{-\beta U[\{\rho\}]}$$

$$\times \prod_{\alpha=1}^{\mathcal{A}} e^{\int \omega_\alpha(\vec{r})(\rho_\alpha(\vec{r}) - \hat{\rho}_\alpha(\vec{r}))\, d\vec{r}}$$

$$= \left[\prod_{\alpha=1}^{\mathcal{A}} \int \mathcal{D}\rho_\alpha \int_{i\infty} \mathcal{D}\omega_\alpha\right] e^{-\beta U[\{\rho\}]+\sum_{\alpha=1}^{\mathcal{A}} \int \omega_\alpha(\vec{r})\rho_\alpha(\vec{r})\, d\vec{r}}$$

$$\times \prod_{j=1}^{J} \left[\frac{1}{n_j! V^{n_j}} \prod_{i_j=1}^{n_j} \int \mathcal{D}\vec{R}_{i_j}^{(j)}\, P_j[\vec{R}_{i_j}^{(j)}; N_j]\right] e^{-\sum_{\alpha=1}^{\mathcal{A}} \int \omega_\alpha(\vec{r})\hat{\rho}_\alpha(\vec{r})\, d\vec{r}}.$$

After inserting the microscopic densities $\hat{\rho}_\alpha$ from equation 2.23, Z becomes

$$Z = \left[\prod_{\alpha=1}^{\mathcal{A}} \int \mathcal{D}\rho_\alpha \int_{i\infty} \mathcal{D}\omega_\alpha\right] e^{-\beta U[\{\rho\}]+\sum_{\alpha=1}^{\mathcal{A}} \int \omega_\alpha(\vec{r})\rho_\alpha(\vec{r})\, d\vec{r}}$$

$$\times \prod_{j=1}^{J} \left[\frac{1}{n_j! V^{n_j}} \prod_{i_j=1}^{n_j} \int \mathcal{D}\vec{R}_{i_j}^{(j)}\, P_j[\vec{R}_{i_j}^{(j)}; N_j] e^{-\sum_{\alpha=1}^{\mathcal{A}} \int_0^{N_j} \gamma_{\alpha,j}(s)\omega_\alpha(\vec{R}_{i_j}^{(j)}(s))\, ds}\right],$$

and introducing the partition function of a single chain in external fields $\{\omega\} = \{\omega_1, \omega_2, ..., \omega_{\mathcal{A}}\}$ given by

$$Q_j[\{\omega\}] = \int \mathcal{D}\vec{R}\, P_j[\vec{R}; N_j] e^{-\sum_{\alpha=1}^{\mathcal{A}} \int_0^{N_j} \omega_\alpha(\vec{R}(s))\gamma_{\alpha,j}(s)\, ds}, \tag{2.27}$$

it simplifies to

$$Z = \left[\prod_{\alpha=1}^{\mathcal{A}} \int \mathcal{D}\rho_\alpha \int_{i\infty} \mathcal{D}\omega_\alpha\right] e^{-\beta \mathcal{F}[\{\rho\},\{\omega\}]} \tag{2.28}$$

with

$$\beta\mathcal{F}[\{\rho\},\{\omega\}] = \beta U[\{\rho\}] - \sum_{\alpha=1}^{\mathcal{A}} \int \omega_\alpha(\vec{r})\rho_\alpha(\vec{r})\, d\vec{r} - \sum_{j=1}^{J} \ln\left(\frac{1}{n_j!} \frac{Q_j^{n_j}[\{\omega\}]}{V^{n_j}}\right)$$

$$\approx \beta U[\{\rho\}] - \sum_{\alpha=1}^{\mathcal{A}} \int \omega_\alpha(\vec{r})\rho_\alpha(\vec{r})\, d\vec{r} - \sum_{j=1}^{J} n_j \left[\ln\left(\frac{Q_j[\{\omega\}]}{n_j V}\right) + 1\right], \tag{2.29}$$

where chain statistics are solely contained in Q_j. The second line of equation 2.29 is obtained by application of Stirling's formula. '+1' in the last term is often neglected as it only contributes a term which is constant in a canonical ensemble.

The central approximation in the Self Consistent Field Theory is a saddle point approximation of the exponent in equation 2.28, i.e. $\mathcal{F}$, to find the configuration $(\{\rho\},\{\omega\})$ that contributes most to Z. Minimizing by means of $\frac{\delta\mathcal{F}}{\delta\omega_\alpha(\vec{r})} = 0\, \forall \alpha \in \{1, ..., \mathcal{A}\}$ establishes a relation between ρ_α and $\{\omega\}$, namely

$$\rho_\alpha(\vec{r})[\{\omega\}] = \langle \hat{\rho}_\alpha(\vec{r}) \rangle [\{\omega\}] = -\sum_{j=1}^{J} n_j \frac{\delta \ln(Q_j[\{\omega\}])}{\delta\omega_\alpha(\vec{r})} = -\sum_{j=1}^{J} \frac{n_j}{Q_j[\{\omega\}]} \frac{\delta Q_j[\{\omega\}]}{\delta\omega_\alpha(\vec{r})}, \tag{2.30}$$

where $\langle \cdot \rangle$ denotes the canonical ensemble average of non-interacting chains subject to external fields $\{\omega\}$. Maximization of $\mathcal{F}$ with respect to $\{\rho\}$ leads to

$$\omega_\alpha(\vec{r})[\{\rho\}] = \frac{\delta\beta U[\{\rho\}]}{\delta\rho_\alpha(\vec{r})}. \tag{2.31}$$

Equations 2.30 and 2.31 form a closed set of equations for $\{\omega\}$ and $\{\rho\}$ that can be solved self-consistently to calculate density profiles in equilibrium. This procedure has been applied to simulate spontaneously self-assembled nanoparticles [93]. Corresponding calculations of

equilibrium structures were also done with Density Functional Theory [94].

A connection to dynamic field theories can be drawn by only performing the minimization with respect to $\{\omega\}$ and approximating equation 2.28 by

$$Z \approx \prod_{\alpha=1}^{\mathcal{A}} \int \mathcal{D}\rho_\alpha e^{-\beta\mathcal{F}[\{\rho\},\{\omega\}[\{\rho\}]]}. \tag{2.32}$$

Equation 2.32 corresponds to equation 2.9. Conclusively, it allows to use the composition of equation 2.29 with the inversion of 2.30, $\{\omega\}[\{\rho\}]$, as the free energy on the right hand side in the dynamical equation 2.7. Since the saddle point approximation neglects fluctuations in the potential fields, it is a mean field description. Explicitly calculating $\{\omega\}[\{\rho\}]$ by inverting equation 2.30 would correspond to a Density Functional approach.

When self-assembly is described by External Potential Dynamics, a formalism that will be introduced in subsection 2.2.4, it proves advantageous to express densities in terms of potential fields rather than the other way around, i.e. to use $\mathcal{F}[\{\rho\}[\{\omega\}],\{\omega\}]$ instead of $\mathcal{F}[\{\rho\},\{\omega\}[\{\rho\}]]$, because this leads to an explicit ω-representation of the corresponding dynamical equation (cp. equation 2.73 in advance). To calculate $\rho_\alpha[\{\omega\}]$ the exact procedure from the Self Consistent Field Theory can be applied. That procedure uses the end-segment distribution functions

$$g_j(\vec{r},s) = \int \mathcal{D}\vec{R}\, P_j[\vec{R};s] e^{-\sum_{\alpha=1}^{\mathcal{A}} \int_0^s \omega_\alpha(\vec{R}(s'))\gamma_{\alpha,j}(s')\,ds'} \delta(\vec{r}-\vec{R}(s)) \tag{2.33}$$

of Gaussian chains. It can be shown that g_j obeys the inhomogeneous diffusion equation

$$\left[\frac{\partial}{\partial s} + \sum_{\alpha=1}^{\mathcal{A}} \gamma_{\alpha,j}(s)\left(-\frac{b_\alpha^2}{6}\Delta + \omega_\alpha(\vec{r})\right)\right] g_j(\vec{r},s) = 0 \text{ with } g_j(\vec{r},0) = 1 \tag{2.34}$$

[95], and is thus accessible in simulations without too much computational effort. The partition function Q_j from equation 2.27 can be written as

$$Q_j = \int g_j(\vec{r},N_j)d\vec{r}. \tag{2.35}$$

Its variation is

$$\left.\frac{d}{d\epsilon}\right|_{\epsilon=0} Q_j[...,\omega_\vartheta+\epsilon\eta,...] = \int \mathcal{D}\vec{R}\, P_j[\vec{R};N_j] \left.\frac{d}{d\epsilon}\right|_{\epsilon=0} e^{-\sum_{\alpha=1}^{\mathcal{A}} \int_0^{N_j} \left[\omega_\alpha(\vec{R}(s))+\delta_{\alpha\vartheta}\,\epsilon\eta(\vec{R}(s))\right]\gamma_{\alpha,j}(s)\,ds}$$

$$= -\int_0^{N_j} \left[\int \mathcal{D}\vec{R}\, P_j[\vec{R},N_j] e^{-\sum_{\alpha=1}^{\mathcal{A}} \int_0^{N_j} \omega_\alpha(\vec{R}(s))\gamma_{\alpha,j}(s)\,ds}\right] \gamma_{\vartheta,j}(s')\eta(\vec{R}(s'))\,ds'$$

$$= -\int \left\{\int_0^{N_j} \left[\int \mathcal{D}\vec{R}\, P_j[\vec{R};N_j] e^{-\sum_{\alpha=1}^{\mathcal{A}} \int_0^{N_j} \omega_\alpha(\vec{R}(s))\gamma_{\alpha,j}(s)\,ds}\right] \gamma_{\vartheta,j}(s')\delta(\vec{r}-\vec{R}(s'))\,ds'\right\} \eta(\vec{r})\,d\vec{r}$$

and thus, the functional derivative reads

$$\frac{\delta Q_j}{\delta\omega_\vartheta(\vec{r})} = -\int_0^{N_j} \gamma_{\vartheta,j}(s') \left[\int \mathcal{D}\vec{R}\, P_j[\vec{R};N_j] e^{-\sum_{\alpha=1}^{\mathcal{A}} \int_0^{N_j} \omega_\alpha(\vec{R}(s))\gamma_{\alpha,j}(s)\,ds}\right] \delta(\vec{r}-\vec{R}(s'))\,ds'. \tag{2.36}$$

Factorizing

$$P_j[\vec{R};N_j]e^{-\sum_{\alpha=1}^{\mathcal{A}}\int_0^{N_j}\omega_\alpha(\vec{R}(s))\gamma_{\alpha,j}(s)\,ds}$$

$$=\mathcal{N}_j e^{-\sum_{\alpha=1}^{\mathcal{A}}\frac{3}{2b_\alpha^2}\int_0^{N_j}\left|\frac{d\vec{R}}{ds}(s)\right|^2\gamma_{\alpha,j}(s)\,ds}e^{-\sum_{\alpha=1}^{\mathcal{A}}\int_0^{N_j}\omega_\alpha(\vec{R}(s))\gamma_{\alpha,j}(s)\,ds}$$

into

$$\mathcal{N}_{j-}\,e^{-\sum_{\alpha=1}^{\mathcal{A}}\frac{3}{2b_\alpha^2}\int_0^{s'}\left|\frac{d\vec{R}}{ds}(s)\right|^2\gamma_{\alpha,j}(s)\,ds}e^{-\sum_{\alpha=1}^{\mathcal{A}}\int_0^{s'}\omega_\alpha(\vec{R}(s))\gamma_{\alpha,j}(s)\,ds}$$

$$\times\mathcal{N}_{j+}\,e^{-\sum_{\alpha=1}^{\mathcal{A}}\frac{3}{2b_\alpha^2}\int_{s'}^{N_j}\left|\frac{d\vec{R}}{ds}(s)\right|^2\gamma_{\alpha,j}(s)\,ds}e^{-\sum_{\alpha=1}^{\mathcal{A}}\int_{s'}^{N_j}\omega_\alpha(\vec{R}(s))\gamma_{\alpha,j}(s)\,ds} \tag{2.37}$$

with the definitions

$$\mathcal{N}_{j-}=V\left(\int\mathcal{D}\vec{R}_-\,e^{-\sum_{\alpha=1}^{\mathcal{A}}\frac{3}{2b_\alpha^2}\int_0^{s'}\left|\frac{dR}{ds}(s)\right|^2\gamma_{\alpha,j}(s)ds}\right)^{-1}$$

and

$$\mathcal{N}_{j+}=\left(\int\mathcal{D}\vec{R}_+\,e^{-\sum_{\alpha=1}^{\mathcal{A}}\frac{3}{2b_\alpha^2}\int_{s'}^{N_j}\left|\frac{dR}{ds}(s)\right|^2\gamma_{\alpha,j}(s)ds}\right)^{-1},$$

where $\int\mathcal{D}\vec{R}_{-/+}$ denotes the path integral over the restrictions $\vec{R}(s)|_{s\leq/>s'}$, allows to rewrite the functional derivative after substitution $s\mapsto N_j-s$ of the integration variable in the second line of equation 2.37 and in $\mathcal{N}_{j+}$ as

$$\frac{\delta Q_j}{\delta\omega_\vartheta(\vec{r})}=-\int_0^{N_j}\gamma_{\vartheta,j}(s')\Bigg[\int\mathcal{D}\vec{R}\,P_j[\vec{R};s']e^{-\sum_{\alpha=1}^{\mathcal{A}}\int_0^{s'}\omega_\alpha(\vec{R}(s))\gamma_{\alpha,j}(s)\,ds}\delta(\vec{r}-\vec{R}(s'))$$

$$\times\mathcal{N}_{j+}\,e^{-\sum_{\alpha=1}^{\mathcal{A}}\frac{3}{2b_\alpha^2}\int_0^{N_j-s'}\left|\frac{d\vec{R}}{ds}(N_j-s)\right|^2\gamma_{\alpha,j}(N_j-s)\,ds}e^{-\sum_{\alpha=1}^{\mathcal{A}}\int_0^{N_j-s'}\omega_\alpha(\vec{R}(N_j-s))\gamma_{\alpha,j}(N_j-s)\,ds}\Bigg]\,ds'$$

$$=-\int_0^{N_j}\gamma_{\vartheta,j}(s')\Bigg[\int\mathcal{D}\vec{R}_-\,\left\{P_j[\vec{R};s']e^{-\sum_{\alpha=1}^{\mathcal{A}}\int_0^{s'}\omega_\alpha(\vec{R}(s))\gamma_{\alpha,j}(s)\,ds}\delta(\vec{r}-\vec{R}(s'))\right\}$$

$$\times\int\mathcal{D}\vec{R}_+\left\{\mathcal{N}_{j+}\,e^{-\sum_{\alpha=1}^{\mathcal{A}}\frac{3}{2b_\alpha^2}\int_0^{N_j-s'}\left|\frac{d\vec{R}}{ds}(N_j-s)\right|^2\gamma_{\alpha,j}(N_j-s)\,ds}\right.$$

$$\left.\times\,e^{-\sum_{\alpha=1}^{\mathcal{A}}\int_0^{N_j-s'}\omega_\alpha(\vec{R}(N_j-s))\gamma_{\alpha,j}(N_j-s)\,ds}\right\}\Bigg]\,ds' \tag{2.38}$$

Replacing $\mathcal{D}\vec{R}_-$ by $\mathcal{D}\vec{R}$ in $\mathcal{N}_{j-}$ and in equation 2.38 does not change its value on the right hand side because the integrands in both equation 2.38 and $\mathcal{N}_{j-}$ only depend on $\vec{R}|_{s\leq s'}$. Inserting the functions $\vec{R}^{(+)}(s)=\vec{R}(N_j-s)$ and $\gamma_{\alpha,j}^{(+)}(s)=\gamma_{\alpha,j}(N_j-s)$, $\mathcal{D}\vec{R}_+$ can be substituted by $\mathcal{D}\vec{R}_-^{(+)}\delta(\vec{r}-\vec{R}^{(+)}(N_j-s'))$ in both $\mathcal{N}_{j+}$ and equation 2.38, where $\mathcal{D}\vec{R}_-^{(+)}$ denotes the path integral over restrictions $\vec{R}^{(+)}(s)|_{s\leq N_j-s'}$ and the delta function accounts for the fact that $\vec{R}(s')=\vec{R}^{(+)}(N_j-s')$ is excluded from $\mathcal{D}\vec{R}_+$. Further substituting $\mathcal{D}\vec{R}_-^{(+)}\delta(\vec{r}-\vec{R}^{(+)}(N_j-$

$s')) \mapsto \mathcal{D}\vec{R}^{(+)}\delta(\vec{r}-\vec{R}^{(+)}(N_j-s'))$ and rewriting

$$\mathcal{N}_{j+} = V\left(V\int \mathcal{D}\vec{R}^{(+)}\delta(\vec{r}-\vec{R}^{(+)}(N_j-s'))e^{-\sum_{\alpha=1}^{\mathcal{A}}\frac{3}{2b_\alpha^2}\int_0^{N_j-s'}\left|\frac{dR^{(+)}}{ds}(s)\right|^2\gamma_{\alpha,j}^{(+)}(s)ds}\right)^{-1}$$

$$= V\left(\left[\int d\vec{r}\right]\int \mathcal{D}\vec{R}^{(+)}\delta(\vec{r}-\vec{R}^{(+)}(N_j-s'))e^{-\sum_{\alpha=1}^{\mathcal{A}}\frac{3}{2b_\alpha^2}\int_0^{N_j-s'}\left|\frac{dR^{(+)}}{ds}(s)\right|^2\gamma_{\alpha,j}^{(+)}(s)ds}\right)^{-1}$$

$$= V\left(\int \mathcal{D}\vec{R}^{(+)}\left[\int \delta(\vec{r}-\vec{R}^{(+)}(N_j-s'))d\vec{r}\right]e^{-\sum_{\alpha=1}^{\mathcal{A}}\frac{3}{2b_\alpha^2}\int_0^{N_j-s'}\left|\frac{dR^{(+)}}{ds}(s)\right|^2\gamma_{\alpha,j}^{(+)}(s)ds}\right)^{-1}$$

$$= V\left(\int \mathcal{D}\vec{R}^{(+)}e^{-\sum_{\alpha=1}^{\mathcal{A}}\frac{3}{2b_\alpha^2}\int_0^{N_j-s'}\left|\frac{dR^{(+)}}{ds}(s)\right|^2\gamma_{\alpha,j}^{(+)}(s)ds}\right)^{-1}$$

finally yields

$$\frac{\delta Q_j}{\delta\omega_\vartheta(\vec{r})} = -\int_0^{N_j}\gamma_{\vartheta,j}(s')\left[\int \mathcal{D}\vec{R}\left\{P_j[\vec{R};s']e^{-\sum_{\alpha=1}^{\mathcal{A}}\int_0^{s'}\omega_\alpha(\vec{R}(s))\gamma_{\alpha,j}(s)\,ds}\delta(\vec{r}-\vec{R}(s'))\right\}\right.$$

$$\left.\times\int \mathcal{D}\vec{R}^{(+)}\left\{P_j[\vec{R}^{(+)};N_j-s']e^{-\sum_{\alpha=1}^{\mathcal{A}}\int_0^{N_j-s'}\omega_\alpha(\vec{R}^{(+)}(s))\gamma_{\alpha,j}^{(+)}(s)\,ds}\delta(\vec{r}-\vec{R}^{(+)}(N_j-s'))\right\}\right]ds'$$

$$= -\int_0^{N_j}\gamma_{\vartheta,j}(s')\left[g_j(\vec{r},s')\times g_j'(\vec{r},N_j-s')\right]ds'. \tag{2.39}$$

$g_j'(\vec{r},s)$ also fulfills the diffusion equation 2.34 (after substituting $\gamma_{\alpha,j}(s)$ by $\gamma_{\alpha,j}^{(+)}(s)$) because it is defined analogously to g_j in equation 2.33. Insertion of equation 2.39 into equation 2.30 enables the calculation of densities $\{\rho\}$ for prescribed potential fields $\{\omega\}$ via g and g', which are specified by equation 2.34.

2.2.3 Random Phase Approximation

The Random Phase Approximation (RPA) is often used in tandem with the Self Consistent Field Theory to study fluctuations around an equilibrium or metastable reference state [96, 97, 98]. In the present section the RPA is performed to bridge the gap between the Self Consistent Field Theory and so-called Flory-Huggins-de Gennes free energy functionals that are utilized in parts of the current work. A replacement of the SCF free energy (equation 2.29) by a Flory-Huggins-de Gennes expression restricts the validity of the free energy to states close to the reference state. However, it allows a speed up of simulations because the end-segment distribution functions g_j and g_j' do not have to be calculated. Inserting a Flory-Huggins-de Gennes approximation to the free energy into dynamic field theories even allows to perform analytically solvable perturbation treatments of the dynamical equations. Such a perturbation treatment will play a central role in interpreting figure 1.3 later on. The RPA also establishes a connection between the structure factor accessible from light scattering experiments and Flory-Huggins interaction parameters that appear in Flory-Huggins-de Gennes free energy functionals [99].

There are different starting points to derive a RPA for a particular system [100]. Here, a

second order Taylor expansion of the free energy functional from equation 2.29 is presented. To this end both the potential fields and the densities are expanded according to

$$\omega_\alpha = \omega_\alpha^{(0)} + \delta\omega_\alpha \text{ and } \rho_\alpha = \rho_\alpha^{(0)} + \delta\rho_\alpha \;\forall\; \alpha, \tag{2.40}$$

where $\omega_\alpha^{(0)}$ and $\rho_\alpha^{(0)}$ are solutions to equations 2.30 and 2.31, i.e. saddle points of the Self Consistent Field Theory, and $\delta\omega_\alpha$ and $\delta\rho_\alpha$ small fluctuations. The second order Taylor expansion of $\mathcal{F}$ is then given by

$$\begin{aligned}\beta\mathcal{F}[\{\rho\},\{\omega\}] &= \beta\mathcal{F}[\{\rho^{(0)}\},\{\omega^{(0)}\}] \\ &+\frac{1}{2}\sum_{\alpha,\gamma=1}^{\mathcal{A}}\int\int\left[(\beta U)^{(2)}_{\alpha\gamma}(\vec{r},\vec{r}\,')\delta\rho_\alpha(\vec{r})\delta\rho_\gamma(\vec{r}\,') + K_{\alpha\gamma}(\vec{r},\vec{r}\,')\delta\omega_\alpha(\vec{r})\delta\omega_\gamma(\vec{r}\,')\right]d\vec{r}\,'d\vec{r}\end{aligned} \tag{2.41}$$

with the short hand notations

$$(\beta U)^{(2)}_{\alpha\gamma}(\vec{r},\vec{r}\,') = \frac{\delta^2(\beta U\{\rho^{(0)}\})}{\delta\rho_\alpha(\vec{r})\delta\rho_\gamma(\vec{r}\,')} \tag{2.42}$$

and

$$K_{\alpha\gamma}(\vec{r},\vec{r}\,') = \sum_{j=1}^{J} n_j \frac{\delta^2 \ln(Q_j[\{\omega^{(0)}\}])}{\delta\omega_\alpha(\vec{r})\delta\omega_\gamma(\vec{r}\,')}. \tag{2.43}$$

By utilizing equation 2.30 density variations can be expressed in terms of potential field variations according to

$$\delta\rho_\alpha(\vec{r}) = -\sum_{\gamma=1}^{\mathcal{A}}\int K_{\alpha\gamma}(\vec{r},\vec{r}\,')\delta\omega_\gamma(\vec{r}\,')\,d\vec{r}\,'. \tag{2.44}$$

Due to the Hohenberg-Kohn theorem [101] there exists a functional inverse to $K_{\alpha\gamma}$, in the following denoted by $K^{-1}_{\alpha\gamma}$, which obeys the relation

$$\sum_{\gamma=1}^{\mathcal{A}}\int K^{-1}_{\alpha\gamma}(\vec{r},\vec{r}\,'')K_{\gamma\beta}(\vec{r}\,'',\vec{r}\,')\,d\vec{r}\,'' = \delta_{\alpha\beta}\delta(\vec{r}-\vec{r}\,'). \tag{2.45}$$

This relation allows to write

$$\delta\omega_\alpha(\vec{r}) = -\sum_{\beta=1}^{\mathcal{A}}\int K^{-1}_{\alpha\beta}(\vec{r},\vec{r}\,')\delta\rho_\beta(\vec{r}\,')\,d\vec{r}\,'. \tag{2.46}$$

Insertion of $\delta\omega_\alpha$ into equation 2.41 and eliminating $\omega^{(0)}$-dependencies by means of equation 2.31 yields

$$\begin{aligned}\beta\mathcal{F}[\{\rho\}] &= \beta\mathcal{F}[\{\rho^{(0)}\}] \\ &+\frac{1}{2}\sum_{\alpha,\gamma=1}^{\mathcal{A}}\int\int\left[(\beta U)^{(2)}_{\alpha\gamma}(\vec{r},\vec{r}\,') + K^{-1}_{\alpha\gamma}(\vec{r},\vec{r}\,')\right]\delta\rho_\alpha(\vec{r})\delta\rho_\gamma(\vec{r}\,')\,d\vec{r}\,'d\vec{r},\end{aligned} \tag{2.47}$$

which is the general form of the RPA expansion. $(\beta U)^{(2)}_{\alpha\gamma}$ and $K^{-1}_{\alpha\gamma}$ are specified by the physical system under consideration.

To arrive at a Flory-Huggins-de Gennes free energy functional we restrict to homopolymer blends in a system of volume V with

$$x_\alpha^{(0)} = \bar{x}_\alpha = \frac{1}{V}\int x_\alpha(\vec{r})\, d\vec{r} \text{ for } x = \rho, \omega \tag{2.48}$$

and assume isotropy of the thereby defined homogeneous reference state, i.e.

$$K_{\alpha\gamma}(\vec{r}, \vec{r}\,') = K_{\alpha\gamma}(\vec{r} - \vec{r}\,') = K_{\alpha\gamma}(-\vec{r} + \vec{r}\,'). \tag{2.49}$$

This analogously holds for $K_{\alpha\gamma}^{-1}$, too, and is reasonable because $K_{\alpha\gamma}(\vec{r}, \vec{r}\,')$ is proportional to cumulant pair correlations $\langle\hat{\rho}_\alpha(\vec{r})\rangle\langle\hat{\rho}_\gamma(\vec{r}\,')\rangle - \langle\hat{\rho}_\alpha(\vec{r})\hat{\rho}_\gamma(\vec{r}\,')\rangle$. As only homopolymers are considered, each chain of type j can be assigned to one single monomer species α, which renders the separation of indices j and α to be redundant. It follows from equation 2.27 that $Q_j[\{\omega\}] = Q_j[\omega_j]$, where ω_j is the potential field acting on the monomers that form type j chains. As a result, it is

$$K_{\alpha\gamma}(\vec{r} - \vec{r}\,') = \delta_{\alpha\gamma}K_{\alpha\alpha}(\vec{r} - \vec{r}\,') = \delta_{\alpha\gamma}n_\alpha\frac{\delta^2\ln(Q_\alpha[\bar{\omega}_\alpha[\{\bar{\rho}\}]])}{\delta\omega_\alpha(\vec{r})\delta\omega_\alpha(\vec{r}\,')}. \tag{2.50}$$

Insertion of the first equality from equation 2.50 into equation 2.45 yields the relation

$$\int K_{\alpha\alpha}^{-1}(\vec{r} - \vec{r}\,'')K_{\alpha\alpha}(\vec{r}\,' - \vec{r}\,'')d\vec{r}\,'' = \delta(\vec{r} - \vec{r}\,'). \tag{2.51}$$

By substituting $\vec{y} = \vec{r}\,'' - \vec{r}$, introducing the short hand notation $\vec{b} = \vec{r} - \vec{r}\,'$, and invoking equation 2.49 this relation appears as a convolution,

$$\delta(\vec{b}) = (K_{\alpha\alpha}^{-1} * K_{\alpha\alpha})(\vec{b}) = \int K_{\alpha\alpha}^{-1}(\vec{y})K_{\alpha\alpha}(\vec{b} - \vec{y})\, d\vec{y}, \tag{2.52}$$

and due to the convolution theorem the Fourier transforms are algebraically connected via

$$\hat{K}_{\alpha\alpha}^{-1}(\vec{k}) = \frac{1}{\hat{K}_{\alpha\alpha}(\vec{k})}. \tag{2.53}$$

For homogeneous reference states $\hat{K}_{\alpha\alpha}$ is given by

$$\hat{K}_{\alpha\alpha}(\vec{k}) = \bar{\rho}_\alpha N_\alpha \hat{g}_D(R_{g,\alpha}^2\vec{k}^2), \tag{2.54}$$

where $R_{g,\alpha}$ is the radius of gyration of α-homopolymers, N_α the number of monomers per chain, and $\hat{g}_D$ the Debye Function $\hat{g}_D(x) = \frac{2}{x^2}[e^{-x} + x - 1]$, which is often approximated by $\hat{g}_D(x) \approx \frac{1}{1+x/2}$ with an error of less than 15 % that decreases with diminishing x (cp. equation 2.83 in reference [102]). The derivation of equation 2.54 is analogous to the calculations leading to equation 3.136 in reference [103]. If so-called Flory-Huggins type interaction potentials

$$\beta U[\{\rho\}] = \int \sum_{i=1}^{\mathcal{A}}\sum_{j=i+1}^{\mathcal{A}} \zeta_{ij}\rho_i(\vec{r})\rho_j(\vec{r})\, d\vec{r} \tag{2.55}$$

are applied, it is

$$(\beta U)^{(2)}_{\alpha\gamma}(\vec{r},\vec{r}\,') = \frac{\delta^2(\beta U[\{\bar{\rho}\}])}{\delta\rho_\alpha(\vec{r})\delta\rho_\gamma(\vec{r}\,')} = \delta(\vec{r}-\vec{r}\,')\zeta_{\alpha\gamma} \text{ with } \zeta_{\alpha\gamma} = \begin{cases}\zeta_{\alpha\gamma} & \alpha<\gamma \\ \zeta_{\gamma\alpha} & \gamma<\alpha\end{cases} \tag{2.56}$$

and after inserting equation 2.56, equation 2.47 becomes

$$\beta\mathcal{F}[\{\rho\}] = \beta\mathcal{F}[\{\bar{\rho}\}] + \frac{1}{2}\sum_{\alpha,\gamma=1}^{\mathcal{A}}\int \zeta_{\alpha\gamma}\delta\rho_\alpha(\vec{r})\delta\rho_\gamma(\vec{r})\,d\vec{r}$$

$$+\frac{1}{2}\sum_{\alpha=1}^{\mathcal{A}}\int\left[\int K^{-1}_{\alpha\alpha}(\vec{r}-\vec{r}\,')\delta\rho_\alpha(\vec{r}\,')\,d\vec{r}\,'\right]\rho_\alpha(\vec{r})\,d\vec{r}. \tag{2.57}$$

Assuming periodic boundary conditions and introducing the Fourier coefficients $\hat{\rho}_\alpha$ via

$$\delta\rho_\alpha(\vec{r}) = \sum_{\vec{k}\neq 0}\hat{\rho}_\alpha(\vec{k})e^{i\vec{k}\cdot\vec{r}} \text{ with } \hat{\rho}_\alpha(\vec{k}) = \frac{1}{V}\int\delta\rho_\alpha(\vec{r})e^{-i\vec{k}\cdot\vec{r}}\,d\vec{r} \tag{2.58}$$

(in the remainder of this chapter $\hat{\rho}_\alpha$ denotes the Fourier coefficient of density fluctuations and not the microscopic density!) the second line of equation 2.57 can be cast into the form

$$\frac{1}{2}\sum_{\alpha=1}^{\mathcal{A}}\int\left[\int K^{-1}_{\alpha\alpha}(\vec{r}-\vec{r}\,')\delta\rho_\alpha(\vec{r}\,')\,d\vec{r}\,'\right]\rho_\alpha(\vec{r})\,d\vec{r}$$

$$= \frac{1}{2}\sum_{\alpha=1}^{\mathcal{A}}\sum_{\vec{k}\neq 0}\sum_{\vec{k}\,'\neq 0}\frac{\hat{\rho}_\alpha(\vec{k})}{\hat{K}_{\alpha\alpha}(\vec{k})}\hat{\rho}_\alpha(\vec{k}\,')\int e^{i(\vec{k}+\vec{k}\,')\cdot\vec{r}}\,d\vec{r} = \frac{1}{2}\sum_{\alpha=1}^{\mathcal{A}}\sum_{\vec{k}\neq 0}\frac{V}{N_\alpha\bar{\rho}_\alpha}\left(1+\frac{R^2_{g,\alpha}\vec{k}^2}{2}\right)\hat{\rho}_\alpha(\vec{k})\hat{\rho}_\alpha(-\vec{k})$$

$$= \frac{V}{2}\sum_{\alpha=1}^{\mathcal{A}}\sum_{\vec{k}\neq 0}\left[\frac{1}{N_\alpha\bar{\rho}_\alpha}\hat{\rho}_\alpha(\vec{k})\hat{\rho}_\alpha(-\vec{k}) + \frac{R^2_{g,\alpha}}{2N_\alpha\bar{\rho}_\alpha}\vec{k}^2\hat{\rho}_\alpha(\vec{k})\hat{\rho}_\alpha(-\vec{k})\right].$$

Translating back into coordinate space, e.g. by formally substituting $V = V\sum_{\vec{k}\,'\neq 0}\delta_{\vec{k},-\vec{k}\,'} = \sum_{\vec{k}\,'\neq 0}\int e^{i(\vec{k}+\vec{k}\,')\cdot\vec{r}}\,d\vec{r}$, results in

$$\beta\mathcal{F}[\{\rho\}] = \beta\mathcal{F}[\{\bar{\rho}\}] + \int\left[\frac{1}{2}\sum_{\alpha,\gamma=1}^{\mathcal{A}}\zeta_{\alpha\gamma}\delta\rho_\alpha(\vec{r})\delta\rho_\gamma(\vec{r}) + \frac{1}{2}\sum_{\alpha=1}^{\mathcal{A}}\frac{(\delta\rho_\alpha(\vec{r}))^2}{N_\alpha\bar{\rho}_\alpha} + \sum_{\alpha=1}^{\mathcal{A}}\frac{R^2_{g,\alpha}}{4N_\alpha\bar{\rho}_\alpha}|\nabla\rho_\alpha(\vec{r})|^2\right]d\vec{r}$$

$$= \beta\mathcal{F}[\{\bar{\rho}\}] + \int\left[\frac{1}{2}\sum_{\alpha,\gamma=1}^{\mathcal{A}}\left(\frac{\delta_{\alpha\gamma}}{N_\alpha\bar{\rho}_\alpha}+\zeta_{\alpha\gamma}\right)\delta\rho_\alpha(\vec{r})\delta\rho_\gamma(\vec{r}) + \sum_{\alpha=1}^{\mathcal{A}}\frac{R^2_{g,\alpha}}{4N_\alpha\bar{\rho}_\alpha}|\nabla\rho_\alpha(\vec{r})|^2\right]d\vec{r}. \tag{2.59}$$

The term in the round brackets, $\frac{\delta_{\alpha\gamma}}{N_\alpha\bar{\rho}_\alpha}+\zeta_{\alpha\gamma}$, can be identified with the second derivative of the Flory-Huggins free energy density f_{FH}, which was originally derived in a lattice model [104]. Expressed in terms of monomer densities $\{\rho\}$, βf_{FH} reads

$$\beta f_{FH} = \sum_{i=1}^{\mathcal{A}}\left[\frac{\rho_i}{N_i}\ln(\nu\rho_i) + \sum_{j=i+1}^{\mathcal{A}}\chi_{ij}\rho_i\nu\rho_j\right] \text{ with } \frac{\partial^2(\beta f_{FH})}{\partial\rho_\alpha\partial\rho_\gamma}(\{\bar{\rho}\}) = \frac{\delta_{\alpha\gamma}}{N_\alpha\bar{\rho}_\alpha}+\nu\chi_{\alpha\gamma}, \tag{2.60}$$

where ν is a constant that describes an elementary monomer volume and χ the well known

Flory-Huggins interaction parameter. Identifying $\nu\chi_{\alpha\gamma} = \zeta_{\alpha\gamma}$, it can be seen that the double-sum over α, γ in the squared brackets in the last line of equation 2.59 corresponds to the second order term in a Taylor expansion of βf_{FH} around a homogeneous reference state. For homopolymers in the homogeneous state it is $\ln(Q_\alpha/V) = \ln(e^{-N_\alpha\bar{\omega}_\alpha}) = -N_\alpha\bar{\omega}_\alpha$, which implies that the zeroth order contribution $\beta F[\{\bar{\rho}\}]$ can be written as

$$\beta\mathcal{F}[\{\bar{\rho}\}] = V\sum_{\alpha=1}^{\mathcal{A}}\sum_{\gamma=\alpha+1}^{\mathcal{A}}\zeta_{\alpha\gamma}\bar{\rho}_\alpha\bar{\rho}_\gamma - V\sum_{\alpha=1}^{\mathcal{A}}\bar{\rho}_\alpha\bar{\omega}_\alpha + \sum_{\alpha=1}^{\mathcal{A}}n_\alpha N_\alpha\bar{\omega}_\alpha + \sum_{\alpha=1}^{\mathcal{A}}n_\alpha\ln(n_\alpha)$$

(cp. equation 2.29). Since $\bar{\rho}_\alpha = {}^{N_\alpha n_\alpha}/_V$, the second and the third term cancel and it is

$$\beta\mathcal{F}[\{\bar{\rho}\}] = V\sum_{\alpha=1}^{\mathcal{A}}\sum_{\gamma=\alpha+1}^{\mathcal{A}}\chi_{\alpha\gamma}\bar{\rho}_\alpha\nu\bar{\rho}_\gamma + V\sum_{\alpha=1}^{\mathcal{A}}\frac{\bar{\rho}_\alpha}{N_\alpha}\ln\left(\frac{V}{\nu N_\alpha}\nu\bar{\rho}_\alpha\right)$$

$$= \int\sum_{\alpha=1}^{\mathcal{A}}\left[\frac{\bar{\rho}_\alpha}{N_\alpha}\ln\left(\nu\bar{\rho}_\alpha\right) + \sum_{\gamma=\alpha+1}^{\mathcal{A}}\chi_{\alpha\gamma}\bar{\rho}_\alpha\nu\bar{\rho}_\gamma\right]d\vec{r} + V\sum_{\alpha=1}^{\mathcal{A}}\frac{\bar{\rho}_\alpha}{N_\alpha}\ln\left(\frac{V}{\nu N_\alpha}\right)$$

$$= \int\beta f_{FH}(\{\bar{\rho}\})\,d\vec{r} + V\sum_{\alpha=1}^{\mathcal{A}}\frac{\bar{\rho}_\alpha}{N_\alpha}\ln\left(\frac{V}{\nu N_\alpha}\right). \tag{2.61}$$

Hence, because the first derivative of βf_{FH} in the homogeneous reference state is zero, the first two addends in the last line of equation 2.59 constitute the second order Taylor expansion of βf_{FH} with an additional term $a(\{\bar{\rho}\}) = V\sum_{\alpha=1}^{\mathcal{A}}\frac{\bar{\rho}_\alpha}{N_\alpha}\ln\left(\frac{V}{\nu N_\alpha}\right)$. Replacing the Taylor series by the complete function βf_{FH} leads to

$$\beta\mathcal{F}[\{\rho\}] = \int\left[\beta f_{FH}(\{\rho(\vec{r})\}) + \sum_{\alpha=1}^{\mathcal{A}}\lambda_\alpha\left|\nabla\rho_\alpha(\vec{r})\right|^2\right]d\vec{r} + a(\{\bar{\rho}\}) \text{ with } \lambda_\alpha = \frac{R_{g,\alpha}^2}{4N_\alpha\bar{\rho}_\alpha}, \tag{2.62}$$

which shows that the free energy functional from the Self Consistent Field Theory can be replaced by Flory-Huggins-de Gennes free energy functional if only small density fluctuations are considered. Since dynamic field theories only contain $\nabla\frac{\delta F}{\delta\rho_\alpha}$, they are unaffected by $a(\{\bar{\rho}\})$. Dynamical equations with Flory-Huggins-de Gennes free energy functionals are often referred to as phase field models.

2.2.4 External Potential Dynamics (EPD)

The explicit calculation of pair correlators P demands excessive computation times when a non-local kinetic coupling model like equation 2.21 is solved numerically. Fortunately, the computational cost can be reduced dramatically by transforming temporal evolutions of density fields $\{\rho\}$ into temporal evolutions of potential fields $\{\omega\}$. The resulting dynamical equations are referred to as External Potential Dynamics [86]. The prerequisites for External Potential Dynamics are two well known results from Density Functional Theory: the invertibility of the assignment $\{\rho\}[\{\omega\}]$ and the identity

$$\frac{\delta\rho_\alpha(\vec{r})}{\delta\omega_\gamma(\vec{r}\,')} = -P_{\alpha\gamma}^{(j(\gamma))}(\vec{r},\vec{r}\,'), \tag{2.63}$$

where ω_γ is a (dimensionless) potential field and $P_{\alpha\gamma}^{(j(\gamma))}(\vec{r},\vec{r}\,')$ the pair correlators defined in equation 2.16. Because the relation between densities and potentials from the Self Consistent Field Theory,

$$\rho_\alpha(\vec{r})[\{\omega\}] = -\sum_{j=1}^{J} \frac{n_j}{Q_j[\{\omega\}]} \frac{\delta Q_j[\{\omega\}]}{\delta\omega_\alpha(\vec{r})}$$

with Q_j from equation 2.27, is identical to the one obtained from the Density Functional Theory for non-interacting polymer chains in external fields $\{\omega\}$ [103], both prerequisites hold for the Self Consistent Field Theory as well. The first one is an implication of the Hohenberg-Kohn theorem [101], and the second one can be verified by rewriting

$$\begin{aligned} Q_j[\{\omega\}] &= \int \mathcal{D}\vec{R}\, P_j[\vec{R}; N_j] e^{-\sum_{\alpha=1}^{\mathcal{A}} \int_0^{N_j} \omega_\alpha(\vec{R}(s))\gamma_{\alpha,j}(s)\, ds} \\ &= \int \mathcal{D}\vec{R}\, P_j[\vec{R}; N_j] e^{-\sum_{\alpha=1}^{\mathcal{A}} \int \omega_\alpha(\vec{r})\hat{\rho}_\alpha^{(c,j)}(\vec{r})\, d\vec{r}} \end{aligned} \tag{2.64}$$

with the monomer density of a continuous chain $\hat{\rho}_\alpha^{(c,j)}(\vec{r}) = \int_0^{N_j} \delta(\vec{r}-\vec{R}(s))\gamma_{\alpha,j}(s)\, ds$. Insertion of Q_j into equation 2.30 yields

$$\frac{\delta\rho_\alpha(\vec{r})}{\delta\omega_\gamma(\vec{r}\,')} = \sum_{j\in J_\alpha\cap J_\gamma} n_j \left[\left\langle \hat{\rho}_\alpha^{(c,j)}(\vec{r}) \right\rangle_c \left\langle \hat{\rho}_\gamma^{(c,j)}(\vec{r}\,') \right\rangle_c - \left\langle \hat{\rho}_\alpha^{(c,j)}(\vec{r}) \hat{\rho}_\gamma^{(c,j)}(\vec{r}\,') \right\rangle_c \right], \tag{2.65}$$

and since the first term in the squared brackets grows with $1/V^2$, while the second one grows with $1/V$, at large volumes V it is

$$\frac{\delta\rho_\alpha(\vec{r})}{\delta\omega_\gamma(\vec{r}\,')} = -\sum_{j\in J_\alpha\cap J_\gamma} n_j \left\langle \hat{\rho}_\alpha^{(c,j)}(\vec{r}) \hat{\rho}_\gamma^{(c,j)}(\vec{r}\,') \right\rangle_c . \tag{2.66}$$

In case a diblock-copolymer solution or a copolymer melt is considered, the sum over j vanishes and

$$\frac{\delta\rho_\alpha(\vec{r})}{\delta\omega_\gamma(\vec{r}\,')} = -n_{j(\gamma)} \left\langle \hat{\rho}_\alpha^{(c,j(\gamma))}(\vec{r}) \hat{\rho}_\gamma^{(c,j(\gamma))}(\vec{r}\,') \right\rangle_c = -P_{\alpha\gamma}^{(j(\gamma))}(\vec{r},\vec{r}\,'), \tag{2.67}$$

where $j(\gamma)$ again denotes the type of the chemical component that contains γ-monomers.

As the invertibility of $\{\rho\}[\{\omega\}]$ implies the existence of a set $\{\omega\}$ that can uniquely generate *any* arbitrary $\{\rho\}$, it is possible to transfer the time dependence of densities $\rho_\alpha(\cdot,t)$ to potentials $\{\omega(\cdot,t)\}$ by setting $\rho_\alpha(\vec{r},t) = \rho_\alpha(\vec{r})[\{\omega(\cdot,t)\}]$. The first step at determining appropriate conditional equations for $\{\omega(\cdot,t)\}$ is differentiating ρ_α and applying equation 2.63 to get

$$\begin{aligned} \frac{\partial\rho_\alpha(\vec{r})[\{\omega(\cdot,t)\}]}{\partial t} &= \sum_{\gamma=1}^{\mathcal{A}} \int \frac{\delta\rho_\alpha(\vec{r})}{\delta\omega_\gamma(\vec{r}\,')} \frac{\partial\omega_\gamma}{\partial t}(\vec{r}\,',t)\, d\vec{r}\,' \\ &= -\sum_{\gamma=1}^{\mathcal{A}} \int P_{\alpha\gamma}^{(j(\gamma))}(\vec{r},\vec{r}\,') \frac{\partial\omega_\gamma}{\partial t}(\vec{r}\,',t)\, d\vec{r}\,'. \end{aligned} \tag{2.68}$$

Therefore, setting $\rho_i(\vec{r},t) = \rho_i(\vec{r})[\{\omega(\cdot,t)\}]$ in equation 2.21 with $\eta_\alpha = 0$ implies

$$\sum_\gamma \beta D_{j(\gamma)} \nabla_{\vec{r}} \cdot \int P_{\alpha\gamma}^{(j(\gamma))}(\vec{r},\vec{r}\,') \nabla_{\vec{r}\,'} \frac{\delta \mathcal{F}[\{\rho[\{\omega(\cdot,t)\}]\}]}{\delta \rho_\gamma(\vec{r}\,')}\, d\vec{r}\,'$$

$$= -\sum_\gamma \int P_{\alpha\gamma}^{(j(\gamma))}(\vec{r},\vec{r}\,') \frac{\partial \omega_\gamma}{\partial t}(\vec{r}\,',t)\, d\vec{r}\,'. \tag{2.69}$$

Assuming $\nabla_{\vec{r}} P_{\alpha\gamma}^{(j(\gamma))}(\vec{r},\vec{r}\,') = -\nabla_{\vec{r}\,'} P_{\alpha\gamma}^{(j(\gamma))}(\vec{r},\vec{r}\,')$ (the physical interpretation is discussed by Maurits et al. [86]) and utilizing the Gaussian integral theorem allows to rewrite

$$\nabla_{\vec{r}} \cdot \int P_{\alpha\gamma}^{(j(\gamma))}(\vec{r},\vec{r}\,') \nabla_{\vec{r}\,'} \frac{\delta \mathcal{F}[\{\rho\}]}{\delta \rho_\gamma(\vec{r}\,')}\, d\vec{r}\,' = \int P_{\alpha\gamma}^{(j(\gamma))}(\vec{r},\vec{r}\,') \nabla_{\vec{r}\,'}^2 \frac{\delta \mathcal{F}[\{\rho\}]}{\delta \rho_\gamma(\vec{r}\,')}\, d\vec{r}\,', \tag{2.70}$$

which is used to rearrange equation 2.69 to

$$\sum_\gamma \int P_{\alpha\gamma}^{(j(\gamma))}(\vec{r},\vec{r}\,') \left[\frac{\partial \omega_\gamma}{\partial t}(\vec{r}\,',t) + \beta D_{j(\gamma)} \nabla_{\vec{r}\,'}^2 \frac{\delta \mathcal{F}[\{\rho[\{\omega(\cdot,t)\}]\}]}{\delta \rho_\gamma(\vec{r}\,')} \right] d\vec{r}\,' = 0. \tag{2.71}$$

The left hand side in the equation above is linear in the square bracket term and can be written in matrix-vector notation according to

$$\sum_\gamma \int P_{\alpha\gamma}^{j(\gamma)}(\vec{r},\vec{r}\,') f_\gamma(\vec{r}\,')\, d\vec{r}\,' = \left(\mathcal{P}(\vec{r}) \vec{f} \right)_\alpha \tag{2.72}$$

with the vector $\vec{f} = (f_1, f_2, f_3, ...)^T$ and the operator matrix $\mathcal{P}$ with entries $\mathcal{P}_{\alpha\gamma}(\vec{r}) = \int d\vec{r}\,' P_{\alpha\gamma}(\vec{r},\vec{r}\,')$. As $\mathcal{P}$ connects $\{\rho\}$ and $\{\omega\}$ via equation 2.68 upon time integration, it has to be bijective due to the Hohenberg-Kohn theorem, and because the kernel of bijective linear mappings contains only 0, it follows from equation 2.71 that

$$\frac{\partial \omega_\gamma}{\partial t}(\vec{r},t) = -D_{j(\gamma)} \nabla_{\vec{r}}^2 \frac{\delta \beta \mathcal{F}[\{\rho[\{\omega(\cdot,t)\}]\}]}{\delta \rho_\gamma(\vec{r})} \,\forall\, \gamma = 1, ..., \mathcal{A}, \tag{2.73}$$

which constitutes the deterministic External Potential Dynamics equations. Equation 2.73 describes (approximately) the same dynamics as equation 2.21, but can be solved computationally much more efficiently because it does not contain the integral over $\vec{r}\,'$. For given $\{\omega\}$, densities may be calculated from equations 2.30, 2.34, and 2.39. The consideration of thermal noise introduces an additive random term η_γ to the right hand side of equation 2.73 obeying

$$\langle \eta_\gamma(\vec{r},t) \rangle = 0 \text{ and } \langle \eta_\alpha(\vec{r},t) \eta_\gamma(\vec{r}\,',t') \rangle = -2 D_{j(\gamma)} \nabla_{\vec{r}}^2 P_{\alpha\gamma}^{-1}(\vec{r},\vec{r}\,') \delta(t-t'), \tag{2.74}$$

where $P_{\alpha\gamma}^{-1}$ is the inverse to $P_{\alpha\gamma}^{j(\gamma)}$ [86]. But due to the lack of possibilities to calculate a noise satisfying these conditions, simpler implementations are usually used [86].

Chapter 3

Mixing mechanisms in interdigital micromixers

A micromixer is a microfluidic device. Microfluidic devices process fluids in geometries with at least one spatial dimension lying on the micrometer scale and their application ranges from biomedical diagnostics and drug development to replacing conventional batch syntheses in the chemical industry. These applications commonly involve reactions between miscible substances with very low diffusivity. As a 'clean' reaction requires the reacting species to be mixed on a molecular scale, the reaction rate or the purity of reaction products is severely limited by the inherently slow interdiffusion of reactants or, in other words, their large mixing time. The purpose of micromixers is to decrease mixing times as much as possible – either to increase throughput or quality in an industrial application or to construct lab-on-a-chip systems for point of care diagnostics, which demand practically direct evaluation or immediate further processing of reaction products.

In the following, 'mixing' is understood as a combination of diffusion and *stirring* [105]. Because only diffusion is able to establish a homogeneous concentration distribution of different species on a molecular scale, it is the final step of (good) mixing. Generally speaking, stirring is a convective process which increases the interface to volume ratio of spatial domains containing an excess of any chemical component in order to accelerate diffusion. In contrast to diffusion, stirring can be directly influenced by the particular design of a micromixer and the process parameters it is operated with. From the most general point of view micromixer designs can be classified into two families depending on how the stirring is done: active and passive. While active micromixers rely on external excitation, for example ultrasonic, passive ones do not need an external source of energy. Since micromixers are usually integrated into microfluidic networks and operated continuously, passive micromixers take the energy required for stirring from the fluid flow. An overview over various mixing principles can be found in the review articles [105], [106], [107], and [108]. All mixers that were used to generate the experimental data in figure 1.3 are passive micromixers. Passive micromixing may be implemented by different *stirring mechanisms*. The Caterpillar Micromixer (CPMM), for example, relies on 'split and recombine' as a stirring mechanism [109], while the Slit Interdigital Micromixer (SIMM) and the Super Focus Interdigital Micromixer (SFIMM) apply 'hydrodynamic focusing' [110].

Despite different stirring mechanisms passive micromixers typically share one specific trait: they respond to increasing flow rates with decreasing mixing times [111]. As it turns out later, the relation between flow rates and mixing times is crucial to the interpretation of figure

1.3, and the following two sections will reveal that this relation is caused by the stirring mechanisms. Because it would go beyond the scope of the present work to cover all passive micromixers in detail, the SFIMM is discussed as an example for hydrodynamic focusing in section 3.1 and the CPMM as an example for the split and recombine mechanism in section 3.2. In the process analytical theories are used, which also provide a mathematical expression to couple the mixing process to the models for particle formation.

3.1 Hydrodynamic focusing

Figure 3.1 shows a schematic drawing of the SFIMM. The SFIMM unites two different features to provide fast mixing of liquids: multilamination and hydrodynamic focusing. Multilamination is the alignment of liquids into a lamella pattern. The term 'interdigital' originates from such lamella patterns and they can be viewed as the first step in creating the desirable large interface to volume ratios. Hydrodynamic focusing constitutes the second step and denotes the decrease in lamella width towards the focusing point. According to the continuity equation a fluid accelerates while traveling through a constricting channel. As a result, lamellae are stretched in flow direction, which increases their surface to volume ratio and in turn accelerates diffusion. In other words, hydrodynamic focusing reduces the diffusion length inside a moving frame of reference (cp. $r(t_1)$ and $r(t_2)$ in figure 3.1) in the direction indicated by the x-axis. The primal purpose of hydrodynamic focusing was to offset the lower bound of lamella widths which arises from manufacturing limitations for the inlet channels. To quantitatively understand why hydrodynamic focusing introduces the flow rate dependence of mixing times that is so essential for the co-solvent method, we apply an analytical theory developed by Drese [112]. It is based on solving a one dimensional diffusion equation after applying an appropriate coordinate transformation. Because the resulting formulae are going to play a major role later on, we present a detailed derivation. In the present work there will be additional physical background in the derivation of the coordinate transformation, which did not appear explicitly in the original publication [112]: it is shown that the approach corresponds to solving a convection diffusion equation if the diffusion in the x-direction dominates the diffusion in the other two spatial directions.

We start with specifying the flow regime by estimating the Reynolds number. The largest Reynolds numbers are naturally encountered in the mixing section, where

$$Re = \frac{U\,d}{\nu} \approx \frac{\frac{v}{w\,h}\,h}{\nu} = \frac{v}{w\nu}.$$

In the second step the definition of a flow rate, $v = A\,U$, is applied. U is a typical flow velocity and $A = w\,h$ the area of the channel cross section. Employing the kinematic viscosity of water at room temperature, $\nu = 10^{-6}\,\frac{\mathrm{m}^2}{s}$, and $w = 0.14$ mm from the technical data sheet of the SFIMM yields

$$Re \approx 114\frac{\mathrm{min}}{\mathrm{ml}} \cdot v,$$

with v being the flow rate in ml/min. In figure 1.3, most flow rates are less than 4.8 ml/min, rendering Re to be smaller than 550. This is way below 2300, which is typically given as the threshold value for the transition into turbulent flow inside a pipe [113]. Therefore, the flow at $Re < 550$ in the SFIMM is assumed to be laminar from now on. In that case, the solid lines along lamella interfaces in figure 3.1 sketch stream lines. In the focusing section stream

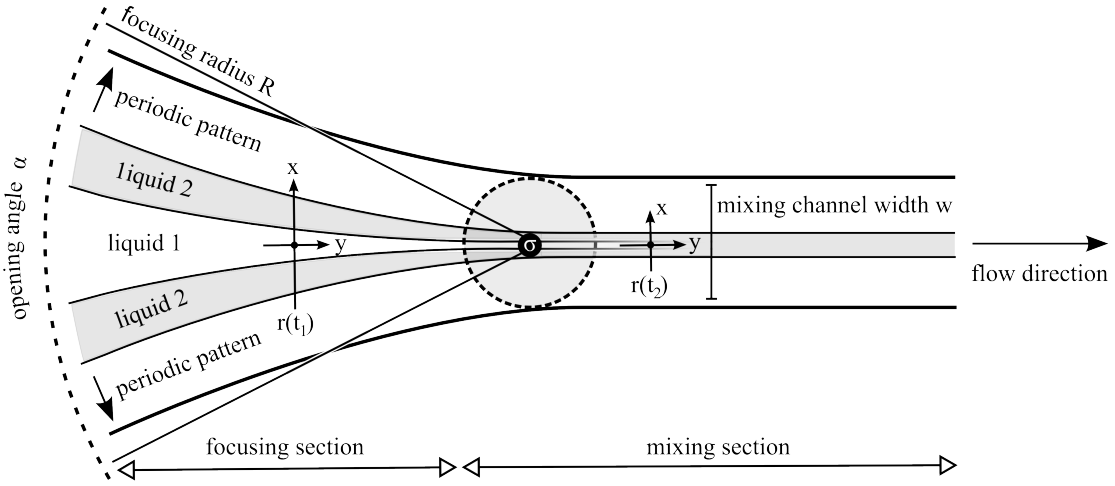

Figure 3.1: *Sketch of a horizontal cross section through the Super Focus Interdigital Micromixer (SFIMM). The mixer geometry is planar in the vertical direction with height h. The cross section is composed of a straight channel with width w, called mixing section, and a circular segment shaped focusing section. The radius of the circular segment is the focusing radius R, its center σ is the focusing point, and its central angle is the opening angle α. Two liquids to be mixed, labeled by 1 and 2, are aligned in a lamella pattern that is composed of L lamellae in total and repeats periodically over the range of the opening angle, which is indicated by two arrows in tangential direction to the leftmost dashed line. The entrance of the mixer is located on the left hand side and conclusively, the flow direction points from left to right. The mixing of liquid 1 and 2 is performed by a combination of diffusion perpendicular to lamella interfaces and hydrodynamic focusing. Hydrodynamic focusing represents the stirring mechanism and accelerates diffusion in a frame of reference traveling from $r(t_1)$ to $r(t_2)$ $(t_1 < t_2)$ by reducing diffusion lengths. In the current sketch most of the mixing is performed in the front of the mixing section between σ and the vertical bar indicating the mixing channel width.*

lines approach the focusing point σ in an approximately radial direction and in the mixing section they are parallel to the channel walls. The analytical model describing the mixing process is built upon a Lagrangian perspective of a small fluid element that moves along a stream line with a velocity U. It is displayed at two different times $t_1 < t_2$ as a black dot with position $r(t_1)$ or $r(t_2)$, respectively. The y-axis of the attached Cartesian coordinate system is tangential to the corresponding stream line. Assuming incompressible flow and completely miscible non-interacting liquids, the temporal concentration evolution in a co-moving frame of reference can be described by the convection diffusion equation

$$\frac{\partial c}{\partial t} = D\Delta c - \vec{u} \cdot \nabla c, \tag{3.1}$$

where $c(x, y, t)$ is the concentration of either liquid 1 or liquid 2, D the corresponding diffusion coefficient, and $\vec{u}(x, y, t)$ the relative flow field with respect to the fluid element under consideration. x and y are the coordinates inside the moving frame of reference. Due to the planar geometry of the mixer hydrodynamic focusing is mainly restricted to the xy-plane and thus, the spatial domain of equation 3.1 is considered to be two dimensional.

The next step is to complete the set of equations, i.e. to find an expression for $\vec{u}$. From

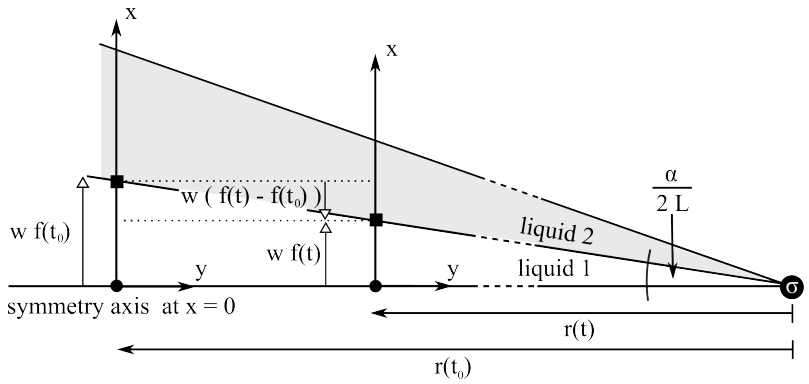

Figure 3.2: *Sketch to determine lateral flow velocities u_x in the SFIMM. During a time interval $dt = t - t_0$ the co-moving frame of reference, whose origin is illustrated by the black dots, travels an infinitesimal distance $r(t) - r(t_0)$. A fluid element sitting at the edge of a lamella (represented by the black rectangles) is simultaneously displaced by $w\,(f(t) - f(t_0))$ in the x-direction. The lamella width at time t is given by $2w\,f(t)$, where w is the mixing channel width and f a dimensionless function. Because of axis symmetry with respect to $x = 0$ only the upper part of a liquid 1 lamella is shown. The '$x = 0$' line is represented by the horizontal line that intersects σ.*

now on, the definition $\vec{u} \coloneqq (u_x, v_y)^T$ is applied with u_x being the x- and u_y the y-component. In the mixing section, both u_x and u_y equal zero. In the focusing section, u_x represents the hydrodynamic focusing as it shifts fluid elements closer towards the origin of the moving frame of reference and u_y is a secondary flow induced by the incompressibility condition. As shown in figure 3.2, an expression for u_x in the focusing section is obtained by considering the displacement of a fluid element (black rectangle) if the co-moving frame of reference travels an infinitesimal distance. For the sake of convenience, we track the displacement of an element at the edge of the liquid 1 lamella because it is easily coupled to geometric quantities like the opening angle α and the total number of lamellae L. It is obvious that

$$w\,f(t) = r(t)\,\tan\left(\frac{\alpha}{2L}\right) \tag{3.2}$$

and hence, the relative velocity in x-direction of a fluid element on the edge of a lamella at $y = 0$ is

$$u_x(w\,f(t), 0, t) \coloneqq \lim_{t_0 \to t}\left(w\,\frac{f(t) - f(t_0)}{t - t_0}\right) = \frac{d}{dt}\left(w\,f(t)\right) = \tan\left(\frac{\alpha}{2L}\right)\,\frac{d}{dt}r(t). \tag{3.3}$$

To determine u_x at an arbitrary position $x = \delta\,w\,f(t)$ with fixed $\delta \in [-1, 1]$, one multiplies equation 3.2 by δ to get

$$u_x(\delta\,w\,f(t), 0, t) \coloneqq \frac{d}{dt}\left(\delta\,w\,f(t)\right) = \delta\,\frac{d}{dt}\left(w\,f(t)\right) = \delta\,\tan\left(\frac{\alpha}{2L}\right)\,\frac{d}{dt}r(t), \tag{3.4}$$

which motivates writing

$$u_x(x, 0, t) = \frac{x}{w\,f(t)}\,u_x(w\,f(t), 0, t) = \frac{x}{r(t)}\,\frac{d}{dt}r(t) = x\,\frac{d}{dt}\ln\left(r(t)\right). \tag{3.5}$$

If the lamella interface is assumed to be a straight line as in figure 3.2, the difference $w\ (f(t) - f(t_0))$ only depends on the displacement of the origin and not on a specific (fixed) y-coordinate inside the moving frame of reference. This allows setting

$$u_x(x, y, t) = u_x(x, 0, t) = x \frac{d}{dt} \ln\left(r(t)\right). \tag{3.6}$$

As the flow is incompressible, u_y can be obtained from the stream function ψ, which satisfies

$$u_x = -\frac{\partial \psi}{\partial y} \text{ and } u_y = \frac{\partial \psi}{\partial x}. \tag{3.7}$$

From equation 3.6 it immediately follows that $\psi = -x\, y\, \frac{d}{dt} \ln(r(t))$ and

$$u_y(x, y, t) = -y \frac{d}{dt} \ln(r(t)). \tag{3.8}$$

If the expressions for u_x and u_y are put into the convection diffusion equation 3.1, it reads

$$\frac{\partial c}{\partial t} = D \left(\frac{\partial^2 c}{\partial x^2} + \frac{\partial^2 c}{\partial y^2} \right) - \left(\frac{d}{dt} \ln(r(t)) \right) \left(x \frac{\partial c}{\partial x} - y \frac{\partial c}{\partial y} \right). \tag{3.9}$$

If only concentration evolutions on a cross section at $y = 0$ are considered, the last term in equation 3.9 vanishes. To arrive at a one dimensional problem like in reference [112], the term $\frac{\partial^2 c}{\partial y^2}$ also needs to be neglected. One could argue that due to the characteristic lamella structure local curvatures of c should be more pronounced in x- than in y-direction, unless the liquids are almost completely mixed. Mathematically speaking, that means $\left|\frac{\partial^2 c}{\partial x^2}\right| \gg \left|\frac{\partial^2 c}{\partial y^2}\right|$.[1] So it should be a suitable approximation to describe the combination of diffusion and hydrodynamic focusing by the idealized one dimensional convection diffusion problem

$$\frac{\partial c}{\partial t} = D \frac{\partial^2 c}{\partial x^2} - u(x, t) \frac{\partial c}{\partial x} \text{ with } u(x, t) = x \frac{d}{dt} \ln(r(t)). \tag{3.10}$$

Because $r(t)$ and $f(t)$ differ only by a time-independent factor (cp. equation 3.2), $u(x, t)$ can also be expressed as

$$u(x, t) = x \frac{d}{dt} \ln(f(t)). \tag{3.11}$$

In the following we apply a suitable coordinate transformation that wipes out the convection term in equation 3.10 and leaves an analytically solvable diffusion equation [112]. The general form of the transformation rule reads

$$\phi : \mathbb{R}^2 \to \mathbb{R}^2, \quad (x, t) \mapsto (\phi_1(x, t), \phi_2(t)) =: \phi(x, t)$$

and a function $\tilde{c}(\zeta, \beta)$ is introduced such that $c(x, t) = \tilde{c}(\phi_1(x, t), \phi_2(t))\ \forall\, (x, t)$. Here, the short hand notation $c(x, 0, t) = c(x, t)$ is applied. Insertion of $\tilde{c}$ into 3.10 and application of the chain rule provides

$$\frac{\partial \phi_2}{\partial t}(t) \frac{\partial \tilde{c}}{\partial \beta}(\phi(x, t)) = D \left(\frac{\partial \phi_1}{\partial x}(x, t) \right)^2 \frac{\partial^2 \tilde{c}}{\partial^2 \zeta}(\phi(x, t)) + \frac{\partial \tilde{c}}{\partial \zeta}(\phi(x, t))\, R(x, t) \tag{3.12}$$

[1] We present an a posteriori estimation of the inequality at the end of section 3.1.

with

$$R(x,t) = D\frac{\partial^2\phi_1}{\partial x^2}(x,t) - u(x,t)\frac{\partial\phi_1}{\partial x}(x,t) - \frac{\partial\phi_1}{\partial t}(x,t) \tag{3.13}$$

The central idea behind the transformation is to map a triangular shaped lamella like in figure 3.2 onto a rectangle with horizontal boundaries at $x = \pm\frac{1}{2}$. Setting $\phi_1(x,t) \coloneqq x\,T(t)$ and demanding $\pm\frac{1}{2} = \phi_1(\pm w\,f(t),t) = \pm w\,f(t)\,T(t)$ leads to $T(t) = \frac{1}{2\,w\,f(t)}$ and

$$\phi_1(x,t) = \frac{x}{2\,w\,f(t)} \tag{3.14}$$

as well as

$$R(x,t) = -\frac{u(x,t)}{2\,w\,f(t)} - \frac{x}{2\,w}\frac{\partial}{\partial t}\frac{1}{f(t)} = -\frac{u(x,t)}{2\,w\,f(t)} + \frac{x}{2\,w\,f(t)}\frac{\partial}{\partial t}\ln(f(t)).$$

Hence, equation 3.11 implies $R(x,t) = 0$ and equation 3.12 can be simplified to

$$\frac{\partial\phi_2}{\partial t}(t)\frac{\partial\tilde{c}}{\partial\beta}(\phi(x,t)) = \frac{D}{(2\,w\,f(t))^2}\frac{\partial^2\tilde{c}}{\partial^2\zeta}(\phi(x,t)). \tag{3.15}$$

If ϕ_2 is chosen to satisfy

$$\frac{\partial\phi_2}{\partial t}(t) = \frac{D\pi^2}{(2\,w\,f(t))^2} \tag{3.16}$$

and if it is taken into account that equation 3.12 holds for any (x,t) as well as transformations being bijective, one finally arrives at an ordinary one dimensional diffusion equation

$$\frac{\partial\tilde{c}}{\partial\beta}(\zeta,\beta) = \frac{1}{\pi^2}\frac{\partial^2\tilde{c}}{\partial\zeta^2}(\zeta,\beta) \quad \forall\,(\zeta,\beta). \tag{3.17}$$

From now on, c or $\tilde{c}$ denote the concentration of liquid 2. The lamella structure in the SFIMM suggests periodic boundary conditions and oscillating rectangles

$$\tilde{c}(\zeta,0) = \begin{cases} c^{(2)} & \text{for } 2wf(0)\,\zeta = \phi_1^{-1}(\zeta,0) = x \text{ in liquid 2 lamella} \\ c^{(1)} & \text{elsewhere} \end{cases}$$

as an initial condition. This implies

$$\tilde{c}(\zeta,\beta) = \frac{c^{(1)}+c^{(2)}}{2} + \sum_{n=0}^{\infty}(-1)^n\frac{c^{(1)}-c^{(2)}}{(2n+1)\pi}\cos\left[(2n+1)\pi\zeta\right]\,e^{-(2n+1)^2\,\beta} \tag{3.18}$$

[114]. Since the derivation is also valid for $u_x \equiv 0$, the solution is applicable both in the focusing and the mixing section. Equation 3.18 is particularly suited to conveniently define the mixing quality ϵ by

$$\epsilon(\beta) = 1 - \sqrt{\frac{1}{2}\int_{-1}^{1}|\tilde{c}(\zeta,\beta)-\bar{c}|^2\,d\zeta}, \tag{3.19}$$

because its representation is independent of the actual mixer geometry. $\bar{c}$ is the temporally conserved mean concentration given by

$$\bar{c} = \frac{1}{2}\int_{-1}^{1}\tilde{c}(\zeta,\beta)\,d\zeta = \frac{1}{2}\int_{-1}^{1}\tilde{c}(\zeta,0)\,d\zeta = \frac{c^{(1)}+c^{(2)}}{2}. \tag{3.20}$$

The mixing time t_{mix} is then given by

$$t_{mix} = \phi_2^{-1}(\beta_{mix}) \text{ with } \beta_{mix} \text{ defined by } \epsilon(\beta_{mix}) = 0.99 \tag{3.21}$$

[112]. The calculation of $c(x,t)$ and t_{mix} requires the explicit representations of $\phi_1(x,t)$ and $\phi_2(t)$ in the variables x and t (the implicit ones are given by equations 3.14 and 3.16).

First, the focusing section is considered. To gain the explicit time dependence of ϕ_1, an expression for $f(t)$ has to be found, which is coupled to $r(t)$ via equation 3.2. For a given flow rate v, $r(t)$ can be calculated by integrating the reciprocal velocity of the co-moving frame of reference $1/U$. If the origin of the radial coordinate r, which describes the position of the moving frame of reference in the fixed polar coordinate system of the focusing section, is placed at σ, the definition of a flow rate leads to $U(r) = -v/A(r)$ with $A(r) = \alpha\, r\, h$ being the channel cross section. Integrating

$$t = \int_{r(0)}^{r(t)} \frac{1}{U(r')}\, dr' = -\int_{r(0)}^{r(t)} \frac{\alpha\, h\, r'}{v}\, dr' = -\frac{\alpha h}{2\, v}\left(r(t)^2 - r(0)^2\right)$$

and setting $r(0) = R$ yields

$$r(t) = \sqrt{R^2 - \frac{2v}{\alpha h}t} = R\sqrt{1 - \frac{2v}{\alpha h R^2}t} = R\sqrt{1 - q\, t} \tag{3.22}$$

with the geometry factor $q \coloneqq \frac{2v}{\alpha h R^2}$. Equation 3.2 then implies that

$$2\, w\, f(t) = 2\, \tan\left(\frac{\alpha}{2L}\right) R\sqrt{1 - qt} = p\sqrt{1 - qt}. \tag{3.23}$$

$p = 2w\, f(0) = 2\tan\left(\frac{\alpha}{2L}\right) R$ is the lamella width at the entrance of the mixer, and combining equation 3.23 with equation 3.14 gives

$$\phi_1(x,t) = \frac{x}{p\,\sqrt{1 - q\, t}}. \tag{3.24}$$

Alternatively inserting equation 3.23 into equation 3.16 yields

$$\frac{\partial \phi_2}{\partial t} = \frac{D\pi^2}{p^2(1 - qt)} \Rightarrow \phi_2(t) - \phi_2(0) = \frac{D\pi^2}{p^2}\int_0^t \frac{1}{1 - qt'}\, dt',$$

which results in

$$\phi_2(t) = -\gamma \ln\left(\sqrt{1 - qt}\right) \tag{3.25}$$

when setting $\phi_2(0) = 0$ and $\gamma \coloneqq \frac{2D\pi^2}{qp^2}$.

The co-moving frame of reference leaves the focusing section at time t_A defined by $r(t_A) = w/2$. Speaking in terms of figure 3.1, it is the time when the fluid element passes the dashed curve encircling σ. Using equation 3.22, it immediately follows hat

$$t_A = \frac{1}{q}\left(1 - \left(\frac{w}{2R}\right)^2\right). \tag{3.26}$$

t_A is called the residence time in the focusing section. The lamella width in the co-moving frame of reference is assumed to stagnate at the constant value $2wf(t_A)$ as soon as the fluid

element enters the mixing section. $2wf(t_A)$ can be determined by the basic trigonometric relation

$$\frac{2wf(t_0)}{r(t_0)} = \frac{2wf(t)}{r(t)}.$$

that can be directly read from figure 3.2. After setting $t_0 = 0$, $t = t_A$, $2wf(0) = p$, $r(0) = R$, and $r(t_A) = {}^{w}/_{2}$ the relation becomes

$$2wf(t_A) = \frac{wp}{2R}. \tag{3.27}$$

Insertion of equation 3.27 into equation 3.14 yields ϕ_1 in the mixing section according to

$$\phi_1(x,t) = \frac{2R}{wp}x \text{ for } t > t_A \tag{3.28}$$

and integrating equation 3.16 leads to

$$\phi_2(t) = \int_0^{t_A} \frac{D\pi^2}{(2wf(t'))^2}\,dt' + \int_{t_A}^{t} \frac{D\pi^2}{(2wf(t'))^2}\,dt' = \phi_2(t_A) + D\pi^2\frac{4R^2}{w^2p^2}(t - t_A).$$

Employing $\sqrt{1 - qt_A} = \frac{w}{2R}$ in $\phi_2(t_A) = -\gamma\ln(\sqrt{1 - qt_A})$ results in

$$\phi_2(t) = \gamma\ln\left(\frac{2R}{w}\right) + 4D\left(\frac{\pi R}{wp}\right)^2(t - t_A) \text{ for } t > t_A. \tag{3.29}$$

Equations 3.24, 3.25, 3.28, and 3.29 define all necessary transformations to express concentrations in terms of (x,t) by substituting $\phi_1(x,t)$ for ζ and $\phi_2(t)$ for β in equation 3.18. Calculating the temporal evolution of concentrations within a fluid element that passes the mixer requires to specify its 'trajectory' $x(t)$. Due to the specific form of the coordinate transformation these trajectories are isolines of ϕ_1. Using x_l as the lamella position at $t = 0$ leads to $\phi_1(x_l, 0) = {}^{x_l}/_{p}$ and thus the concentration in a fluid element $c(x(t),t)$ is obtained by simply inserting $\zeta = {}^{x_l}/_{p}$ into equation 3.18 instead of $\zeta = \phi_1(x,t)$. The concentrations c, the variable transformations ϕ_i, and the included parameters are summarized in table 3.1.

Figure 3.3 shows concentration profiles for two different flow rates and illustrates the operating principle of hydrodynamic focusing. It can be seen in (b) that mixing accelerates considerably once a co-moving frame of reference enters the mixing section. If the focusing section was completely ignored and identical initial concentrations $c^{(i)}$ as in figure 3.3 were directly applied to lamella widths ${}^{w}/_{L}$ as they appeared in the mixing section, it would take only milliseconds to achieve complete mixing [115]. Thus, an upper bound for mixing times in the SFIMM can roughly be expressed by '$t_A +$ *a few milliseconds*'. Since t_A is reciprocal to the flow rate, the upper bound for mixing times adapts accordingly. At low flow rates like $v = 0.1$ ml/min in (a) fluids are completely mixed long before t_A. In that case the mixing process takes barely advantage of hydrodynamic focusing at all, concentration profiles closely resemble solutions to common heat equations, and mixing will be comparatively slow. With increasing flow rates hydrodynamic focusing becomes more and more significant up to the point where mixing times are choked by their upper bound as t_A falls below the time it takes diffusion to achieve complete mixing within the focusing section, which typically creates sharp edges close to t_A that are reminiscent of cutoffs as seen in the lower panel of (b). The fact that mixing times are limited by residence times in the focusing section unambiguously

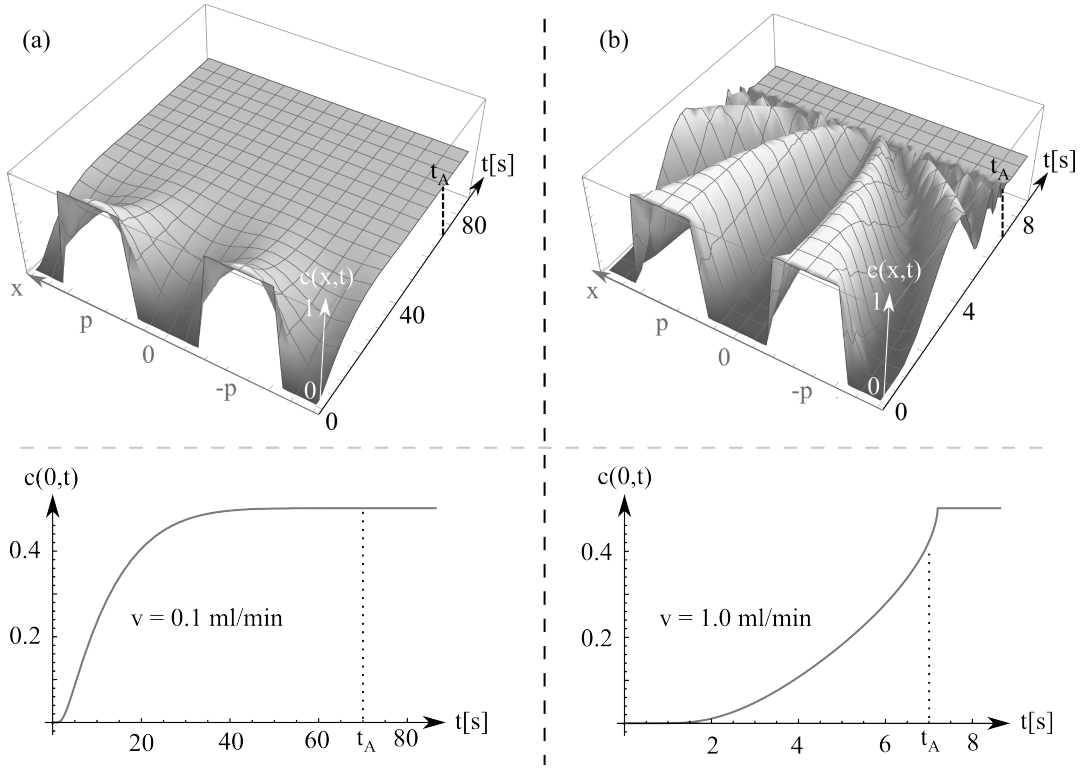

Figure 3.3: *Analytical solution to the convection diffusion equation 3.10 for two different flow rates $v = 0.1$ ml/min (a) and $v = 1.0$ ml/min (b). The respective upper panel depicts $c(x,t)$ for $(x,t) \in [-2p, 2p] \times [0, 1.2t_A]$. $c(x,t)$ denotes the concentration profile in a cross section along the x-axis of a Lagrangian frame of reference (cp. figure 3.1), p is the lamella width at the entrance of the SFIMM, and t_A the residence time in the focusing section. The lower panel shows $c(0,t)$, which is the concentration evolution in a fluid element that travels along the center of the middle lamella. It obviously takes much longer to achieve complete mixing (homogeneous concentration distribution with $c(x,t) = 0.5$) if a low flow rate is applied. Geometry parameters and formulas used to generate the diagrams are listed in table 3.1 and the initial condition is set to $c^{(1)} = 0$, $c^{(2)} = 1$. $c^{(1)} \neq 0$ would account for a premixed amount of liquid 2 in a liquid 1 lamella.*

explains why hydrodynamic focusing naturally induces a strong flow rate dependence of the mixing process, which is the main result of the present section. The additional, more subtle acceleration of diffusion processes that finish mixing within the focusing section for intermediate flow rates between $v = 0.1$ ml/min and $v = 1.0$ ml/min is qualitatively similar and quantitatively described in the equations listed in table 3.1.

The one-dimensional description is, of course, idealized. Flow shearing in micro channels may introduce vertical concentration gradients that lead to Taylor dispersion [116] and hence, the assumption $\frac{\partial^2 c}{\partial z^2} = 0$ or even $\left|\frac{\partial^2 c}{\partial x^2}\right| \gg \left|\frac{\partial^2 c}{\partial z^2}\right|$ might not be strictly valid. Verification would probably require a comparison to numerical solutions of the full Navier-Stokes equations, which was not done in any previous publication and would go beyond the scope of the present work. Quickly assessing the ratio between $\left|\frac{\partial^2 c}{\partial x^2}\right|$ and $\left|\frac{\partial^2 c}{\partial y^2}\right|$ is possible though. To this end equation 3.22 is inverted to investigate the focusing section. Insertion of the resulting $t(r)$ translates the concentration evolution in a Lagrangian frame of reference into a stationary concentration profile $c^{(s)}(x,r) := c(x,t(r))$ seen from the fixed polar coordinate system of

Parameter	Symbol	Value
Diffusion coefficient	D	$10^{-9}\ \frac{\mathrm{m}^2}{\mathrm{s}}$
Focusing radius	R	8 mm
Opening angle	α	1.8 rad
Channel height	h	2 mm
Initial lamella width	p	0.348 mm
Channel width in mixing section	w	0.14 mm
Total number of lamellae	L	40
Residence time in focusing section	t_A	$\frac{\alpha h R^2}{2v}\left(1-\left(\frac{w}{2R}\right)^2\right)$

concentration profile
$c(x,t)=\frac{c^{(1)}+c^{(2)}}{2}+\sum_{n=0}^{\infty}(-1)^n\frac{c^{(1)}-c^{(2)}}{(2n+1)\pi}\cos\left[(2n+1)\pi\phi_1(x,t)\right]\ e^{-(2n+1)^2\,\phi_2(t)}$

concentration evolution $c(x(t),t)$ in a fluid element
$c(x(t),t)=c(x,t)\vert_{\phi_1(x,t)\equiv x_1/p}$ with starting position $x_l\in[-p,p]$

Transformation	$\phi_1(x,t)$	$\phi_2(t)$
$t\le t_A$	$\frac{x}{p\sqrt{1-\frac{2v}{\alpha h R^2}\,t}}$	$-\frac{D\pi^2\alpha h R^2}{p^2 v}\ln\left(\sqrt{1-\frac{2v}{\alpha h R^2}t}\right)$
$t>t_A$	$\frac{2R}{wp}x$	$\phi_2(t_A)+4D\left(\frac{\pi R}{wp}\right)^2(t-t_A)$

Table 3.1: *Compilation of parameter designations and dimensions taken from the technical data sheet of the SFIMM. For the sake of completion, the concentration evolution and the coordinate transformations expressed in terms of these parameters are also listed.*

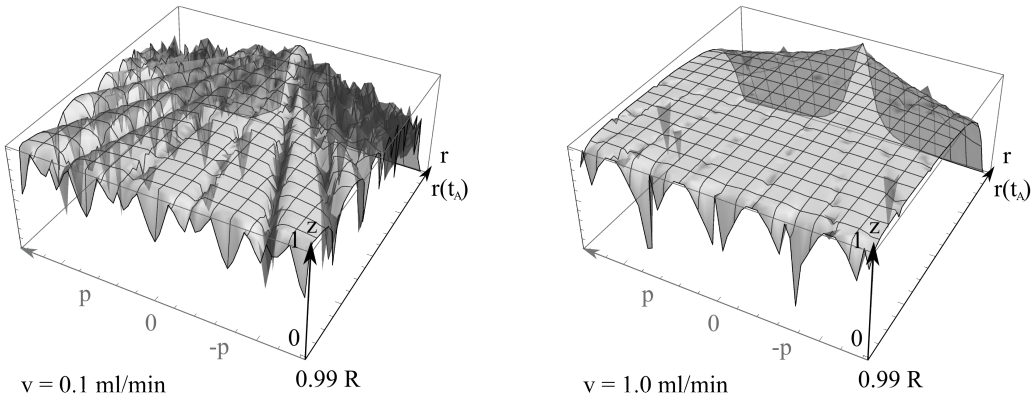

Figure 3.4: *Ratio* $z=\left|\frac{\partial^2 c}{\partial x^2}\right|/\left(\left|\frac{\partial^2 c}{\partial x^2}\right|+\left|\frac{\partial^2 c}{\partial r^2}\right|\right)$ *in the focusing section for two different flow rates.* x *is the lateral direction in a co-moving frame of reference like in figure 3.3 and* r *is the radial distance of its origin from the focusing point. In the largest part of the focusing section* $\frac{\partial^2 c}{\partial x^2}$ *dominates* $\frac{\partial^2 c}{\partial r^2}$*, i.e.* $z\approx 1$*. In the vicinity of* $r(t_A)$ *this relationship turns around because due to the focusing initially distant lamealla appear to be aligned almost parallel to the x-axis.*

the focusing section. $c^{(s)}(x,r)$ looks practically identical to the diagrams in the upper panel of figure 3.3 except that the t-axis is replaced by r. Upon reintroducing the y-variable in c the relation $c(x,\delta y,t) = c^{(s)}(x,r(t)+\delta y)$ suggests estimating $\frac{\partial^2 c}{\partial y^2}$ by $\frac{\partial^2 c}{\partial r^2}$. In fact, $\left|\frac{\partial^2 c}{\partial r^2}\right|$ should actually be larger than the absolute value of $\frac{\partial^2 c}{\partial y^2}$ that would be present if diffusion in y-direction was considered, because the stationary auxiliary field $c^{(s)}$ lacks the accompanied smoothing of the concentration profile in that direction. Figure 3.4 shows the ratio $z = \left|\frac{\partial^2 c}{\partial x^2}\right| / \left(\left|\frac{\partial^2 c}{\partial x^2}\right| + \left|\frac{\partial^2 c}{\partial r^2}\right|\right)$ for the concentration profiles from figure 3.3. It is $z \approx 1$ throughout a vast majority of the focusing section, which supports the assumption $\left|\frac{\partial^2 c}{\partial x^2}\right| \gg \left|\frac{\partial^2 c}{\partial y^2}\right|$ a posteriori. Since analytic solutions to two dimensional heat equations exist [117], solving equation 3.10 with an additional $\frac{\partial^2 c}{\partial y^2}$-term should also be possible by applying a similar transformation as in the one-dimensional case. This is, however, not the focus of the present thesis and might be a topic of future work.

3.2 Split and recombine

In this section the split and recombine mechanism is discussed by presenting an analytical theory developed by Schoenfeld et al. [118]. The working principle of the split and recombine mechanism is illustrated in figure 3.5 together with the CPMM geometry. Even though its implementation is fundamentally different from hydrodynamic focusing, both share a common purpose, namely the reduction of diffusion lengths by deformation of lamellae. The basic structure of the analytical theory from reference [118] resembles the one from section 3.1. It also assumes low Reynolds numbers, neglects flow shearing, and describes an idealized one-dimensional mixing process from a Lagrangian perspective in a moving frame of reference attached to a stream line. In the present case stream lines can roughly be visualized, for instance, by tracing parallel shifts to edges of the outermost red lamella in figure 3.5 (b) in pressure drop direction. The co-moving frame of reference and its associated stream line inside the lower part of a repeat unit are also sketched in figure 3.5 (c).

To describe the split and recombine mechanism mathematically, each repeat unit is treated individually by decomposing the time domain into subsets

$$T_n = \Big[(n-1)t_R, n\,t_R\Big] \text{ with } n = 1,2,3,...,n_{max}, \tag{3.30}$$

where n_{max} is the total number of repeat units in the CPMM and t_R the residence time per repeat unit – i.e. the time it takes the frame of reference to travel through a single unit. Then a diffusion equation

$$\frac{\partial c}{\partial t}(x,t) = \frac{D}{L^2(t)}\frac{\partial^2 c}{\partial x^2}(x,t) \tag{3.31}$$

is solved on every T_n with appropriate initial conditions. x is the direction perpendicular to lamella interfaces, $L(t)$ the channel width inside an upper or lower part of a repeat unit (parts are treated independently from each other), and c the concentration of optionally one of two completely miscible liquids. In the current notation x denotes a rescaled spatial variable similar to ζ or ϕ_1 from section 3.1. It is defined by $x = {}^{x'}/_{L(t)}$, where x' represents the position in meters, and the channel walls are located at $x = \pm{}^1/_2$. To clarify notation we are going to call the solution of equation 3.31 in the n-th repeat unit c_n. Due to a symmetric mixer geometry the concentration evolution inside the upper and lower part of a repeat unit

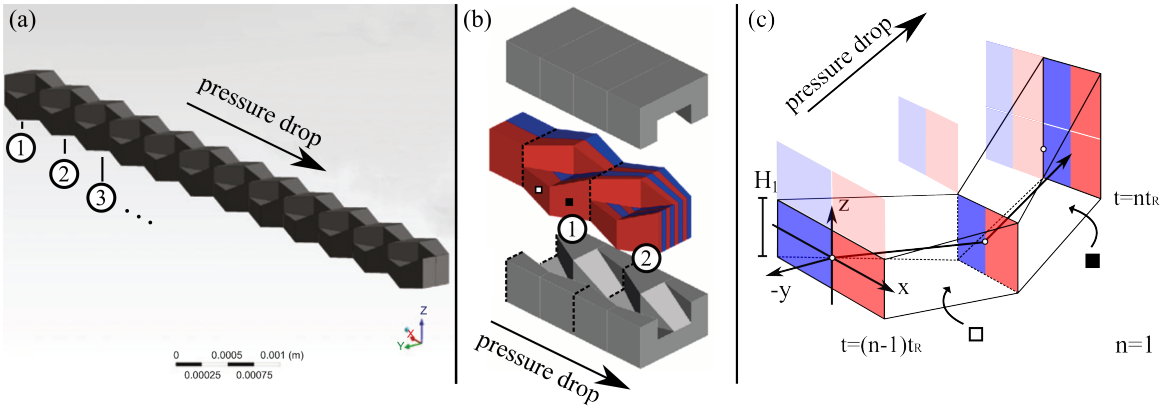

Figure 3.5: *The split and recombine mechanism in the Caterpillar Micromixer (CPMM). The mixer geometry is a succession of identical repeat units labeled by 1, 2, 3, ... as shown in (a). (b) depicts the first two repeat units and the dashed lines indicate their (imaginary) parting planes, while the colors represent two completely immiscible liquids to demonstrate the underlying flow pattern. The black arrow points in pressure drop direction. As the two lamellae from the entrance progress though unit 1 they are split, deformed and eventually recombined to four lamellae with bisected widths at the entrance of unit 2. Since that procedure repeats in every unit, lamella widths have decreased by a factor 2^{-n} at the end of unit n. This successive reduction of diffusion lengths is referred to as the split and recombine mechanism. Each repeat unit is subdivided into two separate parts, which are going to be called 'upper' and 'lower' part. If pallid lamellae are thought away, (c) schematically sketches the lower part of repeat unit $n = 1$. Black and white rectangles in (b) and (c) label same sites and serve as an orientation guide. The full geometry of a repeat unit is recovered if a copy of the wireframe in (c) – the wireframe refers to the black edge lines and excludes the red and blue colors – is rotated by 180° around the y-axis at the entrance and is then shifted upwards by the associated channel height H_1 to match the pallid lamellae. The pallid lamellae belong to the upper part of the repeat unit and the horizontal white line at the exit (slightly above the rightmost arrow head) represents the plane where the lamellae are separated in the successional unit. The juxtaposition of the saturated and pallid lamellae below that line corresponds to the initial lamella configuration in the lower part of unit $n+1 = 2$. The coordinates (x, y, z) belong to the Lagrangian frame of reference applied in the analytical theory by Schoenfeld et al. [118]. Its origin (open circle) follows a stream line within a repeat unit (black arrow connecting open circles). Once the frame of reference reaches the end of a repeat unit its origin is accordingly reset to the middle of the channel in the successive unit, which is indicated by a shift between the open circle and the arrow head of the stream line. The co-moving frame of reference enters unit n at time $t = (n-1)\,t_R$ and leaves it at $t = n\,t_R$, where t_R is its residence time in a repeat unit. Pictures (a) and (b) are taken from Schoenfeld et al. [109] with slight adaptations.*

is identical, meaning c_n can refer to either part. Setting $x = 0$ in the middle of a channel (cp. the open circle in figure 3.5 (c)) makes the concentration profiles point-symmetric. In this case c_n can be written as a Fourier series of the form

$$c_n(x,t) = a_0 + \sum_{i=0}^{\infty} a_{i,n}(t)\sin(k_i x) \quad \text{with } k_i = (2i+1)\pi. \tag{3.32}$$

The Fourier series lacks wave numbers that are even integer multiples of π to ensure Neumann boundary conditions at the channel walls $x = \pm 1/2$. In the process, the concentration profile

inside a channel is considered to be the restriction $c_n|_{x\in[-1/2,1/2]}$ of the 2-periodic function $c_n(\cdot,t)$ defined on $\mathbb{R}$. The imitation of Neumann conditions with periodic functions only works for specific initial conditions $c_1(x,0)$, e.g. the periodic continuation of

$$c_1(x,0) = \begin{cases} c^{(1)} & \text{for } x \in [0,1] \\ c^{(2)} & \text{for } x \in [-1,0] \end{cases} \tag{3.33}$$

as the nature of solutions to a diffusion equation ensures the presence of a maximum and a minimum at $x = \pm 1/2$, i. e.

$$\frac{\partial c_1}{\partial x}(\pm 1/2, t) = 0 \tag{3.34}$$

for all $t \in T_1$. The pattern that is generated by recombining the concentration profiles from the upper and lower part of repeat unit n at $t = n\,t_R$ is set to the initial condition of equation 3.31 on T_{n+1}. In the following the short hand notation $t_{0,n} = (n-1)\,t_R$ is used for the initial time in unit n. As indicated in figure 3.5 (c) $c_{n+1}(x, t_{0,n+1})$ in the $(n+1)$-th repeat unit is constructed by juxtaposing two concentration profiles from the end of the n-th unit. If c' was the concentration expressed in dependence of the position in meters, x', we could simply write

$$c'_{n+1}\left(x', t_{0,n+1}\right) = \begin{cases} c'_n(L(t_R)/2, n\,t_R) & x' = 0 \\ c'_n\left(x' + L(t_R)/2, n\,t_R\right)\Theta(-x') + c'_n\left(x' - L(t_R)/2, n\,t_R\right)\Theta(x') & x' \neq 0 \end{cases}$$

since the channel covers $x' \in [-L(0)/2, L(0)/2] = [-L(t_R), L(t_R)]$ at all $t_{0,n+1}$. In the CPMM it is $L(0) = 2L(t_R)$ and $L(n\,t_R) = L(t_R)$ as well as $L(t_{0,n}) = L(0)$ because all repeat units possess identical geometries.

$$\Theta(x) = \begin{cases} 1 & \text{for } x \geq 0 \\ 0 & \text{for } x < 0 \end{cases}$$

is the Heaviside step function. An expression for the initial condition at $t_{0,n+1}$ in terms of the dimensionless coordinates x and the corresponding concentrations c is achieved by writing

$$x' \pm \frac{L(t_R)}{2} = L(t_R)\left(\frac{x'}{L(t_R)} \pm \frac{1}{2}\right) = L(t_R)\left(\frac{L(0)}{L(t_R)}x \pm \frac{1}{2}\right) = L(t_R)\left(2x \pm \frac{1}{2}\right), \tag{3.35}$$

which states that a rescaled position x in the coordinate frame of the $(n+1)$-th unit at time $t_{0,n+1}$ corresponds to a rescaled position $2x \pm 1/2$ in the coordinate system of unit n at $t = n\,t_R$. Hence, since $c'_n(L(t)x) = c_n(x)$ the initial condition becomes

$$c_{n+1}(x, t_{0,n+1}) = \begin{cases} c_n(1/2, n\,t_R) & x = 0 \\ c_n\left(2\,x + 1/2, n\,t_R\right)\Theta(-x) + c_n\left(2\,x - 1/2, n\,t_R\right)\Theta(x) & x \neq 0 \end{cases}. \tag{3.36}$$

Checking equation 3.36 at $x = \pm 1/2$ verifies that $c_{n+1}(\pm 1/2, t_{0,n+1}) = c_n(\pm 1/2, n\,t_R)$, meaning that the concentrations at the channel walls in the n-the repeat unit are mapped to the channel walls in the $(n+1)$-th one. Thus, it follows by induction from equation 3.34 that

$$\frac{\partial c_n}{\partial x}(\pm 1/2, t) = 0 \quad \forall\, n. \tag{3.37}$$

It should be noted that c_{n+1} from equation 3.36 is not necessarily 2-periodic on $\mathbb{R}$ due to the shift of $\pm 1/2$. It is, however, possible to construct a 2-periodic function by restricting c_{n+1} to $[-1, 1]$ and then periodically extending this restriction to $\mathbb{R}$. As a consequence, expressing c_n by equation 3.32 remains valid for all n.

Now that we have discussed boundary and initial conditions of equation 3.31 on each T_n, we turn our attention to the solutions. Combining equations 3.32 and 3.31 leads to

$$\sum_{i=0}^{\infty} \left(\frac{\partial a_{i,n}}{\partial t}(t) + k_i^2 \frac{D}{L^2(t)} a_{i,n}(t) \right) \sin(k_i t) = 0 \tag{3.38}$$

and because the sine functions are linearly independent it is

$$\frac{\partial a_{i,n}}{\partial t}(t) = -k_i^2 \frac{D}{L^2(t)} a_{i,n}(t) \quad \forall\, i \text{ and } n, \tag{3.39}$$

which is solved by

$$a_{i,n}(t) = a_{i,n}(t_{0,n})\, e^{-k_i^2 D \int_{t_{0,n}}^{t} \frac{1}{L^2(t')} dt'}. \tag{3.40}$$

$a_{i,n}(t_{0,n})$ in equation 3.40 are the Fourier coefficients of the respective initial condition. Applying the standard formula

$$a_{i,n}(t_{0,n}) = \int_{-1}^{1} c_n(x, t_{0,n}) \sin(k_i x)\, dx, \tag{3.41}$$

for 2-periodic functions to equations 3.33 and 3.36 eventually yields a recursive definition for $a_{i,n}(t_{0,n})$ with

$$a_{i,1}(t_{0,1}) = \frac{2(c^{(1)} - c^{(2)})}{k_i}. \tag{3.42}$$

and

$$a_{i,n+1}(t_{0,n+1}) = \sum_{j=0}^{\infty} (-1)^{j+1} \frac{k_i}{k_i^2/4 - k_j^2}\, a_{j,n}(n\, t_R). \tag{3.43}$$

Equation 3.33 also implies

$$a_0 = \frac{c^{(1)} + c^{(2)}}{2}. \tag{3.44}$$

To arrive at the final solution of the diffusion problem, the integral $\int (1/L^2(t'))\, dt'$ in equation 3.40 needs to be evaluated, so in the first place an explicit expression for $L(t)$ has to be constructed. To this end, both parts of a repeat unit are divided into two sections with straight edges as shown in figure 3.6 for the lower part. Using trigonometric relations, the channel width $L(t)$ in section 1 can be expressed in dependence of $l(t)$ according to

$$L(t) = L_1 - \frac{\tilde{L}_1 - \tilde{L}_2}{l_1}\, l(t). \tag{3.45}$$

In repeat unit n $l(t)$ is approximated by

$$l(t) = \frac{v}{A_1}\, (t - t_{0,n}), \tag{3.46}$$

where $A_1 = L_1 H_1$ is the channel cross section at the entrance of a repeat unit and v the

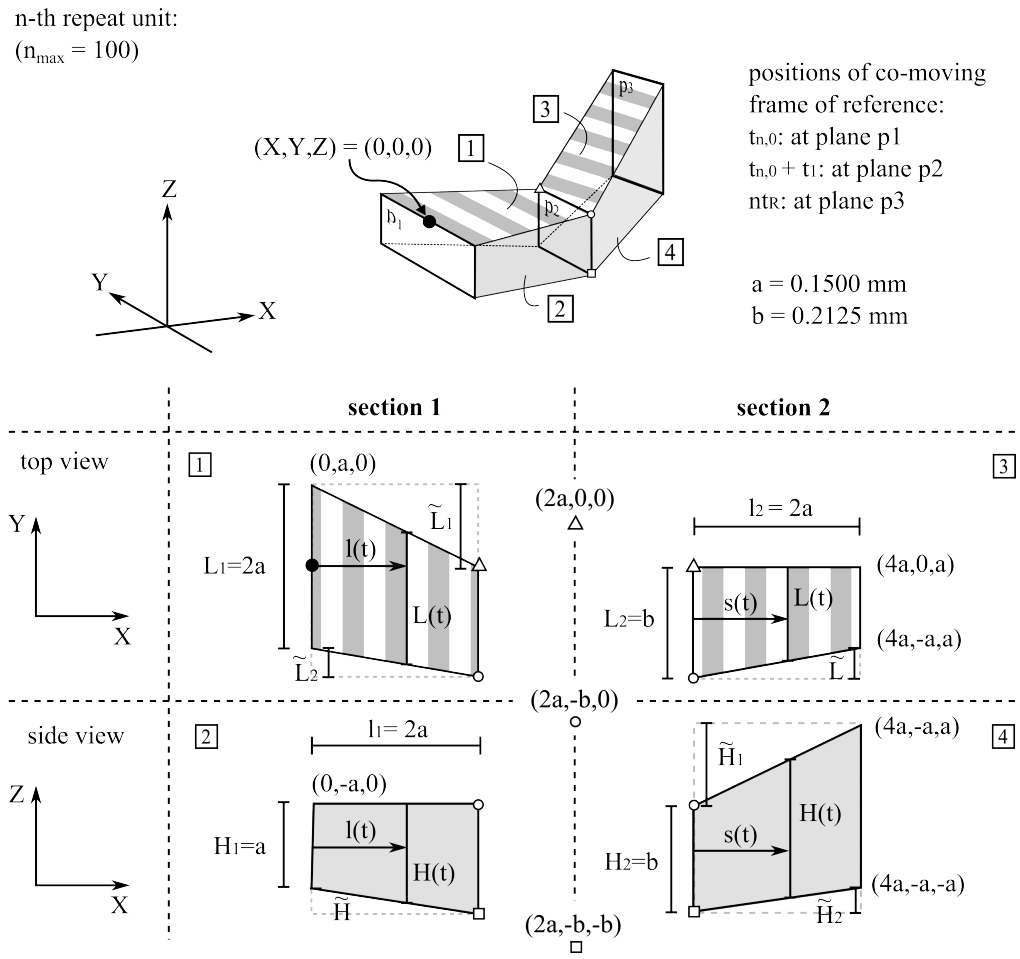

Figure 3.6: *Dimensions of the lower part of a repeat unit n in the CPMM (upper parts are analogous). A part is divided into two sections that are separated by the plane p_2 in the 3D sketch. The sites numbered by 1, 2, 3, and 4 are depicted individually in the table below that sketch. Open circles, rectangles, and triangles label connected corners which lie on p_2. Coordinates of unlabeled corners are shown directly at the corner, while coordinates of labeled corners can be found on the vertical dashed line at the associated symbol. $l(t)$ and $s(t)$ are auxiliary functions used to calculate the integral $\int \frac{1}{L(t')^2} dt'$ in equation 3.40. The small list on the top right summarizes times when the co-moving frame of reference passes a plane p_i.*

flow rate. In this case, v is the flow rate inside a single part of a repeat unit, i.e. one half of the flow rate applied to the mixer. The cross section area is assumed to be constant throughout section 1 of a repeat unit because it is equal at plane p_1 and plane p_2 with only slight variations in between. Hence,

$$L(t) = L_1 - \frac{v\left(\tilde{L}_1 - \tilde{L}_2\right)}{A_1\, l_1}(t - t_{0,n}) =: L_1 - \alpha(t - t_{0,n}) \tag{3.47}$$

and

$$\int_{t_{0,n}}^{t} \frac{1}{L^2(t')} dt' = \frac{1}{\alpha L_1 - \alpha^2(t - t_{n,0})} - \frac{1}{\alpha L_1}. \tag{3.48}$$

This result holds for $t \in [t_{0,n}, t_{0,n} + t_1]$, where $t_1 := {}^{l_1 A_1}/_{v}$ follows from $l(t - t_{0,n} = t_1) = l_1$

and denotes the time that passes while the co-moving frame of reference travels from p_1 to p_2 in figure 3.6. In an analogous fashion the channel width in section 2 is calculated by

$$L(t) = L(t_1) - \frac{\tilde{L}}{l_2} s(t) = L_2 - \frac{\tilde{L} v}{A_2\, l_2}(t - t_{0,n} - t_1) =: L_2 - \beta(t - t_{0,n} - t_1), \tag{3.49}$$

where $s(t)$ is expressed through

$$s(t) = \frac{v}{A_2}(t - t_{0,n} - t_1) \tag{3.50}$$

with $A_2 = L_2 H_2$ since the cross section areas at p_2 and p_3 are identical, too. Inside section 2 the integral in the exponent of equation 3.40 reads

$$\begin{aligned}
&\int_{t_{0,n}}^{t} \frac{1}{L(t')^2} dt' = \int_{t_{0,n}}^{t_{0,n}+t_1} \frac{1}{L(t')^2} dt' + \int_{t_{0,n}+t_1}^{t} \frac{1}{L(t')^2} dt' \\
&= \frac{1}{\alpha L_1 - \alpha^2 t_1} - \frac{1}{\alpha L_1} + \frac{1}{\beta L(t_1) - \beta^2(t - t_1 - t_{0,n})} - \frac{1}{\beta L_1(t_1)} \\
&= \frac{1}{\alpha L_1 - \alpha^2 t_1} - \frac{1}{\alpha L_1} + \frac{1}{\beta L_2 - \beta^2(t - t_1 - t_{0,n})} - \frac{1}{\beta L_2}
\end{aligned} \tag{3.51}$$

with $t \in [t_{0,n} + t_1, n\, t_R]$ and the residence time t_R in a repeat unit is obtained from

$$s(n\, t_R) = l_2 \Leftrightarrow t_R = \frac{l_2 A_2}{v} + t_1 = \frac{l_2 A_2 + l_1 A_1}{v}. \tag{3.52}$$

The co-moving frame of reference leaves the mixer at $t_{max} = t_{0,n_{max}} + t_R = n_{max} t_R$ and enters a tube with a constant cross section $L(0)^2 = L_1^2$. In case $t > t_{max}$ it is

$$\begin{aligned}
&\int_{t_{0,n_{max}}}^{t} \frac{1}{L(t')^2} dt' = \int_{t_{0,n_{max}}}^{t_{max}} \frac{1}{L(t')^2} dt' + \int_{t_{max}}^{t} \frac{1}{L(t')^2} dt' \\
&= \frac{1}{\alpha L_1 - \alpha^2 t_1} - \frac{1}{\alpha L_1} + \frac{1}{\beta L_2 - \beta^2(t_R - t_1)} - \frac{1}{\beta L_2} + \frac{t - t_{max}}{L_1^2/2}.
\end{aligned} \tag{3.53}$$

$L_1^2/2$ in the denominator of the last summand instead of L_1^2 accounts for the fact that fluid from one part of a repeat unit eventually takes only half the cross section of the complete tube. Inserting the integrals from equations 3.48, 3.51 and 3.53 together with the initial conditions from equations 3.42 and 3.43 into the Fourier coefficients from equation 3.40 allows to calculate concentration profiles $c(x,t)$ in the CPMM via equation 3.32, where $c(x,t) = c_n(x,t)$ if $t \in T_n$. The corresponding formulas are summarized in table 3.2 for the sake of clarity.

The mixing quality ϵ and the mixing time t_{mix} are defined analogously to equations 3.19 and 3.21 by

$$\epsilon(t) = 1 - \sqrt{\int_{-1/2}^{1/2} \left| c(x,t) - \frac{c^{(1)} + c^{(2)}}{2} \right|^2 dx} \text{ and } \epsilon(t_{mix}) = 0.99. \tag{3.54}$$

The selected scaling of the spatial coordinate renders the one-dimensional trajectories of fluid parcels from the Lagrangian perspective to be x-isolines as long as considerations are

concentration evolution in a cross section along x
$c(x,t) = c_n(x,t) = \frac{c^{(1)}+c^{(2)}}{2} + \sum_{i=0}^{\infty} a_{i,n}(t)\sin(k_i x)$ for $t \in T_n = \left[(n-1)t_R, n\,t_R\right]$
with $k_i = (2i+1)\pi$ and $a_{i,n}(t) = a_{i,n}(t_{0,n}) \cdot e^{-k_i^2 D \int_{t_{0,n}}^{t} \frac{1}{L^2(t')}\,dt'}$

recursive definition of coefficients
$a_{i,n+1}(t_{0,n+1}) = \sum_{j=0}^{\infty}(-1)^{j+1}\frac{k_i}{k_i^2/4 - k_j^2} a_{j,n}(n\,t_R)$ starting from $a_{i,1}(t_{0,1}) = 2\frac{c^{(1)}-c^{(2)}}{k_i}$

integral in exponent
$I(t-t_{0,n}) \coloneqq \int_{t_{0,n}}^{t} \frac{1}{L^2(t')}\,dt'$
$I(t-t_{0,n}) = \begin{cases} \dfrac{1}{\alpha L_1 - \alpha^2(t-t_{n,0})} - \dfrac{1}{\alpha L_1} & 0 \le t - t_{0,n} \le t_1 \\ I(t_1) + \dfrac{1}{\beta L_2 - \beta^2(t-t_1-t_{0,n})} - \dfrac{1}{\beta L_2} & t_1 < t - t_{0,n} \le t_R \\ I(t_R) + \dfrac{t-t_{max}}{L_1^2/2} & t > t_{max} \end{cases}$

constants
$\alpha = \frac{\tilde{L}_1 - \tilde{L}_2}{A_1 l_1}\,v \quad \beta = \frac{\tilde{L}}{A_2 l_2}\,v \quad t_1 = \frac{l_1 A_1}{v} \quad t_R = t_1 + \frac{l_2 A_2}{v} \quad t_{max} = n_{max} t_R \quad t_{n,0} = (n-1)t_R$

concentration evolution $c(x(t),t)$ in a fluid element
$c(x(t),t) = c(x_n,t)$ for $t \in T_n$ with $x_{n+1} = {}^{x_n}/_2 + {}^{(-1)^n}/_4$
and starting position $x_1 \in [-1/2, 1/2]$

Table 3.2: *Summary of formulas to calculate concentration profiles in the CPMM. The geometry parameters are displayed in figure 3.6.*

restricted to one arbitrary repeat unit. As a result, the calculation of concentration evolutions within a fluid element that travels though the mixer along a trajectory $x(t)$ only requires tracking its x-displacement each time it enters a new repeat unit. As stated in the context of equation 3.35, the position x_n that is mapped onto x_{n+1} is given by $x_n = 2x_{n+1} \pm 1/2$, where x_n denotes the position in the n-th repeat unit. This is equivalent to a recursive expression

$$x_{n+1} = \frac{1}{2}x_n \pm \frac{1}{4} \tag{3.55}$$

for the position of a fluid element. A shift in positive x-direction corresponding to $+$ in the above equation is realized if the fluid element passes a lower part of a repeat unit. Likewise, the position is shifted to the left by $-$ if the fluid element passes the upper part.

Figure 3.7 shows solutions to equation 3.31. Like hydrodynamic focusing, the split and recombine mechanism causes mixing times to decrease with increasing flow rates, because higher flow rates drive fluid elements more quickly into regions where lamellae are thin and diffusion is fast. A striking difference between the CPMM and the SFIMM is the tremendous

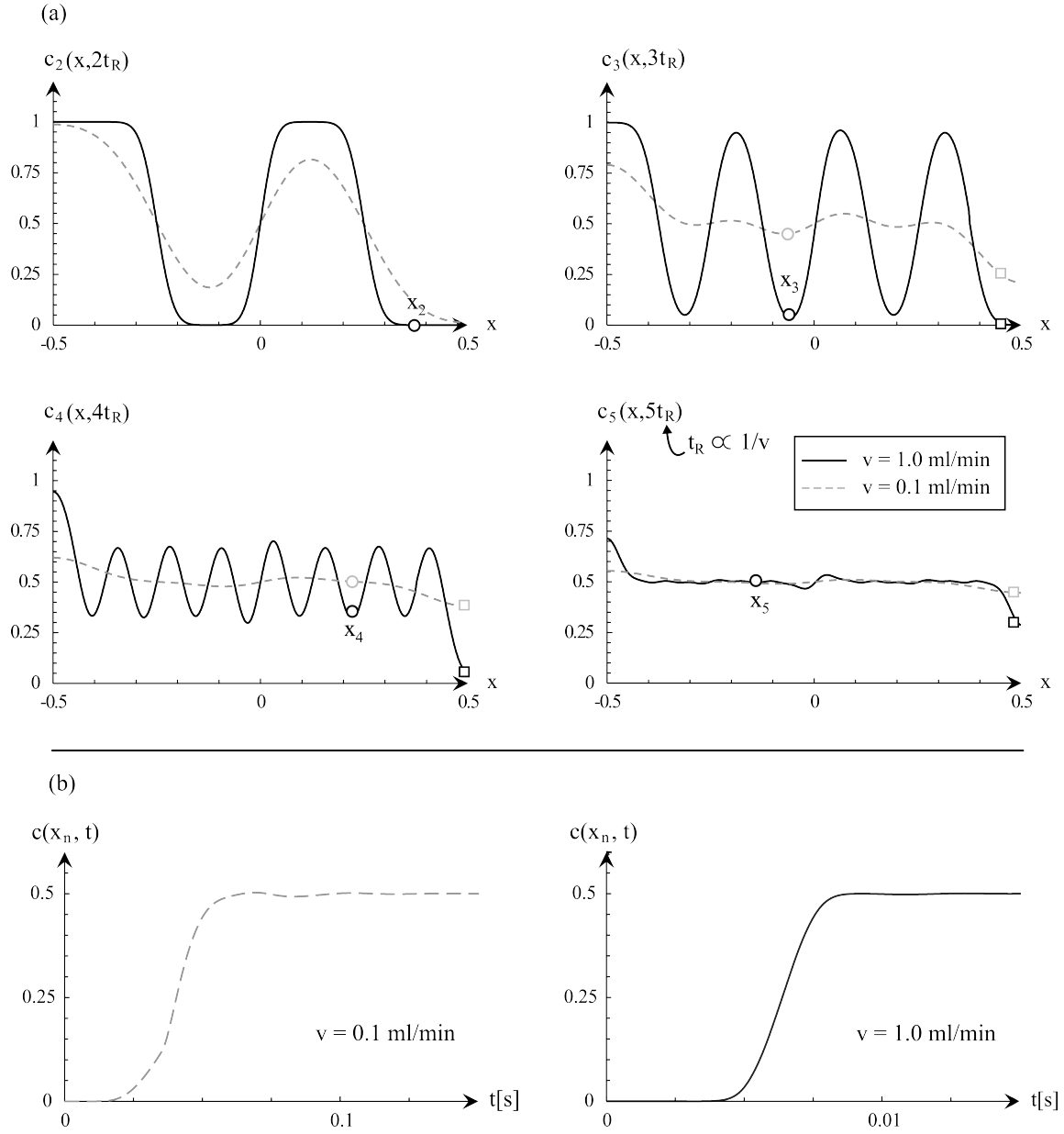

Figure 3.7: *Substance concentrations c in the CPMM at two different flow rates $v = 0.1$ ml/min (dashed grey lines) and $v = 1.0$ ml/min (solid black lines). c is analytically calculated by the formulas in table 3.2 with an initial condition $c^{(1)} = 0$, $c^{(2)} = 1$. (a) shows $c(x, n\,t_R)$ for n =2, 3, 4, and 5 to demonstrate how the split and recombine mechanism affects concentration profiles. Note that $t_R \propto 1/v$ and the displayed concentration profiles belong to either the lower or upper part of the corresponding repeat unit. The open circles represent the positions x_n of a fluid element that is initially located at $x_1 = 1/4$ and travels alternately though upper and lower parts of consecutive repeat units. These positions are calculated by the recursive formula $x_n = {}^{x_{n-1}}/_2 + {}^{(-1)^n}/_4$, which is constructed in accordance with equation 3.55. The open rectangles indicate the positions $x_n = {}^{x_{n-1}}/_2 + 1/4$ the same fluid element would have if it traveled through lower parts only. (b) depicts temporal concentration evolutions $c(x(t), t) = c_n(x_n, t)$ inside a fluid element. The positions x_n correspond to the open circles from (a). Throughout the present work only the alternating passage of upper and lower parts is considered because the values of c_n at the circles are much more representative for the whole cross section than at the rectangular position, which is pushed against the channel wall.*

discrepancy of mixing times. The mixing times in the SFIMM for $v = 0.1$ ml/min and $v = 1.0$ ml/min from figure 3.3 extent to magnitudes of 10 seconds while the mixing times in the CPMM are below 0.1 seconds. This is attributed to much smaller channel cross sections in the CPMM, which results in larger flow velocities at specific flow rates. Another difference is the influence of the flow rate on the qualitative 'shape' of the concentration evolution in the lower panels of figures 3.3 and 3.7. In the SFIMM, the flow rate changes the shape from concave to convex while the CPMM profiles are almost solely compressed along the t-axis as flow rates increase.

Chapter 4

Specification of a theoretical framework for controlled assembly

At spatial resolutions that enable to visualize particles with diameters on the nanometer scale, mixer geometries easily exceed length scales accessible with any simulation technique presented in chapter 2. Since a direct simulation of complete mixer geometries is therefore not possible, modeling the co-solvent method poses a non-trivial spatial multiscale problem. In the present work we approach that problem by describing the particle growth process from a Lagrangian perspective of the fluid elements introduced in chapter 3. According to the experimental setup in figure 1.2, thermodynamic systems of interest, i.e. simulation boxes, are then fluid elements that are initially placed inside a good solvent lamella and filled with additional polymer. For simplicity the amount of polymer inside a fluid element is assumed to be conserved, while the good and selective solvent content may change. This assumption is inspired by the low diffusion coefficient of polymers compared to solvent molecules. Taking into account experimentally determined particle radii of about 50 nm, simulation boxes should have minimum edge lengths somewhere between 100 nm and 1 μm to eventually contain a sufficiently large number of particles for a representative study of size distributions. The initial lamella width is about $p = 0.35$ mm in the SFIMM and $a = 0.15$ mm in the CPMM, so simulation boxes with 1 μm edges, for instance, constitute very tiny subsets of a lamella with roughly ${}^{1\ \mu\mathrm{m}}/_{p} = {}^{1}/_{350}$ to ${}^{1\ \mu\mathrm{m}}/_{a} = {}^{1}/_{150}$ times smaller spatial extensions in diffusion direction x. By the time lamella widths become comparable to 1 μm, the mixing process is close to completion for any experimentally applied flow rate and concentration profiles $c(x,t)$ are almost constant: in the mixing section of the SFIMM or at $t \approx 5t_R$ in the CPMM (cp. figures 3.3 and 3.7), the above factors would increase to $\approx {}^{1\ \mu\mathrm{m}\,L}/_{w} = {}^{1}/_{3.5}$ and $\approx {}^{1\ \mu\mathrm{m}}/_{2^{-5}a} = {}^{1}/_{4.7}$. This suggests that one can approximate the integral solvent concentration ${}^{\int c(\vec{r},t)\,dV}/_{\int dV}$ in such simulation boxes by its value at the center, i.e. by $c(x(t),t)$ from tables 3.1 and 3.2. By convention, we consider liquid 1 to represent good solvent while liquid 2 represents the selective or poor one. $c(x(t),t)$ determines the total number of selective solvent molecules in a simulation box. How we exactly implement $c(x(t),t)$ into the models for particle growth is addressed in later sections where the respective model equations are presented.

In principle, micromixers introduce two flow rate dependent factors: solvent mixing and flow shearing in micro channels. A graphical summary how these factors may potentially affect particle growth inside a small fluid element is depicted in figure 4.1. Subdividing the growth process into two stages, the initial assembly of molecules into aggregates as sketched in figure 4.1 (b) and the further growth of aggregates by collision-induced coagulation (in the

following called collision-coagulation) as illustrated by (c) to (f), leaves four mechanisms that may connect or couple particle sizes to flow rates:

(i) the response of molecular assembly to solvent mixing,

(ii) the response of collision-coagulation and stabilization to solvent mixing,

(iii) the response of molecular assembly to shear flow, and

(iv) the response of collision-coagulation and stabilization to shear flow.

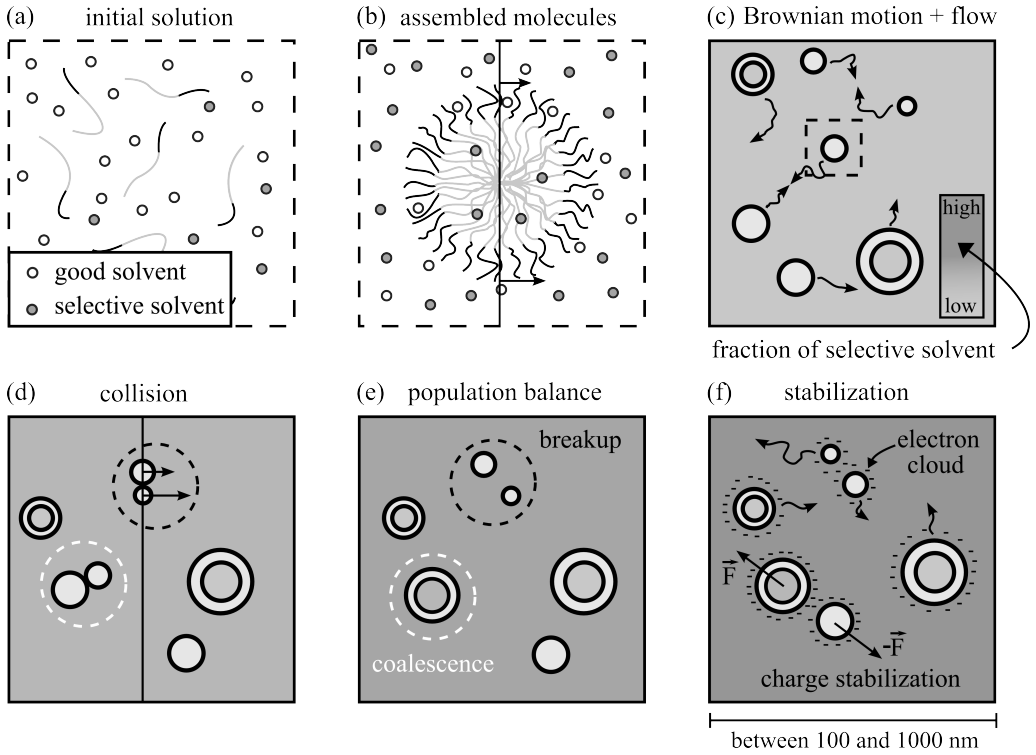

Figure 4.1: *Sketch of particle growth inside a fluid element. (a) and (b) illustrate the assembly of molecules into a micelle on a microscopic length scale. The increasing number of selective solvent molecules (grey dots) from (a) to (b) indicates solvent mixing. Solvent mixing is likely to affect molecular assembly as the latter is driven by interactions between monomers and solvent molecules. The two arrows attached to the vertical line in (b) illustrate flow shearing in micro channels, which might potentially distort or even rupture the micelle into smaller aggregates. The size or shape of the micelle could also be affected by a flow shear induced alignment or stretching of single polymer chains during molecular assembly. The pictures in (a) and (b) are magnifications of the dashed rectangle in (c). (c) shows several particles on a mesoscopic spatial scale, and from there on solvent mixing is illustrated by a change of background colors (the darker the grey the higher the fraction of selective solvent). The twisted arrows symbolize Brownian motion in combination with a potentially flow induced displacement of aggregates, which might cause them to collide as shown in (d). Subsequent (shear induced) breakup or coalescence (dashed black and white circle in (d) and (e)) may change mean sizes of particle populations until a stabilization mechanism interrupts particle growth. Accumulating surface charges that prevent collision by a Coulomb force $\vec{F}$ as shown in (f), for example, constitute such a mechanism. As the development of sufficiently large electron clouds depends on the pH of the solution, solvent mixing might also affect stabilization in the late stage of particle growth.*

Finding out whether experimental results are caused by a combination of the four previously introduced coupling mechanisms or whether there is even a dominating one is fundamental to the explanation of figure 1.3, and thus it is a main objective of the present work. The identification of significantly contributing coupling mechanisms can also be viewed as a necessary preliminary consideration for a potential development of quantitatively accurate simulation tools to describe the co-solvent method in the future. Because a direct numerical simulation of the complete mixer geometry with accurate hydrodynamics is not possible, simplifications are mandatory, and a typical simplification procedure is a separation of significant and insignificant contributions in order to neglect the latter in a mathematical description.

The experimental data from Mueller [36] (cp. figure 1.3 (e)) indicate that the co-solvent method in batch yields similar data point progressions as its continuous implementation and directly draws attention to coupling mechanisms (i) and (ii). The insignificance of shear induced polymer stretching is also supported by values of the Weissenberg number, which is defined by

$$W_i = \dot{\gamma}\tau \tag{4.1}$$

and compares viscous to elastic forces. $\dot{\gamma}$ is a shear rate of a fluid flow and τ the relaxation time of polymer chains. To roughly estimate the range of Weissenberg numbers in micromixers we consider a pipe flow for the sake of simplicity. Given a flow rate v, the shear rate at the inner wall of a pipe with radius r reads

$$\dot{\gamma} = \frac{4v}{\pi r^3}. \tag{4.2}$$

The smallest channel dimensions in the CPMM or SFIMM happen to be at plane p2 in figure 3.6, where the channel cross section is a square with edge lengths $b = 0.2125$ mm. Assuming $r = b/2$ yields $\dot{\gamma} = 17104\,\hat{v}\ \mathrm{sec}^{-1}$ with $\hat{v}$ being the flow rate in units of ml/min. The longest relaxation time of a Gaussian polymer chain with N monomers and Kuhn length k reads

$$\tau = \frac{1}{3\pi^2}\frac{Nk^2}{D_G} \tag{4.3}$$

with the center of mass diffusion coefficient D_G [102]. Substituting the Kuhn length by the radius of gyration R_g through the relation $Nk^2 = 6R_g^2$ for Gaussian chains [103], τ can be cast into the form

$$\tau = \frac{2}{\pi^2}\frac{R_g^2}{D_G}. \tag{4.4}$$

Roughly assuming $N = 190$ (cp. figure 1.3), $R_g = 10$ nm, and $D_G = {}^{10^{-9}}/_{N}\ \mathrm{m^2 sec^{-1}}$ gives $\tau = 3.853 \times 10^{-6}$ sec, and insertion of the experimentally applied flow rates $\hat{v} \in [0.1\ \mathrm{ml/min}, 5\ \mathrm{ml/min}]$ then yields $W_i \in [0.007, 0.329]$. Shear flow tends to distort polymer chains for $W_i \gtrsim 1.3$ [119], which is significantly larger than the Weissenberg numbers in micromixers. As a consequence, the task of '*explaining the experimentally observed flow rate dependence of particle sizes in figure 1.3*' can be generalized to '*explaining particle growth at different solvent mixing speeds (inside a small fluid element)*', which is synonymous with size-controlled assembly according to the definition at the end of chapter 1.

To our current knowledge, the response of particle sizes to solvent mixing speeds in the absence of flow shearing has been simulated only by Spaeth et al. [38] and Nikoubashman

et al. [35], as mentioned in the preliminary remark of part I. The authors of reference [38] apply Dissipative Particle Dynamics and the authors of reference [35] use (coarse grained) Molecular Dynamics. In both studies the spatial extension of simulation boxes is comparable to fluid elements and solvent mixing is implemented by a single solvent with a temporally increasing repulsive force between solvent molecules and monomers.[1] Considering all classical models, Molecular Dynamics is the closest to the Schrödinger equation and thus, it provides the most accurate description of a particle growth process. This accuracy, however, comes at the expense of excessive computation times, which enforce the restriction of simulations to mixing times on the microsecond scale and below. Even on high performance clusters and even if a simplified model for solvent mixing like temporally changing interactions is applied, accessible time scales are up to 10^{-6} to 10^{-4} times lower than mixing times in figure 3.3 or 3.7 [35]. The inaccessibility of realistic mixing times also transfers to the Dissipative Particle Dynamics simulations [38].[2] Therefore, particle models do not manage to readily describe controlled assembly at experimental conditions. Both references [35] and [38] still show particle size dependencies on mixing speeds that exhibit a similar scaling behavior as the data in figure 1.3. However, neither of them explains the origin of this behavior or discusses its validity range. The authors do not directly relate theoretically defined mixing speeds to experimentally applied Reynolds numbers or flow rates, either, and they do not account for mixer geometries.

As opposed to the microscopic perspective in references [35] and [38], the present work approaches controlled assembly from 'large' scales by applying the most coarse grained models discussed in chapter 2: mean field theories and phase field models that allow to study length scales of micrometers on time scales of seconds. There are two motives for the decision to use such coarse grained continuum models. First, we intend to provide mean field continuum descriptions as conceptually complementary content to the particle models and discuss their potential advantages or disadvantages regarding size-controlled assembly in general. Second, since the description of experimental conditions fails with the computational complexity of particle models, a logical consequence is investigating if computationally efficient mean field theories fail with physical accuracy. If they succeed in describing experimental observations, mean field theories should provide a suitable framework to study controlled assembly at experimental conditions. Considering the complexity of the problem as a whole, expecting a perfect numerical match of simulation results and the experimental data in figure 1.3 at the current state of research is elusive (this fact is also supported by Spaeth et al. [38]). For that reason we restrict investigations to principal relations and focus on explaining their general characteristics. Such relations include the scaling behavior of particle size dependencies as seen in figure 1.3, their qualitative response to parameter variations like temperature and mean polymer content in solution, and typical length scales of particle sizes that are created by specific flow rates. We consider a model suited to capture the co-solvent method if it manages to reproduce these fundamental properties and in this context, the present work aims to elaborate whether mean field continuum theories constitute appropriate descriptions for the co-solvent method.

To investigate principal relations in a conceivably general manner and to guarantee a com-

[1] A detailed recapitulation of the Molecular Dynamics model is given during the discussion in subsection 5.3.3.
[2] The largest mixing time in the Molecular Dynamics simulations is 40 μs, and in the Dissipative Particle Dynamics simulations it is 200 μs.

putationally efficient implementation, it is expedient to utilize a model that contains only few physical parameters and possesses an uncomplicated mathematical structure. Hence, we start with describing solvent mixing by time dependent interactions in a phase field model. The qualitative agreement of that rather simplified modeling approach to experimental observations eventually implies that mean field continuum theories could indeed be suitable foundations to develop even quantitatively accurate descriptions of the co-solvent method. Therefore, parts of this work also deal with the development of more realistic implementations of solvent mixing into continuum models than just time dependent interaction parameters. However, we only investigate and explain principal relations by studying 'theoretical model polymers' with these more realistic models as well. A direct numerical comparison to experimental data for a real polymer solution would go beyond the scope of the present work. Although we only had to insert corresponding parameters into our models, obtaining them would have been too time-consuming. The necessary parameters of the PB-PEO-THF-H2O system from figure 1.3 were, unfortunately, not measured during the original experiments.

PART II

CONTROLLED ASSEMBLY OF HOMOPOLYMERS: CAHN-HILLIARD TYPE MODELS

Preliminary Remark

In part II we study the earliest stage of particle growth during solvent mixing, i.e. coupling mechanism (i) in chapter 4, by phase field models with Flory-Huggins-de Gennes free energy functionals. To keep the underlying equations of our first approach as simple as possible we decided to restrict to homopolymer solutions.

With respect to controlled assembly of amphiphilic diblock-copolymers, the simplification to homopolymers is inspired by the notion that phase separation in amphiphilic systems is initially driven by the unfavorable interaction between the solvent and the solvent-phobic block, which results in typical 'Cahn-Hilliard type' composition profiles in simulations with more complex models (without solvent mixing) [88]. Block incompatibility and solvent-philicity of the other block are usually more relevant in later stages characterized by morphology formation or particle stabilization. Thus, replacing a copolymer by a homopolymer corresponding to its solvent-phobic block should still reflect typical length scales in density profiles and their principal relations if only the very early stages of particle formation are considered. The recently discovered possibility to produce electrostatically stabilized homopolymer particles with the co-solvent method [35] also offers a direct application to the models presented in this part. As already stated in chapter 4, Nikoubashman et al. [35] also performed Molecular Dynamics simulations, which provides a benchmark for the phase field model.

Chapter 5

Model I: Time dependent polymer-solvent interactions in a two-component canonical ensemble

As the main effect of solvent mixing is a change of 'mean solvent quality' from 'good' to 'poor', we first incorporate solvent mixing by only taking into account the change in solvent quality. In the current chapter the three-component system from the experiments is modeled by a two-component system containing a polymer and only one solvent, which changes its quality over time. More specifically, at any given time we describe the momentary solvent mixture by one single effective solvent with an associated interaction parameter χ at a polymer-solvent contact. The addition of poor solvent into the solvent mixture is modeled by a temporal increase of χ, which is similar to the approach in reference [35]. Technically speaking, solvent mixing is described by a continuous quench and the mixing speed corresponds to a quench rate. We should note that the fundamental effect of different quench rates on characteristic structure sizes was already investigated in connection with continuous cooling of an alloy in the 60's [120]. Since the χ-parameter plays the analogous role to temperature, we already know that higher quench rates generate smaller correlation lengths in density profiles. In the following the main focus lies in the question whether this simple model is able to describe experimental observations.

Because the controlled assembly of stabilized homopolymer particles was achieved only recently, corresponding experimental data is accordingly scarce. So we are going to compare simulation results for homopolymers to the experimental results for copolymers from figure 1.3. Although this comparison might appear to be odd at first glance, it is still reasonable because it eventually turns out that the size of simulated homopolymer aggregates in the earliest stage of phase separation shows the same general behavior as the final copolymer particles from experiments in practically every single aspect. This similarity includes strong implications about the physical mechanism underlying size-controlled assembly of both homo- and copolymers and is thus a fundamental part of the present work.

5.1 Model equations

The present chapter describes relaxation dynamics in a two-component canonical ensemble containing a homopolymer and a solvent at temperature T and volume V. The total free

energy is expressed by a Flory-Huggins-de Gennes free energy functional

$$\mathcal{F}\left[\rho_P, \rho_S\right] = \int_V \left(\hat{f}\left(\rho_P(\vec{r}), \rho_S(\vec{r})\right) + \frac{\Lambda_P}{2} \left|\nabla \rho_P(\vec{r})\right|^2 + \frac{\Lambda_S}{2} \left|\nabla \rho_S(\vec{r})\right|^2 \right) d\vec{r}, \tag{5.1}$$

which is physically accurate in the weak segregation regime, where amplitudes of composition fluctuations are low and their gradients weak (cp. subsection 2.2.3). ρ_P and ρ_S denote number concentration profiles of polymer and solvent molecules, and Λ_P and Λ_S are the respective gradient energy parameters. $\hat{f}\left(\rho_P, \rho_S\right)$ is the Flory-Huggins free energy density of a homogeneous system and is given by

$$\hat{f}(\rho_P, \rho_S) = k_B T \left[\rho_S \ln(\phi_S) + \rho_P \ln(\phi_P) + \chi \rho_S \phi_P\right] \tag{5.2}$$

[104]. In the framework of the Flory-Huggins theory of polymer solutions so called segments, molecules or (coarse grained) particles with an elementary volume ν, constitute the monomeric units in a system. The parameter χ is the Flory-Huggins interaction parameter that quantifies the interaction between solvent and polymer segments: large values indicate repulsion and small values attraction. ϕ_P and ϕ_S are the segment number fractions. If one solvent molecule corresponds to one segment, a homogeneous system of arbitrary volume $dV \gg \nu$ – for example an infinitesimally small subsystem at a particular position $\vec{r}$ within V – contains $n_S = \rho_S dV$ solvent segments and it is $\nu_S = \nu$ with ν_S being the molecular volume of the solvent. Each polymer molecule of molecular volume ν_P is then a chain of $N = {}^{\nu_P}/_{\nu}$ segments, and the total number of segments in dV is $n = n_S + N n_P$, where $n_P = \rho_P dV$ is the number of polymer chains. Conclusively, the number fractions of solvent and polymer segments are defined by $\phi_S = {}^{n_S}/_{n}$ and $\phi_P = {}^{N n_P}/_{n}$. Introducing the total volumes $V_S = \nu n_S$ and $V_P = \nu_P n_P$ of the components with $V_S + V_P = dV$ yields

$$\phi_S = \frac{\nu n_S}{\nu n_S + \nu_P n_P} = \frac{V_S}{dV} = \nu \rho_S \text{ and } \phi_P = \frac{\nu_P n_P}{\nu n_S + \nu_P n_P} = \frac{V_P}{dV} = \nu_P \rho_P = N \nu \rho_P, \tag{5.3}$$

which shows that the segment number fractions equal the volume fractions of the molecules. Equations 5.3 also include a relation between ϕ_i and ρ_i to express the homogeneous free energy density from equation 5.2 in terms of concentrations only as

$$\hat{f}(\rho_P, \rho_S) = k_B T \left[\rho_S \ln(\nu \rho_S) + \rho_P \ln(\nu N \rho_P) + \chi \rho_S \nu N \rho_P\right]. \tag{5.4}$$

In case no external fields are present, relaxation dynamics are governed by a set of generalized diffusion equations. If a local kinetic coupling model is applied, these equations read

$$\frac{\partial \rho_i}{\partial t}(\vec{r}, t) = \nabla \cdot \left(\frac{D_i}{k_B T} \left[\rho_i(\vec{r}, t) \nabla \frac{\delta \mathcal{F}[\{\rho_j(\cdot, t)\}_j]}{\delta \rho_i(\vec{r})} + \eta_i(\vec{r}, t) \right] \right) \text{ with } i = P, S. \tag{5.5}$$

D_P and D_S are the diffusion coefficients of the polymer chains and the solvent molecules[1], and η_i is the realization of a stochastic random noise in accordance with equation 2.13 (the prefactor has to be adapted because ${}^{D_i}/_{k_B T} = {}^{\beta D_\alpha}/_{N_\alpha}$ is factored out). Ignoring chain connectivity by application of a local coupling model affects relaxation rates quantitatively, but

[1]Note that ρ_P is the density of polymer *chains*, while ρ_α in equation 2.12 was the density of *monomers*. Therefore, it is $D_P = {}^{D_\alpha}/_{N}$, since $\rho_P = {}^{\rho_\alpha}/_{N}$.

does not change the qualitative nature of dynamics [121] we aim to describe in the current section.

It is convenient to replace concentrations ρ_i by volume fractions ϕ_i when an incompressibility constraint is introduced to account for the typically high compressive moduli of polymer solutions. The constraint reads $\phi_P + \phi_S = 1 \Leftrightarrow \phi_S = 1 - \phi_P$ and eventually reduces two differential equations to only one. Multiplying the equation

$$\frac{\partial \rho_P}{\partial t} = \nabla \cdot \left(\frac{D_P}{k_B T} \left[\rho_P \nabla \frac{\delta \mathcal{F}}{\delta \rho_P} + \eta_i \right] \right) \tag{5.6}$$

by $N\nu$, setting $D_P = {}^{D_0}/_{N}$, and applying equations 5.3 leads to

$$\frac{\partial \phi_P}{\partial t} = \nabla \cdot \left(\frac{D_0}{k_B T} \left[\rho_P \nabla \frac{\delta(\nu \mathcal{F})}{\delta \rho_P} + \nu \eta_P \right] \right)$$

$$= \nabla \cdot \left(\frac{D_0}{k_B T} \left[\rho_P \frac{\nu N}{\nu N} \nabla \frac{\delta(\nu \mathcal{F})}{\delta \rho_P} + \nu \eta_P \right] \right) = \nabla \cdot \left(\frac{D_0}{k_B T} \left[\phi_P \nabla \frac{\delta(\nu \mathcal{F})}{\delta \phi_P} + \nu \eta_P \right] \right). \tag{5.7}$$

The dynamical equation for ϕ_S is obtained analogously by substituting $N \to 1$ and $D_0 \to D_S$. To express $\nu\mathcal{F}$ in terms of ϕ_P and ϕ_S, equation 5.2 is multiplied by ν, which leads to

$$\nu \hat{f}(\rho_P, \rho_S) = k_B T \left[\nu \rho_S \ln(\phi_S) + \nu \rho_P \ln(\phi_P) + \chi \nu \rho_S \phi_P \right], \tag{5.8}$$

and employing the identities from equations 5.3 again leaves

$$\nu \hat{f}(\rho_P, \rho_P) = k_B T \left[\phi_S \ln(\phi_S) + \frac{\phi_P}{N} \ln(\phi_P) + \chi \phi_S \phi_P \right] =: f(\phi_P, \phi_S), \tag{5.9}$$

where $f(\phi_P, \phi_S)$ is the homogeneous free energy per segment. Using equation 5.1 immediately yields

$$\begin{aligned} \nu\mathcal{F}[\rho_P, \rho_S] &= \int_V \nu \hat{f}(\rho_P, \rho_S) + \frac{\nu \Lambda_P}{2} |\nabla \rho_P|^2 + \frac{\nu \Lambda_S}{2} |\nabla \rho_S|^2 \, d\vec{r} \\ &= \int_V f(\phi_P, \phi_S) + \frac{\nu \Lambda_P}{2(N\nu)^2} |\nabla \phi_P|^2 + \frac{\nu \Lambda_S}{2(\nu)^2} |\nabla \phi_S|^2 \, d\vec{r} \\ &=: \int_V f(\phi_P, \phi_S) + \frac{\lambda_P}{2} |\nabla \phi_P|^2 + \frac{\lambda_S}{2} |\nabla \phi_S|^2 \, d\vec{r} = F[\phi_P, \phi_S], \end{aligned} \tag{5.10}$$

and insertion of F into equation 5.7 gives

$$\frac{\partial \phi_i}{\partial t} = -\nabla \cdot J_i \text{ for } i = P, S \text{ with}$$

$$J_P = -\frac{D_0}{k_B T} \left[\phi_P \nabla \frac{\delta F}{\delta \phi_P} + \nu \eta_P \right] \text{ and } J_S = -\frac{D_S}{k_B T} \left[\phi_S \nabla \frac{\delta F}{\delta \phi_S} + \nu \eta_S \right]. \tag{5.11}$$

J_i is the local flux of component i. If λ_P and λ_S are assumed to be independent of $\rho_i(\vec{r})$, which is consistent with equation 2.62 for conserved $\bar{\rho}_i$, the chemical potentials are given by

$$\mu_i \coloneqq \frac{\delta F}{\delta \phi_i} = \frac{\partial f}{\partial \phi_i} - \lambda_i \Delta \phi_i. \tag{5.12}$$

Incompressible dynamics are obtained by modifying fluxes with a constraining force Z to

fulfill the constraint

$$J_P + J_S = 0 \tag{5.13}$$

[122]. The modified fluxes read

$$J_P = -\frac{D_0}{k_B T}\left(\phi_P\left[\nabla\mu_P + Z\right] + \nu\eta_P\right) \text{ and } J_S = -\frac{D_S}{k_B T}\left(\phi_S\left[\nabla\mu_S + Z\right] + \nu\eta_S\right), \tag{5.14}$$

so equation 5.13 implies

$$Z = -\frac{D_0\phi_P\nabla\mu_P + D_S\phi_S\nabla\mu_S}{D_0\phi_P + D_S\phi_S} - \frac{D_0\nu\eta_P + D_S\nu\eta_S}{D_0\phi_P + D_S\phi_S}. \tag{5.15}$$

Insertion of equation 5.15 into the modified flux J_P, employing that flux in the dynamical equation 5.11 for $i = P$, assuming $D_0 = D_S$, and setting $\phi_S = 1 - \phi_P$ results in

$$\frac{\partial\phi_P}{\partial t} = \frac{D_0}{k_B T}\nabla\cdot\left[\phi_p(1-\phi_p)\nabla\left(\mu_P - \mu_S\right) + R\right]$$

$$= \frac{D_0}{k_B T}\nabla\cdot\left[M(\phi_P)\nabla\left(\frac{\partial f}{\partial\phi_P}(\phi_P, 1-\phi_P) - \frac{\partial f}{\partial\phi_S}(\phi_P, 1-\phi_P) - \lambda\Delta\phi_P\right) + R\right] \tag{5.16}$$

with $\lambda \coloneqq \lambda_P + \lambda_S$, $M(\phi_P) \coloneqq \phi_P(1-\phi_P)$ and the random term $R = (1-\phi_P)\nu\eta_P - \phi_P\nu\eta_S$. If $\eta_P = \eta_S \equiv 0$ one obtains the well known Cahn-Hilliard equation [123, 124]. It is the simplest mathematical model that is able to describe the dynamics of isothermal and incompressible phase separation. ϕ_S is determined by the algebraic relation $\phi_S(\vec{r}, t) = 1 - \phi_P(\vec{r}, t)$ for any $\vec{r}$ and t. If the length and time scales are given in units of $l_0 = \sqrt{\lambda/k_B T}$ and $t_0 = l_0^2/D_0$, respectively, and

$$\mu_r \coloneqq \frac{1}{k_B T}\left(\frac{\partial f}{\partial\phi_P}(\phi_P, 1-\phi_P) - \frac{\partial f}{\partial\phi_S}(\phi_P, 1-\phi_P)\right)$$

$$= \frac{\ln(\phi_P)}{N} - \ln(1-\phi_P) + \chi(1-2\phi_P) + \frac{1}{N} - 1 \tag{5.17}$$

is defined, the Cahn-Hilliard equation can be cast into the dimensionless form

$$\frac{\partial\phi_P}{\partial t} = \nabla\cdot\left[M(\phi_P)\nabla\left(\mu_r - \Delta\phi_P\right)\right]. \tag{5.18}$$

The gradient energy parameter for polymer-solvent systems takes values with magnitude $k_B T R_g^2$, where R_g is the radius of gyration of the polymer (cp. reference [125] or equation 2.62). Approximating λ by $k_B T R_g^2$ leads to $l_0 = R_g$ and $t_0 = R_g^2/D_0$.

A spontaneous decomposition into polymer- and solvent-rich phases during relaxation occurs, if χ is larger than the spinodal interaction $\chi^{(Spin)}$ defined by the condition

$$\frac{\partial\mu_r}{\partial\phi_P}\left(\phi_P = f_P, \chi = \chi^{(Spin)}\right) = 0 \Leftrightarrow \chi^{(Spin)} = \frac{1}{2}\left(\frac{1}{N f_P} + \frac{1}{1-f_P}\right), \tag{5.19}$$

where f_P is the conserved mean polymer volume fraction

$$f_P = \frac{1}{V}\int_V \phi_P(\vec{r}, t)\, d\vec{r}. \tag{5.20}$$

As already mentioned, solvent mixing is modeled by time dependent χ-parameters, i.e. by substituting $\chi \mapsto \chi(t)$, which corresponds to replacing one solvent by another one at each time. In the present chapter a linear interpolation of χ in the selective solvent volume fraction

$$\chi(t) = \chi_{GS} + \frac{\chi_{SS} - \chi_{GS}}{1 - f_P}\varphi_{SS}(t) \tag{5.21}$$

is used. χ_{GS} and χ_{SS} denote the interaction parameters between the polymer and the good or selective solvent, respectively. φ_{SS} represents the mean volume fraction of the selective solvent in the system. $\varphi_{SS} = 0$ corresponds to good solvent, meaning $\chi = \chi_{GS}$. If the complete solvent consists of selective solvent, that is if $\varphi_{SS} = 1 - f_P$, it is $\chi = \chi_{SS}$. In the following the functions φ_{SS} are called *mixing profiles*.

Equation 5.18 with the relative chemical potential from equation 5.17 and an interaction parameter given by equation 5.21 constitutes model I. The dynamical equation is solved for periodic boundary conditions.

5.2 Numerical integration schemes

If we talk about solving equation 5.18 numerically, we also have to talk about stiffness of differential equations. Stiffness was first discussed by Curtiss and Hirschfelder [126] in connection with numerical studies about substance conversions during simultaneous chemical reactions with very dissimilar reaction rates. They described it as the necessity to choose extremely small step sizes in order to ensure stability of their explicit numerical integration schemes although the actual solution appeared to exhibit only slow temporal variations. Stiffness is obviously a bad trait since iterating through slow dynamics with extremely small time steps leads to infeasible computation times. It quickly turned out that there is a variety of physical equations showing such a behavior and these equations are called stiff. One example for stiff equations is the diffusion or heat equation [127]. As far as the present work is concerned, stiffness is important because equation 5.18 is a generalized diffusion equation and thus, also stiff. We should note though that it is even 'stiffer' than the ordinary heat equation because it contains a squared Laplacian. There is still no mathematically rigorous definition of stiffness, but it commonly – not always [128] – refers to large stiffness ratios

$$S = \frac{\max|\lambda_i|}{\min|\lambda_i|}, \tag{5.22}$$

where λ_i are the eigenvalues of the Jacobian obtained by linearization of the equations under consideration [128, 129]. Large S typically indicate that the solution contains both rapidly and slowly varying contributions and in the example above, such contributions are reflected in the dissimilar reaction rates. Stiffness can be approached by application of A-stable integration schemes. As defined by Dahlquist [130], "*a k-step method is called A-stable, if [numerical approximations $x^{(n)}$ to $x(t_n = nh)$] tend to zero, as $n \to \infty$, when the method is applied with fixed positive [step size] h to any differential equation of the form, $dx/dt = qx$,[the Dahlquist test equation,] where q is a complex constant with negative real part*". It can be shown that stability properties of A-stable methods transfer from the Dahlquist test equation to any ordinary differential equation. The authors of reference [126] already observed that there are implicit methods that do not suffer from the severe step size restrictions imposed on explicit

methods, and eventually Dahlquist [130] showed that A-stable methods have to be implicit. There are also other test functions and approaches to stiffness, for example the ones by Gear [131], but with respect to the present discussion the concept of A-stability is sufficient.

In the following the specific equation

$$\frac{\partial \phi}{\partial t}(\vec{r},t) = \Delta^{\alpha/2}\phi(\vec{r},t) \text{ with } \alpha \in 2 \cdot \mathbb{N} \tag{5.23}$$

is used to exemplarily clarify why the application of explicit integrators to stiff equations is problematic and why A-stable or implicit methods are desirable. Its Fourier representation is a system of Dahlquist test equations

$$\frac{\partial \hat{\phi}}{\partial t}(\vec{k},t) = -k^{\alpha}\hat{\phi}(\vec{k},t) \tag{5.24}$$

with $k = |\vec{k}|$ and known exact solutions $\hat{\phi}(\vec{k},t) \propto e^{-k^{\alpha}t}$, called modes. If equation 5.24 was discretized in the $\vec{k}$-space, the discrete values of $-k^{\alpha}$ would correspond to the eigenvalues λ_i in equation 5.22. As the maximum occurring value of k^{α} is likely to increase dramatically with the spatial resolution of a simulation, high resolution simulations of diffusion problems often have a large stiffness ratio S and are thus prime examples for stiff equations. In the heat equation it is $\alpha = 2$ and in equation 5.18 there is even a term with $\alpha = 4$. Application of the explicit Euler method $\hat{\phi}^{(n+1)} = \hat{\phi}^{(n)} + h\, f(\hat{\phi}^{(n)})$ with $f(\hat{\phi}) = -k^{\alpha}\hat{\phi}$ yields

$$\hat{\phi}^{(n+1)} = (1 - k^{\alpha}h)\,\hat{\phi}^{(n)}, \tag{5.25}$$

where we omit $\vec{k}$-arguments for the sake of a convenient notation and denote the numerical approximation to $\hat{\phi}(t_n)$ by $\hat{\phi}^{(n)}$. Now, one can either calculate the error amplification

$$\frac{\epsilon^{(n+1)}}{\epsilon^{(n)}} = (1 - k^{\alpha}h) \tag{5.26}$$

by employing error-perturbed solutions $\hat{\phi}^{(j)} = \hat{\phi}^{(j)}_{exact} + \epsilon^{(j)}$ for $j = n, n+1$ in equation 5.25 or insert $\hat{\phi}^{(n)}$, $\hat{\phi}^{(n-1)}$, ..., $\hat{\phi}^{(0)}$ recursively to arrive at

$$\hat{\phi}^{(n+1)} = (1 - k^{\alpha}h)^{n+1}\hat{\phi}^{(0)}. \tag{5.27}$$

Because there exists a step size h such that $|1 - k^{\alpha}h| > 1$, the explicit Euler method is not A-stable. Equivalently, such a value of h would lead to an error growth $\left|\epsilon^{(n+1)}/\epsilon^{(n)}\right| > 1$. The stability criterion for the explicit Euler method reads

$$|1 - k^{\alpha}h| < 1 \Leftrightarrow 0 < h < \frac{2}{k^{\alpha}}, \tag{5.28}$$

which is a severe restriction, especially for high resolutions (i.e. large values of k), large α, or in other words: large stiffness ratios. Stiffness is attributed to the fact that the numerical integration scheme is only stable if each single mode is stably integrated. Thus, the largest value of k dictates the upper bound of the step size h. However, since $\hat{\phi} \propto e^{-k^{\alpha}t}$, the corresponding mode decays very quickly and does not contribute significantly to the solution after a very short time period. That means the actual dynamics is mainly dominated by

modes decaying on much larger time scales. Therefore, the essential problem with the explicit method is the necessity to apply extremely small step sizes to stabilize rapidly varying modes while the time scale of the dynamics is largely determined by the slowly varying ones. The probably most prominent example of an A-stable integrator is the implicit Euler method $\hat{\phi}^{(n+1)} = \hat{\phi}^{(n)} + h\, f(\hat{\phi}^{(n+1)})$. Employing $f(\hat{\phi}) = -k^\alpha \hat{\phi}$ leads to

$$\hat{\phi}^{(n+1)} = \frac{\hat{\phi}^{(n)}}{1 + k^\alpha h} = \frac{\hat{\phi}^{(0)}}{(1 + k^\alpha h)^{n+1}} \text{ with } \frac{\epsilon^{(n+1)}}{\epsilon^{(n)}} = \frac{1}{1 + k^\alpha h}. \tag{5.29}$$

The error amplification is smaller than 1 for any positive h, which cancels out the severe step size restriction of the explicit scheme and allows to take step sizes fitting the time scale that is generated by the superposition of all modes. Loosely speaking, implicit methods do not suffer from the severe step size restrictions of explicit schemes since they tend to have 'increased denominators' in error amplifications $\left|\epsilon^{(n+1)}/\epsilon^{(n)}\right|$. Since A-stable integration schemes are stable for any h, they constitute the numerically most robust approach to stiffness.

Unfortunately, not all equations allow an easy treatment like equation 5.24. Implicit integrators often involve iterative methods to (numerically) invert equations in every time step, which may consume a significant amount of computation time. It might even be difficult to cast a system of equations into an appropriate form to use these iterative solvers.[2] This motivates the introduction of semi-implicit methods, which are also called implicit-explicit methods or in short, IMEX schemes. These integration schemes aim to extend stability regions at a possibly low additional computational cost with respect to explicit methods. A common strategy is approximating only the 'stiffest' terms by an implicit method to increase denominators in error amplifications similar to the example above, while an explicit scheme is applied to the remaining terms. If partial differential equations are spatially discretized, these stiffest terms very often arise from the highest order spatial derivatives. Semi-implicit methods are generally not stable for any h. However, from a practical point of view it is very often sufficient to extend the stability region to computationally feasible step sizes as extremely large h introduce significant truncation errors anyway. In that context, one also refers to stiffness when step sizes are not determined by accuracy but by stability. A general discussion about semi-implicit methods is difficult because they are usually tailored to specific sets of equations. Applications can be found for example in references [81], [132], and [133] or chapter 7. The work from Zhu et al. [132] is now of particular interest because it describes a scheme for equation 5.18, which is a first order time accurate pseudo spectral method.

The leading stiffness term in equation 5.18 is $-M(\phi_P)\Delta^2\phi_P$. In case the mobility M depends on ϕ_P this contribution is non-linear in ϕ_P and treating it directly implicitly is not ideal from a computational point of view as it results in a non-linear implicit equation for $\phi_P^{(n+1)}$, which had to be solved with an iterative method at each time step. To improve stability without utilization of iterative methods, one can modify equation 5.18 by zero-padding its right hand side according to

$$\frac{\partial \phi_P}{\partial t} = \nabla \cdot \left[M(\phi_P)\nabla\left(\mu_r - \Delta\phi_P\right)\right] + \alpha\Delta^2\phi_P - \alpha\Delta^2\phi_P \tag{5.30}$$

[132], where $\alpha \in \mathbb{R}$. The semi-implicit integrator is eventually built by treating $-\alpha\Delta^2\phi_P$

[2] We are going to encounter such a problem in part III of this work in the form of a system containing integro-differential equations.

implicitly while explicit approximations are applied to the remaining terms. Choosing an appropriate value for α is key to an optimal increase of the stability region. To specify α, equation 5.30 is rearranged to

$$\frac{\partial \phi_P}{\partial t} = \nabla \cdot [M(\phi_P)\nabla \mu_r] - \nabla \Delta \phi_P \cdot \nabla M(\phi_P) - \alpha \Delta^2 \phi_P - (M(\phi_P) - \alpha)\Delta^2 \phi_P. \tag{5.31}$$

The last term on the right hand side, $(M(\phi_P) - \alpha)\Delta^2\phi_P$, contains the leading non-linear stiffness contribution that is going to be treated explicitly. If α was variable and set to $M(\phi_P)$, this term would vanish and only $-\alpha\Delta^2\phi_P$ was left. Among all choices of α, setting $\alpha = M(\phi_P)$ would lead to the numerically most stable semi-implicit scheme since it would correspond to a completely implicit treatment of the leading stiffness contribution. But one also had to apply iterative methods to eventually invert with respect to $\phi_P^{(n+1)}$. As α is constant, the last term does not vanish. However, stiffness can be suppressed as much as possible if this term is kept possibly close to zero by setting

$$\alpha = \underset{\tilde{\alpha} \in \mathbb{R}}{\operatorname{argmin}} \left[\sup_{\phi_P \in [0,1]} |M(\phi_P) - \tilde{\alpha}| \right] = \frac{1}{8}.$$

A semi-implicit scheme with this choice of α enables to take roughly two orders of magnitude larger step sizes compared to an explicit Euler method without additional computational costs due to numerical inversion [132].

To derive the semi-implicit update rule for ϕ_P, we define $\mu \coloneqq \mu_r - \Delta\phi_P$ and

$$\begin{pmatrix} G_1 \\ G_2 \\ G_3 \end{pmatrix} = \begin{pmatrix} M(\phi_P)\partial\mu/\partial r_1 \\ M(\phi_P)\partial\mu/\partial r_2 \\ M(\phi_P)\partial\mu/\partial r_3 \end{pmatrix}$$

for the sake of brevity. Equation 5.30 then becomes

$$\frac{\partial \phi_P}{\partial t} = \sum_{j=1}^{d} \frac{\partial G_j}{\partial r_j} + \alpha \Delta^2 \phi_P - \alpha \Delta^2 \phi_P, \tag{5.32}$$

where d is the spatial dimension and $\vec{r} = (r_1, ..., r_d)^T$. When pseudo spectral methods are applied to solve equations with periodic boundary conditions on a rectangular domain $[0, L_1)$ $\times ... \times$ $[0, L_d)$, every unknown scalar function f is approximated by a trigonometric interpolation polynomial

$$p^{[f]}(\vec{r}, t) = \sum_{\vec{k} \in \mathcal{K}} \hat{f}(\vec{k}, t) e^{i\vec{k}\cdot\vec{r}} \tag{5.33}$$

with the short hand notations $\vec{k} = (k_1, ..., k_d)^T$ and

$$\mathcal{K} = \left\{ \frac{2\pi}{L_1}\left(-\frac{n_1}{2} + 1\right), ..., \frac{2\pi}{L_1}\frac{n_1}{2} \right\} \times ... \times \left\{ \frac{2\pi}{L_d}\left(-\frac{n_d}{2} + 1\right), ..., \frac{2\pi}{L_d}\frac{n_d}{2} \right\}, \tag{5.34}$$

where $n_1, ..., n_d \in \mathbb{N}$ are even numbers. If the spatial domain is discretized with $m = n_1 \times ... \times n_d$ grid points, the coefficients $\hat{f}(\vec{k}, t) \in \mathbb{C}$ are uniquely determined by the conditions

$$p^{[f]}(\vec{r}_i, t) = f(\vec{r}_i, t) \in \mathbb{R} \quad \forall\, i = 0, ..., m - 1. \tag{5.35}$$

It immediately follows from equation 5.35 that the field $(\hat{f}(\vec{k},t))_{\vec{k}\in\mathcal{K}}$ is the discrete Fourier transform of $(f(\vec{r}_i,t))_{i=0,...,m-1}$. Unknown scalar functions in equation 5.32 are ϕ_P and G_j. Inserting the respective interpolation polynomials with $f \in \{\phi_P, G_j\}$, applying the orthogonality of complex exponential functions, and integrating in time leads to

$$\hat{\phi}_P(\vec{k},t_{n+1}) - \hat{\phi}_P(\vec{k},t_n) = \int_{t_n}^{t_{n+1}} \sum_{j=1}^{d} ik_j \hat{G}_j(\vec{k},t)dt$$

$$+\alpha \int_{t_n}^{t_{n+1}} k^4 \hat{\phi}_P(\vec{k},t)dt - \alpha \int_{t_n}^{t_{n+1}} k^4 \hat{\phi}_P(\vec{k},t)dt. \tag{5.36}$$

As stated before, Zhu et al. [132] approximate the first two terms on the right hand side explicitly and the last one implicitly with first order time accurate Euler methods. This corresponds to the application of Euler forward and backward quadrature rules to the integrals in equation 5.36. Thus,

$$\hat{\phi}_P(\vec{k},t_{n+1}) - \hat{\phi}_P(\vec{k},t_n) = h\sum_{j=1}^{d} ik_j \hat{G}_j(\vec{k},t_n) + \tau_1$$

$$+\alpha h k^4 \hat{\phi}_P(\vec{k},t_n) - \alpha h k^4 \hat{\phi}_P(\vec{k},t_{n+1}) + \alpha(\tau_2 - \tau_3). \tag{5.37}$$

$h = t_{n+1} - t_n$ is the step size and τ_1, τ_2, and $\tau_3 \in \mathcal{O}(h^2)$ are the truncation errors of the first, second, and third integral, respectively. The application of different quadrature rules to the last two integrals in equation 5.36 introduces an additional, α-proportional error $\alpha(\tau_2 - \tau_3)$. Therefore, α should never be greater than 1 even if large α-values yield good stability. The corresponding numerical scheme reads

$$\hat{\phi}_P^{(n+1)}(\vec{k}) - \hat{\phi}_P^{(n)}(\vec{k}) = h\sum_{j=1}^{d} ik_j \hat{G}_j^{(n)}(\vec{k}) + \alpha h k^4 \hat{\phi}_P^{(n)}(\vec{k}) - \alpha h k^4 \hat{\phi}_P^{(n+1)}(\vec{k})$$

$$\Leftrightarrow \hat{\phi}_P^{(n+1)}(\vec{k}) = \hat{\phi}_P^{(n)}(\vec{k}) + \frac{h}{(1+\alpha h k^4)} \sum_{j=1}^{d} ik_j \hat{G}_j^{(n)}(\vec{k}), \tag{5.38}$$

where $\hat{\phi}_P^{(n)}(\vec{k})$ is the numerical approximation to $\hat{\phi}_P(\vec{k},t_n)$ etc. As the discrete Fourier transforms of two identical fields are equal, $\hat{G}_j^{(n)}$ is calculated via

$$\hat{G}_j^{(n)}(\vec{k}) = \mathcal{F}_{\vec{k}}\left[\left(M\left(\phi_P^{(n)}(\vec{r}_s)\right)\frac{\partial \mu^{(n)}}{\partial r_j}(\vec{r}_s)\right)_s\right] = \mathcal{F}_{\vec{k}}\left[\left(M\left(\phi_P^{(n)}(\vec{r}_s)\right)\mathcal{F}_s^{-1}\left[\left(ik_j\hat{\mu}^{(n)}(\vec{k})\right)_{\vec{k}}\right]\right)_s\right],$$

where $\mathcal{F}_{\vec{k}}$ denotes the discrete Fourier transform evaluated at wave number $\vec{k} \in \mathcal{K}$ and $\mathcal{F}_s^{-1}$ the inverse discrete Fourier transform evaluated at position $\vec{r}_s$ with $s = 0, ..., m-1$. Indexed brackets $(...)_{\vec{k}}$ and $(...)_s$ are respective short hand notations for the fields $(...)_{\vec{k}\in\mathcal{K}}$ in the wave number space and $(...)_{i=0,...,m-1}$ in the coordinate space. All discrete Fourier transforms are calculated by the FFTW library [134].

In a similar manner we construct a second order time accurate scheme to check the influence of temporal truncation errors on simulation results later on. To this end, the first two integrals in equation 5.36 are approximated by a two-step Adams-Bashforth scheme with the general

form

$$\int_{t_n}^{t_{n+1}} f(\phi_P(t),t)\,dt = \frac{h}{2}\left(3f(\phi_P^{(n)},t_n) - f(\phi_P^{(n-1)},t_{n-1})\right) + \mathcal{O}(h^3) \tag{5.39}$$

and the last one by an Adams-Moulton method or trapezoidal rule

$$\int_{t_n}^{t_{n+1}} f(\phi_P(t),t)\,dt = \frac{h}{2}\left(f(\phi_P^{(n+1)},t_{n+1}) + f(\phi_P^{(n)},t_n)\right) + \mathcal{O}(h^3) \tag{5.40}$$

[135]. Inserting and rearranging eventually yields

$$\hat{\phi}_P^{(n+1)}(\vec{k}) = \frac{1}{1+\alpha\frac{h}{2}k^4}$$

$$\times\left[(1+\alpha h k^4)\hat{\phi}_P^{(n)}(\vec{k}) + \frac{h}{2}\left(\sum_{j=1}^{d} ik_j\left\{3\hat{G}_j^{(n)}(\vec{k}) - \hat{G}_j^{(n-1)}(\vec{k})\right\} - \alpha k^4\hat{\phi}_P^{(n-1)}(\vec{k})\right)\right]. \tag{5.41}$$

Equations 5.38 (first order time accurate) and 5.41 (second order time accurate) constitute the numerical update rules for Fourier coefficients, and the spatial volume fraction profiles are obtained by application of an inverse discrete Fourier transformation, i.e.

$$\phi_P^{(n+1)}(\vec{r_s}) = \mathcal{F}_s^{-1}\left[\left(\hat{\phi}_P^{(n+1)}(\vec{k})\right)_{\vec{k}\in\mathcal{K}}\right] \quad \forall\, s = 0,...,m-1. \tag{5.42}$$

If not stated otherwise, simulations in the present chapter are performed with the first order time accurate scheme due to its better stability properties.

The Cahn-Hilliard equation is a well-known standard problem in mathematics and there are also unconditionally stable algorithms, e.g. the one proposed by Vollmayr-Lee and Rutenberg [136]. The unconditional stability is especially useful when late-stage coarsening is studied, because it provides the possibility to accelerate simulations by increasing step sizes h when dynamics become slow without considering stability constraints. In the present case, however, unconditionally stable schemes are dispensable because we restrict to the early stages of phase separation, where dynamics are fast and the semi-implicit scheme should be rather limited by accuracy than stability. In addition, the semi-implicit scheme is as computationally efficient as possible since it possesses the same complexity as an explicit scheme.

5.3 Rate-size relations for linear mixing profiles

If linearly time dependent mixing profiles

$$\varphi_{SS}(t) = \begin{cases} \varphi_0 + s\,t & \text{for } t \le t_{max} \\ \varphi_{max} & \text{for } t > t_{max} \end{cases} \tag{5.43}$$

with $t_{max} \coloneqq {}^{(\varphi_{max}-\varphi_0)}/_{s}$ and constants s, φ_0, φ_{max} are employed, equation 5.21 becomes

$$\chi(t) = \left\{\begin{matrix} \left(\chi_{GS} + \dfrac{\chi_{SS}-\chi_{GS}}{1-f_P}\varphi_0\right) + \dfrac{\chi_{SS}-\chi_{GS}}{1-f_P}s\,t \\ \chi_{GS} + \dfrac{\chi_{SS}-\chi_{GS}}{1-f_P}\varphi_{max} \end{matrix}\right\} =: \begin{cases} \chi_0 + s_\chi t & \text{for } t \le t_{max} \\ \chi^{(max)} & \text{for } t > t_{max} \end{cases}, \tag{5.44}$$

which reduces the set of associated parameters to describe solvent mixing from s, χ_{GS}, χ_{SS}, φ_0, and φ_{max} to only s_χ, χ_0, and $\chi^{(max)}$. Therefore, linear mixing profiles are particularly appealing to perform primary investigations with model I in small parameter spaces.

If initial solutions of $\mathrm{PB}_x - \mathrm{PEO}_y$, tetrahydrofuran (good solvent), and premixed water (selective solvent) from the experiments in figure 1.3 are not fed into a micromixer but if water is added in titration experiments instead, it can be observed that a solution tarnishes almost instantaneously as soon as its water content is increased. Such a rapid phase separation is characteristic for spinodal decomposition. Thus, the state of the initial solution should already be close to the unstable area in the corresponding phase diagram and the spinodal line should be crossed during solvent mixing inside a mixer, which suggests setting $\chi^{(max)} > \chi^{(Spin)}$. Additionally, typical mixing times are milliseconds. Therefore, we assume that the system crosses the spinodal line before a significant particle growth in the metastable regime though a comparatively slow nucleation and growth process with energy barriers takes place. As a consequence, investigations are restricted to the spinodal area, i.e. we set $\chi_0 = \chi^{(Spin)}$ with the spinodal interaction $\chi^{(Spin)}$ defined by equation 5.19. This means that solvent mixing is described by time dependent quenches with a constant rate s_χ and a maximum depth $\chi^{(max)}$.

Relations between typical structure sizes in simulated density profiles and the quench rate s_χ are going to be called *rate-size relations*

5.3.1 Simulation setup

All simulation results that will be presented in the current section are averages over 5 independent simulation runs with different uniformly distributed random initial conditions

$$\phi_P^{(0)}(\vec{r}_s) \in [f_P - 0.001, f_P + 0.001] \quad \forall\, s = 0, ..., m-1.$$

The initial conditions are created by the random number generator from Matsumoto and Nishimura [137]. Thermal fluctuations are disabled, i.e. $\eta_i \equiv 0$, because phase separation in the spinodal area is a thermodynamically driven process without energy barriers.

The *physical* parameters contained by the model equations 5.17, 5.18, and 5.44 with $\chi_0 = \chi^{(Spin)}$ from equation 5.19 are

- the mean polymer volume fraction f_P,
- the number of segments per polymer chain N,
- the quench rate s_χ, and
- the maximum quench depth $\chi^{(max)}$.

Additional *numerical* parameters are

- the number of grid points of the spatial lattice m,
- their distance, i.e. the lattice constant, Δl, and
- the temporal step size h.

Simulations in the current section are performed on a spatial lattice of $m = 400 \times 400$ grid points in 2D and $m = 64 \times 64 \times 64$ in 3D. The lattice constant Δl has to ensure that the size of the smallest structures observed in simulations is not limited by the size of lattice cells. For constant interaction one could eliminate corresponding limitations on Δl by rescaling the spatial coordinate with the quench depth $\Delta\chi$ as originally done by Kotnis and Muthukumar[138], but this creates numerical artifacts which cause a seemingly entropically driven freezing or pinning of structures close to the spinodal line. Although these artifacts can be removed by a more sophisticated scaling [139], we decided not to use it, because $\Delta\chi$ increases with time and rescaling Δl in every time step would violate the constraint of constant volume in a canonical ensemble when the number of grid points is fixed as it is customary in simulations. Otherwise, the implementation would require unnecessarily complicated adaptive memory allocations. The concomitant temporal decrease of the lattice constant would also affect stiffness and most probably provoke numerical instabilities. Besides provoking instabilities, rescaling with the constant maximum quench depth $\Delta\chi^{(max)} = \chi^{(max)} - \chi_0$ is disadvantageous as well because it would lead to quite small Δl, which had to be compensated by undesirably high m to achieve sufficient spatial extensions of simulation boxes at low s_χ when systems remain close to the spinodal line for a long time and structures become large. In 3D we use $\Delta l = 1$ and in 2D we afford higher resolutions with $\Delta l = 0.25$. It should be noted though that a pinning effect in polymer solutions was indeed observed in experiments [140]. However, this effect is not entropically driven but coupled to the viscoelasticity of polymers. There are models for phase separation that account for this physical pinning effect [141], but model I does not because pinning was not observed in the experiments we aim to describe. In every simulation an initial time step of $h = 0.005$ is used. h is automatically reduced by our corresponding C program if an argument of a logarithm in the chemical potential impends to be negative due to numerical truncation errors.

Subsection 5.3.2 considers a model problem with fixed physical parameters

$$f_P = 0.1,\ N = 14, \text{ and } \chi^{(max)} = 2 \tag{5.45}$$

while s_χ is varied to generate an exemplary rate-size relation. How that relation responds to parameter variations is subsequently discussed in subsection 5.3.3. The discussion of the exemplary model problem can be considered as general because subsection 5.3.4 eventually provides strong evidence that the characteristics of rate-size relations are independent of the particular parameter choice.

5.3.2 Evaluation method and simulation results

a) Qualitative discussion of composition profiles and evaluation method

In all simulation runs with physical parameters from equation 5.45 and different s_χ, phase separation takes place in a similar manner as in the case of an instantaneous quench. In the first stage, the spinodal decomposition, initially perturbed homogeneous concentration distributions evolve into bicontinuous patterns, which coarsen quickly while amplitudes of composition fluctuations remain relatively low. This early stage coarsening is illustrated by figure 5.2 (a) and (c) or (b) and (d). The patterns eventually concentrate rapidly until two different phases with a well defined sharp interface emerge. Their appearance labels the end

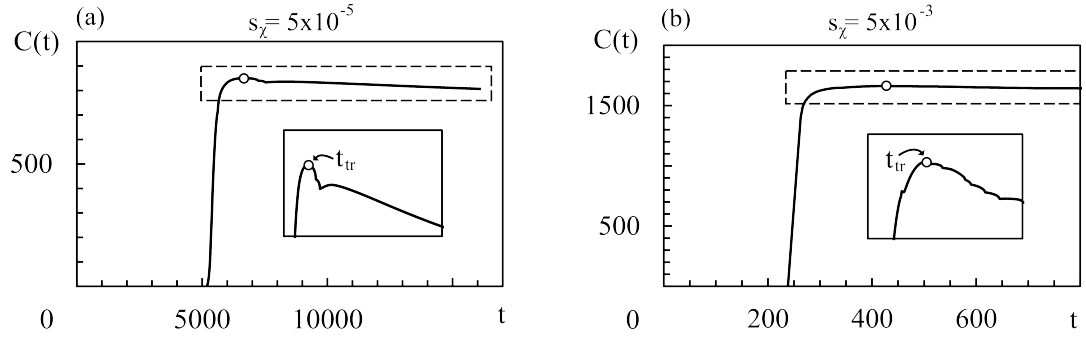

Figure 5.1: *Temporal evolution of the Minkowski functional C for $s_\chi = 5\times10^{-5}$ (a) and $s_\chi = 5\times10^{-3}$ (b) with a threshold value $\phi_P^{(th)} = 0.3$. The inset shows a magnification of the part inside the dashed rectangle. There is a distinct global maximum at the open circle, which labels the transition time t_{tr}. It is placed at $t_{tr} = 6678$ for $s_\chi = 5 \times 10^{-5}$ and $t_{tr} = 425$ for $s_\chi = 5 \times 10^{-3}$.*

of spinodal decomposition and they are shown in 5.2 (e) or (f). In the second stage of phase separation follows a very slow coarsening of the hitherto formed sharp composition profile, where large structures of high polymer concentration grow at the expense of smaller ones. Due to its phenomenological nature this second stage is called Ostwald Ripening. In the Cahn-Hilliard theory structure growth during Ostwald Ripening obeys the Lifshitz-Slyozov law [132, 142, 143].

The crossover time between spinodal decomposition and Ostwald Ripening can be determined with a procedure proposed by Sofonea and Mecke [144], which is based on Minkowski functionals [145]. Minkowski functionals are a complete set of translation invariant measures for convex rings. Each functional assigns one real number to any composition profile depending on its morphology, and since the morphology of composition patterns changes with time, the associated Minkowski functionals also do. One of these measures, from here on denoted by C, is the total boundary contour length (in 2D) or surface area (in 3D) of the union over all subsets in the spatial domain where the polymer volume fraction ϕ_P exceeds a predefined threshold $\phi_P^{(th)}$. The rapid concentration of structures at the end of spinodal decomposition leads to a very steep temporal increase of C and the slow Ostwald Ripening to a flat decrease. This creates two characteristic regimes in the time series of C, which is shown in figure 5.1. We calculated Minkowski functionals with the algorithm proposed by Mantz et al. [146]. Each curve has a clear global maximum that separates fast and slow dynamics. The associated time is called transition time t_{tr} and it represents the time when spinodal decomposition is considered to be finished. It can already be seen from figure 5.1 that spinodal decomposition is much faster for the larger value of s_χ.

How time dependent quench rates affect composition profiles is shown in figure 5.2. The upper panel (parts (a), (c), (e)) and the lower panel (parts (b), (d), (f)) show temporal evolutions of the same initial polymer volume fraction profile for $s_\chi = 5 \times 10^{-5}$ and $s_\chi = 5 \times 10^{-3}$, respectively. At t=10 the composition profiles look very similar ((a) and (b)). At t=200, however, they deviate significantly from each other ((c) and (d)) and at the end of spinodal decomposition smaller polymer aggregates have formed for the larger quench rate ((e) and (f)). The pictorial explanation of the mechanism that causes the deviation of aggregate sizes at transition time is a competition between repulsive interactions and

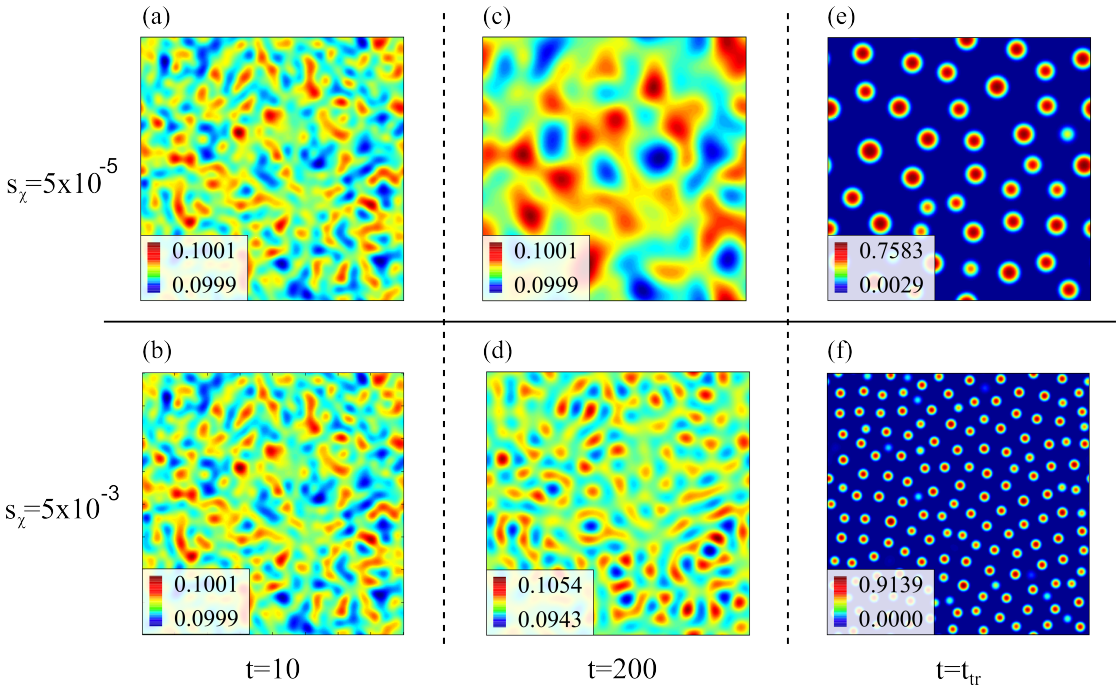

Figure 5.2: *Color coded snapshots of polymer volume fractions ϕ_P (composition profiles), simulated with model I in 2D for two different quench rates $s_\chi = 5\times10^{-5}$ (upper panel) and $s_\chi = 5\times10^{-3}$ (lower panel). t_{tr} is the transition time from figure 5.1 and indicates the end of spinodal decomposition.*

interfacial tension. Speaking in terms of equation 5.18, early stage coarsening proceeds as long as interfacial tension, represented by $\Delta\phi_P$, dominates the repulsion of the components covered by μ_r. Meanwhile, volume fraction profiles are smoothened similar to solutions of a conventional diffusion equation and $|\Delta\phi_P|$ tends to decrease. At the very beginning $\chi(t) - \chi^{(Spin)}$ is negligibly small for both quench rates and the initial dynamics is determined by the $\Delta\phi_P$-term, leading to the formation of almost exactly the same composition pattern at $t = 10$. During the temporal evolution from $t = 10$ to $t = 200$ at $s_\chi = 5\times10^{-5}$ ((a) to (c)) the smoothing continues. Once the interaction term in μ_r constitutes the leading contribution to the polymer flux, dynamics are dictated by repulsion and the bicontinuous pattern rapidly concentrates, while typical structure sizes tend to stagnate. This happens between $t = 10$ and $t = 200$ at $s_\chi = 5\times10^{-3}$ in (b) and (d). Since the pattern from (d) further appears to imprint onto (f), the aggregate size at the end of spinodal decomposition seems to be determined by the typical structure size that is present once repulsive interactions start to outweigh interfacial tension while fluctuation amplitudes are still weak. The larger s_χ, the sooner the termination of early stage coarsening by repulsive interactions happens. As structures at earlier times are less coarse, increasing s_χ leads to smaller characteristic aggregate sizes at transition time. In subsection 5.3.4 this explanation is verified in a quantitative manner.

All parameter sets applied in the present work possess a relatively low mean polymer content f_P to ensure the development of a 'droplet pattern' like in figure 5.2 (e) and (f). We do not encounter any bicontinuous network – both in 2D and in 3D. For the sake of convenience we are going to call the structures of high polymer content at transition time *droplets*. This terminology is introduced to distinguish the polymer aggregates at transition

time obtained by model I from polymer *particles*. Throughout this work the term 'particle' refers to stabilized polymer aggregates in thermodynamic equilibrium or a metastable state. Droplets are neither equilibrium nor metastable structures as Cahn-Hilliard dynamics always develop towards macroscopic phase separation (only one single polymer aggregate is left in equilibrium) because the free energy does not include any stabilization mechanisms. In that sense, droplets represent the first structures with a well defined interface obtained by the simplest model for the dynamics of phase separation. As figure 5.2 indicates that their size is likely to decrease with increasing quench rates, i.e. mixing speeds, they constitute interesting objects because they possess a fundamental commonality with particles from the experiments. Therefore, the remainder of the current section deals with rate-size relations between the quench rate s_χ and the associated characteristic droplet size.

Denoting the total number of droplets at transition time n_D, the volume equivalent radius of droplet i with $i = 1, 2, 3, ..., n_D$ is given by

$$R_i = \begin{cases} \sqrt{\dfrac{A_i}{\pi}} & \text{in 2D} \\ \sqrt[3]{\dfrac{3V_i}{4\pi}} & \text{in 3D} \end{cases}, \tag{5.46}$$

where A_i or V_i denotes its occupied area or volume. One measure for the characteristic droplet size is simply the mean value

$$R = \frac{1}{n_D} \sum_{i=1}^{n_D} R_i, \tag{5.47}$$

and the standard deviation

$$\Delta R = \sqrt{\frac{1}{n_D} \sum_{i=1}^{n_D} (R_i - R)^2} \tag{5.48}$$

serves as a measure of polydispersity. To determine both n_D and A_i or V_i, composition fields at transition time are first converted into binary images. Each pixel or voxel where $\phi_P > \phi_P^{(th)}$ is assigned a value of 1 and all others are set to 0. Then a standard 4- or 6-connected component recursive algorithm is applied to label the (binary) droplets [147]. The algorithm assigns value i to pixels or voxels belonging to droplet i, which allows identification and isolation of particular droplets and also provides the value of n_D. A_i or V_i are subsequently calculated for every isolated droplet with the Minkowski functional algorithm from Mantz et al. [146]. As far as the Minkowski functionals are concerned, we only use C and the total area (in 2D) or the total volume (in 3D) as described above. In two spatial dimensions, the remaining Minkowski functional besides C and the area is the Euler characteristic, which is a measure of connectivity and yields an equivalent estimate for the transition time as C[144]. In three dimensions the Euler characteristic and the mean breadth, which is related to mean curvature, constitute the remaining two Minkowski functionals besides C and the volume [148]. In the present case, one could determine n_D from the Euler characteristic but for the vesicles that appear in part III this procedure would fail. Since we always get a droplet pattern we are not interested in connectivity either, and thus the Euler characteristic does not play any role in the present work. The mean breadth in 3D is redundant, too, as we

already have another procedure to calculate R_i.

Characteristic structure sizes are also quantified by the maximum and the first moment of the normalized radially averaged structure factor S. If the spatial domain is discretized with m grid points, it is defined by

$$S(k,t) = \frac{S_c(k,t)}{m\left(\langle\phi_P^2\rangle - \langle\phi_P\rangle^2\right)}. \tag{5.49}$$

$S_c(k,t)$ is obtained by averaging the absolute value of the Fourier transform of composition correlations,

$$\mathbb{S}(\vec{k},t) = \left|\sum_{\vec{r},\vec{r}'} e^{-i\vec{k}\cdot\vec{r}'}\left[\phi_P(\vec{r}+\vec{r}',t)\phi_P(\vec{r},t) - \langle\phi_P\rangle^2\right]\right|, \tag{5.50}$$

over the disc $\left\{\vec{k}\in\mathcal{K} : |\vec{k}| \in [k, k+{}^{2\pi}/_{L}]\right\}$, where the discretized Fourier space $\mathcal{K}$ is defined by equation 5.34. Simulations were only performed in quadratic or cubic simulation boxes with side lengths $L_1 = ... = L_d = L$. The summation is carried out over all grid points $\vec{r}$ and distances $\vec{r}'$ in the coordinate space, and $\langle x\rangle$ denotes the mean value of the quantity x over the grid. The first moment of S is

$$k_1(t) = \frac{\sum_k k\, S(k,t)}{\sum_k S(k,t)} \tag{5.51}$$

and we estimate mean droplet radii by

$$l_1 = \gamma\frac{2\pi}{k_1(t_{tr})} \text{ and } l_{max} = \gamma\frac{2\pi}{\underset{k}{\operatorname{argmax}}\left(S(k,t_{tr})\right)} \tag{5.52}$$

with $\gamma = {}^1/_4$, meaning characteristic droplet radii are considered to be quartered wave lengths.

b) Simulated rate-size relations

Figure 5.3 shows simulation results for R, l_1, l_{max} and the transition time t_{tr} in dependence on the quench rate s_χ. All rate-size relations share a common characteristic attribution independent of the spatial dimension, and every single diagram can be divided into two regimes: an asymptotic regime, where the data points approach simulation results for an instantaneous quench to $\chi^{(max)}$ (dashed horizontal lines), and a non-asymptotic regime where the dependence on s_χ follows a scaling law, which appears as a straight line in double logarithmic representation. Here, the asymptotic regime is defined to be the range of s_χ for which the cutoff of $\chi(t)$ in equation 5.44 affects simulation results. This is clearly the case if $t_{tr} > t_{max}$, meaning the asymptotic regime begins at the value of s_χ where the dash-dotted line and the data points in figure 5.3 (d) and (h) intersect. That data points eventually converge to the results for constant $\chi(t) = \chi^{(max)}$ does not come as a surprise since it immediately follows from equation 5.44 and the definition of t_{max} that

$$\lim_{s\to\infty}\chi(t) = \chi^{(max)}. \tag{5.53}$$

The exponents of the regression lines to R, l_1, and l_{max} in the non-asymptotic regime scatter around an average -0.161 with a standard deviation 0.006.

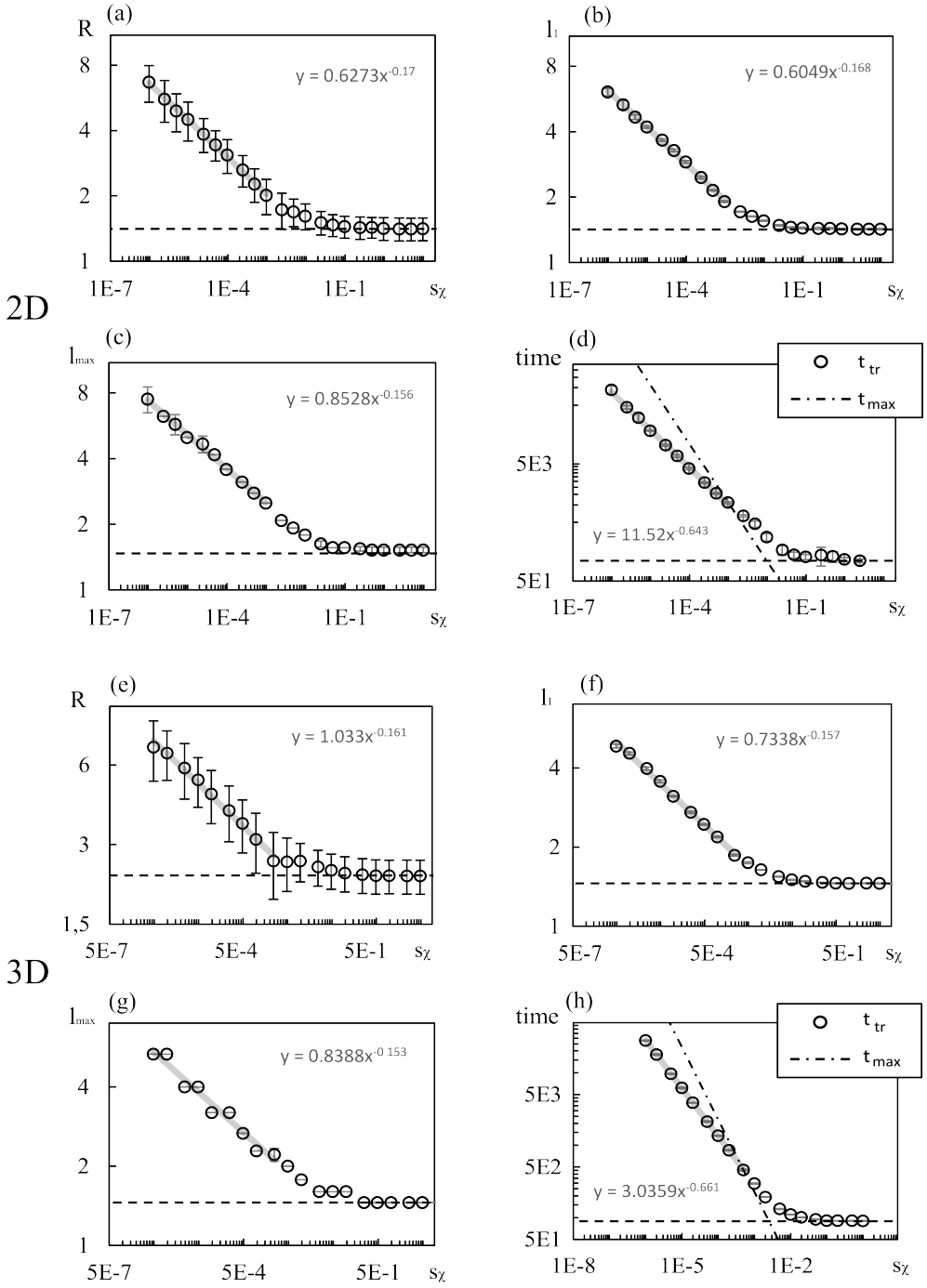

Figure 5.3: *Rate-size relations from model I for linear mixing profiles in double logarithmic representation. The data points represent simulated droplet sizes (R, l_1, l_{max}) and transition times (t_{tr}) in 2D (a to d) and 3D (e to h). The dashed horizontal lines indicate simulation results for an instantaneous quench with $\chi(t) \equiv \chi^{(max)}$ and the grey lines are regression lines to the non-asymptotic regime that correspond to the trend line equations $y = \beta\, x^{\alpha}$. Except for (a) and (e), error bars represent the statistical standard deviation of all 5 simulation runs with different initial conditions. Error bars in (a) and (e) indicate the polydispersity ΔR from equation 5.48; the statistical variance of R resembles the variance of the other quantities. The physical input parameters of the simulations are summarized in equation 5.45.*

Before the origin of that scaling behavior is analyzed in a quantitative manner, figure 5.3 is compared to the Molecular Dynamics simulations from Nikoubashman et al. [35]. The comparison eventually suggests an interpretation how droplets relate to stable homopolymer particles.

5.3.3 Related Molecular Dynamics simulations and parameter variations

In reference [35] controlled assembly of the homopolymer polystyrene in a mixture of tetrahydrofuran and water is studied both with experiments and with Molecular Dynamics simulations. Like in the present work, they consider the impact of experimentally adjustable parameters like mixing times on nanoparticle size, which provides the possibility to compare the early stage spinodal decomposition model to a much more complex particle model that accurately covers every stage of particle growth.

In the Molecular Dynamics simulations solvent mixing is described by linearly time dependent repulsive forces between monomers and solvent molecules of diameter σ. More specifically, monomer-solvent interactions are expressed by the potential

$$U_{MS}(r_{ij}) = \gamma U_{WCA}(r_{ij}) + (1-\gamma)U_{MM}(r_{ij}), \tag{5.54}$$

where γ increases linearly in time. U_{MM} is a standard attractive Lennard Jones potential

$$U_{MM} = 4k_BT\left[\left(\frac{\sigma}{r_{ij}}\right)^{12} - \left(\frac{\sigma}{r_{ij}}\right)^{6}\right] \tag{5.55}$$

that also acts between nonbonded monomers and U_{WCA} the purely repulsive Weeks-Chandler-Andersen potential [149], which is a truncation of $k_BT + U_{MM}$ at $r_{ij} = 2^{1/6}\sigma$. r_{ij} denotes the distance between two monomeric units labeled by i and j. The solvent is treated explicitly as a liquid of Lennard Jones particles and covalent bonds between monomers are modeled by a finitely extensible nonlinear elastic potential [150, 151]. The temperature is maintained by a Nosé-Hoover thermostat. A main result of the experimental part in reference [35] is the unexpected stabilization of nanocolloidal aggregates despite the lack of a hydrophilic block or charged end groups attached to the hydrophobic homopolymer. Although the utilized homopolymer is electroneutral, the colloids are stabilized by repulsive electrostatic forces most likely originating from ζ-potentials due to the adhesion of hydroxide ions to their hydrophobic surface. This charge stabilization is modeled by placing a virtual charged particle into the center of each polymer aggregate. The electrostatic interaction between aggregate I and J with distance r_{IJ} is described by a Yukawa potential

$$U_{Yukawa}(r_{IJ}) = \lambda_B\left(\frac{Z_I^* e^{\kappa a_I}}{1+\kappa a_I}\right)\left(\frac{Z_J^* e^{\kappa a_J}}{1+\kappa a_J}\right)\frac{e^{-\kappa r_{IJ}}}{r_{IJ}}. \tag{5.56}$$

$\lambda_B = {e^2}/{4\pi\epsilon_0\epsilon_r k_BT}$ is a constant called the Bjerrum length, κ the inverse Debye screening length, a_I the radius of aggregate I, and Z_I^* its size dependent net charge, which is calculated analytically [3] via

$$\frac{Z_I^*\lambda_B}{a_I} = (1+\kappa a_I)\frac{e\zeta}{k_BT}, \tag{5.57}$$

where ζ is the value of the ζ-potential and e the elementary charge.

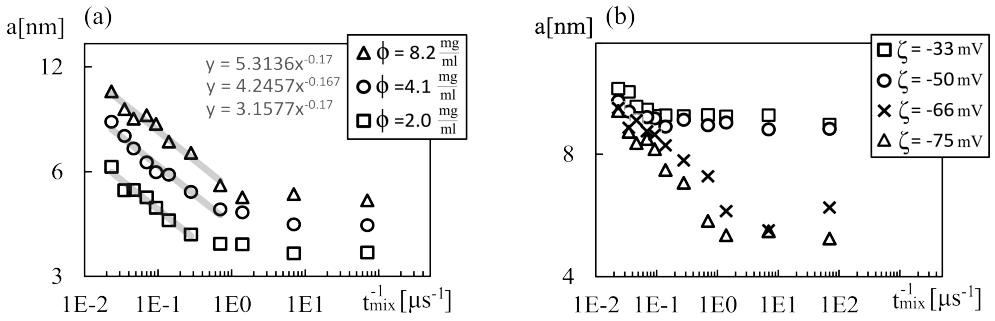

Figure 5.4: *Results of Molecular Dynamics simulations from Nikoubashman et al. [35] in double logarithmic representation (the layout was adapted). Both diagrams show nanoparticle radii a in dependence on an inverse mixing time t_{mix}^{-1}. (a) depicts an array of curves generated by different mean polymer concentrations ϕ with a fixed ζ-potential at $\zeta = -75$ mV. The grey lines are regression lines to data points associated with mixing times greater than a threshold time $\tau_{thr} \approx 5\tau_l$, where τ_l is the mean contact time of polymer coils defined in reference [35]. The trend line equations belong from top to bottom to triangles, circles and squares, respectively. In (b) the ζ-potential from equation 5.57 is varied while the mean polymer concentration is fixed at $\phi = 8.2$ mg/ml. Triangles in (a) and (b) label the same data.*

Figure 5.4 shows results of the Molecular Dynamics simulations. A peculiarity is the striking similarity of the general data point progression in comparison to figure 5.3. An agreement of absolute values for aggregate sizes cannot be expected due to different input parameters, but the exponents of the regression lines in figure 5.4 (a) come very close. As triangles in figure 5.4 (a) and (b) label the same data, it is evident that regression lines in (b) possess comparable exponents although they are not displayed. In the phase field model t_{max} from equation 5.44 corresponds to a mixing time. Since s or s_χ are proportional to t_{max}^{-1} we can roughly set $s, s_\chi \propto t_{mix}^{-1}$, which allows considering the horizontal axes in figures 5.3 and 5.4 as equivalent. Consequently, the characteristic attribution of rate-size relations from model I is in accordance with much more complex Molecular Dynamics simulations.

To continue the comparison with figure 5.4, the response of rate-size relations to parameter variations is investigated. As a reminder, the physical parameters besides s_χ are the mean polymer volume fraction f_P, the number of segments per polymer molecule N, and the maximum interaction parameter $\chi^{(max)}$.

Rate-size relations with different $\chi^{(max)}$ were simulated, but the results are not explicitly shown. We already argued in the short discussion about figure 5.3 that the asymptote corresponds to droplet sizes obtained for $\chi(t) \equiv \chi^{(max)}$. It is also well known from studies of the Cahn-Hilliard equation with constant interaction parameters that increasing quench depths decrease characteristic structure sizes. So it is clear that an increase of $\chi^{(max)}$ shifts the asymptote downwards and in the process, the non-asymptotic regime extends towards larger values of s_χ. A very similar response is also produced by increasing the absolute value of the ζ-potential in the Molecular Dynamics simulations as it is shown in figure 5.4 (b). Thus, one can identify a control parameter in the phase field model that provokes comparable changes of aggregate sizes to the ζ-potential. This correspondence, however, does not indicate any physical relation between $\chi^{(max)}$ and ζ. $\chi^{(max)}$ describes an interaction between solvent and polymer segments. Decreasing values of $\chi^{(max)}$ increase the characteristic size of droplets

in the limit of infinitely fast solvent mixing by affecting early stage coarsening in a similar manner as discussed in subsection 5.3.2, A). In contrast, the ζ-potential determines an interaction between already formed colloids and affects particle sizes by introducing an electrostatic stabilization mechanism that prevents them from coagulating in considerably later stages of particle growth (cp. figure 4.1, (f)). As the Yukawa potential grows with increasing colloid radii not only due to the explicit a_I- and a_J-dependencies but also due to the implicit a-dependencies in Z_I^* and Z_J^*, colloids become stable particles once they exceed a critical size where the electrostatic repulsion of accumulated electrons on their surface compensates van der Waals attractions described by the Lennard Jones potentials. Equation 5.57 states that the net charge $|Z_I^*|$ increases with the absolute value of the ζ-potential for a fixed colloid radius. A reduction of $|\zeta|$ therefore increases the particle size necessary to prevent coagulation of aggregates and lifts the lower bound for mean nanoparticle sizes, which is approached in the respective asymptotic regime. Summarized, both the maximum quench depth and the ζ-potential prescribe a lower bound of particle sizes that is reached at infinitely fast solvent mixing. That circumstance is reflected in their similar effect on quench rate dependencies, but the physical mechanism how that limitation is generated is fundamentally different. The difference implies that the definition of the asymptotic regime from subsection 5.3.2, B) and the definition in reference [35] are not equivalent. Therefore, we are going to use the term 'non-asymptotic regime' in a more loose context if we refer to sections where particle or droplet sizes show the scaling behavior with exponents $\approx 0.15 - 0.17$. The direct analogue to $\chi^{(max)}$ in the Molecular Dynamics simulation is most probably the cutoff or maximum value of γ in equation 5.54, which was unfortunately not varied in reference [35]. So drawing that comparison could potentially be touched on in future work.

Nevertheless, the correspondence of $\chi^{(max)}$ and ζ is still interesting since it implies that ζ mainly affects the placement of the asymptote. Likewise, it can be seen in figure 5.4 (b) that in the asymptotic regime, a seems to be very sensitive to changes in ζ, while in the non-asymptotic regime, it is not. Since ζ determines the interaction between polymer aggregates or colloids, this sensitivity should be an indicator for the significance of late stage collision-coagulation processes during particle growth. Keeping in mind that the free energy functional in model I is physically accurate in the weak segregation regime and that typical droplet sizes are likely to be determined during that regime (cp. the discussion to figure 5.2), the first aggregates of well defined shape that appear in the Molecular Dynamics simulations should be comparable to droplets. The ζ-sensitivity of a in the asymptotic regime indicates that these droplet-comparable aggregates grow to particles by colliding and coagulating. Collision-coagulation is not described by model I since it is a mean field description. As a result, droplets and particles are different. The low ζ-sensitivity in the non-asymptotic regime, however, indicates that collision-coagulation is insignificant and that droplet-comparable aggregates seem to be large enough for an almost direct charge stabilization once they have concentrated from the coarse composition pattern that is determined by solvent mixing in the very early stages. In that case, droplets can be identified with particles, which is also consistent with their practically identical scaling behavior.

Although the physical interpretation of measuring droplet sizes was not mentioned in subsection 5.3.2 to keep the description of the evaluation method as clear and concise as possible, there is one: namely the assumption that structure growth stops at transition time, which constitutes an imitation of any stabilization mechanism that prevents or suppresses

Ostwald Ripening and collision-coagulation growth of droplets. One candidate for such a mechanism is the steric stabilization that can occur if amphiphilic copolymers are used instead of homopolymers [88]. According to the above discussion, electrostatic stabilization through repulsion of aggregates is another one as long as considerations are restricted to the non-asymptotic regime. In this context it is emphasized that model I does not contain any physical stabilization mechanism to prevent Ostwald Ripening and is also not able to describe Brownian motion of droplets and the accompanying collision-induced coagulation in the late stages of particle growth – 'stabilizing' by termination at transition time is a purely artificial auxiliary construct! The transition to the asymptotic regime in the Molecular Dynamics model should happen once droplet-comparable aggregates become smaller than the critical size that is needed to prevent significant collision-coagulation growth. Hence, particle sizes might be underestimated by droplet sizes in the asymptotic regime when collision-coagulation processes are significant. In the case of very high ζ-potentials, which could appear in solutions of very high pH, the maximum value of γ could dictate the placement of the asymptote instead of ζ because collision-coagulation processes become less and less significant as smaller particles can be stabilized. In his case, the asymptotes of model I and the Molecular Dynamics simulations should agree. So in solutions of high pH, droplets are likely to correspond to particles in the asymptotic regime as well.

How rate-size relations respond to variations of f_P and N is displayed in figure 5.5, where the open circles always denote the reference parameter set from figure 5.3. The impact of f_P-variations can be understood as a consistency check. If droplets can be identified with particles in the non-asymptotic regime, rate-size relations should exhibit the same response as the data in figure 5.4 (a). The response of rate-size relations is shown in figure 5.5 (a), (b), and (c). To imitate the experimental conditions and the setup of the Molecular Dynamics simulations, χ_{SS} and χ_{GS} are kept constant as listed in the corresponding table below the diagrams because in contrast to $\chi^{(max)}$ or $\Delta\chi^{(max)}$, χ_{SS} and χ_{GS} constitute material data which should remain unchanged when the mean volume fraction of a specific polymer is modified. The remaining quantities in the table are calculated from f_P, N, χ_{GS}, and χ_{SS} according to the definitions of χ_0 and $\chi^{(max)}$ in equation 5.44 with $\chi_0 = \chi^{(Spin)}$ and $\varphi_{max} = {}^{(1+\varphi_0)}/_2$. The threshold volume fraction for conversion into binary images is set to $\phi_P^{(th)} = 0.3$. In double logarithmic representation diminishing volume fractions are associated with a downward shift of rate-size relations in the non-asymptotic regime, which is in agreement with the results from the Molecular Dynamics simulations in figure 5.4 (a). l_{max} though appears to be a rather bad measure for the current comparison. Its shift is very weak because it only takes into account the highest peak in the structure factor without properly weighting other contributions or even secondary maxima, which typically indicate moderate changes in mean droplet sizes. The response in the asymptotic regime depends on the applied measure. For R, the uppermost data points correspond to the largest mean volume fraction and the lowermost belong to the lowest f_P for any s_χ as seen in figure 5.5 (a). Data curves of l_1 and l_{max} shown in (b) and (c) intersect and their arrangement in the asymptotic regime is upside down, i.e. decreasing mean volume fractions leads to larger droplets. If the threshold value is set in relation to f_P, for example if $\phi_P^{(th)} = 3f_P$ is used, it would be $\phi_P^{(th)} = 0.15$ for $f_P = 0.05$. Data points for this choice are shown in (d). This time, the placement of asymptotes agrees with l_1 and l_{max}, which reveals a crucial threshold dependence of R that might either distort results and their interpretation or lead to a debate of principles how

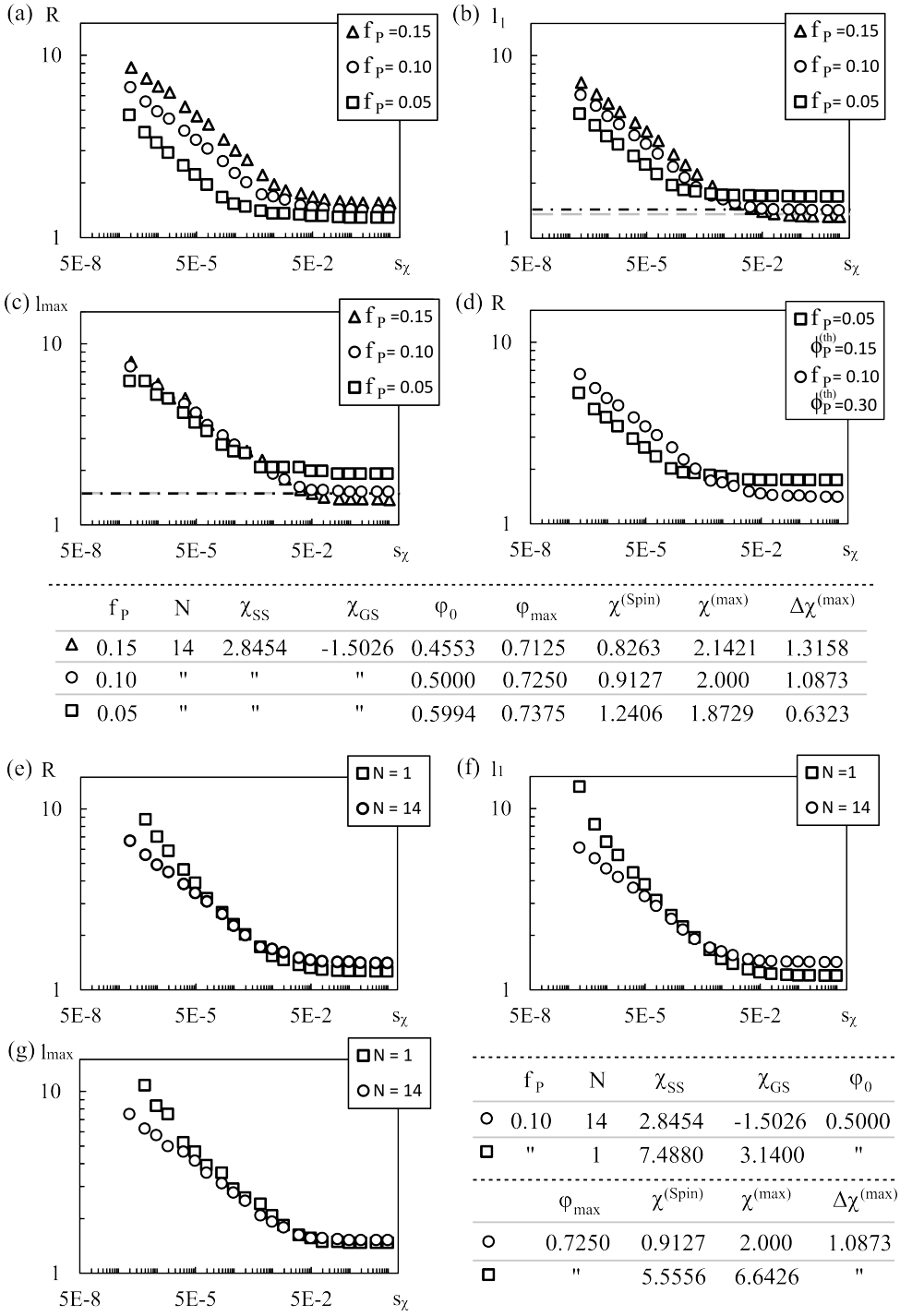

	f_P	N	χ_{SS}	χ_{GS}	φ_0	φ_{max}	$\chi^{(Spin)}$	$\chi^{(max)}$	$\Delta\chi^{(max)}$
△	0.15	14	2.8454	-1.5026	0.4553	0.7125	0.8263	2.1421	1.3158
○	0.10	"	"	"	0.5000	0.7250	0.9127	2.000	1.0873
□	0.05	"	"	"	0.5994	0.7375	1.2406	1.8729	0.6323

	f_P	N	χ_{SS}	χ_{GS}	φ_0
○	0.10	14	2.8454	-1.5026	0.5000
□	"	1	7.4880	3.1400	"

	φ_{max}	$\chi^{(Spin)}$	$\chi^{(max)}$	$\Delta\chi^{(max)}$
○	0.7250	0.9127	2.000	1.0873
□	"	5.5556	6.6426	"

Figure 5.5: *Response of 2D-data from figure 5.3 to f_P- and N-variations. f_P is the mean polymer volume fraction in solution and N the polymer chain length. (a), (b), and (c) show rate-size relations for different f_P with a threshold $\phi_P^{(th)} = 0.3$. The complete parameter set for a specific value of f_P is summarized in the upper table and the open circles represent the reference data from figure 5.3. The dashed grey lines in (b) and (c) correspond to the result for $f_P = 0.05$ and $\chi(t) \equiv \chi^{(Spin)} + 1.0873 = 2.3279$, while the dash-dotted black ones indicate the results for $f_P = 0.15$ and $\chi(t) \equiv \chi^{(Spin)} + 1.0873 = 1.9136$. In (d) the impact of $\phi_P^{(th)}$ on the relative placement of asymptotes for R is demonstrated by exemplarily setting $\phi_P^{(th)} = 0.15$ for $f_P = 0.05$. (e), (f), and (g) display rate-size relations for varying N. Error bars are similar to figure 5.3 and omitted for the sake of clarity.*

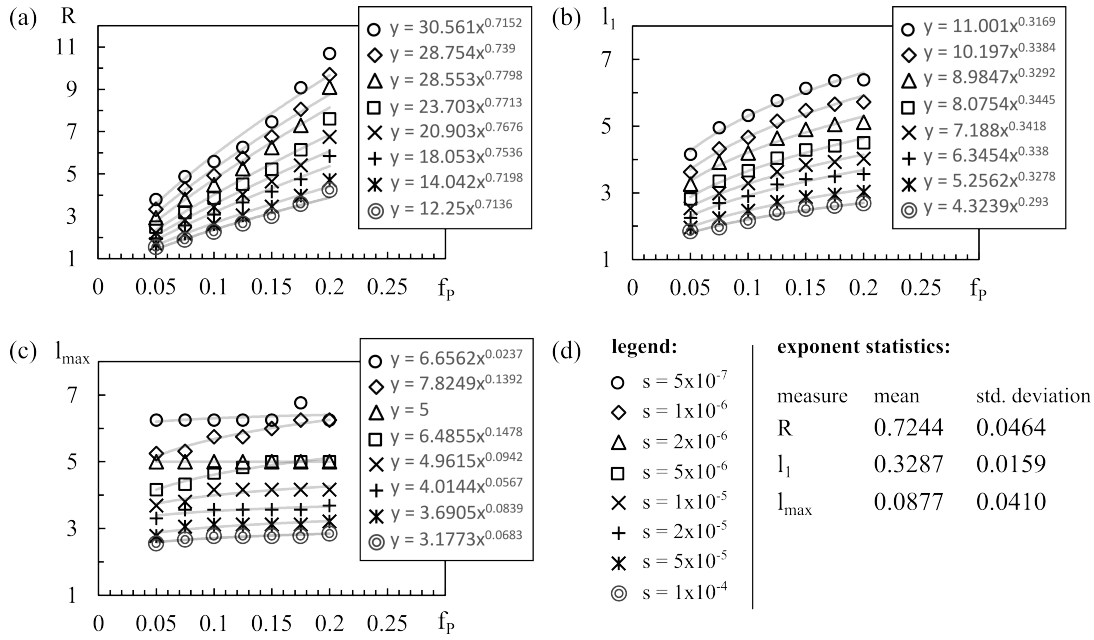

Figure 5.6: *Droplet sizes in dependence on the mean polymer volume fraction f_P, simulated with model I. (a), (b), and (c) show R, l_1, and l_{max}, respectively. Like in figure 5.5, chain lengths and interactions are fixed at $N = 14$, $\chi_{GS} = -1.5026$, and $\chi_{SS} = 2.8454$. The curve arrays are generated by different fixed mixing speeds s (cp. equation 5.44) as given by the legend in (d). Grey lines are regression lines and the trend line equations are shown in the corresponding inset. (d) also depicts the mean value and the standard deviation of exponents, calculated from all regression lines for one specific measure of droplet size. The threshold for binary conversion is set to $\phi_P^{(th)} = 0.3$.*

to chose $\phi_P^{(th)}$. Therefore, we suggest that R is a problematic measure as far as comparing different parameter sets is concerned, although it is the most accurate measure of mean particle size once – or better, if – an appropriate $\phi_P^{(th)}$ is found. The curves of l_1 and l_{max} for $\phi_P^{(th)} = 0.15$ at $f_P = 0.05$ are not shown but they do not exhibit such a threshold dependence. Due to the shortcomings of both l_{max} and R, we propose l_1 to be the most suitable measure for the investigation of parameter variations with model I. The crossing of data curves at the transition to the asymptotic regime and their upside down arrangement with respect to the non-asymptotic regime is caused by the decrease of $\chi^{(max)}$ for decreasing f_P in our parameter choices. The horizontal lines in figure 5.5 represent the asymptotes calculated by simulations with a constant quench depth $\Delta\chi^{(max)} = 1.0873$ (which corresponds to the maximum quench depth of the reference set) for $f_P = 0.005$ and $f_P = 0.15$, respectively, and it can be seen that the particle size in the asymptotic regime also decreases with diminishing f_P if $\Delta\chi^{(max)}$ is kept constant. So qualitatively, the response of droplet sizes to f_P-variations agrees with molecular dynamics simulations.

Nikoubashman et al. [35] report the particle radius a to scale like $a \propto \Phi^n$ in both simulations and experiments, where Φ is the mean polymer concentration in solution and $n \approx 0.3$. Furthermore, the proportionality as well as n appear to be independent of the mixing speed. Droplet sizes in dependence on f_P at several mixing speeds s within the non-asymptotic regime are shown in figure 5.6. All measures for droplet size grow with f_P, but the growth law severely depends on the measure. If we apply scaling laws $x \propto f_P^{n_x}$ with $x \in \{R, l_1, l_{max}\}$ as re-

gression lines, the exponents scatter around averages of 0.7244 (n_R), 0.3287 (n_{l_1}), and 0.0877 ($n_{l_{max}}$) as listed in figure 5.6 (d) with the respective standard deviation. $n_{l_1} = 0.3287 \pm 0.0159$ is close to $n \approx 0.3$, so it agrees with the Molecular Dynamics simulations. The much larger values for n_R are most likely caused by the $\phi_P^{(th)}$-dependence of R and are even expected because the closer $\phi_P^{(th)}$ gets to f_P, the larger droplets become at fixed remaining parameters. One reason why $n_{l_{max}}$ takes a rather low value of 0.0877 on average is probably the size of the simulation box, which seems to result in (discrete) Fourier space resolutions that are not fine enough to capture changes in droplet sizes by a shift of the structure factor's maximum alone. Most curves of the array in figure 5.6 (c) contain four or more data points that take exactly the same value l_{max}. However, there are two exceptions, namely the diamonds with an exponent 0.1392 and the squares with an exponent 0.1478, so l_{max} seems to scale differently from l_1 even if the resolution was high enough. This already indicates that the scaling of droplet sizes with f_P also depends on the applied measure regardless of 'numerical discretization issues'. In subsection 5.3.4 we are going to show that l_{max} is indeed expected to follow a scaling law $l_{\max} \propto f_P^m$ with $m \approx 0.14$.

Figure 5.5 (e), (f), and (g) show variations of the polymer chain length N. The data point progressions look very similar for moderate to large s_χ but deviate for small quench rates. The deviation from the characteristic scaling behavior is most likely caused by stronger Ostwald Ripening contributions because the entropic term in the free energy scales with $1/N$ and because the transition between spinodal decomposition and Ostwald ripening is not cleanly separated: some aggregates may have already developed a sharp interface and grow by Ostwald ripening, while in other regions of space, the dynamics is still dominated by spinodal decomposition. The increasing nonlinear contributions from Ostwald ripening generate a third regime at low s_χ and very short polymers, where the scaling behavior breaks.

In summary, we found that f_P-variations vertically shift the non-asymptotic regime of rate-size relations regardless of the applied measure for droplet size. This shift is in qualitative agreement with Molecular Dynamics simulations. In addition, l_1 is quantitatively consistent with the relation 'size $\propto$ (mean polymer content)^n', where $n \approx 0.3$. Together with the very similar scaling behavior in dependence of mixing speeds, this consistency provides strong evidence that in the non-asymptotic regime droplets can be identified with stable homopolymer particles. As a consequence, the characteristic attributions of rate-size relations in that regime seem to be independent of the applied dynamical model for phase separation. In the asymptotic regime droplets and particles may be different but as far as size-controlled assembly in experiments is concerned, the asymptotic regime is rather uninteresting anyway because it does not allow for the desired size-control by variations of mixing times. In other words, if experimental data resemble figure 1.3, they most likely show a section from a non-asymptotic regime.

5.3.4 Perturbation theory and scaling laws

Rate-size relations are not only similar to results from Molecular Dynamics simulations, but they also show a close qualitative resemblance to analytical results for defect sizes during continuous cooling of an alloy, which were derived within a perturbation approximation to a Cahn-Hilliard equation a long time ago [120]. This resemblance relates to the characteristic scaling behavior of the defect sizes as functions on quench rates (the analytical theory predicts

an exponent of $-1/6$), and can be attributed to a formal analogy of continuous temperature changes to time dependent interaction parameters. In the present subsection we explicitly transfer the perturbation approximation to model I in order to extract an analytical explanation for the scaling behavior in the non-asymptotic regime. In the process, it is also shown that the perturbation theory predicts simulation results from figure 5.3, i.e. droplet sizes, quantitatively. Since droplets may be identified with stable homopolymer particles in Molecular Dynamics simulations, the results from following considerations should count for these particles as well.

The starting point is to linearize the dynamical equation of model I, equation 5.18, around a homogeneous ground state. To this end the polymer volume fraction is split into the sum $\phi_P(\vec{r},t) = f_P + u_P(\vec{r},t)$, and if the perturbation u_P fulfills $|u_P(\vec{r},t)| \ll 1$, the chemical potential μ_r may be Taylor expanded to

$$\mu_r(\phi_P,t) = \mu_r(f_P,t) + \frac{\partial \mu_r}{\partial \phi_P}(f_P,t)\cdot u_P. \tag{5.58}$$

Insertion of the Taylor expansion and $\phi_P(\vec{r},t) = f_P + u_P(\vec{r},t)$ into equation 5.18, neglecting $\mathcal{O}(u_P^2)$ terms[3], and a subsequent Fourier transformation in space lead to a system of linear ordinary differential equations

$$\frac{\partial \hat{u}_P}{\partial t}(\vec{k},t) = a(k,t)\hat{u}_P(\vec{k},t) \tag{5.59}$$

with

$$a(k,t) = -M(f_P)k^2\left[k^2 + \frac{\partial \mu_r}{\partial \phi_P}(f_P,t)\right] \tag{5.60}$$

and the usual notation $k = |\vec{k}|$ for the Euclidean norm of the wave vectors. $\hat{u}_P$ are the Fourier coefficients of u_P. The solution to equation 5.59 are the modes

$$\hat{u}_P(\vec{k},t) = \hat{u}_P(\vec{k},0)\cdot e^{\int_0^t a(k,t')dt'} \tag{5.61}$$

with the exponent

$$\int_0^t a(k,t')dt' = -M(f_P)k^2\left[\int_0^t \frac{\partial \mu_r}{\partial \phi_P}(f_P,t')dt' + k^2 t\right],$$

or in full representation

$$\hat{u}_P(\vec{k},t) = \hat{u}_P(\vec{k},0)e^{-M(f_P)k^4 t}e^{-M(f_p)k^2\int_0^t \frac{\partial \mu_r}{\partial \phi_P}(f_p,t')dt'}. \tag{5.62}$$

The two exponential functions reflect one respective flux in the pictorial interpretation from subsection 5.3.2, A). The first exponential function represents the interfacial tension driven coarsening (cp. figure 5.2 (a) and (c)), which rapidly damps modes of large wave numbers k and removes high curvatures from composition profiles in the process. The second one accounts for the repulsion of the components. Inserting the derivative of μ_r from equation 5.17,

$$\frac{\partial \mu_r}{\partial \phi_P}(f_P,t) = \frac{1}{N f_P} + \frac{1}{1-f_P} - 2\chi(t) = 2\left[\chi^{(Spin)} - \chi(t)\right], \tag{5.63}$$

[3]Including $u_P\nabla u_P$ and $u_P\nabla\Delta u_P$, i.e. gradients and curvatures are assumed to be weak, too.

the second exponential function can be cast into the form

$$e^{2M(f_P)k^2 \int_0^t (\chi(t')-\chi^{(Spin)})dt'}.$$

In contrast to the first exponential function, the exponent of the second one is strictly positive inside the spinodal area and grows with k. The synergy of both e-functions favors the growth of modes that belong to wave numbers in a specific time dependent band width, which is enclosed by the roots of $\int_0^t a(k,t')dt' = 0$ in k-direction.

To estimate droplet sizes we utilize the Euclidean norm of wave vectors that are associated to modes with maximum amplification at a specific time t, for instance at transition time $t = t_{tr}$. Thus, in demand is k_p such that

$$\left(\frac{\partial}{\partial k}\int_0^t a(k,t')dt'\right)\Big|_{k=k_p(t)} = 0,$$

which is equivalent to

$$k_p(t) = \sqrt{-\frac{1}{2t}\int_0^t \frac{\partial \mu_r}{\partial \phi_P}(f_P,t')dt'}. \tag{5.64}$$

From now on the short hand notation

$$\overline{\Delta\chi}(t) \coloneqq -\frac{1}{2t}\int_0^t \frac{\partial \mu_r}{\partial \phi_P}(f_P,t')dt' = \frac{1}{t}\int_0^t \left[\chi(t') - \chi^{(Spin)}\right]dt' \tag{5.65}$$

is applied. At the moment this is just a notational simplification, but in subsection 5.3.6 its interpretation as an effective constant quench depth is discussed. Employing the restriction to $t \leq t_{max}$ of the linear mixing profile from equation 5.44 into $\overline{\Delta\chi}$ gives

$$\overline{\Delta\chi}(t) = \frac{1}{t}\int_0^t \left[(\chi_0 + s_\chi t') - \chi^{(Spin)}\right]dt',$$

and recalling that $\chi_0 = \chi^{(Spin)}$, the integral collapses to

$$\overline{\Delta\chi}(t) = \frac{1}{t}\int_0^t s_\chi t' dt' = \frac{s_\chi t}{2}.$$

For $t > t_{max}$ it is

$$\overline{\Delta\chi}(t) = \frac{1}{t}\int_0^{t_{max}} s_\chi t' dt' + \frac{1}{t}\int_{t_{max}}^t \left[\chi^{(max)} - \chi^{(Spin)}\right]dt' = \frac{s_\chi t_{max}^2}{2t} + (\chi^{(max)} - \chi^{(Spin)})\frac{t - t_{max}}{t}$$

$$= (\chi^{(max)} - \chi^{(Spin)})\frac{t_{max}}{2t} + (\chi^{(max)} - \chi^{(Spin)})\frac{t - t_{max}}{t} = \left(1 - \frac{t_{max}}{2t}\right)(\chi^{(max)} - \chi^{(Spin)}),$$

and combining the two cases leads to

$$k_p(t) = \sqrt{\overline{\Delta\chi}(t)} \text{ with } \overline{\Delta\chi}(t) = \begin{cases} \dfrac{s_\chi t}{2}, & t \leq t_{max} \\ \left(1 - \dfrac{t_{max}}{2t}\right)\left(\chi^{(max)} - \chi^{(Spin)}\right), & t > t_{max} \end{cases}. \tag{5.66}$$

Within the perturbation theory droplet radii may be estimated analogously to equation 5.52

by

$$l_p(t_{tr}) = \gamma \frac{2\pi}{k_p(t_{tr})} = \frac{\pi}{2\sqrt{\overline{\Delta\chi}(t_{tr})}}. \tag{5.67}$$

A comparison between $l_p(t_{tr})$ and the simulation results from figure 5.3 is shown in figure 5.7. It can be seen that the simulation results and prediction from the perturbation theory are relatively close. As it is evident from figure 5.7 (b) and (d), the relative deviation lies below 20 % except for R in 3 dimensions at large $\overline{\Delta\chi}(t_{tr})$. Since $l_p(t_{tr})$ is calculated from the wave length of the mode with the largest amplification at t_{tr}, it should yield the best approximation to l_{max}. The deviation of $l_p(t_{tr})$ and l_{max} is indeed below 10 % for the most part and consequently, mean droplet radii can be described by the perturbation theory within a good accuracy. The agreement of simulation results with predictions from a theory that is only valid close to the homogeneous initial state implies that droplet sizes are mainly determined in the weak segregation regime. Therefore, the illustrative phrase that composition patterns towards the end of early stage coarsening like in figure 5.2 (d) imprint onto composition profiles at transition time like in (f) can be understood literally. Since contributions of repulsion between components and interfacial tension have already been

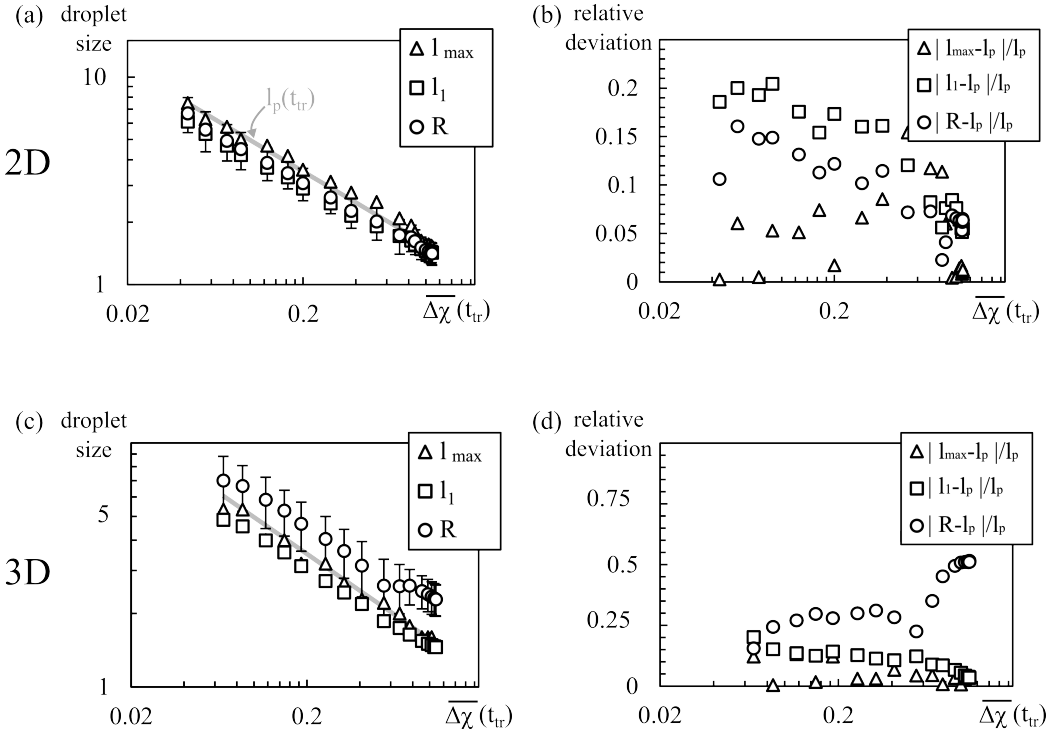

Figure 5.7: *Comparison between simulation results and the prediction from the perturbation theory for model I. The data points in (a) and (c) are taken from figure 5.3 and the grey line represents the prediction from the perturbation theory at transition time, $l_p(t_{tr})$ from equation 5.67. On the horizontal axis is $\overline{\Delta\chi}(t_{tr})$ from equation 5.66, which renders $l_P(t_{tr})$ a straight line with slope $-1/2$ in double logarithmic representation. $\overline{\Delta\chi}(t_{tr})$ is calculated with the simulation results for t_{tr} from figure 5.3 (d) and (h). The asymptote becomes an accumulation point at $\lim_{s_\chi \to \infty} \overline{\Delta\chi}(t_{tr}) = \chi^{(max)} - \chi^{(Spin)}$, which follows from equation 5.66 and the fact that t_{tr} possesses a lower bound while t_{max} tends towards zero as $s_\chi \to \infty$ (cp. figure 5.3 (d) and (h)). (b) and (d) show the relative deviations of simulation results from $l_p(t_{tr})$.*

identified in the linearized solution given by equation 5.62 as separate exponential functions with opposite signs of the exponents, the agreement also verifies the pictorial interpretation of competing fluxes from subsection 5.3.2, A) in a quantitative manner. If the solution to the linearized equation in the Fourier space is considered, increasing s_χ simply enhances the wave number $k_p(t_{tr})$ of the mode with largest amplification at t_{tr}, which results in smaller droplets.

To derive the theoretical value for the exponent in the non-asymptotic regime of rate-size relations, an amplification time of composition fluctuations is calculated. Rearrangement of equation 5.61 leads to

$$\ln\left(\frac{\hat{u}_P(\vec{k},t)}{\hat{u}_P(\vec{k},0)}\right) = \int_0^t a(k,t')dt' \tag{5.68}$$

and defining the amplification $A(k,t) = {}^{\hat{u}_P(\vec{k},t)}/_{\hat{u}_P(\vec{k},0)}$ yields

$$\begin{aligned}\ln(A(k,t)) &= -M(f_P)k^2\left(k^2 t + \int_0^t \frac{\partial \mu_r}{\partial \phi_P}(f_P,t')\,dt'\right)\\ &= -M(f_P)k^2\left(k^2 - 2\overline{\Delta\chi}(t)\right)t.\end{aligned} \tag{5.69}$$

Since we are interested in the growth time of the most unstable mode with wave number $k_p(t) = \sqrt{\overline{\Delta\chi}(t)}$ we set $k = k_p(t)$ and get

$$\ln(A(k_p(t),t)) = -M(f_P)\overline{\Delta\chi}(t)\left(\overline{\Delta\chi}(t) - 2\overline{\Delta\chi}(t)\right)t = M(f_P)\left(\overline{\Delta\chi}(t)\right)^2 t. \tag{5.70}$$

Upon insertion of $\overline{\Delta\chi}$ from equation 5.66 this expression becomes

$$\ln(A(k_p(t),t)) = \begin{cases} \dfrac{M(f_P)}{4}s_\chi^2 t^3, & t \le t_{max} \\ M(f_P)\Delta\chi_{max}^2\left(1 - \dfrac{t_{max}}{2t}\right)^2 t, & t > t_{max} \end{cases} \tag{5.71}$$

with $\Delta\chi_{max} = (\chi^{(max)} - \chi^{(Spin)})$, which is equivalent to the implicit relation

$$t = \begin{cases} \sqrt[3]{\dfrac{4\ln(A(k_p(t),t))}{M(f_P)}}\, s_\chi^{-2/3}, & t \le t_{max} \\ \dfrac{t_{\max} + z(t)}{2} + \dfrac{1}{2}\sqrt{z(t)\,(2t_{max} + z(t))}, & t > t_{max} \end{cases} \tag{5.72}$$

for the amplification time t, where the short hand notation

$$z(t) = \frac{\ln(A(k_p(t),t))}{M(f_P)\Delta\chi_{max}^2} \tag{5.73}$$

is applied. Eliminating the explicit t-dependencies in equation 5.66 by inserting equation

5.72 results in

$$l_p(t) = \begin{cases} \gamma 2^{3/2}\pi \sqrt[6]{\dfrac{M(f_P)}{4\ln(A(k_p(t),t))}}\, s_\chi^{-1/6}, & t \le t_{max} \\ \dfrac{\gamma 2\pi}{\sqrt{\Delta\chi_{max}\left(1-\frac{t_{max}}{2}\left[\frac{t_{\max}+z(t)}{2}+\frac{1}{2}\sqrt{z(t)\left(2t_{max}+z(t)\right)}\right]^{-1}\right)}}, & t > t_{max} \end{cases} . \quad (5.74)$$

As the exponents of the regression lines to t_{tr} in figure 5.3 (d) and (h) are -0.643 in 2D and -0.661 in 3D, which is very close to $-2/3$ from equation 5.72, the transition time in the non-asymptotic regime exhibits the scaling behavior of an amplification time. Setting $t = t_{tr}$ in equation 5.74 immediately provides the theoretical exponent $-1/6$ for droplet sizes $l_p(t_{tr})$ in the non-asymptotic regime. The exponents from simulations are listed in table 5.1 and it shows that the deviations from $-1/6$ are below 10 %. Both the functional dependency $l_p \propto s_\chi^\alpha$ and the exponent $\alpha = -1/6$ are independent of the input parameters, so they constitute universal characteristics of model I with linear mixing profiles. The deviations between the perturbation theory and simulation results are caused by non-linear contributions as $|\hat{u}_P(\vec{r},t)| \ll 1$ is not strictly valid for any t.

Equation 5.74 also suggests an interpretation why droplet sizes decrease with diminishing mean polymer volume fractions f_P. Taking the natural logarithm of both sides leads to

$$\ln\left(l_p(t_{tr})\right) = \ln\left(\frac{\gamma 2^{3/2}\pi}{\sqrt[6]{4\ln\left(A(k_p(t_{tr}),t_{tr})\right)}}\right) + \frac{1}{6}\ln\left(f_P(1-f_P)\right) - \frac{1}{6}\ln\left(s_\chi\right) \quad (5.75)$$

and shows that changing f_P from 0.1 to 0.15 or 0.05 results in an upward or downward shift in double logarithmic representation, which is in agreement with simulations (upper part of figure 5.5 and figure 5.4 (a)). If we further rewrite equation 5.75 to

$$l_p(t_{tr}) \propto \left(f_P(1-f_P)\right)^{1/6}, \quad (5.76)$$

insert the f_P-values 0.05, 0.075, 0.1, 0.125, 0.15, 0.175, 0.2 like in figure 5.6, and approximate the resulting $l_p(t_{tr})$ by a regression line, we obtain $l_p(t_{tr}) \propto f_P^m$ with $m \approx 0.1462$, which is consistent with the scaling of the squares and diamonds in figure 5.6 (c). This indicates that the decrease of droplet sizes with decreasing f_P is not caused by a depletion of polymer but by a slowdown of dynamics in the very early stages of spinodal decomposition, which

dimension	exponent α			relative deviation		
	R	l_1	l_{max}	R	l_1	l_{max}
2D	-0.170	-0.168	-0.156	-0.020	-0.008	0.064
3D	-0.161	-0.157	-0.153	0.034	0.058	0.082

Table 5.1: *Exponents α from the trend line equations $y \propto s_\chi^\alpha$ in figure 5.3 with $y \in \{R, l_1, l_{max}\}$ and their relative deviation from $-1/6$. The deviation is calculated by the formula $\frac{\alpha+1/6}{1/6}$. Exponents from Molecular Dynamics simulations can be found in figure 5.4 (a) and read -0.170 and -0.167.*

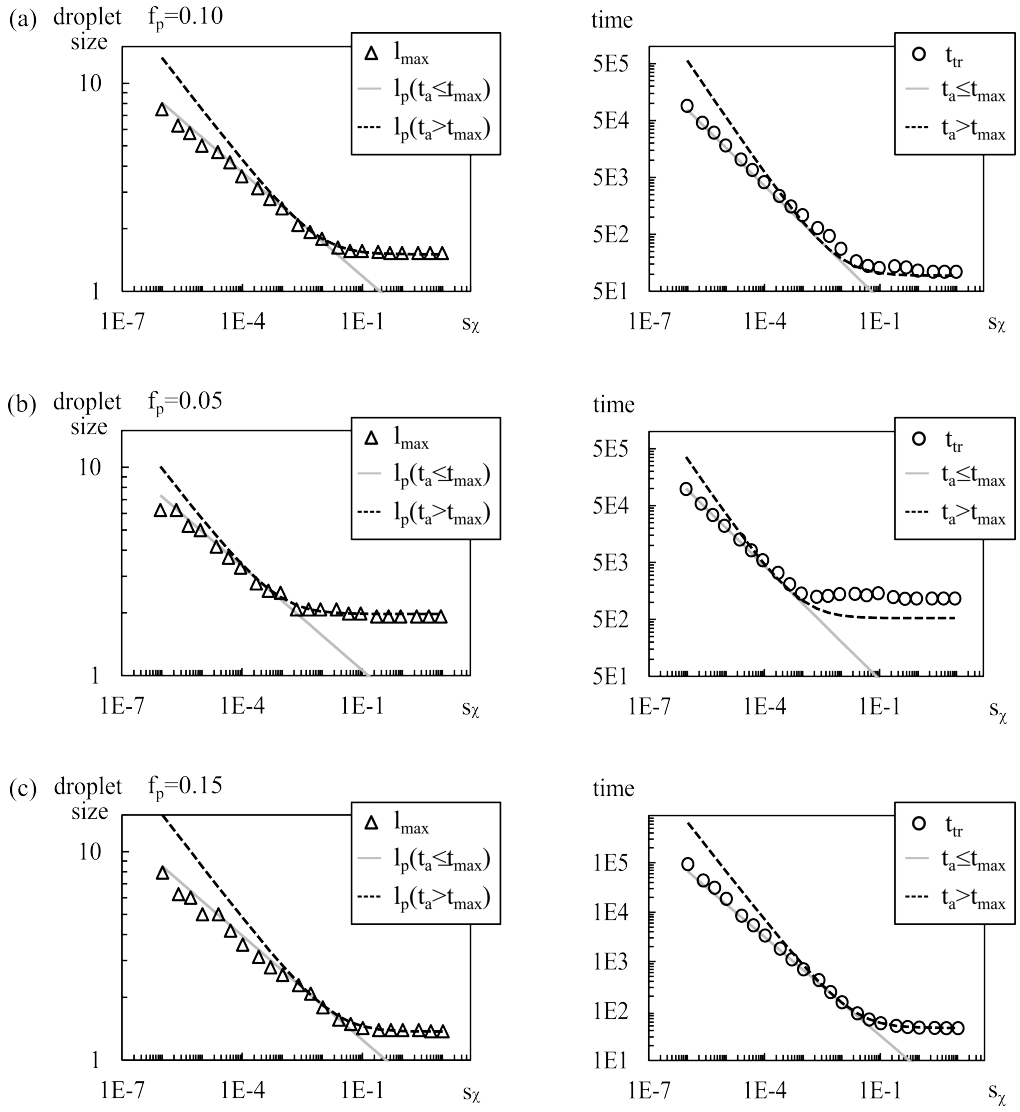

Figure 5.8: *Simulation results for l_{max} from model I compared to semi-analytical approximations $l_p(t_a)$. The simulation results for l_{max} are taken from the upper panel of figure 5.5: data points in (a) correspond $f_P = 0.1$, data points in (b) to $f_P = 0.05$, and data points in (c) to $f_P = 0.15$. $l_p(t_a \leq t_{max})$ denotes the first line in equation 5.74 and $l_p(t_a > t_{max})$ the second one, where t_a is defined by $\ln(A(k_p(t_a), t_a)) = 10$. The two branches of l_p intersect at the transition from the non-asymptotic to the asymptotic regime. The respective t_a, which are shown in the right panel together with the transition times t_{tr}, are calculated from $l_p(t_a)$ via equation 5.70 with $\overline{\Delta\chi}(t_a) = \left(\gamma 2\pi / l_p(t_a)\right)^2$.*

eventually produces smaller droplets. As a consequence, the depletion of polymer should be mainly responsible for the decreasing number of droplets and their decreasing final polymer content with diminishing f_P that we observed in our simulations.

The predictive power of the perturbation theory is unfortunately limited by the fact that the amplification $A(k_p(t_{tr}), t_{tr})$ is an analytically rather inaccessible quantity as it could for example depend on the random initial condition, which determines $\hat{u}_P(k_p, 0)$. It should also exhibit a certain dependence on $\phi_P^{(th)}$ and on the quench rate. s_χ affects the polymer content in droplets, i.e. $\hat{u}_P(k_p(t_{tr}), t_{tr})$, as is evident from the color bars in figure 5.2 (e) and (f). Despite

the lack of an analytical expression for A it is noted that we found good approximations to l_{max} by setting the logarithm of the amplification factor in equation 5.74 to $\ln(A) = 10$. The results are shown in figure 5.8 for different parameter sets. Especially because the slope $1/A$ of $\ln(A)$ is very low at $A = e^{10}$, minor variations of A due to changes of $\phi_P^{(th)}$ or s_χ could have negligible impact on l_p. The lacking explicit expression for $A(k_p(t), t)$ prevents inverting $\ln(A(k_p(t_a), t_a)) = 10$ with respect to t_a, so it is not known a priori if $t_a \leq t_{max}$ or $t_a > t_{max}$. For this reason, both cases in equation 5.74 are plotted (the quench rate dependence in the second line is contained in $t_{max} = (\chi^{(max)} - \chi^{(Spin)})/s_\chi$). The transition from the non-asymptotic to the asymptotic regime can then be determined graphically by their intersection. Since the data points can be approximated by the left branch of $l_p(t_a \leq t_{max})$ and the right one of $l_p(t_a > t_{max})$, semi-analytic descriptions by assuming constant A should be possible. Here, l_p denotes the inverse wave length with maximum amplification at a specific time, but expressions for the inverse first moment should be deducible in an analogous manner.

In the present work, however, the possibility for semi-analytical approaches constitutes only a side note. The main result of the current subsection is the good quantitative agreement of the perturbation theoretical prediction l_p to simulation results for droplet radii from model I. The perturbation approximation explains the characteristic scaling behavior of rate-size relations by a competition between molecular repulsion and interfacial tension in the very early stages of phase separation and therefore, it provides an interpretation to the 'working principle' of mechanism (i) from chapter 4. It also follows that both the scaling behavior 'size $\propto$ (quench rate)$^\alpha$' and the exponent $\alpha = -1/6$ are independent of the input parameters and thus, universal to linear mixing profiles in model I.

5.3.5 Comparison to experiments

In the preceding two subsections we discussed basic properties of model I from a purely theoretical point of view. In this subsection the principal characteristics of rate-size relations are compared to the experimentally observed trends from figure 1.3 in order to investigate in how far our previous considerations are relevant to experiments.

a) Qualitative comparison: scaling behavior and parameter variations

Considering the batch implementation of the co-solvent method it appears reasonable to interpret s from equation 5.44 as the constant water injection rate r_I, which enables a direct comparison of the experimental exponent -0.131 in figure 1.3 (e) with the theoretical value $-1/6$ from equation 5.74. Taking into account the dramatic simplifications in our model, the exponents are surprisingly close. To compare rate-size relations with experimental data for micromixers, s or s_χ need to be translated into flow rates v. As a first estimation, s and v could be linked by linear interpolations of arbitrary mixing profiles between $t = 0$ and the mixing time $t = t_{mix}$ if $t = 0$ labels the time when a fluid parcel enters a mixer. Such interpolations correspond to equation 5.44 where t_{max} represents the mixing time. Since mixing times in continuous flow micromixers are approximately proportional to the inverse Reynolds number Re [111], and thus proportional to $1/v$, $s \propto 1/t_{max}$ can be expressed as $s \propto v$ leading to $l_p \propto s^{-1/6} \propto v^{-1/6}$. The average of all exponents α in the trend line equations beneath the diagrams in figure 1.3 reads $\bar{\alpha} = -0.158$ with a standard deviation $\sigma_\alpha = 0.058$. Therefore, the scaling behavior from the spinodal decomposition model is also reflected in

the experimental data from micromixers.

Figure 1.3 (c) indicates that an increase of the mean polymer concentration mainly shifts the data points to larger values, which also agrees with the response of rate-size relations to f_P-variations in the non-asymptotic regime (cp. figure 5.5). Model I is further able to reproduce the impact of temperature changes depicted in figure 1.3 (d) because the Flory-Huggins interaction parameters χ_{GS} and χ_{SS} depend on T. The temperature dependence of a χ-parameter is frequently cast into the form $\chi = \chi^{(0)} + {}^{\alpha}/_{T}$ with constants $\chi^{(0)}$ and α [152, 153, 154, 155, 156]. Assuming

$$\chi_{GS} = \chi_{GS}^{(0)} + \frac{\alpha_{GS}}{T} \text{ and } \chi_{SS} = \chi_{SS}^{(0)} + \frac{\alpha_{SS}}{T}, \tag{5.77}$$

s_χ defined by equation 5.44 becomes

$$\begin{aligned} s_\chi &= \left[\left(\chi_{SS}^{(0)} + \frac{\alpha_{SS}}{T}\right) - \left(\chi_{GS}^{(0)} + \frac{\alpha_{GS}}{T}\right)\right] \frac{s}{1-f_P} \\ &= \left[\left(\chi_{SS}^{(0)} - \chi_{GS}^{(0)}\right) + \frac{(\alpha_{SS} - \alpha_{GS})}{T}\right] \frac{s}{1-f_P}. \end{aligned} \tag{5.78}$$

Considering a logarithmic representation of the horizontal axis and formally writing the particle size R as a function of the quench rate $R(\ln(s_\chi))$, insertion of equation 5.78 leads to

$$R(\ln(s_\chi)) = R\left(\ln\left(\frac{1}{1-f_P}\left[\left(\chi_{SS}^{(0)} - \chi_{GS}^{(0)}\right) + \frac{(\alpha_{SS} - \alpha_{GS})}{T}\right]\right) + \ln(s)\right) =: \widetilde{R}(\ln(s)). \tag{5.79}$$

$\widetilde{R}(\ln(s))$ denotes the particle size as a function of the logarithmic mixing speed $s \propto v$ and mimics $R_{DLS}(\ln(v))$ in figure 1.3. Equation 5.79 immediately shows that the temperature affects the horizontal axis shift of $\widetilde{R}$. If $\alpha_{SS} - \alpha_{GS} > 0$, a decrease of T shifts the graph of $\widetilde{R}$ to the left. Provided double logarithmic scaling, $R(\ln(s_\chi))$ is a straight line in the non-asymptotic regime and a horizontal left shift of $\widetilde{R}$ also appears as vertical downward shift if one only considers a compact set on the $\ln(s)$-axis that does not contain any part of the asymptotic regime. This vertical shift coincides with the response of the experimental data from figure 1.3 (d). For $(\alpha_{SS} - \alpha_{GS}) < 0$ one observes the contrary behavior. Unfortunately, neither the values of α_{GS} and α_{SS} nor the temperature dependence of the interaction parameters were measured during the experiments, which renders the relating discussion a little bit vague. But we still consider it noteworthy that the model is principally able to reproduce temperature dependencies appearing in the experimental data. The same response of particle sizes on temperature variations follows from the perturbation theory if s_χ from equation 5.78 is inserted into equation 5.75.

b) Quantitative comparison: length and time scales

The above elaboration of qualitative similarities between simulated rate-size relations and the experimental results is followed by the investigation of how they compare quantitatively, i.e. we investigate if model I produces aggregate radii in the range of ≈ 10 to 100 nm at flow rates $v \in [0.1\ \text{ml/min}, 5\ \text{ml/min}]$ as it is the case in figure 1.3. This indirectly checks whether time scales of spinodal decomposition are likely to match realistic mixing times or whether spinodal decomposition is too fast to be affected by solvent mixing on realistic time scales.

To this end mixing times in the SFIMM and CPMM are explicitly calculated for different flow rates via the respective equations 3.21 or 3.54. The results are shown in figure 5.9. In section 3.2 v referred to the flow rate inside an upper or lower part of a repeat unit in the CPMM, $v_{\text{section3.2}}$. In the following v refers to the total flow rate in the CPMM, which is $v = 2\, v_{\text{section3.2}}$. If the cutoff time t_{max} in equation 5.43 is set to $t_{max} = {}^{t_{mix}}\!/_{t_0}$, where t_{mix} is the mixing time in seconds and $t_0 = {}^{R_g^2}\!/_{D_0}$ the time scale, s_χ becomes

$$s_\chi = \frac{\chi^{(max)} - \chi_0}{t_{max}} = (\chi^{(max)} - \chi_0)\frac{t_0}{t_{mix}}, \tag{5.80}$$

and inserting the trend line equations from figure 5.9 yields

$$s_\chi \approx \left(\chi^{(max)} - \chi_0\right) \frac{R_g^2}{D_0} \cdot \begin{cases} {}^1\!/_6 \ (v \ {}^{\text{min}}\!/_{\text{ml}})^{0.852} \ \text{sec}^{-1} & \text{in the SFIMM} \\ 50 \ (v \ {}^{\text{min}}\!/_{\text{ml}})^{0.932} \ \text{sec}^{-1} & \text{in the CPMM} \end{cases} . \tag{5.81}$$

After specifying the segment diffusion coefficient D_0 and the polymer's radius of gyration R_g, the quench rate can be mapped onto a flow rate. The amphiphilic diblock-copolymer $\text{PB}_{130} - \text{PEO}_{66}$ possesses a molar mass of approximately $M_P = 10\, {}^{\text{kg}}\!/_{\text{mol}}$ [23]. Because model I can only describe homopolymers, we replace the copolymer by a homopolymer of its hydrophobic polybutadiene block without changing M_P. The molar mass of butadiene is known to be $M_B = 54\, {}^{\text{g}}\!/_{\text{mol}}$, resulting in a chain length of $N = {}^{M_P}\!/_{M_B} = {}^{10}\!/_{(54 \cdot 10^{-3})} \approx 185$ segments, which is rounded to $N = 190$. Using M_P to estimate R_g with a relation valid for polybutadiene in tetrahydrofuran [157],

$$R_g = 0.0448 \cdot \left(M_P \, \frac{\text{mol}}{\text{g}}\right)^{0.53 \pm 0.01} \text{ nm with } M_P \text{ in } \frac{\text{g}}{\text{mol}}, \tag{5.82}$$

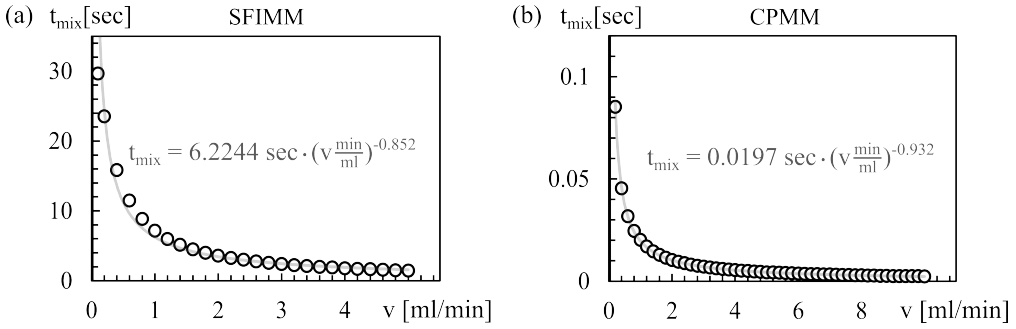

Figure 5.9: *Flow rate dependence of the mixing time t_{mix} in the SFIMM (a) and the CPMM (b). The data points in (a) are determined by solving equation 3.21 numerically. The equation in the diagram belongs to the grey trend line and inserting the flow rate v in ml/min yields t_{mix} in seconds. (b) shows the same for the CPMM except that mixing times are calculated from equation 3.54. In accordance to measurements from figure 1.3 (a) and (b) the initial solution is considered to be an approximate 50/50 % mixture of good and selective solvent, i.e. it is $\varphi_{SS}^{(1)} = 0.5$ and $\varphi_{SS}^{(2)} = 1$, where $\varphi_{SS}^{(i)}$ corresponds to the initial condition $c^{(i)}$ in chapter 3. Concentrations c can be translated into volume fractions φ_{SS} by multiplication with the molecular volume of selective solvent ν. Multiplying the corresponding equations in table 3.1 and 3.2 with ν is formally equivalent to substituting the symbol c by φ_{SS}. This substitution can be employed in the definitions of the mixing quality ϵ in equations 3.21 and 3.54 as well.*

leads to $R_g \approx 5$ nm. The density of PB_{130} was measured during the experiments as $\rho_{PB} = 960\ {}^{\mathrm{kg}}/_{\mathrm{m}^3}$, and the molar volume of monomeric butadiene units is roughly estimated by $\nu_B = {}^{M_P}/_{(\rho_{PB} N)} = {}^{10}/_{(960 \cdot 190)}\ {}^{\mathrm{m}^3}/_{\mathrm{mol}} \approx 5.48 \cdot 10^{-5}\ {}^{\mathrm{m}^3}/_{\mathrm{mol}}$. The molar mass and the density of tetrahydrofuran and water are $M_{THF} = 72.11\ {}^{\mathrm{g}}/_{\mathrm{mol}}$, $M_W = 18.02\ {}^{\mathrm{g}}/_{\mathrm{mol}}$, $\rho_{THF} = 889\ {}^{\mathrm{kg}}/_{\mathrm{m}^3}$, and $\rho_W = 1000\ {}^{\mathrm{kg}}/_{\mathrm{m}^3}$, which leads to an estimated mean molar volume of the solvent

$$\nu_L = \frac{M_{THF} + M_W}{\rho_{THF} + \rho_W} \approx 4.76 \cdot 10^{-5} \frac{\mathrm{m}^3}{\mathrm{mol}}. \tag{5.83}$$

Because ν_B and ν_L are close, we can regard solvent molecules as segments. Consequently, the segment diffusion coefficient D_0 is assumed to have the magnitude of the solvent interdiffusion coefficient, $10^{-9}\ {}^{\mathrm{m}^2}/_{\mathrm{sec}}$. Inserting

$$\frac{R_g^2}{D_0} = \frac{(5 \cdot 10^{-9}\ \mathrm{m})^2}{10^{-9}\ {}^{\mathrm{m}^2}/_{\mathrm{sec}}} = 2.5 \cdot 10^{-8}\ \mathrm{sec} \tag{5.84}$$

into equation 5.81 yields

$$s_\chi \approx \left(\chi^{(max)} - \chi_0\right) 2.5 \cdot 10^{-8} \cdot \begin{cases} {}^1/_6\ \left(v\ {}^{\mathrm{min}}/_{\mathrm{ml}}\right)^{0.852} & \text{in the SFIMM} \\ 50\ \left(v\ {}^{\mathrm{min}}/_{\mathrm{ml}}\right)^{0.932} & \text{in the CPMM} \end{cases}. \tag{5.85}$$

A typical mean polymer concentration in the experiments from reference [23] is

$$c = 4\ \frac{\text{g polymer}}{\text{liter solvent}}.$$

If m_P denotes the total mass of the polymer in solution, V_P its total volume, and V_L the total volume of the solvents, application of

$$c = \frac{m_P}{V_L} = \rho_P \frac{V_P}{V_L} \Leftrightarrow V_P = \frac{c}{\rho_P} V_L \tag{5.86}$$

leads to

$$f_P = \frac{V_P}{V_P + V_L} = \frac{\frac{c}{\rho_P} V_L}{\frac{c}{\rho_P} V_L + V_L} = \frac{\frac{c}{\rho_P}}{1 + \frac{c}{\rho_P}}. \tag{5.87}$$

With $c = 4\ {}^{\text{g polymer}}/_{\text{liter solvent}}$ and $\rho_P = \rho_{PB} = 960\ {}^{\mathrm{kg}}/_{\mathrm{m}^3}$, it is $f_P \approx 0.004$.

Simulation results for $f_P = 0.004$, $N = 190$ and $\chi^{(max)} = 16.160$ are shown in figure 5.10 in comparison to experimental data form figure 1.3 (a). As no asymptotic regime is present in 1.3 (a), we choose a rather large $\Delta\chi^{(max)}$ to ensure that there also appears no asymptotic regime for the simulations inside the interval $v \in [0.1\ \mathrm{ml/min}, 5\ \mathrm{ml/min}]$. The simulated data points for l_1 in figure 5.10 (b) are very close to the experimental results. R underestimates particle sizes but their simulated length scales still match the experimental ones. One should also keep in mind that R exhibits a critical dependence on the threshold $\phi_P^{(th)}$ as discussed in context with the f_P-variations in subsection 5.3.3. If a smaller $\phi_P^{(th)}$ was chosen, R would be on par with l_1. Nevertheless, model I is able to reproduce appropriate scales of particle sizes for given flow rates in the CPMM. In the SFIMM the same quench rates translate into much larger flow rates exceeding the experimentally applied range. An extrapolation of l_1 to low flow rates yields particle sizes of about 150 to 200 nm and consequently overestimates the experimental data in figure 1.3 (a) by a factor of approximately 4, which is not as

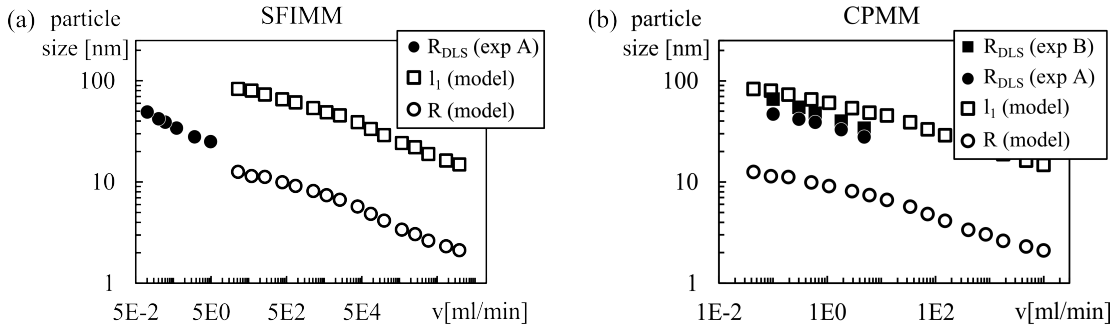

Figure 5.10: *Simulation results from model I with linear mixing profiles in direct comparison to experimental data. (a) refers to the SFIMM and (b) to the CPMM. The open symbols represent simulated droplet sizes and the solid ones label experimental data from figure 1.3 (a), where A and B denote the end groups of the polymer. Simulations are performed for quench rates* $s_\chi \in \left[10^{-6}, 0.1\right]$*, which have been translated to flow rates by means of equation 5.85. The remaining physical parameters are set to* $f_P = 0.004$*,* $N = 190$*,* $\chi^{(max)} = 16.160$*, and the numerical parameters read* $m = 256 \times 256$*,* $\Delta l = 0.25$*,* $h = 0.01$*. The threshold for binary conversion is* $\phi_P^{(th)} = 0.01$*.*

good as the agreement in the CPMM but length scales still match – especially taking into account that R_{DLS} in figure 1.3 (d) and (f), for example, also exceeds 100 nm. At this point it is emphasized that one should not be too picky about a perfect match of experimental data and simulation results since experimental *copolymer* data are compared to simulation results for *homopolymers*, material data are only roughly estimated, and mixing profiles are approximated by linear interpolations.

In the present subsection we have seen that the characteristic scaling behavior of rate-size relations from model I is clearly reflected in experimental trends and that the qualitative response to f_P- and T-variations also agrees with experiments. In addition, length scales of droplets match length scales of particles for experimentally applied flow rates, i.e. realistic mixing times. Taken together, these similarities provide strong evidence that the response of molecular assembly to solvent mixing, i.e. coupling mechanism (i) in chapter 4, is the dominant physical mechanism behind the co-solvent method, which is not only the main conclusion of the present subsection but the central result of the complete chapter. This result implies that mean field theories should be suitable frameworks to describe the co-solvent method and that statements from model I may be qualitatively transferable to experiments. The correspondence of data point progressions for homopolymers and copolymers further indicates that this mechanism might work independent of the actual polymer architecture. This is consistent with the idea that spinodal decomposition is mainly driven by unfavorable interactions between the solvent and the solvent-phobic block.

5.3.6 Effective and constant interaction parameters

All equations in subsection 5.3.4 up to 5.65 are also valid for constant interaction parameters, i.e. if $\chi(t) \equiv \chi_c$. In this case, equation 5.65 becomes

$$\Delta\chi_c := -\frac{1}{2t}\int_0^t \frac{\partial \mu_r}{\partial \phi_P}(f_P, t)\, dt = \chi_c - \chi^{(Spin)}. \tag{5.88}$$

In the same manner as before the mean droplet sizes can be estimated by $l_p = \gamma 2\pi/\sqrt{\Delta\chi_c}$.

The analogy of l_p to equation 5.67 provides $\overline{\Delta\chi}$ the interpretation of an effective quench depth in the sense that a time dependent interaction parameter produces the same mean droplet size as a constant quench depth $\Delta\chi_c = \overline{\Delta\chi}(t_{tr})$. A general discussion about the Cahn-Hilliard equation for constant interaction parameter including the perturbation treatment can be found, for example, in references [124], [158], or [159]. The present subsection restricts to a brief comparison between $\overline{\Delta\chi}$, $\Delta\chi_c$, and resulting droplet sizes. The data points in figure 5.11 (a) and (c) represent simulation results for constant interaction parameters χ_c and the corresponding prediction from the perturbation theory, $l_p = \gamma 2\pi/\sqrt{\Delta\chi_c}$, is illustrated by a straight line. Figure 5.11 looks very similar to figure 5.7, which graphically demonstrates $\overline{\Delta\chi}$'s interpretation of an effective quench depth. The relative deviation of simulation results from l_p is practically the same in both figures and implies that the perturbation theory in the time dependent case is as accurate as in the case of constant interaction parameters.

From a process technological point of view the correspondence of $\overline{\Delta\chi}$ and $\Delta\chi_c$ might be interesting because it provides two different methods to produce droplets of a specific size: either by a time dependent quench with an associated effective quench depth $\overline{\Delta\chi}(t_{tr})$ or by an instantaneous quench to $\Delta\chi_c = \overline{\Delta\chi}(t_{tr})$. The process of choice would be the one yielding lower polydispersities. Judging from figure 5.12, the relative polydispersity is almost the same in 2D. In 3D, it is about an eventually rather insignificant amount of 5 to 10 % lower for

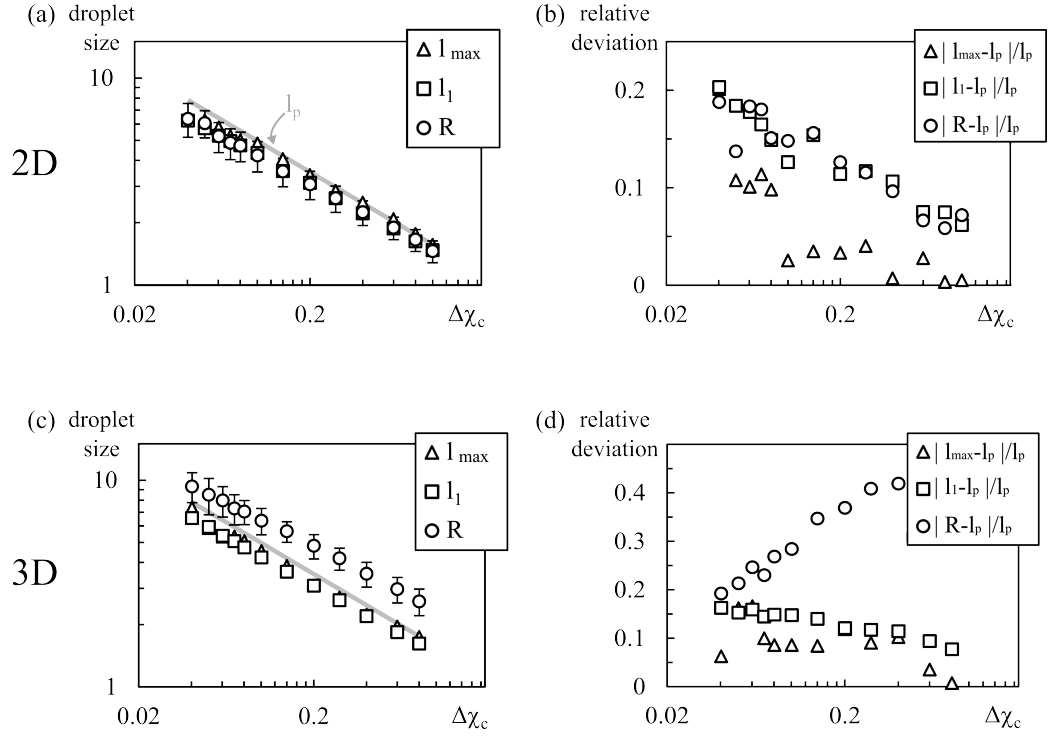

Figure 5.11: *Simulated droplet sizes in comparison to the prediction from the perturbation theory for the Cahn-Hilliard equation with constant interaction parameters χ_c. Data points in (a) are droplet sizes for instantaneous quenches with depths $\Delta\chi_c$ and the grey line represents the prediction from the perturbation theory, $l_p = \gamma 2\pi/\sqrt{\Delta\chi_c}$. (b) depicts relative deviations of simulation results from l_p. (a) and (b) refer to 2D simulations, (c) and (d) show the same in 3D. Numerical parameters, f_P, and N are identical to figure 5.3.*

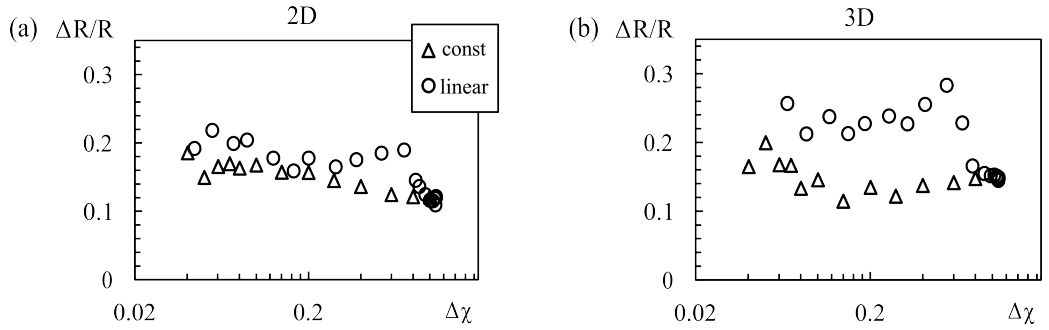

Figure 5.12: *Relative polydispersities $^{\Delta R}/_{R}$ for constant and linearly time dependent interaction parameters in two (a) and three (b) spatial dimensions. ΔR is defined by equation 5.48. Circles represent $^{\Delta R}/_{R}$ for linearly time dependent interaction parameters (cp. error bars in figure 5.7) and triangles refer to constant interaction parameters (cp. error bars in figure 5.11). $\Delta\chi$ on the horizontal axis denotes the effective quench depth $\overline{\Delta\chi}(t_{tr})$ from equation 5.66 for the circles and $\Delta\chi_c$ from equation 5.88 for the triangles.*

the instantaneous quench. Thus, not only the mean size of droplets transfers from constant to time dependent quenches but also the variance of size distributions, which is essentially the main statement of the current subsection. This close analogy between constant and linearly time dependent interaction parameters indicates that a time dependence of χ alone introduces no degree of freedom that could be used to specifically control polydispersity without affecting the mean size. The standard deviation of R is approximately fixed at $\Delta R = xR$ with a constant $x \approx 0.15 - 0.25$ according to figure 5.12.

5.3.7 Impact of numerical truncation errors

Because droplet sizes are determined close to the homogeneous state where concentration fluctuations are very small, it is justified to question the application of a first order time accurate scheme with step size $h = 0.005$ or even $h = 0.01$ like in figure 5.10. To test the expected numerical error, two simulation runs are performed for identical initial conditions in a 2D box with 400×400 grid points, a lattice constant $\Delta l = 0.75$, and a step size $h = 0.005$. Both share the physical parameters $f_P = 0.1$, $N = 14$, $\chi_0 = \chi^{(Spin)}$, and $\chi^{(max)} = 2$, but in one simulation run the first order scheme from equation 5.38 with truncation errors $\mathcal{O}(h) = \mathcal{O}(0.005)$ is used, while the second order scheme from equation 5.41 with $\mathcal{O}(h^2) = \mathcal{O}(2.5 \cdot 10^{-5})$ is applied for the other one. The resulting relative deviation of transition times and droplet sizes is shown in figure 5.13. The maximum deviation in t_{tr} is about 4 % and the deviation in particle sizes is below 0.4 %, which negligible in comparison the experimental errors. Consequently, the application of first order time accurate schemes is not expected to introduce any significant distortion of simulation results.

5.4 Rate-size relations for the SFIMM- and CPMM-profiles

Equation 5.21, $\chi(t) = \chi_{GS} + {}^{(\chi_{SS}-\chi_{GS})}/_{(1-f_P)}\,\varphi_{SS}(t)$, takes the role of a coupling interface between droplet formation on the nanometer scale and solvent mixing which is determined by mixer geometries on millimeter scales or above. Within the multiscale approach from chapter

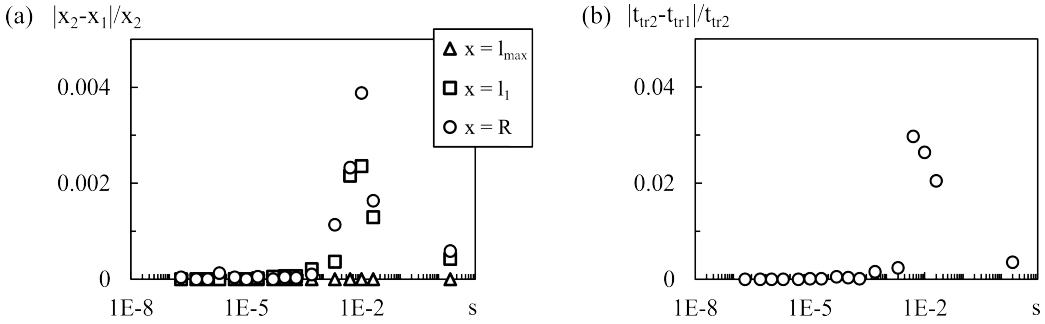

Figure 5.13: *Relative deviations that are caused by temporal truncation errors of applied numerical integration schemes. (a) shows deviations of particle sizes and (b) illustrates deviations of t_{tr}. x_i refers to quantity x calculated by the i-th order time accurate integration scheme (cp. equations 5.38 and 5.41).*

4, $\varphi_{SS}(t)$ may represent the mean selective solvent volume fraction inside a fluid element. In the present section we insert the theoretical descriptions of solvent mixing from chapter 3 into equation 5.21 and compare resulting rate-size relations to the experimental data for the SFIMM and the CPMM.

Formulas to calculate the number concentration of solvents $c(x(t), t)$ in fluid elements are listed in tables 3.1 and 3.2 for the SFIMM and the CPMM, respectively. The concentrations are converted to volume fractions φ_{SS} by multiplication with the molecular volume ν of the selective solvent. As already addressed in figure 5.9, multiplying $c(x, t)$ in table 3.1 and 3.2 with ν is formally equivalent to a substitution of the symbol c by φ_{SS}. As a quick reminder, x is the coordinate perpendicular to stream lines in a Lagrangian frame of reference and will be referred to as *lamella position* in the following. In chapter 3, t denoted the real time in seconds that passed since a fluid element had entered the mixer. To prevent confusion we are going to denote this time t' because in the present chapter the symbol t is already taken by the dimensionless system time in the dynamical equation 5.18. $c(x(t'), t')$ is expressed in terms of that dimensionless time by setting $t' = t_0\,(t + t_s)$, where t_0 is the time scale as usual. t_s introduces an appropriate shift of origins: as in case of linear mixing profiles we identify $t = 0$ with the time when the system crosses the spinodal line, i.e. $\chi(t = 0) = \chi^{(Spin)}$ with $\chi^{(Spin)}$ from equation 5.19. Via equation 5.21 each $\chi^{(Spin)}$ can be assigned a spinodal solvent composition $\varphi_{SS}(t = 0) \coloneqq \varphi_{Spin}$. As a result, t_s which is implicitly given by

$$\varphi_{Spin} = \nu\, c(x(t_0 t_s), t_0 t_s) \tag{5.89}$$

is the dimensionless time elapsed until the selective solvent volume fraction inside a fluid element is large enough to trigger spinodal decomposition. t_s will be called *spinodal time shift*. In our simulations t_s is calculated numerically with a bisection method from equation 5.89. In summary, the mixing profiles in the present section are given by

$$\varphi_{SS}(t) = \nu\, c\left(x(t'(t)), t'(t)\right) \text{ with } t'(t) = t_0\,(t + t_s) \tag{5.90}$$

and the number concentrations $c(x(t'), t')$ from tables 3.1 and 3.2.

Since mixer geometries are fixed as listed in table 3.1 (SFIMM) and shown in figure 3.6

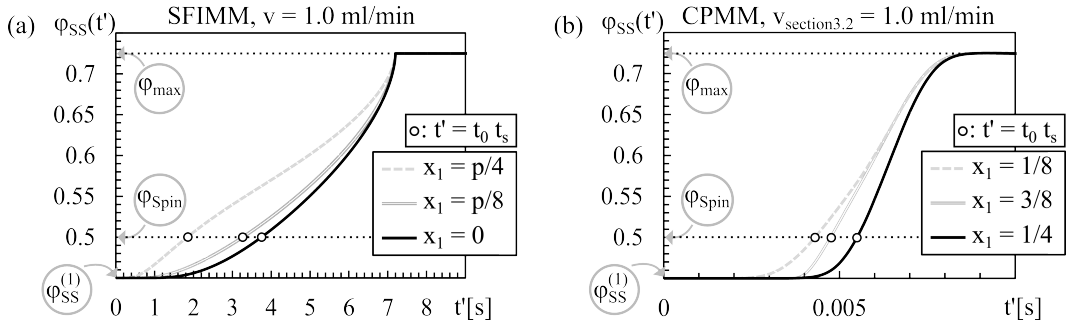

Figure 5.14: *Mixing profiles in the SFIMM (a) and CPMM (b) at a fixed flow rate v. To keep the notation concise, the vertical axis is labeled by $\varphi_{SS}(t')$, which is defined by $\varphi_{SS}(t') \coloneqq \varphi_{SS}(t(t')) = \nu c(x(t'), t')$ in accordance with equation 5.90. $\varphi_{SS}(t')$ represents the selective solvent volume fraction inside a fluid element and the curve arrays inside the diagrams are generated by different initial lamella positions x_1 as shown in the respective legend. In the SFIMM $x_1 = 0$ corresponds to a fluid element that travels along the center of a polymer containing good solvent lamella. Its mixing profile is illustrated by the black line in (a), which is identical to the one from figure 3.3 (b). Setting $x_1 = p/8$ and $x_1 = p/4$ puts the fluid element further towards a selective solvent lamella and 'flattens' the ascending part of a mixing profile. p denotes the initial lamella width at the entrance of the SFIMM where the edge of the good solvent lamella is located at $x_1 = \pm p/2$. Due to symmetry the profiles for $x_1 = -p/8, -p/4$ coincide with the ones from $x_1 = p/8, p/4$, so it is sufficient to consider only positive values of x_1 during simulations. In the CPMM $x_1 = 1/4$ (black line in (b)) is associated with a fluid element traveling in the center of a good solvent lamella with a trajectory as indicated by the open circle in figure 3.7 (a). The black line coincides with the black line in figure 3.7 (b). $x_1 = 1/8$ is closer to the selective solvent lamella, which is located at negative x-values, and $x_1 = 3/8$ is associated with a position further towards the channel wall. A shift $x_1 = 1/4 \mapsto x_1 = 1/8$ of the initial lamella position towards the selective solvent lamella flattens the ascent of the mixing profile as in the SFIMM. The reason why the profile of $x_1 = 3/8$ is also flattened in comparison to $x_1 = 1/4$ is because the channel wall in the first repeat unit is replaced by a selective solvent lamella in the second one. $\varphi_{SS}^{(1)}$ represents the premixed selective solvent volume fraction within a fluid element, φ_{max} its maximum amount, and φ_{Spin} the spinodal composition. The open circles indicate the spinodal time shift t_s and also correspond to the origin of the system time, i.e. they label $t = 0$ for each mixing profile. In both mixers, mixing profiles are completely characterized by v, x_1, $\varphi_{SS}^{(1)}$, and φ_{max}.*

(CPMM), associated mixing profiles introduce the flow rate v, the initial lamella position x_1, the premixed selective solvent volume fraction inside a fluid element $\varphi_{SS}^{(1)} = \nu\, c^{(1)}$, and the premixed selective solvent volume fraction in a solvent lamella $\varphi_{SS}^{(2)} = \nu\, c^{(2)}$ as adjustable parameters. It is convenient to substitute $\varphi_{SS}^{(2)}$ by φ_{max} via

$$\varphi_{max} = \frac{\varphi_{SS}^{(1)} + \varphi_{SS}^{(2)}}{2}. \tag{5.91}$$

φ_{max} denotes the maximum selective solvent volume fraction inside a fluid element and in contrast to $\varphi_{SS}^{(2)}$, it can be directly read from a mixing profile as it is the value that is approximated at $t \to \infty$. The dependence of φ_{max} on $\varphi_{SS}^{(1)}$ and $\varphi_{SS}^{(2)}$ follows from the formulas in tables 3.1 and 3.2. The lower panel of figure 3.3 and figure 3.7 (b) display examples for the mixing profiles $c = \varphi_{SS}/\nu$ at one single initial lamella position. In a mixer there should be a multitude of fluid elements that travel simultaneously at different lamella positions, so

a description of the particle size distribution at the output of a mixer involves averaging over different x_1 for fixed remaining parameters. Figure 5.14 exemplarily illustrates the impact of varying initial lamella positions x_1 and graphically summarizes the independent parameters introduced by the mixing profiles. In the previous section the time scale t_0 could be absorbed into the quench rate due to the linearity of φ_{SS} in t. Such a simplification is not possible in the present case, so t_0 is another parameter that needs to be specified before each simulation run. Although the spinodal time shift t_s is also introduced as a new variable, it depends on the remaining quantities according to equation 5.89 and contributes no additional degree of freedom. The flow rate v takes the role of a quench rate because it affects mixing times as discussed in the context of figures 3.3 and 3.7. Hence, in the remainder of section 5.4 the term rate-size relation refers to the dependence of droplet sizes on flow rates.

When examining rate-size relations, it is convenient to express the Flory-Huggins interaction parameters χ_{GS} and χ_{SS} in equation 5.21 through 'distinctive quantities' that can be directly related to mixing profiles or rate-size relations. In the present case these distinctive quantities are the spinodal composition φ_{Spin} and the maximum interaction parameter $\chi^{(max)}$. Inserting $t = 0$ into equation 5.21 yields

$$\chi^{(Spin)} = \chi(0) = \chi_{GS} + \frac{\chi_{SS} - \chi_{GS}}{1 - f_P}\varphi_{Spin}, \tag{5.92}$$

and φ_{max} can be used to define

$$\chi^{(max)} = \chi_{GS} + \frac{\chi_{SS} - \chi_{GS}}{1 - f_P}\varphi_{max}. \tag{5.93}$$

Rearranging equations 5.92 and 5.93 leads to

$$\chi_{SS} = \chi_{GS} + \left(\chi^{(Spin)} - \chi_{GS}\right)\frac{1 - f_P}{\varphi_{Spin}} \tag{5.94}$$

and

$$\chi_{GS} = \frac{\varphi_{Spin}\chi^{(max)} - \varphi_{max}\chi^{(Spin)}}{\varphi_{Spin} - \varphi_{max}}. \tag{5.95}$$

A translation of χ_{GS} and χ_{SS} into φ_{Spin} and $\chi^{(max)}$ is reasonable because the interaction parameters between the polymer and the solvents were not measured by references [22], [23], or [36], but as the polymer solution is reported to tarnish rapidly at a water volume fraction of approximately 0.5 in titration experiments [22], we know that $\varphi_{Spin} \approx 0.5$. $\chi^{(max)}$ may be estimated by the placement of an experimentally measured asymptote via the relation $l_p(s \to \infty) = {}^{0.5\pi}/\sqrt{\chi^{(max)} - \chi^{(Spin)}}$. So unknown material data is translated into data that can be directly related to measurements – assuming a linear interpolation of χ-parameters in compositions φ_{SS} like in equation 5.21 and provided that the asymptotic regimes in the phase field model and Molecular Dynamics are identical, e.g. at high pH.

5.4.1 Simulation setup

The set of numerical parameters from subsection 5.3.1 remains unchanged. We restrict to two spatial dimensions because figure 5.3 indicates that dimensionality is unimportant, and use $m = 400 \times 400$ grid points with a lattice constant $\Delta l = 0.5$. Since temporal truncation

errors appeared to be negligible in subsection 5.3.7, the initial time step is increased to $h = 0.025$ in order to compensate for large mixing times signaled by figure 5.14 (a). Again, all data points represent averages over 5 independent simulation runs with different uniformly distributed random initial conditions $\phi_P^{(0)}(\vec{r}_s) \in [f_P - 0.001, f_P + 0.001] \; \forall \, s = 0, ..., m-1$. Like in subsection 5.3.5, the horizontal axes of all diagrams where the CPMM is considered show the total flow rate $v = 2\, v_{\text{section3.2}}$.

If SFIMM- or CPMM-mixing profiles are applied, the physical input parameters of model I become

- the mean polymer volume fraction f_P,
- the number of segments per polymer molecule N,
- the maximum quench depth $\chi^{(max)}$,
- the time scale t_0,
- the premixed selective solvent volume fraction $\varphi_{SS}^{(1)}$,
- the maximum selective solvent volume fraction φ_{max},
- the flow rate v,
- the initial lamella position x_1, and
- the spinodal composition φ_{Spin}.

In the present section the first three parameters are fixed at

$$f_P = 0.1,\ N = 14, \text{ and } \chi^{(max)} = 2,$$

except for subsection 5.4.2 B). The time scale is set to $t_0 = 10^{-6}$ seconds, which corresponds to a polymer with a radius of gyration $R_g = 10$ nm and a segment diffusion coefficient $D_0 = 10^{-9}\,\mathrm{m^2/sec}$. R_g and D_0 should represent the scales of values belonging to the polymer utilized in the experiments (cp. subsection 5.3.5). To account for a 50/50 % mixture of tetrahydrofuran and water before polymer addition like in figure 1.3 (a) and (b), we set $\varphi_{SS}^{(1)} = {}^{(1-f_P)}/_2 = 0.450$. Since the selective solvent lamella contains only selective solvent when fluid elements enter a mixer, it is $\varphi_{SS}^{(2)} = 1$ or equivalently $\varphi_{max} = {}^{(1+\varphi_{SS}^{(1)})}/_2 = 0.725$. Flow rates, initial lamella positions, and spinodal compositions are variable.

5.4.2 Simulation results and comparison to experiments

a) Length scales and qualitative progression of rate-size relations

Initially, the spinodal composition is set to $\varphi_{Spin} = 0.5$, which is slightly larger than $\varphi_{SS}^{(1)} = 0.45$, to imitate the experimental observation that the initial solution tarnished in titration experiments if only a slight amount of water was added. Figure 5.15 depicts corresponding rate-size relations. It provides two major statements.

First, droplet sizes still match experimentally observed lengths scales of particle radii for realistic time scales of mixing at $v \in [0.1\ \mathrm{ml/min}, 5\ \mathrm{ml/min}]$. In the SFIMM droplet sizes decrease from about $10R_g$ to $4R_g$. In the CPMM they are generally smaller and fall from

approximately $4R_g$ to $2R_g$, but in both cases their scales match R_{DLS} in figure 1.3 if $R_g \approx 5 - 10$ nm. Second, the scaling law in the non-asymptotic regime is evidently a universal characteristic only if linear mixing profiles are applied, since simulation results for the SFIMM in (c) clearly possess a hitherto undefined progression. That being said, it is particularly remarkable that rate-size relations for the CPMM in (d) are in exceptionally good agreement with the experimental results as they do exhibit an approximate scaling behavior with an exponent of -0.16 just like in the case of linear mixing profiles. On the one hand the susceptibility of rate-size relations to the functional form of $\varphi_{SS}(t)$ is welcome because it equips model I with a degree of freedom to eventually capture potential deviations from the scaling behavior $R \propto v^{-\alpha}$ that might arise under certain experimental conditions. On the other hand the observation is unwelcome since the mixing profiles from chapter 3 are constructed to represent the experimental conditions in figure 1.3, and thus the SFIMM profile should also reproduce progressions like the CPMM profile in order to agree with experiments. The trend line for R in figure 5.15 (c) is not supposed to be the best fit to the data but to give an impression of its mean trend if a scaling law is used as an approximation. The resulting exponent reads -0.133, which is still very close to the experimental values.

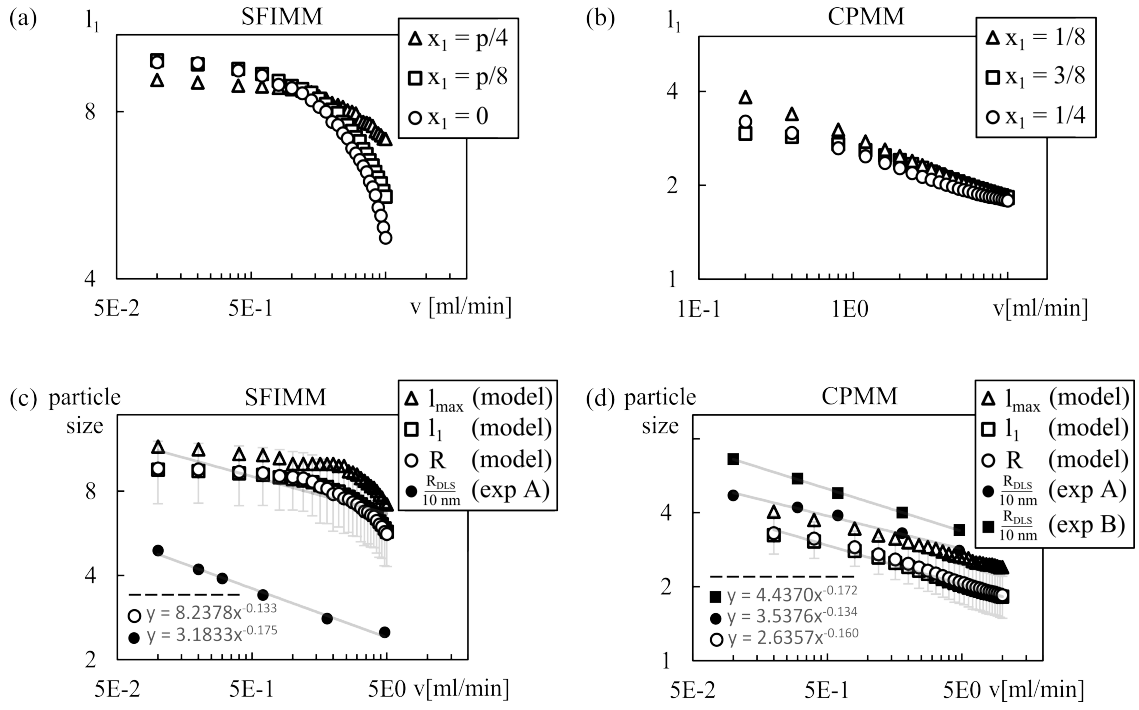

Figure 5.15: *Simulated droplet sizes from model I with SFIMM- and CPMM-mixing profiles in comparison to experimental results. In (a) and (b) l_1 is plotted against the flow rate v for different x_1 to demonstrate the effect of varying initial lamella positions. Results for R and l_{max} look similar and are omitted for the sake of clarity. The data points in (c) and (d) represent the mean over the x_1-vales from (a) and (b). The error bars indicate the averaged polydispersity ΔR from equation 5.48. The statistical standard deviation over different simulation runs is not shown because it is practically as small as in figure 5.3. For comparison, the solid black symbols in (c) and (d) show the respective experimental data from figure 1.3 (a), divided by an assumed radius of gyration of $R_g = 10$ nm. Solid grey lines are regression lines to R and the corresponding trend line equations are shown below the dashed horizontal lines.*

Thus, the mixing profile of the SFIMM might generate wrong data progressions but it is still able to reproduce the 'mean general trend'.

To rationalize the discrepancies between rate-size relations in the SFIMM and the CPMM the duration of spinodal decomposition is correlated to mixing profiles by considering $\varphi_{SS}(t_{tr})$ as shown in figure 5.16. Because a variation of x_1 does not dramatically change the course of graphs in figure 5.15 (a) or (b), the consideration is restricted to the middle of a polymer lamella, i.e. to $x_1 = 0$ in the SFIMM and $x_1 = 1/4$ in the CPMM. Figure 5.16 (a) demonstrates that $\varphi_{SS}(t_{tr})$ responds completely different to an increase of flow rates in both mixers. In the CPMM it covers the whole range $[\varphi_{Spin}, \varphi_{max}]$ for $v \in [0.1\ \text{ml/min}, 5\ \text{ml/min}]$ whereas it remains very close to φ_{Spin} in the SFIMM. This already explains why the mean droplet radii in the SFIMM are larger compared to the CPMM. Lower $\varphi_{SS}(t_{tr})$ translate into smaller $\chi(t_{tr})$, which in turn leads to larger droplets, since $\chi(t)$ remains closer to $\chi^{(Spin)}$ for a longer time span. The resemblance of $\varphi_{SS}(t_{tr})$ in the CPMM and the linear case, which is shown in figure 5.16 (b), might be the reason why both mixing profiles share a common scaling law for droplet sizes and why a substitution of the CPMM-profile by a linear interpolation does not change the principle behavior of rate-size relations (cp. figure 5.10 (b) and 5.15 (d)). That solvent compositions in the SFIMM remain close to φ_{Spin} indicates that particle sizes only depend on local conditions of the mixing profile close to the spinodal line, i.e. close to the open circles shown in figure 5.15 (a).

This motivates analyzing how a shift of φ_{Spin} changes rate-size relations and if it is possible to recover a scaling law in the SFIMM by such shifts. l_1 at different φ_{Spin} is illustrated in figure 5.17. Increasing φ_{Spin} reveals the asymptotic regime for the SFIMM at flow rates close to $v = 5.0$ ml/min as depicted by figure 5.17 (a) and the steep descent to the left of that regime is caused by the fluid element crossing the focusing point. Variations of φ_{Spin} apparently do not lead to scaling laws and in fact, increasing the spinodal composition results in significant deviations of the mean trend with exponent -0.133 from figure 5.15 (a), which is represented by the grey trend line. Accelerating mixing in the SFIMM relative to phase separation by increasing t_0 or decreasing f_P so that $\varphi_{SS}(t_{tr})$ in figure 5.16 covers the whole range $[\varphi_{Spin}, \varphi_{max}]$ would not reproduce a scaling law either (according simulation results

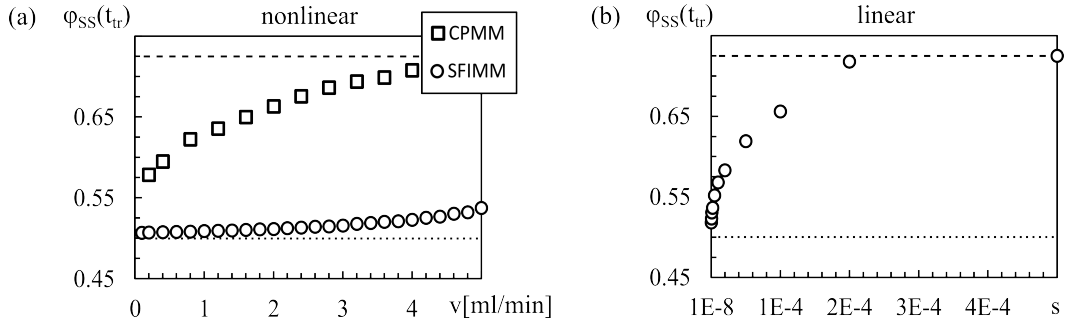

Figure 5.16: *Compilation of $\varphi_{SS}(t_{tr})$ for all mixing profiles. (a) shows $\varphi_{SS}(t_{tr})$ at $x_1 = 0$ in the SFIMM (circles) and $x_1 = 1/4$ in the CPMM (squares). The transition times t_{tr} are taken from the simulations which were used to generate figure 5.15. (b) depicts the same for linear mixing profiles. The corresponding transition times are taken from figure 5.3 in 2D, and s is the slope of the selective solvent volume fraction from equation 5.43. The dashed horizontal lines label φ_{max} and the dotted lines φ_{Spin}.*

are not shown).

If the scaling law cannot be obtained by parameter variations, there remain the following reasons why the SFIMM mixing profile does not produce the experimentally observed scaling behavior:

- the underlying mechanism that controls droplet sizes might be different from section 5.3 (checked in subsection 5.4.3),
- φ_{SS} can principally reproduce the scaling behavior but the implementation of solvent mixing by time dependent interaction parameters distorts rate-size relations (checked in section 6.4),
- φ_{SS} can principally reproduce the scaling behavior but the restriction to homopolymers distorts rate-size relations (checked in section 8.2), or
- φ_{SS} per se contains an assumption about solvent mixing that distorts the progression of rate-size relations regardless of the implementation of solvent mixing and polymer architecture.

As indicated by the brackets in the above list, we are going to check the first three possibilities in the present work. It eventually will turn out that in all cases rate-size relations in the SFIMM look very similar to the ones in the current section. So to reproduce experimental trends, the SFIMM profile itself needs to be revised quite probably. This revision could include the consideration of Taylor dispersion or secondary flows in z-direction that are induced by the hydrodynamic focusing in combination with flow sharing or lamella tilting. To some degree, these 'secondary' effects appear in the CPMM as well, but in the SFIMM their contribution to real solvent mixing might be larger, since the 'primary' diffusion across lamella interfaces in x-direction is considerably slower than in the CPMM (cp. the t'-axes in figure 5.14). In any case we refrain from an appropriate revision of SFIMM-profiles, because the present work focuses on more general aspects of controlled assembly. The revision is a highly specific topic as only the description of one single mixer would benefit from it.

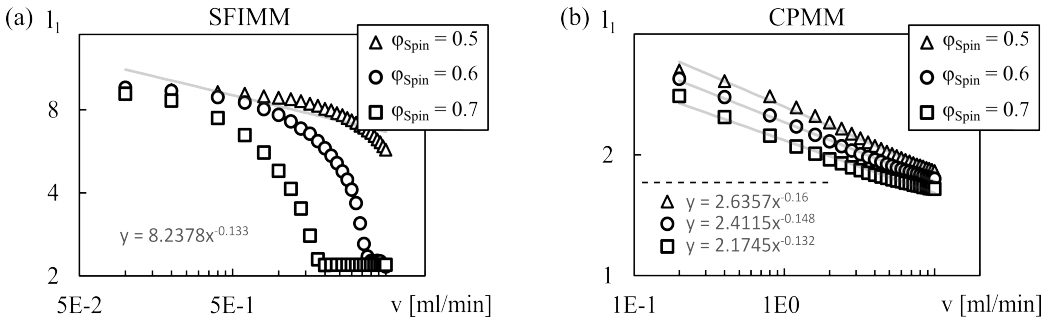

Figure 5.17: *Response of rate-size relations to variations of φ_{Spin} with SFIMM- (a) and CPMM-mixing profiles (b). Data points are averaged over the same initial lamella positions as in figure 5.15. Due to the similarity of simulation results for R, l_1 and l_{max}, again only l_1 is depicted as a representative. The triangles in this figure label the same data as the squares in figure 5.15 (c) and (d), and the grey lines are regression lines.*

b) Parameter variations in the CPMM

Since the qualitative progression of rate-size relations for the CPMM profile agrees with the experimentally observed scaling behavior, it is further tested whether the responses to variations in temperature and mean polymer volume fraction are also consistent.

The interaction parameters $\chi_{GS} = \chi_{GS}^{(0)} + \alpha_{GS}/T$ and $\chi_{SS} = \chi_{SS}^{(0)} + \alpha_{SS}/T$ are contained in φ_{Spin} and $\chi^{(max)}$. So as long as no asymptotic regime appears for $v \in [0.1\ \text{ml/min}, 10\ \text{ml/min}]$, a temperature variation corresponds to a change of the spinodal composition according to equation 5.92. If φ_{Spin} increases or decreases with increasing T depends on α_{GS} and α_{SS} just like in the case of linear mixing profiles, and a direct comparison to experimental results is again not possible because neither α was measured. The experimentally observed vertical shift of rate-size relations for varying temperature (i.e. varying φ_{Spin}) and an accompanied change of the exponent from figure 1.3 (d) is, however, reflected in figure 5.17 (b). How rate-size relations for the CPMM profile respond to changes in the mean polymer volume fraction f_P is displayed in figure 5.18 (a). Droplet sizes decrease with diminishing f_P, and in accordance to figure 1.3 (c), the exponent decreases as well.

In the present subsection we showed that model I reproduces the experimental observations from figure 1.3 qualitatively if we employ the CPMM-mixing profile by Schoenfeld et al. [118]. This agreement indicates that the concept of fluid elements should be a promising and computationally very efficient multiscale approach to describe size-controlled assembly in consideration of mixer geometries. Consequently, φ_{SS} may indeed be used as a coupling interface to incorporate different micromixer types, i.e. micromixer geometries, into model I. We believe this conclusion can be drawn despite the disagreement in the SFIMM since the discrepancies are most likely caused by the SFIMM profile itself and not simplifications

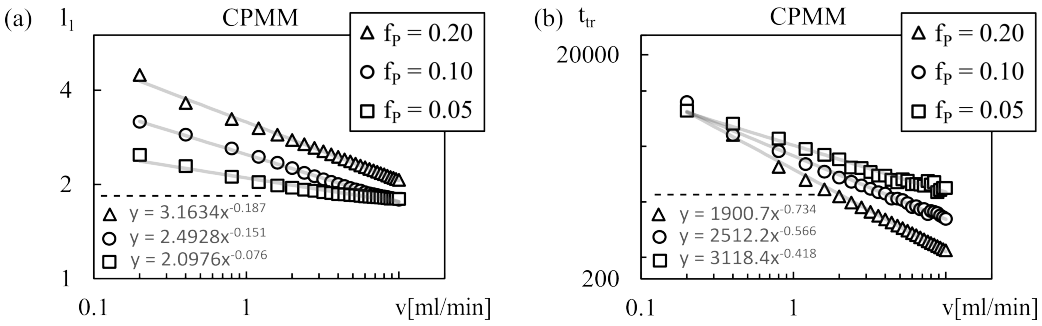

Figure 5.18: *Simulation results from model I with the CPMM mixing profile at $x_1 = 1/4$ and different mean polymer volume fractions f_P. (a) shows the response of rate-size relations to f_P-variations. Grey lines are regression lines and the corresponding trend line equations are shown beneath the dashed horizontal line. The change in exponents that did not occur for linear mixing profiles originates from different $\varphi_{SS}^{(1)} = (1-f_P)/2$ and φ_{Spin}, because the section of a mixing profile that affects spinodal decomposition varies with their values. While changing f_P, we kept χ_{GS} and χ_{GS} constant just like in the upper panel of figure 5.5, and used the same values as there. For given χ_{GS} and χ_{SS}, φ_{Spin} and $\chi^{(max)}$ can be calculated from equations 5.92 and 5.93. For $f_P = 0.05$ it is $\varphi_{Spin} = 0.599$, for $f_P = 0.1$ it is $\varphi_{Spin} = 0.5$, and for $f_P = 0.2$ it is $\varphi_{Spin} = 0.424$. Hitherto not mentioned physical input parameters are still $N = 14$, $t_0 = 10^{-6}$ sec, and $\varphi_{max} = (\varphi_{SS}^{(1)}+1)/2$. (b) depicts transition times and indicates that larger droplets are generated for faster phase separation dynamics. This is consistent with equation 5.75 stating that larger droplets are generated by a larger mobility.*

specific to model I.

5.4.3 Perturbation theory

To examine whether the interpretation of the underlying mechanism from section 5.3 still holds true for the SFIMM profiles, a perturbation theory is applied. The starting point is again equation 5.65, which reads

$$\overline{\Delta\chi}(t_{tr}) = \frac{1}{t_{tr}}\int_0^{t_{tr}} \left[\chi(\tau) - \chi^{(Spin)}\right] d\tau = \frac{1}{t_{tr}}\int_0^{t_{tr}} \left[\chi_{GS} + \frac{\chi_{SS}-\chi_{GS}}{1-f_P}\varphi_{SS}(\tau)\right] d\tau - \chi^{(Spin)}$$

$$= \left(\chi_{GS} - \chi^{(Spin)}\right) + \frac{\chi_{SS}-\chi_{GS}}{1-f_P}\frac{1}{t_{tr}}\int_0^{t_{tr}} \varphi_{SS}(\tau)\, d\tau. \tag{5.96}$$

φ_{SS} is easily integrated analytically, but to obtain the value of the integral we wrote a Mathematica script to perform the summation in the Fourier series in table 3.1. Like for linear mixing profiles the droplet size from the perturbation theory is estimated by $l_p(t_{tr}) = \gamma^{2\pi}/\sqrt{\overline{\Delta\chi}(t_{tr})}$ with $\gamma = 1/4$. Figure 5.19 demonstrates that simulation results can be approximated by the perturbation theory, i.e. the droplet size is still determined during the early stages of phase separation and the interpretation from linear profiles transfers to nonlinear profiles. This also implies that it is possible to define effective constant interaction parameters in micro mixers and that the flow rate introduces no degree of freedom to control polydispersities just like

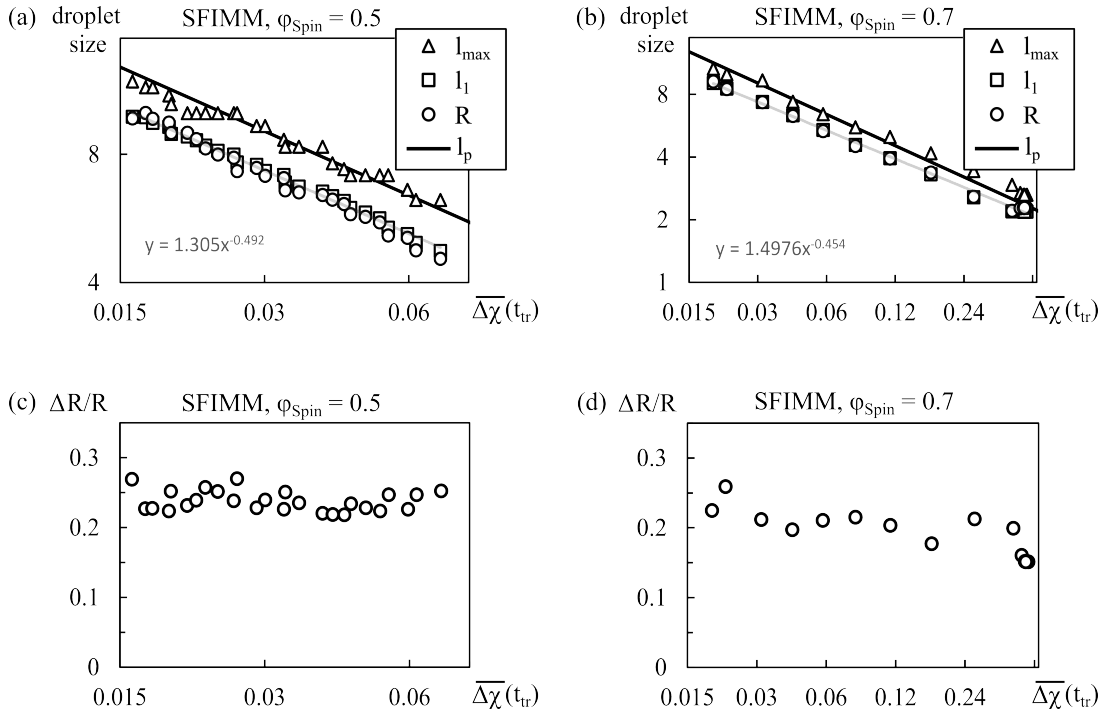

Figure 5.19: *Simulation results for the SFIMM from figure 5.17 in comparison to the result from the perturbation theory $l_p(t_{tr}) = \gamma^{2\pi}/\sqrt{\overline{\Delta\chi}(t_{tr})}$. As an example the data for two spinodal compositions is shown. (a) refers to $\varphi_{Spin} = 0.5$ and (b) to $\varphi_{Spin} = 0.7$. $\overline{\Delta\chi}(t_{tr})$ is defined by equation 5.96. (c) and (d) depict the respective relative polydispersities $^{\Delta R}/_{R}$ with ΔR defined by equation 5.48. Grey lines are regression lines to R and as for linear profiles, the slope of the regression lines is close to $-1/2$.*

the slope of linear mixing profiles. Similar to figure 5.12 the polydispersity is $\Delta R \approx x \cdot R$ with $x = 0.15 - 0.25$.

5.5 Chapter summary and main conclusions

In the present chapter the Cahn-Hilliard equation is applied to describe spinodal decomposition in an incompressible two-component canonical ensemble with a Flory-Huggins-de Gennes free energy functional for homopolymer solutions. Solvent mixing is modeled by a time dependent Flory-Huggins interaction parameter $\chi(t)$, which is assumed to depend linearly on the selective solvent volume fraction as given in equation 5.21. This description is called model I, and it is only able to capture coupling mechanism (i) from chapter 4 (see page 50) with a simplified implementation of solvent mixing.[4] The very first structures of well defined shape that emerge during spinodal decomposition are introduced as *droplets* and the dependence of droplet size on either the quench rate s_χ or the flow rate v is referred to as a *rate-size relation*.

In subsection 5.3.3 rate-size relations for linear mixing profiles are compared to results from Molecular Dynamics simulations [35], where solvent mixing is implemented similarly to model I by linearly time dependent solvent-monomer interaction potentials. In contrast to phase field models, Molecular Dynamics accurately describes the complete particle growth process but the qualitative comparison shows a good agreement, which eventually implies the identification of droplets with stable homopolymer nanoparticles. The identification of droplets as particles is further supported by the Molecular Dynamics model itself since the insensitivity of particle sizes to the ζ-potential in the non-asymptotic regime hints at an insignificant collision-coagulation growth. This means that model I is on par with much more complex particle models as far as rate-size relations are concerned. As a consequence, both models can be viewed as alternative descriptions with respective advantages. An advantage of the Molecular Dynamics model is, of course, its accuracy whereas two advantages of model I are its accessible mathematical structure and its computational efficiency. The accessible mathematical structure enables an analytically solvable perturbation theory and the perturbation approximation to droplet sizes in subsection 5.3.4 shows a good agreement with simulation results. Therefore, the analytical theory gains central importance because it directly shows that the origination of the scaling behavior in rate-size relations is a synergy of interfacial tension with the time dependent repulsion of chemical components in the weak segregation regime. It also predicts a theoretical exponent $-1/6$, which is independent of physical parameters and is also reflected in the results from the Molecular Dynamics simulations.

After discussing its properties from a theoretical perspective, we collected evidence that mechanism (i) – or more precisely, model I – is capable of reproducing experimental observations. An important criterion at investigating whether a certain physical mechanism may contribute to a phenomenon observed in experiments is the relation of inherent scales of the mechanism to experimentally relevant scales. In this case, the experimentally observed phenomenon is the particle size dependence in figure 1.3, relevant length scales are given by measured particle sizes, and relevant time scales are set by mixing times or flow rates. If time scales of spinodal decomposition, for instance, were much lower than mixing times in

[4] Mean field theories lack Brownian motion of droplets and the concomitant collision-induced coagulation in the late stages of particle growth.

the micromixers, mechanism (i) would most likely not be contributing to controlled assembly, since molecular organization would be too fast to be significantly affected by solvent mixing. A similar conclusion could be drawn if length scales of droplet sizes did not match particle sizes. Such a direct comparison to experimentally relevant scales is only possible because the computational efficiency of model I allows to simulate realistic mixing times, which go beyond the scope of Molecular Dynamics simulations. Subsections 5.3.5 (cp. figure 5.10) and 5.4.2 (cp. figure 5.15) indicate a match of scales. They confirm that length scales of simulated droplet sizes for realistic flow rates agree with experimental particle sizes. The s_χ-dependence of the transition time in figure 5.3 or its v-dependence in figure 5.18 further state that the time scale of spinodal decomposition is actually dictated by the mixing time. Despite the apparently simple description of solvent mixing, characteristic scaling laws very similar to the one predicted by model I are also present in the experimental data from figure 1.3 (the mean value of all measurements is $\bar{\alpha} \approx -0.158$), and model I additionally reproduces experimentally observed responses to variations in temperature and mean polymer volume fraction qualitatively.

Taken together, the fact that droplets can be identified with stable particles and the striking qualitative similarity of rate-size relations to experimental data provide strong evidence that coupling mechanism (i) does not only contribute to size-controlled assembly but is the dominating determinant of particle sizes. This is the most important conclusion of the present chapter. As a consequence, the perturbation theory provides an analytical explanation to the fundamental working principle of the co-solvent method. The accordance of simulated homopolymer data and experimentally measured copolymer data further suggests that, in principle, the co-solvent method might work independently from polymer architecture. Subsection 5.3.6 implies that mechanism (i) does not allow to control the polydispersity of size distributions without changing the mean size of droplets.

Section 5.4 shows that the typical scaling behavior can be broken by applying particular non-linear mixing profiles: while the CPMM-profile reproduces the scaling laws really well, the SFIMM-profile does not. Since the deviation from the experimentally observed scaling law in the SFIMM was discussed to be caused most likely by the functional form of φ_{SS} and not by simplifications specific to model I, the agreement to experimental observations for the CPMM-profile indicates that embedding particle growth into fluid elements should be a promising multiscale approach to describe controlled assembly under experimental conditions in different mixers. The possibility to algebraically couple analytically calculated volume fraction evolutions inside fluid elements into $\chi(t)$ completely avoids any computational and numerical difficulties associated with the different length scales of particle sizes and mixer geometries.

Scaling laws $l \propto \alpha^{-1/6}$ were also found in a recent publication by Schaefer et al. [160], who considered the structuring of polymer solutions in the spinodal area upon solvent evaporation. Here, l is a typical structure size and α a constant evaporation rate. The authors added α as a source term in a Cahn-Hilliard-Cook equation. Within a typical 'Flory-Huggins'-phase diagram with axes f_P and χ, they advance into the spinodal area in the f_P-direction, while we move in the χ-direction. The fact that both processes yield the same scaling behavior could imply that it could just depend on the distance to the spinodal line independent of the direction in the f_P-χ-plane. Thus, taking into account a loss of polymer in fluid elements by a source term and giving up the assumption of conserved polymer content might leave

the scaling behavior unaffected. Testing this presumption could be subject to future work. Exponents close to $-1/6$ also indicate that particle sizes are determined most probably during liquid-liquid demixing where crystallization and solidification effects can be neglected. Recent experiments on semi-crystalline copolymers have shown that the effect of solvent exchange (in this case, solvent evaporation) on the dynamics is very different if demixing interferes with solidification [161]. For example, the characteristic length scales of the resulting structures no longer depend on the solvent evaporation rate, and the experiments can be described within a model based on homogeneous nucleation theory.

Chapter 6

Model II: Time dependent chemical potentials in an effective two-component semi-grand canonical ensemble

The time dependent interaction parameters from chapter 5 correspond to a complete replacement of one single solvent at each time step. Such an implementation of solvent mixing was designed as a simple and in terms of computation efficiently implementable thought experiment to study principle relations on realistic time scales of mixing with the objective to develop a basic understanding of size-controlled assembly. However, the $\vec{r}$-independent global change of χ in model I does not describe solvent quality distributions correctly. In real mixtures the concentration of good or selective solvent at position $\vec{r}$ depends on local polymer concentrations because polymer repels selective solvent and may attract the good one. The resulting independent motion of both solvents leads to unequal solvent mixture compositions at different $\vec{r}$, meaning that the solvent quality for the polymer varies in space. Since the solvent quality determines droplet sizes, its spatial variation is very likely to affect rate-size relations.

In this chapter the description of solvent mixing is refined. The standard way to describe an independent motion of the two solvents would be based on three-component systems where the temporal evolution was described by three dynamical equations as given by equation 2.12, for example, where α is replaced by indices for the polymer, the good solvent, and the poor or selective solvent. The straightforward and probably most accurate implementation of solvent mixing into such a three-component model would be the computationally unfeasible direct numerical simulation of the complete mixer geometry. All other implementations involve more or less simplifications regarding, for instance, solvent fluxes over boundaries of a fluid element. The effect of such simplifications on rate-size relations cannot be foreseen, since we learned in section 5.4 that their characteristic attribution is sensitive to the implementation of solvent mixing. So in case of an easily conceivable oversimplification, the agreement to experimentally observed trends, e.g. the scaling behavior, might be even worse than in model I. Consequently, the construction of a system with three evolution equations and a suitable but simplified implementation of solvent mixing is of course possible and reasonable in general, but from the knowledge gained in chapter 5, constructing such a description appears as a 'step aside' rather than a 'step forward' in the line of argumentation in the present work – meaning we could build another model with three dynamical equations, but it would neither guarantee a more accurate reproduction of experimental observations compared to model I

nor directly provide deeper insight into the results from chapter 5.

For that reason, we decided to expand on model I rather than to construct a completely different model with three dynamical equations. Our approach involves the development of a theoretical framework which eventually enables to combine the multiscale approach from model I with a more realistic description of solvent mixing. We are going to call this framework *effective two-component systems* and it is motivated by the link of model I to a three-component system. In the end, this link will also provide an interpretation why model I is able to describe experimental observations despite the very simplified implementation of solvent mixing.

6.1 The notion of effective two-component systems

a) Motivation: the connection of model I to a three-component system

We establish a connection between model I and a three-component system to get an idea what assumption about solvent mixing hides behind the time dependent interaction parameters from equation 5.21. To reduce a three-component system to model I, we start from a canonical ensemble with a Flory-Huggins-de Gennes free energy functional

$$F_0[\phi_P, \phi_{SS}, \phi_{GS}] = \int_V \left(f_0(\phi_P(\vec{r}), \phi_{SS}(\vec{r}), \phi_{GS}(\vec{r})) + \frac{\lambda}{2} \left|\nabla \phi_P(\vec{r})\right|^2 \right) d\vec{r}. \tag{6.1}$$

The notation is analogous to chapter 5. ϕ_P, ϕ_{SS}, and ϕ_{GS} are volume fractions of the polymer, the selective solvent, and the good solvent, respectively, and λ is a gradient energy parameter. Equation 6.1 neglects all energy contributions containing $\nabla\phi_{SS}$ and $\nabla\phi_{GS}$. This means that diffuse interfaces between good and selective solvent do not have an interfacial tension. In addition, the free energy does not distinguish between an interface separating polymer from good solvent or an interface separating polymer from selective solvent, either. The calculations presented in this subsection reveal that only the interfacial contribution $\lambda/2 \left|\nabla\phi_P\right|^2$ enables the reduction of the three-component system to the two-component system from model I. This is not surprising because in chapter 5 we changed only the homogeneous part of the free energy by introducing a time dependence in the interaction parameter χ, which renders interfaces to be independent of solvent compositions. Assuming the interaction parameter between good and selective solvent to be zero, the homogeneous Flory-Huggins free energy per segment f_0 is given by

$$\frac{f_0(\phi_P, \phi_{SS}, \phi_{GS})}{k_B T} = \frac{\phi_P}{N} \ln(\phi_P) + \phi_{SS} \ln(\phi_{SS}) + \phi_{GS} \ln(\phi_{GS}) + \chi_{SS}\phi_P\phi_{SS} + \chi_{GS}\phi_P\phi_{GS}, \tag{6.2}$$

where N is again the number of segments per polymer molecule, and χ_{GS} or χ_{SS} the Flory-Huggins interaction parameter between the polymer and the good or selective solvent.

At first, a variable transformation

$$(\phi_P, \phi_{SS}, \phi_{GS}) \mapsto (\phi_P, \phi_S, \alpha) \text{ with}$$

$$\phi_S[\phi_{SS}, \phi_{GS}] = \phi_{SS} + \phi_{GS} \text{ and } \alpha[\phi_{SS}, \phi_{GS}] = \frac{\phi_{SS}}{\phi_{SS} + \phi_{GS}} \tag{6.3}$$

is applied, where ϕ_S is the total solvent volume fraction and α the solvent composition. Since

it follows from the transformation equations that $\phi_{SS}[\phi_S, \alpha] = \alpha\phi_S$ and $\phi_{GS}[\phi_S, \alpha] = (1 - \alpha)\phi_S$, the homogeneous free energy per segment in the transformed variable space becomes

$$\frac{f(\phi_P, \phi_S, \alpha)}{k_B T} = \frac{\phi_P}{N} \ln(\phi_P) + \alpha\phi_S \ln(\alpha\phi_S) + (1 - \alpha)\phi_S \ln((1 - \alpha)\phi_S) + [\alpha\chi_{SS} + (1 - \alpha)\chi_{GS}]\, \phi_P\phi_S \tag{6.4}$$

with $f_0(\phi_P, \phi_{SS}, \phi_{GS}) = f(\phi_P, \phi_S[\phi_{SS}, \phi_{GS}], \alpha[\phi_{SS}, \phi_{GS}])$. The corresponding free energy functional

$$F[\phi_P, \phi_S, \alpha] = \int_V \left(f(\phi_P(\vec{r}), \phi_S(\vec{r}), \alpha(\vec{r})) + \frac{\lambda}{2} |\nabla\phi_P(\vec{r})|^2 \right) d\vec{r} \tag{6.5}$$

accordingly fulfills

$$F[\phi_P, \phi_S[\phi_{SS}, \phi_{GS}], \alpha[\phi_{SS}, \phi_{GS}]] = F_0[\phi_P, \phi_{SS}, \phi_{GS}]. \tag{6.6}$$

In a three-component canonical ensemble with neglected thermal fluctuations, the local polymer volume fraction obeys a continuity equation

$$\frac{\partial\phi_P}{\partial t} = \nabla \cdot \left(\frac{D_0}{k_B T} \phi_P \nabla \frac{\delta F_0[\phi_P, \phi_{SS}, \phi_{GS}]}{\delta\phi_P} \right) \tag{6.7}$$

just like in section 5.1, where $D_0 = {}^{D_P}/_N$ is the segment diffusion coefficient. Since it directly follows from equation 6.6 that

$$\frac{\delta F_0[\phi_P, \phi_{SS}, \phi_{GS}]}{\delta\phi_P} = \frac{\delta F[\phi_P, \phi_S[\phi_{SS}, \phi_{GS}], \alpha[\phi_{SS}, \phi_{GS}]]}{\delta\phi_P}, \tag{6.8}$$

the continuity equation in the new variables reads

$$\frac{\partial\phi_P}{\partial t} = \nabla \cdot \left(\frac{D_0}{k_B T} \phi_P \nabla \frac{\delta F[\phi_P, \phi_S, \alpha]}{\delta\phi_P} \right). \tag{6.9}$$

As a reminder: for any set Φ, $\frac{\delta F[\Phi]}{\delta\phi_i}$ denotes $\frac{\delta F}{\delta\phi_i}$ evaluated at Φ. To arrive at model I, it has to be assumed that the solvent composition α is independent of the position $\vec{r}$. This makes F a function in α, i.e. $F[\phi_P, \phi_S, \alpha] = F[\phi_P, \phi_S](\alpha)$. In this case $\frac{\delta F}{\delta\phi_S}$ becomes the sole phenomenological thermodynamic driving force besides $\frac{\delta F}{\delta\phi_P}$, which motivates writing the temporal evolution of ϕ_S in accordance with the Onsager Reciprocal relations for a canonical two-component system as

$$\frac{\partial\phi_S}{\partial t} = \nabla \cdot \left(\frac{D_S}{k_B T} \phi_S \nabla \frac{\delta F[\phi_P, \phi_S, \alpha]}{\delta\phi_S} \right). \tag{6.10}$$

Because application of the chain rule for functional derivatives to

$$F[\phi_P, \phi_S, \alpha] = F_0[\phi_P, \phi_{SS}[\phi_S, \alpha], \phi_{GS}[\phi_S, \alpha]] = F_0[\phi_P, \alpha\phi_S, (1 - \alpha)\phi_S] \tag{6.11}$$

(which is equivalent to equation 6.6) yields

$$\frac{\partial\phi_{SS}}{\partial t}(\vec{r}) + \frac{\partial\phi_{GS}}{\partial t}(\vec{r}) = \frac{\partial\phi_S}{\partial t}(\vec{r}) = \nabla \cdot \left(\frac{D_S}{k_B T} \phi_S(\vec{r}) \nabla \frac{\delta F[\phi_P, \phi_S, \alpha]}{\delta\phi_S(\vec{r})} \right)$$

$$= \nabla \cdot \left(\frac{D_S}{k_B T} \phi_S(\vec{r}) \nabla \int \left[\frac{\delta F_0}{\delta \phi_{SS}(\vec{r}\,')}\Big|_\alpha \frac{\delta \phi_{SS}(\vec{r}\,')}{\delta \phi_S(\vec{r})} + \frac{\delta F_0}{\delta \phi_{GS}(\vec{r}\,')}\Big|_\alpha \frac{\delta \phi_{GS}(\vec{r}\,')}{\delta \phi_S(\vec{r})} \right] d\vec{r}\,' \right)$$

$$= \nabla \cdot \left(\frac{D_S}{k_B T} \alpha \phi_S(\vec{r}) \nabla \frac{\delta F_0}{\delta \phi_{SS}(\vec{r})}\Big|_\alpha \right) + \nabla \cdot \left(\frac{D_S}{k_B T} (1-\alpha) \phi_S(\vec{r}) \nabla \frac{\delta F_0}{\delta \phi_{GS}(\vec{r})}\Big|_\alpha \right)$$

$$= \nabla \cdot \left(\frac{D_S}{k_B T} \phi_{SS}(\vec{r}) \nabla \frac{\delta F_0}{\delta \phi_{SS}(\vec{r})}\Big|_\alpha \right) + \nabla \cdot \left(\frac{D_S}{k_B T} \phi_{GS}(\vec{r}) \nabla \frac{\delta F_0}{\delta \phi_{GS}(\vec{r})}\Big|_\alpha \right), \tag{6.12}$$

equation 6.10 corresponds to the sum of dynamical equations

$$\frac{\partial \phi_i}{\partial t} = \nabla \cdot \left(\frac{D_i}{k_B T} \phi_i \nabla \frac{\delta F_0}{\delta \phi_i}\Big|_\alpha \right) \text{ for } i \in \{SS, GS\} \tag{6.13}$$

with $D_{GS} = D_{SS} = D_S$. Here, the short hand notation

$$\frac{\delta F_0}{\delta \phi_i}\Big|_\alpha := \frac{\delta F_0[\phi_P, \alpha\phi_S, (1-\alpha)\phi_S]}{\delta \phi_i} \tag{6.14}$$

is introduced to emphasize that variational derivatives $\frac{\delta F_0}{\delta \phi_i}$ are always evaluated at constant, i.e. $\vec{r}$-independent, solvent compositions α. Thus, equation 6.10 is consistent with the dynamical equations for the solvent volume fractions in a three-component canonical ensemble under the constraints $\phi_{SS}(\vec{r}) = \alpha\phi_S(\vec{r})$ and $\phi_{GS}(\vec{r}) = (1-\alpha)\phi_S(\vec{r})$. Identically to the derivation of equation 5.16, an incompressibility constraint can be imposed by modifying the fluxes in equations 6.9 and 6.10 with a constraining force Z. Upon applying the relations $\phi_P + \phi_S = 1$ and $D_0 = D_S$, this leaves one evolution equation, namely

$$\frac{\partial \phi_P}{\partial t} = \nabla \cdot \left(\frac{D_0}{k_B T} \phi_P (1-\phi_P) \nabla \left[\frac{\delta F}{\delta \phi_P} - \frac{\delta F}{\delta \phi_S} \right] \right). \tag{6.15}$$

The functional derivatives of equation 6.5 with f from equation 6.4 read

$$\frac{1}{k_B T} \frac{\delta F}{\delta \phi_P} = \frac{1}{N} \ln(\phi_P) + \frac{1}{N} + \left[\alpha\chi_{SS} + (1-\alpha)\chi_{GS} \right] \phi_S - \lambda \Delta \phi_P \tag{6.16}$$

and

$$\frac{1}{k_B T} \frac{\delta F}{\delta \phi_S} = \ln(\phi_S) + \left[\alpha\chi_{SS} + (1-\alpha)\chi_{GS} \right] \phi_P + \left\{ \alpha \ln(\alpha) + \alpha + (1-\alpha)\ln(1-\alpha) + (1-\alpha) \right\}. \tag{6.17}$$

Since the term in curly braces is independent of $\vec{r}$ it follows that

$$\frac{1}{k_B T} \nabla \left[\frac{\delta F}{\delta \phi_P} - \frac{\delta F}{\delta \phi_S} \right] = \nabla \left[\frac{1}{N} \ln(\phi_P) - \ln(1-\phi_P) + \chi(1-2\phi_P) - \lambda \Delta \phi_P \right] \tag{6.18}$$

with the definition

$$\chi = \alpha\chi_{SS} + (1-\alpha)\chi_{GS}. \tag{6.19}$$

The right hand side of equation 6.18 is identical to $\nabla \left[\mu_r - \lambda \Delta \phi_P \right]$ with μ_r from equation 5.17. Therefore, the dimensionless version of equation 6.15 is identical to equation 5.18. Setting the position independent solvent composition to

$$\alpha = \frac{\varphi_{SS}}{1 - f_P} \tag{6.20}$$

leads to equation 5.21,

$$\chi = \chi_{GS} + \frac{\chi_{SS} - \chi_{GS}}{1 - f_P}\varphi_{SS}, \tag{6.21}$$

and thus, we obtain model I.

Since equation 6.15 is consistent with equations 6.7 and 6.13, model I describes canonical three-component dynamics under the constraint of a homogeneous solvent composition ${\phi_{SS}(\vec{r})}/{(\phi_{SS}(\vec{r})+\phi_{GS}(\vec{r}))} = \alpha = {\varphi_{SS}}/{(1-f_P)}$ throughout an entire system or fluid element. The complete solvent mixing process is incorporated into the temporal increase of the solvent composition α. Hence, solvent mixing specifies an 'internal degree of freedom' of the solvent mixture. Such an implementation of solvent mixing makes model I a special case of what we are going to call an incompressible effective two-component system in the following.

b) The definition of effective two-component systems

The nomenclature accounts for the fact that dynamical equations only describe the temporal evolution of the polymer (ϕ_P) and the total solvent (ϕ_S). Deriving an additional evolution equation for a $\vec{r}$-dependent solvent composition variable from the dynamical equations $\frac{\partial \phi_i}{\partial t} = \nabla \cdot \left[\beta D_i \nabla \frac{\delta F_0}{\delta \phi_i}\right]$ for $i = P, SS, GS$ would just cast the three-component system in a different representation. The fundamental characteristic of our notion of an effective two-component system is the substitution of this additional evolution equation by an algebraic relation for the composition variable, e.g. by equation 6.20 in case of model I. Solvent mixing is then implemented as a constraining condition by a time dependence in this relation. What distinguishes different effective two-component systems is the choice of the composition variable.

Based on the steps we applied to reduce a three-component system to model I in paragraph A), one may formulate the following generalized construction procedure for effective two-component systems:

- Choose a free energy functional $F_0[\phi_P, \phi_{SS}, \phi_{GS}]$ (cp. equations 6.1 and 6.2).
- Transform variables $(\phi_P, \phi_{SS}, \phi_{GS}) \mapsto (\phi_P, \phi_S, \alpha)$, where $\phi_S = \phi_{SS} + \phi_{GS}$ is the total volume fraction of the solvent mixture and α characterizes the solvent composition (cp. equation 6.3).
- Express $F_0[\phi_P, \phi_{SS}, \phi_{GS}]$ in terms of the new variables, such that the resulting free energy becomes a function of solvent composition, i.e. $F_0[\phi_P, \phi_{SS}, \phi_{GS}] \mapsto F[\phi_P, \phi_S](\alpha)$.
- Apply dynamical equations

  $$\frac{\partial \phi_P}{\partial t} = \nabla \cdot \left(\frac{D_0}{k_B T}\phi_P \nabla \frac{\delta F[\phi_P, \phi_S](\alpha)}{\delta \phi_P}\right)$$

  and

  $$\frac{\partial \phi_S}{\partial t} = \nabla \cdot \left(\frac{D_S}{k_B T}\phi_S \nabla \frac{\delta F[\phi_P, \phi_S](\alpha)}{\delta \phi_S}\right)$$

  to describe phase separation (cp. equations 6.9 and 6.10).
- Implement solvent mixing by prescribing a time dependence of α (cp. equation 6.20 with $\varphi_{SS} = \varphi_{SS}(t)$).

The implementation by a time dependent composition constraint assumes solvent mixing to be fast in comparison to the phase separation. It will be discussed later that such an assumption should be reasonable, for instance, in incompressible dilute polymer solutions, which correspond to the experimental conditions from figure 1.3. The assumption is also supported by the fact that model I reproduces experimental observations. So ideally, $\alpha(t)$ should reflect realistic solvent compositions that attune rapidly during fast solvent mixing at fixed density profiles ϕ_P and ϕ_S (in incompressible systems ϕ_S is fixed when ϕ_P is fixed because $\phi_S(\vec{r},t) = 1 - \phi_S(\vec{r},t)$). As selective solvent tends to avoid regions of high polymer concentrations while good solvent should accumulate in these regions, a position independent solvent composition like in model I is a rather unphysical choice. In the next section we perform the procedure listed above with a chemical potential as a composition variable to develop an effective two-component system from a semi-grand canonical ensemble in order to refine the description of solvent mixing. We are going to call the result 'model II'.

6.2 Derivation of model II

As before, the starting point is the free energy functional

$$F_0[\phi_P, \phi_{SS}, \phi_{GS}] = \int_V \left(f_0(\phi_P(\vec{r}), \phi_{SS}(\vec{r}), \phi_{GS}(\vec{r})) + \frac{\lambda}{2} |\nabla \phi_P(\vec{r})|^2 \right) d\vec{r} \tag{6.22}$$

with f_0 from equation 6.2,

$$\frac{f_0(\phi_P, \phi_{SS}, \phi_{GS})}{k_B T} = \frac{\phi_P}{N} \ln(\phi_P) + \phi_{SS} \ln(\phi_{SS}) + \phi_{GS} \ln(\phi_{GS}) + \chi_{SS} \phi_P \phi_{SS} + \chi_{GS} \phi_P \phi_{GS}. \tag{6.23}$$

It would be unproblematic to introduce an interaction term $\chi_S \phi_{SS} \phi_{GS}$ for the two solvents or interfacial energy contributions that contain $\nabla\phi_{SS}$ and $\nabla\phi_{GS}$, but here we neglect them like in section 6.1 to keep the analogy to model I.

This time the variable transformation is performed in two separate steps. The first step is the transformation $(\phi_P, \phi_{SS}, \phi_{GS}) \mapsto (\phi_P, \phi_{SS}, \phi_S)$ with $\phi_S[\phi_{SS}, \phi_{GS}] = \phi_{SS} + \phi_{GS}$ yielding

$$\begin{aligned} \widetilde{F}[\phi_P, \phi_{SS}, \phi_S] = \int_V k_B T \Big[& \frac{\phi_P}{N} \ln(\phi_P) + \phi_{SS} \ln(\phi_{SS}) + (\phi_S - \phi_{SS}) \ln(\phi_S - \phi_{SS}) \\ & + \chi_{SS} \phi_P \phi_{SS} + \chi_{GS} \phi_P (\phi_S - \phi_{SS}) \Big] + \frac{\lambda}{2} |\nabla \phi_P|^2 \, d\vec{r} \end{aligned} \tag{6.24}$$

with $\widetilde{F}[\phi_P, \phi_{SS}, \phi_S[\phi_{SS}, \phi_{GS}]] = F_0[\phi_P, \phi_{SS}, \phi_{GS}]$. Then the dimensionless relative chemical potential of the two solvents is calculated as

$$\mu_s \coloneqq \frac{1}{k_B T} \frac{\delta \widetilde{F}}{\delta \phi_{SS}} = \ln\left(\frac{\phi_{SS}}{\phi_S - \phi_{SS}} \right) + \Delta\chi \phi_P \text{ with } \Delta\chi \coloneqq \chi_{SS} - \chi_{GS}, \tag{6.25}$$

which enables to express ϕ_{SS} by

$$\phi_{SS}[\phi_P, \phi_S, \mu_s] = \frac{1}{e^{\Delta\chi\phi_P - \mu_s} + 1} \phi_S =: \phi_{SS}(\mu_s). \tag{6.26}$$

Substituting ϕ_{SS} by μ_s via a Legendre transformation constitutes the second step of the variable transformation and the transition into a semi-grand canonical ensemble. Elementary

calculations lead to

$$F[\phi_P, \mu_s, \phi_S] = \widetilde{F}[\phi_P, \phi_{SS}(\mu_s), \phi_S] - k_B T \int_V \mu_s \, \phi_{SS}(\mu_s) d\vec{r}$$

$$= \int_V \left(f(\phi_P, \mu_s, \phi_S) + \frac{\lambda}{2} \left| \nabla \phi_P \right|^2 \right) d\vec{r} \tag{6.27}$$

with

$$\frac{f(\phi_P, \mu_s, \phi_S)}{k_B T} = \frac{\phi_P}{N} \ln(\phi_P) + \phi_S \ln(\phi_S) + \chi_{SS} \phi_P \phi_S - \left(\ln\left(1 + e^{\Delta\chi \phi_P - \mu_s}\right) + \mu_s \right) \phi_S. \tag{6.28}$$

Here, μ_s plays the role of the composition variable α. If the relaxation of good and selective solvent density profiles is very fast compared to the phase separation, it is plausible to assume that the selective and the good solvent equilibrate instantaneously at fixed volume fraction profiles $\phi_P(\vec{r}, t)$ and $\phi_S(\vec{r}, t)$. In the equilibrated state μ_s is homogeneous throughout the system, i.e. independent of $\vec{r}$. F is then a function of the composition variable μ_s and can be written as $F[\phi_P, \phi_S](\mu_s)$.

Since F needs to be minimal in equilibrium, the gradients of $\frac{\delta F}{\delta \phi_P}$ and $\frac{\delta F}{\delta \phi_S}$ can be identified as the phenomenological thermodynamic forces driving the phase separation at spatially constant μ_s. Calculating the functional derivative of $F[\phi_P, \mu_s, \phi_S] = \widetilde{F}[\phi_P, \phi_{SS}[\phi_P, \phi_S, \mu_s], \phi_S] - k_B T \int \mu_s \phi_{SS}[\phi_P, \phi_S, \mu_s] \, d\vec{r}$ with respect to ϕ_P and remembering that $\mu_s = \frac{1}{k_B T} \frac{\delta \widetilde{F}}{\delta \phi_{SS}}$ leads to

$$\frac{\delta F[\phi_P, \phi_S, \mu_s]}{\delta \phi_P} = \frac{\delta \widetilde{F}[\phi_P, \phi_{SS}[\phi_P, \phi_S, \mu_s], \phi_S]}{\delta \phi_P}. \tag{6.29}$$

Taking into account that $\widetilde{F}[\phi_P, \phi_{SS}, \phi_S] = F_0[\phi_P, \phi_{SS}, \phi_{GS}[\phi_S, \phi_{SS}]]$ further gives

$$\frac{\delta \widetilde{F}[\phi_P, \phi_{SS}, \phi_S]}{\delta \phi_P} = \frac{\delta F_0[\phi_P, \phi_{SS}, \phi_{GS}[\phi_S, \phi_{SS}]]}{\delta \phi_P} \tag{6.30}$$

and hence,

$$\frac{\delta F[\phi_P, \phi_S, \mu_s]}{\delta \phi_P} = \frac{\delta F_0[\phi_P, \phi_{SS}[\phi_P, \phi_S, \mu_s], \phi_{GS}[\phi_S, \phi_{SS}[\phi_P, \phi_S, \mu_s]]]}{\delta \phi_P} =: \left. \frac{\delta F_0}{\delta \phi_P} \right|_{\mu_s}. \tag{6.31}$$

This allows to write down the dynamical equation

$$\frac{\partial \phi_P}{\partial t} = \nabla \cdot \left(\frac{D_0}{k_B T} \phi_P \nabla \left. \frac{\delta F_0}{\delta \phi_P} \right|_{\mu_s} \right) = \nabla \cdot \left(\frac{D_0}{k_B T} \phi_P \nabla \frac{\delta F[\phi_P, \phi_S](\mu_s)}{\delta \phi_P} \right) \tag{6.32}$$

just like equation 6.9, provided $f_P = \int \phi_P d\vec{r}/V$ is conserved. $\left. \frac{\delta F_0}{\delta \phi_P} \right|_{\mu_s}$ denotes the functional derivative of F_0 evaluated at solvent compositions that are set by μ_s. Therefore, the polymer moves in a solvent with a constrained composition. This composition corresponds to the equilibrium composition that attunes at fixed $\phi_P(\vec{r}, t)$ and $\phi_S(\vec{r}, t)$. Although the integral volume fractions $f_{SS} = \int \phi_{SS} d\vec{r}/V$ and $f_{GS} = \int \phi_{GS} d\vec{r}/V$ are not necessarily conserved globally in a semi-grand canonical ensemble, $f_S = f_{SS} + f_{GS}$ still remains constant. This motivates

to introduce the phenomenological continuity equation

$$\frac{\partial \phi_S}{\partial t} = \nabla \cdot \left(\frac{D_S}{k_B T} \phi_S \nabla \frac{\delta F[\phi_P, \phi_S](\mu_s)}{\delta \phi_S} \right), \tag{6.33}$$

where D_S is interpreted as the diffusion coefficient of the solvent mixture. The absence of a cross-coupling term with the thermodynamic driving force $\nabla \frac{\delta F}{\delta \phi_S}$ in the dynamical equation for ϕ_P inspires omitting $\nabla \frac{\delta F}{\delta \phi_P}$ from the dynamical equation for ϕ_S as well to obtain a symmetric mobility matrix in consistency with the Onsager Reciprocal Relations in a two-component canonical ensemble. It should be noted though that equation 6.33 is a phenomenological equation that is *not* consistent with canonical dynamics at fixed μ_s, i.e. a calculation like in equation 6.12 is not possible because the prefactor in front of ϕ_S in equation 6.26 depends on $\phi_P(\vec{r})$. As a consequence, equation 6.33 conserves ϕ_S locally but equation 6.26 does not imply the local conservation of ϕ_{SS}. That ϕ_{SS} and likewise $\phi_{GS} = \phi_S - \phi_{SS}$ are not locally conserved does not obligatorily contradict the local conservation of ϕ_S. The disparate conservation behavior of ϕ_S and ϕ_{SS} rather reflects the separation of time scales assumed by effective two-component systems: if good and selective solvent interdiffuse much faster than ϕ_S varies in time, good and selective solvent molecules should be able to cross the whole system volume while total solvent only transitions to neighboring lattice cells. Incompressible dilute polymer solutions constitute a physical situation where this separation of time scales is imaginable, because the minority component, the polymer, sets the speed of phase separation and slows down the exchange of the complete solvent mixture ($\phi_S = 1 - \phi_P$) between lattice cells while good and selective solvent can diffuse unhindered *within* the solvent mixture. The current set of dynamical equations conclusively contains the assumption of separated time scales not only in the implementation of solvent mixing (time dependent μ_s) but also in the dynamics at time-independent μ_s.

Transforming equations 6.32 and 6.33 into an equation for incompressible dynamics is completely analogous to subsection 5.1 and leads to

$$\frac{\partial \phi_P}{\partial t} = \nabla \cdot (D_0 \phi_P (1 - \phi_P) \nabla \mu) \tag{6.34}$$

with $D_0 = D_S$ and the short hand notation

$$\mu \coloneqq \frac{1}{k_B T} \left(\frac{\delta F}{\delta \phi_P} - \frac{\delta F}{\delta \phi_S} \right). \tag{6.35}$$

In dilute solutions, setting $D_0 = D_S$ does not contradict the assumption of fast solvent relaxation compared to the phase separation. This issue is discussed in section 6.5. Using equations 6.27 and 6.28 to calculate

$$\frac{1}{k_B T} \frac{\delta F}{\delta \phi_P} = \frac{\ln(\phi_P)}{N} + \frac{1}{N} + \chi_{SS} \phi_S - \Delta\chi \frac{\phi_S}{1 + e^{-\Delta\chi\phi_P + \mu_s}} - \frac{\lambda}{k_B T} \Delta\phi_P \tag{6.36}$$

and

$$\frac{1}{k_B T} \frac{\delta F}{\delta \phi_S} = \ln(\phi_S) + 1 + \chi_{SS} \phi_P - \ln\left(1 + e^{\Delta\chi\phi_P - \mu_s}\right) - \mu_s \tag{6.37}$$

gives

$$\mu = \frac{\ln(\phi_P)}{N} + \frac{1}{N} - \ln(1 - \phi_P) - 1 + \chi_{SS}(1 - 2\phi_P)$$

$$+\ln(1+e^{\Delta\chi\phi_P-\mu_s})+\mu_s-\Delta\chi\frac{1-\phi_P}{1+e^{-\Delta\chi\phi_P+\mu_s}}-\frac{\lambda}{k_BT}\Delta\phi_P. \tag{6.38}$$

To implement solvent mixing we insert $\phi_S = 1-\phi_P$ into equation 6.26 and set

$$\varphi_{SS}(t)=\phi_{SS}[\phi_P=0]=\frac{1}{1+e^{-\mu_s}} \Leftrightarrow \mu_s=-\ln\left(\frac{1}{\varphi_{SS}(t)}-1\right). \tag{6.39}$$

This condition states that the volume fraction φ_{SS} is set at positions or in lattice cells where no polymer is present, which makes sense because the mixing profiles in chapter 3 were derived in the absence of polymer. Equations 6.34, 6.38 and 6.39 constitute model II. Expressing lengths in units of $l_0=\sqrt{\lambda/k_BT}$ and times in units of $t_0=l_0^2/D_0$ allows substituting $D_0 \mapsto 1$ in equation 6.34 and $\lambda \mapsto k_BT$ in equation 6.38 without loss of generality. Lengths and times are given in units of l_0 and t_0 throughout the remainder of this chapter. Equation 6.34 can be solved numerically using the schemes given by equations 5.38 and 5.41.

Casting equation 6.28 into the form

$$\frac{f}{k_BT}=\frac{\phi_P}{N}\ln(\phi_P)+\phi_S\ln(\phi_S)+\chi(\phi_P,t)\phi_P\phi_S \tag{6.40}$$

with a composition and time dependent interaction parameter

$$\chi(\phi_P,t)=\chi_{SS}-\frac{\ln\left(1+e^{\Delta\chi\phi_P-\mu_s(t)}\right)+\mu_s(t)}{\phi_P} \tag{6.41}$$

shows that the only formal difference between model II and model I is the functional form of the interaction parameter in the free energy. In contrast to model I, model II describes spatially varying solvent qualities because χ depends on $\phi_P(\vec{r})$. In analogy to model I we use the terminology

$$\mu=\mu_r-\frac{\lambda}{k_BT}\Delta\phi_P. \tag{6.42}$$

In model II, μ_r contains additional terms resulting from the variational derivatives of $\chi(\phi_P,t)$ with respect to ϕ_P (cp. equation 6.38). We again assume mixing times to be low enough so that the system crosses the spinodal line before significant particle growth in the metastable area occurs. In the present case the spinodal line is defined by

$$0=\frac{\partial\mu_r}{\partial\phi_P}(\phi_P=f_P)=\frac{1}{Nf_P}+\frac{1}{1-f_P}-2\chi_{SS}+\frac{\Delta\chi}{1+e^{-\Delta\chi f_P+\mu_s}}\left(2-\frac{(1-f_P)\Delta\chi}{1+e^{\Delta\chi f_P-\mu_s}}\right). \tag{6.43}$$

At this point it is emphasized that model II is a novel *phenomenological* model introduced to describe spatially varying solvent qualities. In sections 6.3 and 6.4 we utilize model II to exemplarily investigate potential effects of spatially varying solvent quality distributions on rate-size relations in principle and how they compare to model I, without talking about the physical accuracy or validity of assumptions made to arrive at model II. We note in advance that the characteristic attribution of rate-size relations from model II is very similar to model I. The crucial difference between model I and model II as well as the validity of the assumptions is addressed in section 6.5. Section 6.5 shows that an approach using chemical potentials μ_s quantitatively agrees with conventional three-component dynamics in dilute polymer solutions, while model I disagrees.

6.3 Rate-size relations for linear mixing profiles

We start the comparison of rate-size relations from model I and model II by employing linear mixing profiles

$$\varphi_{SS}(t) = \begin{cases} \varphi_0 + s\,t'(t) & \text{for } t'(t) \leq t'_{max} \\ \varphi_{max} & \text{for } t'(t) > t'_{max} \end{cases} \tag{6.44}$$

in equation 6.39, where $t'_{max} = {}^{(\varphi_{max}-\varphi_0)}/_{s}$. The relation between t' and the system time t from equation 6.34 reads $t'(t) = t + t_s$ like in section 5.4, except that t_0 is substituted by 1 since it can be absorbed into the slope s. The spinodal time shift t_s is defined by $\varphi_{SS}(t=0) = \varphi_{Spin}$, where φ_{Spin} is the spinodal solvent composition. It is determined from equation 6.43 upon setting $\mu_s = -\ln({}^{1}/_{\varphi_{Spin}} - 1)$. Linear mixing profiles in model II require a distinction between t and t', because they translate into nonlinear quenches according to

$$\chi(\phi_P, t) = \chi_{SS} - \frac{\ln\left(1 + e^{\Delta\chi\phi_P - \mu_s(t)}\right) + \mu_s(t)}{\phi_P} \tag{6.45}$$

with $\mu_s(t) = -\ln({}^{1}/_{\varphi_{SS}(t)} - 1)$. Strictly speaking, there is no constant quench rate, but in the following the term 'quench rate' is being used in a more loose context and refers to the slope of the mixing profile s.

6.3.1 Simulation setup

Unlike in model I it is not possible to absorb the interaction parameters into an analogue to s_χ (cp. equation 5.44), so the adjustable physical parameters are

- the mean polymer volume fraction f_P,
- the segments per polymer molecule N,
- the interaction parameters of the good and selective solvent χ_{SS} and χ_{GS},
- the quench rate s,
- the premixed selective solvent fraction φ_0, and
- the maximum selective solvent fraction φ_{max}.

The number of segments per polymer molecule is again set to $N = 14$. If not stated otherwise, model cases with interaction parameters $\chi_{SS} = 2$ and $\chi_{GS} = 0$ are considered. $\chi_{SS} = 2$ is the value of the maximum interaction parameter from section 5.3 and setting $\chi_{GS} = 0$ implies a purely combinatoric good solvent, i.e. good solvent only contributes an entropic term to the free energy functional. The maximum selective solvent volume fraction in the absence of polymer is set to $\varphi_{max} = {}^{(1+\varphi_0)}/_{2}$. f_P, s and φ_0 are varied.

The numerical parameters are identical to model I. All simulations in this section are performed on a two dimensional lattice with $m = 400 \times 400$ grid points, a lattice constant $\Delta l = 0.25$, an initial time step size $h = 0.005$, and a threshold value $\phi_P^{(th)} = 0.3$ for the conversion into binary images to determine the Minkowski functionals. Like in chapter 5 all data points represent averages over 5 independent simulation runs with different uniformly distributed random initial conditions $\phi_P^{(0)}(\vec{r}_s) \in [f_P - 0.001, f_P + 0.001]\ \forall\, s = 0, ..., m-1$.

6.3.2 Simulation results

Qualitatively, the temporal evolution of polymer volume fraction profiles is practically identical to model I. A spinodal decomposition characterized by fast phase separation (cp. figure 5.2) is followed by a considerably slower coarsening of polymer droplets. This leads to time series of Minkowski functionals similar to figure 5.1 and allows an analogous definition of the transition time t_{tr} and droplets. Figure 6.1 shows snapshots of the composition fields ϕ_P, ϕ_{SS} and ϕ_{GS} at t_{tr} for an exemplary simulation run. Comparing figure 6.1 (b) and (c) demonstrates that the model does indeed describe position dependent solvent compositions. The good solvent mainly accumulates at interfaces between the selective solvent and the polymer, which manifests as coronae of high good solvent volume fractions around blue to yellow spots in snapshot (c). Such a distribution is expected because due to incompressibility the non-interacting good solvent ($\chi_{GS} = 0$) is pushed out of domains where either the selective solvent or the polymer concentrate owing to their repulsion. Droplet radii are determined in the same manner as described in subsection 5.3.2, and in the current section the term rate-size relation refers to the relation between droplet sizes and s from equation 6.44.

Figure 6.2 shows rate-size relations for two different mean polymer volume fractions, $f_P = 0.038$ and $f_P = 0.100$. Constant interaction parameters χ_{SS} and χ_{GS} require an adaptation of the premixed selective solvent volume fraction φ_0 to ensure that the system is not located above the spinodal line at $t = 0$. According to equation 6.43 with $\mu_s = -\ln(1/\varphi_{Spin} - 1)$, increasing f_P from 0.038 to 0.100 reduces the spinodal solvent composition from $\varphi_{Spin} = 0.5$ to $\varphi_{Spin} = 0.318$. At $f_P = 0.038$ we set $\varphi_0 = (1-f_P)/2 = 0.482$ in accordance to figure 1.3 (a) and (b), which is close to $\varphi_{Spin} = 0.5$. For $f_P = 0.100$ the premixed selective solvent volume fraction is simplistically set to $\varphi_0 = \varphi_{Spin} = 0.318$. Despite a completely different implementation of solvent mixing the data point progressions look very similar to the results from model I in figure 5.3. One can identify an asymptotic regime and a non-asymptotic regime, where droplet radii are described by scaling laws $x \propto s^\alpha$ with $x \in \{R, l_1, l_{max}\}$ and typical exponents $\alpha \approx -1/6$. As before, the transition from the non-asymptotic to the asymptotic regime happens once t_{tr} exceeds $t_{max} = t'_{max} - t_s$. The response of rate-size relations to f_P-variations also reminds of the results in figure 5.5, as a diminishing mean polymer content leads to a downward shift in the non-asymptotic regime and a crossing of

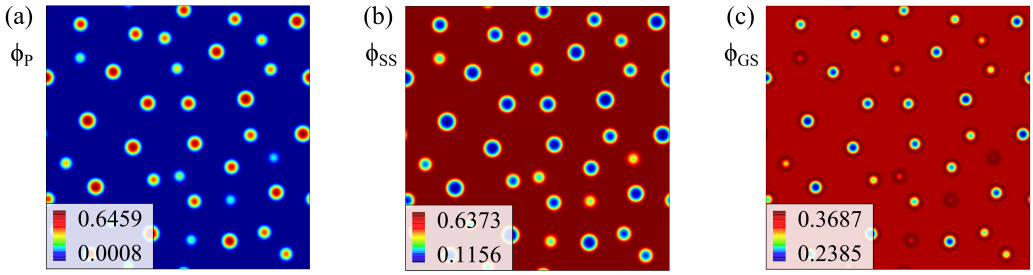

Figure 6.1: *Color coded 2D volume fraction profiles ϕ_P (a), ϕ_{SS} (b) and ϕ_{GS} (c) at transition time, simulated by model II with a linear mixing profile. The quench rate is set to $s = 10^{-5}$, the mean polymer volume fraction to $f_P = 0.038$ and the premixed selective solvent fraction to $\varphi_0 = (1-f_P)/2 = 0.482$.*

the data sets for l_1 and l_{max} close to the beginning of the asymptotic regime. For the high polymer volume fraction of $f_P = 0.100$ it is

$$\varphi_{max} - \varphi_{Spin} = \frac{1 + \varphi_0}{2} - \varphi_{Spin} = \frac{1 + 0.318}{2} - 0.318 = 0.341. \tag{6.46}$$

If we set $f_P = 0.038$ it is

$$\varphi_{max} - \varphi_{Spin} = \frac{1 + \varphi_0}{2} - \varphi_{Spin} = \frac{1 + 0.482}{2} - 0.5 = 0.241. \tag{6.47}$$

This means the maximum quench depth for $f_P = 0.038$ (corresponding to the circles in figure 6.2) is lower than the maximum quench depth for $f_P = 0.100$ (represented by squares), which explains why the asymptote of the squares lies below the one associated with the circles in figure 6.2 (b) and (c).

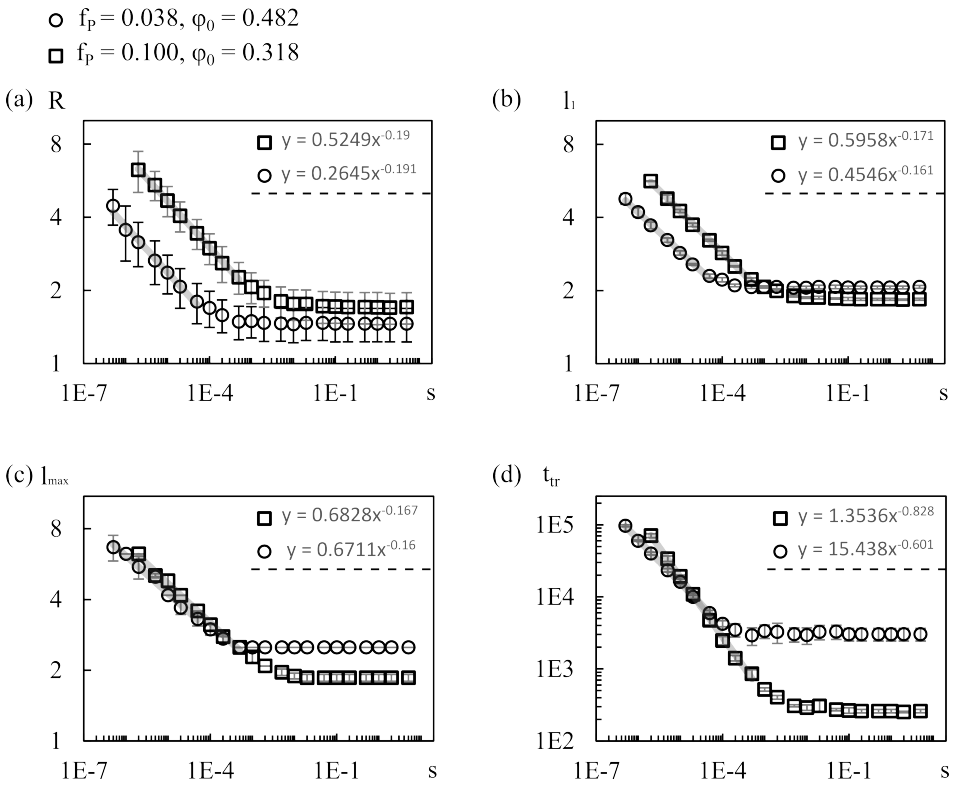

Figure 6.2: *Rate-size relations and transition times, simulated by model II with linear mixing profiles in two spatial dimensions. Circles correspond to simulation results at $f_P = 0.038$ and $\varphi_0 = 0.482$, while squares refer to $f_P = 0.100$ with $\varphi_0 = 0.318$. The remaining parameters are specified in subsection 6.3.1. Grey lines are regression lines to data points in the non-asymptotic regime. The trend line equations are shown above the dashed horizontal lines and are labeled by the corresponding symbol. Like in figure 5.3 error bars in (a) illustrate the polydispersity ΔR from equation 5.48. In (b) - (d) they indicate standard deviations over five simulation runs with different uniformly distributed random initial conditions.*

6.3.3 Perturbation theory and parameter variations

To verify that droplet sizes are still determined during the early stages of phase separation, a perturbation theory similar to subsection 5.3.4 is applied. General equations that can be directly transferred from subsection 5.3.4 to model II are the following three: equation 5.64, which reads

$$k_p^2(t) = \overline{\Delta\chi}(t) = -\frac{1}{2t}\int_0^t \frac{\partial \mu_r}{\partial \phi_p}(f_P, t')\, dt' \tag{6.48}$$

and gives the wave number k_p of the mode with the largest amplitude at a specific time t, equation 5.67,

$$l_p(t) = \frac{\pi}{2\sqrt{\overline{\Delta\chi}(t)}} = \frac{\pi}{2}\left(-\frac{1}{2t}\int_0^t \frac{\partial \mu_r}{\partial \phi_p}(f_P, t')\, dt'\right)^{-1/2}, \tag{6.49}$$

which estimates the corresponding aggregate radius, and equation 5.70, which implicitly defines an amplification time via

$$t = \frac{\ln(A(k_p(t), t))}{M(f_P)\overline{\Delta\chi}^2(t)} = \frac{\ln(A(k_p(t), t))}{M(f_P)}\left(-\frac{1}{2t}\int_0^t \frac{\partial \mu_r}{\partial \phi_p}(f_P, t')\, dt'\right)^{-2}, \tag{6.50}$$

where $M(f_P) = f_P(1 - f_P)$ is the mobility and $A(k_p(t), t)$ the amplification of the mode with wave number $k_p(t)$ at time t. For model II, $\frac{\partial \mu_r}{\partial \phi_P}(f_P, t)$ is obtained by inserting μ_s from equation 6.39 into the right hand side of equation 6.43.

Figure 6.3 shows $l_p(t_{tr})$ and $l_p(t_a)$ in comparison to the simulation results from figure 6.2. $l_p(t_a)$ is calculated by solving equation 6.50 for t_a with $\ln(A(k_p(t_a), t_a)) = 10$ and inserting the result into equation 6.49. As equation 6.50 is rather nested and complicated to solve by hand, we determine the amplification time t_a numerically with a Mathematica script for any given parameter set and dispense with writing down an explicit expression. The calculation of $l_p(t)$ for both $t = t_{tr}$ and $t = t_a$ is performed by the script as well. The values for t_{tr} are the simulation results from figure 6.2 (d). In contrast to subsection 5.3.4, $l_p(t_{tr})$ completely fails to approximate the simulation results for droplet sizes at low quench rates, but $l_p(t_a)$ still comes very close.

Comparing the respective left and right panels in figure 6.3 (a) and (b) indicates that negative deviations $t_{tr} - t_a$ lead to positive deviations $l_p(t_{tr}) - l_{max}$ and vice versa. Additionally, the deviation of l_{max} and $l_p(t_a)$ from $l_p(t_{tr})$ seems to be much more pronounced than the deviation of t_{tr} from t_a, which is especially highlighted by the sudden kink of squares in the left panel of figure 6.3 (b) at $s \approx 10^{-4}$, whereas the incipient deviation of t_{tr} from t_a at that quench rate in the right panel looks comparatively smooth. This suggests a very sensitive dependence of $l_p(t_{tr})$ on t_{tr} in model II, which could be the reason why $l_p(t_{tr})$ fails to predict the simulation results as small discrepancies between the transition time and an amplification time translate into large differences of droplet sizes. Such discrepancies could for example arise because the transition time may lie in time periods where dynamics are affected by non-linearity and mean droplet sizes change only slowly – cp. figure 5.1 (b) where it lies on a plateau. This means simulated droplet sizes are very insensitive to t_{tr}, while droplet sizes predicted by the perturbation theory are not (because it only describes linear contributions). Thus, combining simulation results for t_{tr} with the perturbation theory may distort its predictions, which renders $l_p(t_a)$ more suited to perform a perturbation analysis

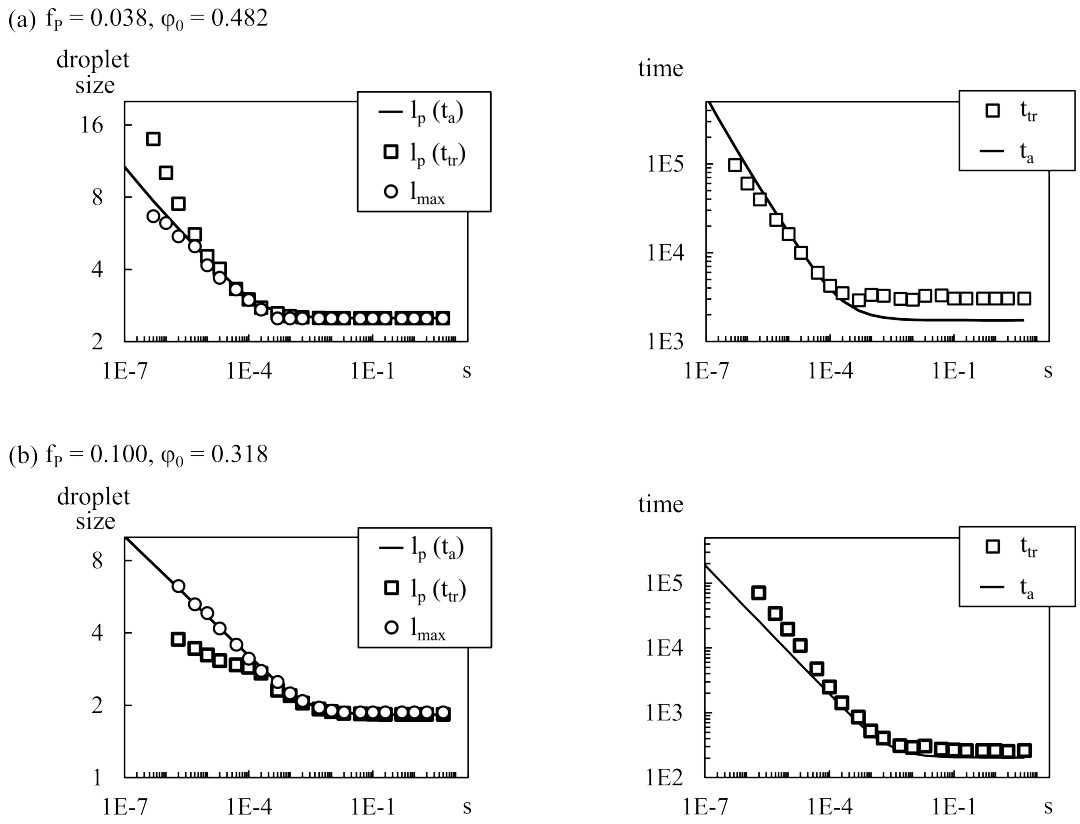

Figure 6.3: *Comparison of simulation results l_{max} to predictions from the perturbation theory l_p for model II. The circles in the left panel of (a) represent the simulation results for l_{max} from figure 6.2 at $f_P = 0.038$. The solid line illustrates $l_p(t_a)$ and the rectangles correspond to $l_p(t_{tr})$. The right panel shows the transition time t_{tr} (squares) and the amplification time t_a (solid line). (b) depicts the same for $f_P = 0.100$.*

in general. Because $l_p(t_a)$ succeeds to reproduce simulation results, droplet sizes in model II are determined during the early stages of phase separation as well.

This knowledge provides an interpretation why resulting rate-size relations resemble the ones observed in model I. There is one special case where the spatially homogeneous solvent composition assumed by model I is also present in model II, namely at $t = 0$ in the initial homogeneous state. As droplet sizes are determined close to this homogeneous state, model I might still be sufficiently accurate to capture characteristic features of rate-size relations despite not being exact. The mechanism that controls droplet sizes in model II is a competition between interfacial tension and repulsion of chemical components, too, but this time it is not the increasing interaction of one single solvent that eventually terminates early stage coarsening but the increasing amount of selective solvent. In other words, if we consider a repulsive free energy contribution of the form $\chi\phi_{SS}\phi_P$, ϕ_{SS} increases instead of χ.

The fact that the application of t_a defined by $\ln(A(k_p(t_a), t_a)) = 10$ yields very good approximations for both model I (cp. figure 5.8) and model II with respective different physical parameter sets could motivate generally setting $\ln(A) = 10$. This would enable to analyze controlled assembly of homopolymers semi-analytically, where the term 'semi' accounts for the fact that $\ln(A)$ is chosen heuristically from experience with simulations.

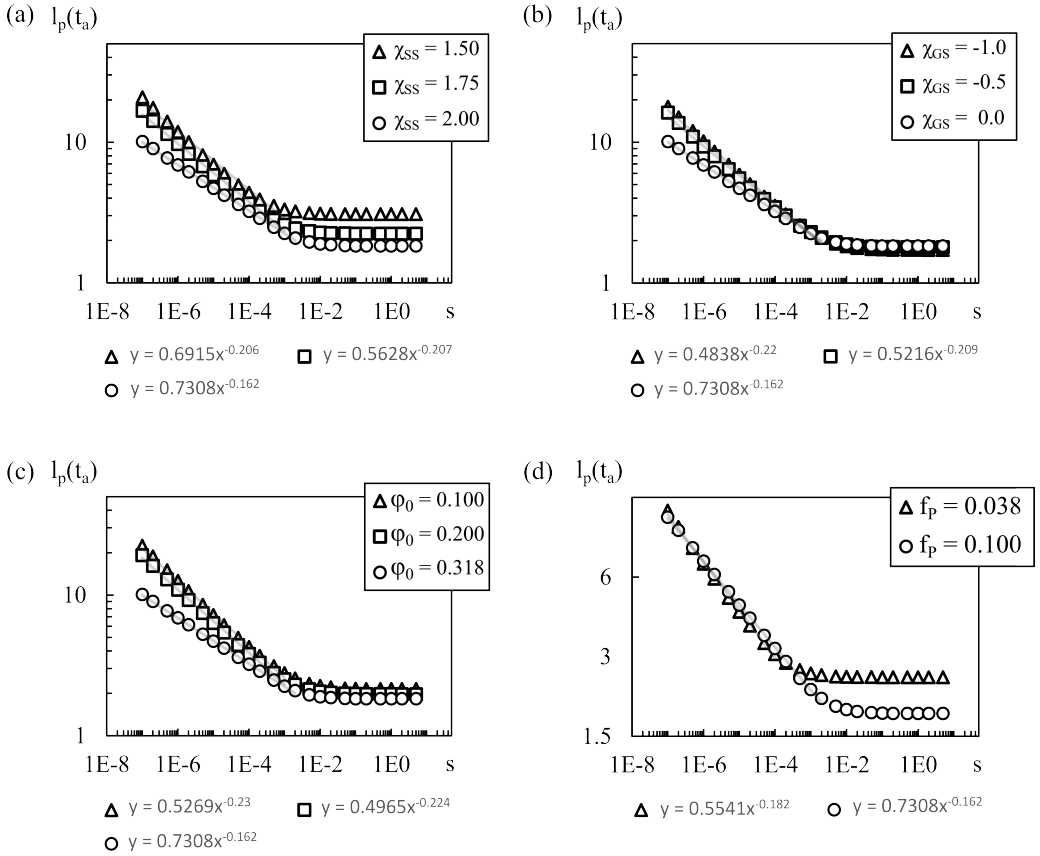

Figure 6.4: *Response of rate-size relations to parameter variations in model II, calculated by the perturbation theory with $t = t_a$. The reference set of parameters is $f_P = 0.1$, $\varphi_0 = 0.318$, and remaining parameters as specified in subsection 6.3.1. In diagrams (a), (b) and (c) only the parameter in the respective legend is changed and the open circles always label the reference set. (a) illustrates how variations of χ_{SS} affect rate-size relations, (b) illustrates the impact of changes in χ_{GS}, and in (c) the premixed selective solvent volume fraction φ_0 is varied. (d) compares the perturbation theory predictions for the parameter sets in figure 6.2. The triangles correspond to $f_P = 0.038$ with $\varphi_0 = 0.482$ and the open circles represent the set with $f_P = 0.1$ and $\varphi_0 = 0.318$. The equations below the diagrams belong to the grey regression lines in the non-asymptotic regime defined by $t_a \leq t_{max}$.*

However, since an extensive validation of $\ln(A)$-values for different parameters is not the focus of the present work, we leave this observation as a remark to be potentially addressed it in the future.

Due to its agreement with preceding simulations $l_p(t_a)$ is utilized to investigate the impact of parameter variations as illustrated in figure 6.4. The current approach is not analytical though because t_a is determined numerically by a Mathematica script. Applying the perturbation theory is still advantageous as calculating $l_p(t_a)$ takes a few seconds maximum while obtaining droplet sizes by simulations typically takes five to ten days. It can be seen in figure 6.4 (a) that a decrease in χ_{SS} increases droplet sizes, which is plausible because lower χ_{SS} lead to later terminations of early stage coarsening. This also agrees with figure 6.4 (b), where shrinking χ_{GS} enhance particle sizes. Assuming a temperature dependence

$$\chi_{SS} = \chi_{SS}^{(0)} + \frac{\alpha}{T} \text{ with } \alpha > 0 \tag{6.51}$$

figure 6.4 (a), for example, states that temperature variations lead to a vertical shift of droplet sizes in the non-asymptotic regime with slight changes of exponents, which is in accordance with the experimental observations in figure 1.3 (d). Similar statements hold for figure 6.4 (b). In model I with linear mixing profiles a change in φ_0 would only shift the asymptote since it solely affected the maximum quench depth. In model II with linear mixing profiles, droplet sizes decrease with increasing premixed selective solvent volume fractions φ_0 even in the non-asymptotic regime as shown in figure 6.4 (c). Because linear mixing profiles do not translate into linear quenches like in model I and because section 5.4 showed that shapes of rate-size relations can be changed by non-linear quenches, such a response of the non-asymptotic regime is reasonable. Figure 6.4 (d) looks very similar to figure 6.2 (c) and shows that the perturbation theory also predicts the impact of mean polymer volume fraction variations seen in the simulation results, although this shift appears to be very weak in l_{max} or $l_p(t_a)$ for reasons already mentioned in the discussion about figure 5.5. It also follows from figure 6.4 that parameter variations retain the functional dependencies $l_p \propto s^\alpha$ in the non-asymptotic regime, but they affect exponents α, which range from -0.162 to -0.230. As the exponents in the experiments (cp. figure 1.3) also deviate from $-1/6$ predicted by model I, we have identified the position dependent solvent composition in combination with different parameter choices as 'higher order' contributions that might be responsible for the experimentally observed deviations of the exponents from $-1/6$ and are not captured by model I.

The main statement of the current section is that spatial variations of solvent quality do not seem to change the characteristic attribution of rate-size relations or the interpretation to mechanism (i) dramatically, but only introduce a slight change of exponents, which is consistent with experimental observations.

6.4 Rate-size relations for the SFIMM- and CPMM-profiles

Application of the SFIMM and CPMM mixing profiles to model I in section 5.4 showed that CPMM-profiles reproduce scaling laws $R \propto v^\alpha$ with $\alpha \approx -1/6$ while the SFIMM-profiles do not. In the present section it is briefly investigated how these mixing profiles connect to model II. The physical parameters are

- the mean polymer fraction f_P,
- the segments per polymer molecule N,
- the interaction parameters of the good and selective solvent χ_{GS} and χ_{SS},
- the time scale t_0,
- the premixed selective solvent volume fraction $\varphi_{SS}^{(1)}$,
- the maximum selective solvent volume fraction φ_{max}
- the flow rate v, and
- the initial lamella position x_1.

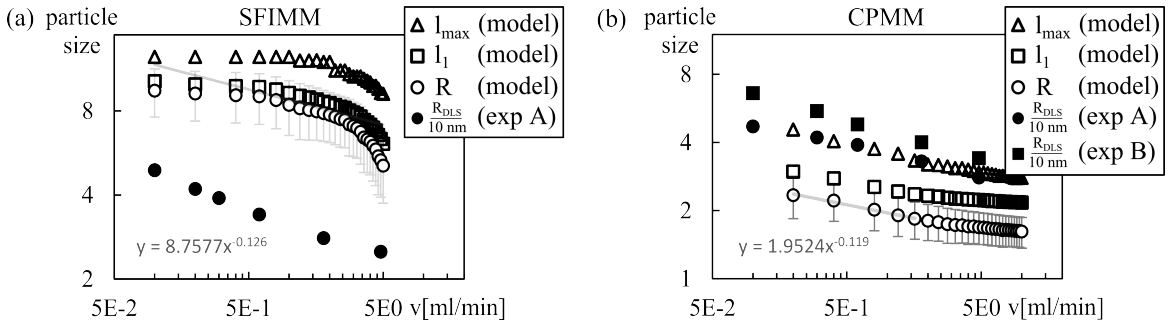

Figure 6.5: *Droplet sizes simulated by model II with SFIMM- (a) and CPMM-mixing profiles (b) in direct comparison to experimental data. All three measures for droplet radii are shown in dependence on the flow rate v, and the results are averaged over the same initial lamella positions as in figure 5.15. Error bars correspond to R and indicate the polydispersity ΔR from equation 5.48. The grey lines are trend lines to data points of R and the corresponding equation is shown in the diagram. The solid symbols represent the experimental data from figure 1.3 (a), just like in figure 5.15. Standard deviations from averaging over different initial conditions are similar to figure 6.2 and not shown for the sake of clarity.*

This list is identical to subsection 5.4.1 except that χ_{GS} and χ_{SS} are not substituted by φ_{Spin} and $\chi^{(max)}$. The physical parameters are set to $f_P = 0.0388$, $N = 14$, $\chi_{SS} = 2$, $\chi_{GS} = 0$, $t_0 = 10^{-6}$ seconds, $\varphi_{SS}^{(1)} = {}^{(1-f_P)}/_2 = 0.482$, and $\varphi_{max} = {}^{(1+\varphi_{SS}^{(1)})}/_2 = 0.741$. The spinodal composition is calculated to $\varphi_{Spin} = 0.5$, and numerical parameters are taken from to subsection 5.4.1. Simulation results are given by figure 6.5.

Like in the case of linear mixing profiles the qualitative progression does not differ from the results obtained with model I (cp. figure 5.15). In the CPMM there appears an asymptotic regime at $v > 1.6$ ml/min, but data points in the non-asymptotic regime still exhibit a scaling behavior. Although the exponent -0.119 is a little bit lower it is still in the experimental range given by figure 1.3. The characteristic progression of rate-size relations in figure 6.5 (a) closely resembles figure 5.15 (c), so two different implementations of solvent mixing (model I and model II) produce almost identical progressions. Therefore, the implementation of solvent mixing is unlikely to cause the deviation of simulation results for SFIMM-profiles from the experimentally observed scaling behavior (cp. second item in the list at the end of subsection 5.4.2 A).

6.5 Comparison of an effective two- and a three-component system

The dynamics of model II are only meaningful in situations where they are consistent with the standard approach for phase separation dynamics in three-component systems. In case of a local coupling model, this standard approach is given by equation 2.12 with $\alpha = P, SS, GS$. In the present section we compare an effective two-component system to such conventional three-component dynamics. However, the effective two-component system under consideration is not directly model II but a canonical version of it. This means we substitute the relation for the chemical potential μ_s, i.e. equation 6.39, by another equation that keeps $\varphi_{SS} = {}^1/_V \int \phi_{SS}(\vec{r}, t)\, d\vec{r}$ fixed at any time t. The reason why we consider a canonical version of model II is because we want to exclusively examine the critical assumptions concerning phase

separation dynamics and these critical assumptions relate to equations 6.26 and 6.33 in model II, but not the time dependence of μ_s in equation 6.39. If we took solvent mixing into account, we would corrupt the comparability of the two models since we also had to find an implementation of solvent mixing into the conventional three-component dynamics. And since solvent mixing had to be implemented differently from model II, we would not be able to distinguish if discrepancies are generated by the implementation of solvent mixing or the critical assumptions about dynamics.

6.5.1 Equations for the canonical dynamics

A canonical three-component system comprises one dynamical equation like 5.7 for each composition field. Neglecting thermal fluctuations, the equations read

$$\frac{\partial \phi_P}{\partial t} = -\nabla \cdot J_P = \nabla \cdot \left(\frac{D_0}{k_B T} \phi_P \left[\nabla \frac{\delta F_0}{\delta \phi_P} + Z \right] \right), \tag{6.52}$$

$$\frac{\partial \phi_{SS}}{\partial t} = -\nabla \cdot J_{SS} = \nabla \cdot \left(\frac{D_S}{k_B T} \phi_{SS} \left[\nabla \frac{\delta F_0}{\delta \phi_{SS}} + Z \right] \right), \tag{6.53}$$

and

$$\frac{\partial \phi_{GS}}{\partial t} = -\nabla \cdot J_{GS} = \nabla \cdot \left(\frac{D_S}{k_B T} \phi_{GS} \left[\nabla \frac{\delta F_0}{\delta \phi_{GS}} + Z \right] \right). \tag{6.54}$$

As a free energy functional we use F_0 defined by equations 6.22 and 6.23, which was the starting point for the deviation of model II. The constraining force Z is added to ensure incompressibility $\sum_{i \in \mathcal{C}} J_i = 0$, where $\mathcal{C} \coloneqq \{P, SS, GS\}$ is the set of component indices and

$$J_i = -\frac{D_i}{k_B T} \phi_i \left[\nabla \frac{\delta F_0}{\delta \phi_i} + Z \right] \tag{6.55}$$

the volume flux density of component i. It immediately follows from the incompressibility constraint that the differential equation for ϕ_{GS}, for example, can be substituted by the algebraic equation $\phi_{GS} = 1 - \phi_P - \phi_{SS}$ and that the constraining force is given by

$$Z = -\frac{D_0 \phi_P \nabla \frac{\delta F_0}{\delta \phi_P} + D_S \phi_{SS} \nabla \frac{\delta F_0}{\delta \phi_{SS}} + D_S \phi_{GS} \nabla \frac{\delta F_0}{\delta \phi_{GS}}}{D_0 \phi_P + D_S \phi_{SS} + D_S \phi_{GS}}. \tag{6.56}$$

Assuming $D_0 = D_S$ and inserting Z into J_P and J_{SS} leads to

$$J_P = -\frac{D_0}{k_B T} \left[\phi_P (1 - \phi_P) \nabla \left(\frac{\delta F_0}{\delta \phi_P} - \frac{\delta F_0}{\delta \phi_{GS}} \right) - \phi_P \phi_{SS} \nabla \left(\frac{\delta F_0}{\delta \phi_{SS}} - \frac{\delta F_0}{\delta \phi_{GS}} \right) \right] \tag{6.57}$$

and

$$J_{SS} = -\frac{D_0}{k_B T} \left[\phi_{SS} (1 - \phi_{SS}) \nabla \left(\frac{\delta F_0}{\delta \phi_{SS}} - \frac{\delta F_0}{\delta \phi_{GS}} \right) - \phi_P \phi_{SS} \nabla \left(\frac{\delta F_0}{\delta \phi_P} - \frac{\delta F_0}{\delta \phi_{GS}} \right) \right]. \tag{6.58}$$

The normalized relative chemical potentials are

$$\begin{aligned} \frac{1}{k_B T} \left(\frac{\delta F_0}{\delta \phi_P} - \frac{\delta F_0}{\delta \phi_{GS}} \right) &= \frac{\ln(\phi_P)}{N} - \ln(1 - \phi_P - \phi_{SS}) + \frac{1}{N} - 1 \\ &+ (\chi_{SS} - \chi_{GS}) \phi_{SS} + \chi_{GS} (1 - 2\phi_P) - \frac{\lambda}{k_B T} \Delta \phi_P \end{aligned} \tag{6.59}$$

and

$$\frac{1}{k_BT}\left(\frac{\delta F_0}{\delta\phi_{SS}}-\frac{\delta F_0}{\delta\phi_{GS}}\right)=\ln(\phi_{SS})-\ln(1-\phi_P-\phi_{SS})+(\chi_{SS}-\chi_{GS})\phi_P. \tag{6.60}$$

Inserting the fluxes from equations 6.57 and 6.58 with the relative chemical potentials from equations 6.59 and 6.60 into the dynamical equations $\frac{\partial\phi_i}{\partial t}=-\nabla\cdot J_i$ with $i\in\{P,SS\}$ yields the conventional model equations to describe phase separation in an incompressible three-component system. Random perturbations of a homogeneous state with $(\phi_P(\vec{r},0),\phi_{SS}(\vec{r},0))=(f_P,\varphi_{SS})$ are used as initial conditions and we apply periodic boundary conditions. To solve the two differential equations numerically, the schemes from equations 5.38 and 5.41 can be applied with

$$\hat{G}_j^{(n)}(\vec{k})=\mathcal{F}_{\vec{k}}\left[\left(-J_j^{(n)}(\vec{r}_s)\right)_s\right],$$

where J_j is the j-th component of J_P or J_{SS} in the dynamical equation of ϕ_P and ϕ_{SS}, respectively. Gradients in a flux are calculated by discrete Fourier transformations and the first order time accurate scheme is used in the following. In the scheme for the evolution equation of ϕ_P we choose the damping coefficient $\alpha=1/8$ as usual and for ϕ_{SS} we set $\alpha=0$ because it contains no Δ^2-term. The spinodal line is determined from the Hessian H of the homogeneous free energy contribution

$$\begin{aligned}\frac{f_0}{k_BT}&=\frac{\phi_P}{N}\ln(\phi_P)+(1-\phi_P-\phi_{GS})\ln(1-\phi_P-\phi_{GS})\\&+\phi_{GS}\ln(\phi_{GS})+\chi_{SS}\phi_P(1-\phi_P-\phi_{GS})+\chi_{GS}\phi_P\phi_{GS}\end{aligned} \tag{6.61}$$

with respect to ϕ_P and ϕ_{GS}. It is

$$H=\begin{pmatrix}\frac{1}{N\phi_P}+\frac{1}{\phi_{SS}}-2\chi_{SS} & \frac{1}{\phi_{SS}}-(\chi_{SS}-\chi_{GS})\\ \frac{1}{\phi_{SS}}-(\chi_{SS}-\chi_{GS}) & \frac{1}{1-\phi_P-\phi_{SS}}+\frac{1}{\phi_{SS}}\end{pmatrix}. \tag{6.62}$$

The system is stable if f_0 is convex, which is equivalent to the principal minors of H being positive. The first principal minor of H reads

$$h_1(\phi_P,\phi_{SS})=\frac{1}{N\phi_P}+\frac{1}{\phi_{SS}}-2\chi_{SS}, \tag{6.63}$$

the second one is

$$\begin{aligned}h_2(\phi_P,\phi_{SS})=&\left(\frac{1}{N\phi_P}+\frac{1}{\phi_{SS}}-2\chi_{SS}\right)\left(\frac{1}{1-\phi_p-\phi_{SS}}+\frac{1}{\phi_{SS}}\right)\\&-\left(\frac{1}{\phi_{SS}}-(\chi_{SS}-\chi_{GS})\right)^2,\end{aligned} \tag{6.64}$$

and the spinodal solvent composition φ_{Spin} of the conventional three-component model is defined by

$$\min\{h_1(f_P,\varphi_{Spin}),h_2(f_P,\varphi_{Spin})\}=0. \tag{6.65}$$

As already mentioned, the effective two component system we consider in the present

section is a canonical version of model II, where equation 6.39 is substituted by

$$\varphi_{SS} \equiv f_{SS} = \frac{1}{V}\int_V \phi_{SS}(\vec{r},t)\,d\vec{r} = \frac{1}{V}\int_V \frac{1-\phi_P(\vec{r})}{e^{\Delta\chi\phi_P(\vec{r})-\mu_s}+1}\,d\vec{r} \tag{6.66}$$

to keep f_{SS} constant. If equation 6.39 was not substituted, the two models would not be comparable, because in the three-component system f_{SS} is fixed while it varies in model II with equation 6.39. The $\vec{r}$-independent relative chemical potential μ_s for a given φ_{SS} is determined by a bisection method after spatial discretization of the integral in equation 6.66 with a rectangle method.

The adjustable physical parameters in both models are f_P, N, χ_{SS}, χ_{GS} and $f_{SS} = \varphi_{SS}$. In the following, lengths and times are given in units of $l_0 = \sqrt{\lambda/k_BT}$ and $t_0 = l_0^2/D_0$ again, which allows to substitute $D_0 \mapsto 1$ in equations 6.57 and 6.58 as well as $\lambda \mapsto k_BT$ in equation 6.59 without loss of generality.

6.5.2 Comparison of particle sizes

For conventional three-component dynamics the temporal evolution of polymer volume fraction profiles is qualitatively identical to model II, which allows an analogous evaluation procedure. The left panel in figure 6.6 shows droplet sizes at transition time. Large symbols are simulated with conventional three-component dynamics and the small ones with the canonical version of model II. Data points in figure 6.6 (a) represent simulation results for a parameter set with a low polymer volume fraction of $f_P = 0.038$ and a corresponding spinodal solvent composition $\varphi_{Spin} = 0.462$. The value of φ_{Spin} is identical in both canonical models and simulations have been performed for the mean selective solvent volume fractions $\varphi_{SS} = 0.525$, 0.550, 0.600, 0.650, and 0.700. The relative deviation between the simulation results is shown in the right panel and it is evidently smaller than 3%. Consequently, the models agree very well and the assumption of fast solvent relaxation that is made by model II is valid. Although solvent and polymer segment diffusion coefficients are assumed to be equal, i.e. $D_S = D_0$, the interdiffusion between the good and selective solvent can still be fast in comparison to the polymer phase separation because fluxes in equations 6.52 - 6.54 are proportional to volume fractions (the prefactors in front of the squared brackets read ${}^{D_i}/_{k_BT\phi_i}$). So as long as $\phi_P \ll \phi_{SS}, \phi_{GS}$ holds, the fluxes of the solvents are much larger than the fluxes of the polymer and the total solvent. This is possible because the incompressibility constraint only enforces the diffusion of the *total* solvent to be on time scales of polymer phase separation. The variation of good and selective solvent profiles *within* a slowly varying $\phi_S = \phi_{GS} + \phi_{SS}$ can still be fast. In the early stages when particle sizes are determined, the approximate values of prefactors read $D_0 f_P$, $D_S f_{SS}$ or $D_S f_{GS}$. Since $f_P = 0.038$, while $f_{SS}, f_{GS} \geq 0.3$, the prefactors are one order of magnitude larger for the solvents than for the polymer. Figure 6.6 (b) shows the same as (a) for a higher mean polymer volume fraction of $f_P = 0.100$ with a corresponding spinodal solvent composition $\varphi_{Spin} = 0.248$ at $\varphi_{SS} = 0.30$, 0.35, 0.40, 0.45, 0.50. For $\varphi_{SS} \geq 0.35$ the deviations are less than 6% and the models also agree. At $\varphi_{SS} = 0.30$, however, there is a significant deviation of up to 40%. As the distance $\varphi_{SS} - \varphi_{Spin} = 0.3 - 0.248 = 0.052$ is comparable to its counterpart for the low volume fraction in (a), $0.525 - 0.462 = 0.063$, the deviation should not be caused by that distance. It most likely originates from the fact that the selective solvent volume fraction is 0.3 while polymer

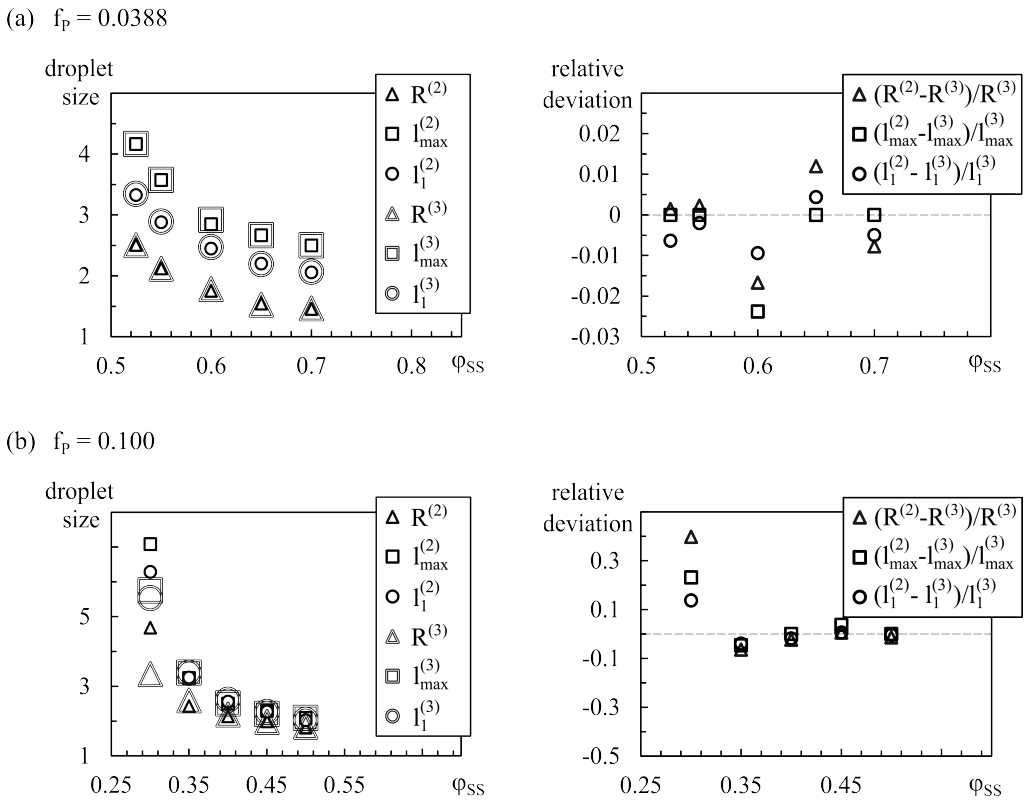

Figure 6.6: *Comparison of droplet sizes in a conventional three- and an effective two-component system at fixed mean selective solvent volume fractions φ_{SS}. $x^{(3)}$ with $x \in \{R, l_{max}, l_1\}$ denotes simulation results from the conventional three-component system and $x^{(2)}$ the results from the effective two-component system. The left panel in (a) displays a direct comparison of simulation results for $f_P = 0.038$ at different φ_{SS} and the right panel shows the corresponding relative deviations, where the dashed line represents the zero-axis. (b) shows the same for $f_P = 0.100$. Simulation results are averaged over five simulation runs with different random initial conditions with an amplitude of 0.001. The remaining parameters are $N = 14$, $\chi_{SS} = 2$ and $\chi_{BS} = 0$.*

volume fraction is 0.1. Therefore, their fluxes in the very early stages of phase separation become comparable and the assumption of instantaneous solvent relaxation for fixed polymer volume fraction profiles distorts the results.

As a consequence, the results from the present section confirm that an effective two-component model is a reasonable approximation for incompressible and dilute polymer solutions. As the polymer volume fractions in the experiments are very low (cp. $f_P = 0.004$ in subsection 5.3.5), effective two-component systems should be suited to describe the co-solvent method at experimental conditions.

Note that the exclusive agreement in dilute solutions expresses the conceptual difference between the assumption behind immediate solvent relaxation in effective two-component systems and an adiabatic approximation like the Born Oppenheimer approximation. The Born Oppenheimer approximation exploits the fact that the relaxation time of *every single* electron is very low compared to time scales of nuclear motion. In the context of the present work, an analogous adiabatic approximation would assume $D_{GS}, D_{SS} \gg D_0 = ND_P$, where D_0, D_{GS}, and D_{SS} are the diffusion coefficients of polymer, good, and selective solvent

segments, respectively. Such an approximation implied single solvent segments to diffuse much faster than monomers of a polymer chain and would also be valid in dense polymer solutions. But since both solvent and polymer segments possess a comparable molecular volume, it is approximately $D_0 = D_{GS} = D_{SS}$ in a local coupling model. The central assumption behind model II reads $\frac{\partial \phi_{GS}}{\partial t}, \frac{\partial \phi_{SS}}{\partial t} \gg \frac{\partial \phi_P}{\partial t}$. If $D_0 = D_{GS} = D_{SS}$, that assumption is only valid in dilute solutions with $\phi_{GS}, \phi_{SS} \gg \phi_P$, because fluxes are proportional to $D_0\phi_P$, $D_0\phi_{GS}$, and $D_0\phi_{SS}$.

Model I has to be excluded from figure 6.6, because if the constant selective solvent volume fractions φ_{SS} used in figure 6.6 are inserted into equation 5.21, the corresponding system in model I is located outside the spinodal area for the most part. As a result, model I disagrees with the other two models and χ_{GS}, χ_{SS} in equation 5.21 cannot be viewed as the experimentally measurable interaction parameters of the components. Due to the qualitative similarity of rate-size relations from model I and II, it might be possible to view them as fit parameters and construct an approximate mapping to physical χ-parameters, but such a mapping should be redundant when model II is already available.

6.6 Chapter summary and main conclusions

Section 6.1 shows that model I is equivalent to three-component dynamics with the constraint of spatially homogeneous solvent compositions $\phi_{SS}(\vec{r},t)/\phi_S(\vec{r},t) = \varphi_{SS}(t)/(1-f_P)$. In general, this constraint is, of course, unphysical because the percentage of good and selective solvent in a real solvent mixture at a specific position depends on the local polymer volume fraction $\phi_P(\vec{r},t)$. The homogeneous state at $t = 0$ satisfies the constraint because $(\phi_{SS}(\vec{r},0), \phi_S(\vec{r},0)) = (\varphi_{SS}(0), 1 - f_P)$ (except for an initial perturbation with a very small amplitude), but the longer phase separation progresses the more inaccurate the constrained dynamics of model I become. The reason why rate-size relations from model I still reflect qualitative characteristics of experimental data is most likely that particle sizes are determined while composition fluctuations are low, i.e. close to homogeneous states with $\phi_{SS}(\vec{r},t) \approx \varphi_{SS}(t)$, where the constraint is not strictly valid but apparently not yet inaccurate enough to cause a complete misrepresentation of experimentally observed trends. As a result, the possibility to capture experimental trends by ϕ_P-*independent* solvent conditions may be viewed as another indication that the response of early stage coarsening to solvent mixing constitutes the dominating determinant in the co-solvent method. The strength of model I is the illustrative interpretation to the working principle of size-controlled assembly but not a realistic description of solvent mixing.

In section 6.2 we refine the description of solvent mixing by developing a phenomenological effective two-component model, called model II, that accounts for $\phi_P(\vec{r})$-dependent solvent compositions. The $\phi_P(\vec{r})$-dependence is implemented by algebraically specifying a relative chemical potential μ_s of solvents in equilibrium with fixed polymer volume fraction profiles. In sections 6.3 and 6.4 we apply model II to estimate the general effect of spatially varying solvent conditions on rate-size relations. The characteristic attribution of rate-size relations from model II is found to be qualitatively identical to model I, a perturbation analysis in subsection 6.3.3 verifies that droplet sizes are still determined during the very early stages of phase separation, and the response to variations in temperature or the mean polymer volume fraction is also very similar. The main difference between rate-size relations from model

I and model II is of quantitative nature: while the perturbation theory for model I with linear mixing profiles always predicts scaling laws $R \propto s^{-1/6}$ in the non-asymptotic regime, the effective exponents predicted by the perturbation theory for model II depend on the choice of physical parameters. Consequently, spatially varying solvent conditions introduce degrees of freedom that describe a deviation of exponents from $-1/6$, which also appears in experiments (cp. figure 1.3). In section 6.5 the canonical version of model II is shown to agree with conventional incompressible three-component dynamics in dilute polymer solutions (cp. figure 6.6). This agreement constitutes the most crucial improvement of model II in comparison to model I.

The advantage of model II over conventional three-component models is the mathematical structure of its coupling interface for solvent mixing. While conventional three-component dynamics would require the specification of potentially complicated source terms or Neumann conditions at the boundaries of a fluid element, model II simply replaces the algebraic coupling interface from model I (equation 5.21) by another one (cp. equation 6.41) without introducing any significant additional computational cost. That means, the only differential equation in model II is nothing but a Cahn-Hilliard equation with periodic boundary conditions and the solvent mixing process – including its dependence on micromixer geometries and flow rates – is still completely incorporated into an algebraic relation for the interaction term in the free energy. Hence, compared to conventional three-component dynamics, our approach leads to a much easier handling of solvent mixing from a mathematical point of view as principal results (e.g. the application of a perturbation theory) and numerical integrators can be directly transferred from model I. On top of that, the already existing unconditionally stable numerical integration schemes for the Cahn-Hilliard equation like the one from Vollmayr-Lee and Rutenberg [136] should be applicable as well. The numerical implementation of model II should be generally even more robust than the implementation of conventional three-component dynamics in dilute solutions. In conventional three-component dynamics the width of time steps in explicit or semi-implicit integration schemes is limited by the stability conditions for the differential equations describing the fast solvent motion, whereas in model II time steps can be chosen on scales of the slow polymer motion because the fast solvent motion only appears as an algebraic relation. For these reasons, model II constitutes probably one of the computationally most efficient multiscale implementations to describe size-controlled assembly with a $\phi_P(\vec{r})$-dependent solvent quality.

As concepts from equilibrium thermodynamics are applied to derive model II, the concomitant refinement of solvent mixing should be exclusive to continuum theories, which demonstrates another advantage of continuum models over particle models when it comes to the description of size-controlled assembly.

In essence, model II combines the advantages of model I with spatially varying solvent conditions that agree with conventional three-component dynamics. However, the agreement only holds in incompressible dilute polymer solutions. Since incompressible dilute solutions correspond to experimental conditions of the co-solvent method and since the implementation of solvent mixing for CPMM-profiles reproduces experimentally observed trends as well (cp. figure 6.5 b), effective two-component models like model II[1] might be a promising foundation for potential quantitative descriptions of size-controlled assembly on realistic time scales of

[1]Probably with additional $|\nabla\phi_{GS}|^2$-, $|\nabla\phi_{SS}|^2$-, or $\chi_S\phi_{SS}\phi_{GS}$-terms in the free energy F_0 from equation 6.22. χ-parameters may also depend on temperature and volume fractions as proposed by Wolf [153].

solvent mixing. This finding is the final conclusion of chapter 6. Therefore, a logical next step would be checking whether model II provides a sufficient accuracy by inserting experimentally measured parameters and directly compare simulated droplet sizes to experimentally determined particle sizes. But because a direct comparison would require experimental data for homopolymers and corresponding input parameters which are both, unfortunately, not available, we leave the quantitative comparison for potential future work. We also note that the consistency of model II with conventional three-component dynamics was tested for only two sets of physical input parameters, so a more detailed comparison could be subject to future work as well.

PART III

CONTROLLED ASSEMBLY OF COPOLYMERS: SCF-EPD MODELS

Preliminary Remark

We have not mentioned it up to this point, but there is yet another important attribute of drug delivery systems: their morphology. Like the particle size, the morphology is affected by solvent mixing [22, 23]. However, while experimentally observed trends for particle sizes in diblock-copolymer solutions (cp. figure 1.3) are found to be reproduced by the homopolymer models from part II, complex morphologies cannot be captured by these models. To include the effect of solvent mixing on particle morphologies into our investigations, we have to couple solvent mixing into a more elaborate field theory and drop the restriction to homopolymers.

To this end, in part III the dynamics of phase separation is described by combining the Self Consistent Field Theory (SCF) for a diblock-copolymer solution with External Potential Dynamics (EPD). This combination will be refered to as the SCF-EPD equations in the following. It has been successfully applied to study spontaneous self-assembly of copolymers [88, 89] and is not only able to capture various particle morphologies but also introduces a steric stabilization of nanoparticles [88]. Therefore, we do not need to employ an artificial stabilization method like in model I and II but can simulate stable particles instead of just droplets. In addition, the SCF-EPD model eliminates some technical assumptions from part II, namely local kinetic coupling and the utilization of a Flory-Huggins-de Gennes free energy functional. The validity of the SCF model is not restricted to low fluctuation amplitudes. To describe solvent mixing we apply time dependent interaction parameters in the first place since they are easy to implement and because we learned in part II that the qualitative behavior of simulation results is similar to the results obtained from time dependent chemical potentials.

Chapter 7

A numerical scheme to handle the stiffness of the SCF-EPD equations

Although inserting time dependent interaction parameters into the SCF-EPD equations is easy, finding a numerical implementation that enables a satisfactory evaluation turned out to be rather non-trivial. In the present chapter we are going to study occurring numerical problems and develop an appropriate implementation before the simulation results are presented in chapter 8.

7.1 The SCF-EPD equations for a diblock-copolymer solution

This section briefly recapitulates the SCF-EPD equations from He and Schmid [88]. In the process, a canonical ensemble of volume V containing a solvent S and an AB-diblock-copolymer P at temperature T is considered. Each polymer molecule is a Gaussian chain composed of N monomers spread over the two different blocks labeled by A and B with identical Kuhn lengths b. n_A and n_B represent the total number of A- and B-monomers in the system, while N_A and N_B denote their number per polymer chain. n_S and $n_P = {}^{(n_A+n_B)}/_N$ are the total number of solvent and polymer molecules, respectively. In the following, f_S and f_P are the mean number fractions of solvent molecules and polymer monomers, i.e. $f_S = {}^{n_S}/_n$ and $f_P = {}^{Nn_P}/_n$ with $n = n_S + Nn_P$. If solvent molecules and monomers are attributed identical elementary volumes ν like in section 5.1, f_S and f_P can also be interpreted as volume fractions of molecules because

$$f_S = \frac{n_S}{n} = \frac{\nu}{\nu}\frac{n_S}{n} = \frac{V_S}{V} \text{ and } f_P = \frac{Nn_P}{n} = \frac{\nu}{\nu}\frac{Nn_P}{n} = \frac{V_P}{V}. \tag{7.1}$$

Defining the set of component indices $\mathcal{C} \coloneqq \{A, B, S\}$, ϕ_i with $i \in \mathcal{C}$ is introduced as a normalized number density,

$$\phi_i(\vec{r}) = \frac{\rho_i(\vec{r})}{\rho_0} \text{ where } \rho_0 = \frac{n}{V} = \frac{1}{\nu}. \tag{7.2}$$

In case the interaction potential between monomers is given by

$$\beta U[\phi_A, \phi_B, \phi_S] = \rho_0 \int_V \Big[\chi_{AB}\phi_A(\vec{r})\phi_B(\vec{r}) + \chi_{AS}\phi_A(\vec{r})\phi_S(\vec{r}) + \chi_{BS}\phi_B(\vec{r})\phi_S(\vec{r})$$

$$+\frac{\kappa_H}{2}\Big(\phi_A(\vec{r})+\phi_B(\vec{r})+\phi_S(\vec{r})-1\Big)^2\Big]d\vec{r}, \tag{7.3}$$

the SCF free energy functional F can be expressed as

$$\frac{1}{n}\beta F=-f_S\ln\left(\frac{Q_S}{Vf_S}\right)-\frac{f_P}{N}\ln\left(\frac{Q_PN}{Vf_P}\right)+\frac{1}{V}\int_V\Big[-\omega_A\phi_A-\omega_B\phi_B-\omega_S\phi_S$$

$$+\chi_{AB}\phi_A\phi_B+\chi_{AS}\phi_A\phi_S+\chi_{BS}\phi_B\phi_S+\frac{\kappa_H}{2}\left(\phi_A+\phi_B+\phi_S-1\right)^2\Big]d\vec{r}. \tag{7.4}$$

βF corresponds to $\beta\mathcal{F}$ from equation 2.29 except for an additive constant. χ_{ij} are the Flory-Huggins interaction parameters between monomers of type i and j, κ_H is the compressive modulus [91], $Q_S=\int_V e^{-\omega_S(\vec{r})}\,d\vec{r}$ the partition function of a solvent molecule in an external potential ω_S, and $Q_P=\int_V g(\vec{r},1)d\vec{r}$ the partition function of a single Gaussian polymer chain exposed to ω_A and ω_B. The end-segment distribution function $g(\vec{r},s)$ is obtained by solving the diffusion equation

$$\frac{\partial g}{\partial s}(\vec{r},s)=\Delta g(\vec{r},s)-N\omega(\vec{r})g(\vec{r},s)\text{ with }g(\vec{r},0)=1\text{ and }\omega=\begin{cases}\omega_A, & 0<s<c_A\\ \omega_B, & c_A<s<1\end{cases}, \tag{7.5}$$

where $s\in[0,1]$ is the contour variable along a polymer backbone normalized by N, while the spatial coordinate $\vec{r}$ is given in units of the polymer's radius of gyration $R_g=b\sqrt{N/6}$. $c_A={}^{N_A}/_N$ represents the fraction of A-monomers in a polymer chain, and analogously one can define $c_B={}^{N_B}/_N=1-c_A$ as the fraction of B-monomers. In combination with $g'(\vec{r},s)$, which also satisfies equation 7.5 with

$$\omega=\begin{cases}\omega_B, & 0<s<c_B\\ \omega_A, & c_B<s<1\end{cases}, \tag{7.6}$$

the densities for specified $\{\omega_A,\omega_B,\omega_S\}$ are calculated by

$$\phi_A(\vec{r})[\omega_A]=\frac{Vf_P}{Q_P}\int_0^{c_A}g(\vec{r},s)g'(\vec{r},1-s)\,ds, \tag{7.7}$$

$$\phi_B(\vec{r})[\omega_B]=\frac{Vf_P}{Q_P}\int_{c_A}^{1}g(\vec{r},s)g'(\vec{r},1-s)\,ds, \tag{7.8}$$

and

$$\phi_S(\vec{r})[\omega_S]=\frac{Vf_S}{Q_S}e^{-\omega_S(\vec{r})} \tag{7.9}$$

in accordance to subsection 2.2.2. The dynamical equations for the potential fields read

$$\frac{\partial\omega_i}{\partial t}(\vec{r},t)=-D_i\Delta\left(\frac{1}{\rho_0}\frac{\delta\beta F[\phi_A[\omega_A(\cdot,t)],\phi_B[\omega_B(\cdot,t)],\phi_S[\omega_S(\cdot,t)]]}{\delta\phi_i(\vec{r})}+\eta_i(\vec{r},t)\right)\text{ with }i\in\mathcal{C}$$

$$\text{and }D_i=\begin{cases}D_P={}^{D_0}/_N, & i=A,B\\ D_S=D_0, & i=S\end{cases} \tag{7.10}$$

(cp. equation 2.73), where D_0 is a segment diffusion coefficient. As already mentioned at the end of subsection 2.2.4, the random noise η_i that fulfills the fluctuation dissipation theorem

is usually substituted by a simpler expression in External Potential Dynamics. In reference [88] it is

$$\langle \eta_i(\vec{r},t)\rangle = 0$$

$$\langle \eta_i(\vec{r},t)\eta_j(\vec{r}',t')\rangle = \epsilon\delta_{ij}\delta(t-t')\delta(\vec{r}-\vec{r}'), \tag{7.11}$$

which should be only applied in non-equilibrium situations when the exact expression of a noise term is not essential. ϵ is an amplitude in $\mathrm{m}^3\mathrm{sec}$. Keeping in mind that

$$Q_P = Q_P\left[\omega_A[\phi_A],\omega_B[\phi_B]\right],\ Q_S = Q_S\left[\omega_S[\phi_S]\right], \tag{7.12}$$

$$\phi_i = -\frac{1}{\rho_0}\frac{n_P}{Q_P}\frac{\delta Q_P}{\delta\omega_i} \text{ for } i = A,B,\ \phi_S = -\frac{1}{\rho_0}\frac{n_S}{Q_S}\frac{\delta Q_S}{\delta\omega_S}, \tag{7.13}$$

and applying the variational chain rule, the functional derivatives of $F[\phi_A,\phi_B,\phi_S]$ at fixed f_P, f_S, and n become

$$\frac{1}{\rho_0}\frac{\delta\beta F[\phi_A,\phi_B,\phi_S]}{\delta\phi_A} = \chi_{AB}\phi_B + \chi_{AS}\phi_S + \kappa_H\left(\phi_A+\phi_B+\phi_S-1\right) - \omega_A, \tag{7.14}$$

$$\frac{1}{\rho_0}\frac{\delta\beta F[\phi_A,\phi_B,\phi_S]}{\delta\phi_B} = \chi_{AB}\phi_A + \chi_{BS}\phi_S + \kappa_H(\phi_A+\phi_B+\phi_S-1) - \omega_B, \tag{7.15}$$

$$\frac{1}{\rho_0}\frac{\delta\beta F[\phi_A,\phi_B,\phi_S]}{\phi_S} = \chi_{AS}\phi_A + \chi_{BS}\phi_B + \kappa_H(\phi_A+\phi_B+\phi_S-1) - \omega_S. \tag{7.16}$$

Inserting $\phi_i[\omega_i]$ from equations 7.7, 7.8, and 7.9 into the variational derivatives from equations 7.14, 7.15, and 7.16 closes equation 7.10. Together with equation 7.5, the equations in the last sentence constitute the SCF-EPD equations.

Initial conditions are chosen to be randomly perturbed homogeneous potentials ω_i for $i \in \mathcal{C}$, and equation 7.10 is solved numerically by algorithms based on the following sequence. First, g and g' are determined from the diffusion equation 7.5 for given ω, and then the densities ϕ_i are calculated by means of equation 7.7 – 7.9. The specification of ϕ finally allows to update the potentials via equation 7.10. This procedure is repeated at every time step. Independent physical parameters in the model are f_P, N_A, N_B, χ_{AB}, χ_{AS}, χ_{BS}, κ_H, and D_0. The spinodal line is calculated with the Flory-Huggins approximation $F_{FH}(f_P,f_S)$ of F, which is obtained by insertion of the homogeneous state into equation 7.4. After insertion of $f_A = c_A f_P$, $f_B = c_B f_P$, and $f_S = 1 - f_P$ the spinodal line is given by

$$0 = \frac{\partial^2 F_{FH}}{\partial f_P^2} = \frac{1}{2Nc_B f_P} + \frac{1}{2c_B(1-f_P)} + \chi_{AB}c_A - \chi_{AS}\frac{c_A}{c_B} - \chi_{BS}. \tag{7.17}$$

We implement solvent mixing into the SCF-EPD equations by inserting time dependent interaction parameters

$$\chi_{iS} = \chi_{iGS} + \frac{\chi_{iSS}-\chi_{iGS}}{1-f_P}\varphi_{SS}(t), \tag{7.18}$$

where φ_{SS} denotes the mixing profiles from part II and $i = A,B$. χ_{iGS} or χ_{iSS} refers to the interaction between i-monomers and the good or selective solvent, respectively.

7.2 Numerical instabilities in the conventional scheme

Since equations from He and Schmid [88] are applied, it is also natural to adopt their numerical integrators in the first instance. But when simulations with these integrators are performed, it becomes quickly evident that there is a wide range of physical parameters where the width of applicable time steps is dictated by numerical stability rather than desired accuracy. For the sake of terminological convenience we are going to refer to the integrators from reference [88] as the *conventional scheme*, because they are also used in further studies, e.g. reference [89], and because we do not know of any preceding attempts to address its stability issues.

The conventional scheme is described in subsection 7.2.1 and subsection 7.2.2 characterizes the associated numerical instabilities. The characterization is done exemplarily with two simulation runs and includes discussing which physical parameters produce instabilities, why we want to choose such parameters in the context of the present work, and what distinctive properties the instabilities possess. These considerations motivate the development of a new scheme in subsection 7.3.1 that allows three orders of magnitude larger step sizes

7.2.1 The conventional scheme

The conventional scheme comprises three integrators. One to solve equation 7.5 for g and g', one to approximate the integrals in equations 7.7 – 7.9, and one to determine the potential fields ω_i via equation 7.10 for all $i \in \mathcal{C}$.

Equation 7.5 is solved with a pseudo spectral method proposed by Tzeremes et al. [162]. Like in section 5.2 periodic boundary conditions in a d-dimensional spatial domain $[0, L_1) \times ... \times [0, L_d)$ are directly implemented by approximating unknown functions f with trigonometric interpolation polynomials

$$p^{[f]}(\vec{r}, s) = \sum_{\vec{k} \in \mathcal{K}} \hat{f}(\vec{k}, s) e^{i\vec{k}\cdot\vec{r}}. \tag{7.19}$$

The short hand notations $\vec{k} = (k_1, ..., k_d)^T$ and

$$\mathcal{K} = \left\{ \frac{2\pi}{L_1} \left(-\frac{n_1}{2} + 1 \right), ..., \frac{2\pi}{L_1} \frac{n_1}{2} \right\} \times ... \times \left\{ \frac{2\pi}{L_d} \left(-\frac{n_d}{2} + 1 \right), ..., \frac{2\pi}{L_d} \frac{n_d}{2} \right\} \tag{7.20}$$

are hereby repeated for the sake of reading comfort. $n_1, ..., n_d \in \mathbb{N}$ are even numbers and the spatial domain is again discretized into $m = n_1 \times ... \times n_d$ grid points, so the field $(\hat{f}(\vec{k}, s))_{\vec{k} \in \mathcal{K}}$ is the discrete Fourier transform of $(f(\vec{r_i}, s))_{i=0,...,m-1}$. If both fields are arranged in respective m-dimensional vectors $\underline{f}(s) = (f(\vec{r_0}, s), ..., f(\vec{r}_{m-1}, s))^T$ and $\underline{\hat{f}}(s)$, for instance in lexicographic order, the linearity of the discrete Fourier transformation implies that there exists a matrix W such that $\underline{\hat{f}}(s) = W \underline{f}(s)$. In the present case the unknown functions are g and ωg. Employing the corresponding interpolation polynomials with $f = g$ and $f = \omega g$ in equation 7.5 yields

$$\frac{\partial}{\partial s} \hat{g}(\vec{k}, s) = -|\vec{k}|^2 \hat{g}(\vec{k}, s) - N \widehat{\omega g}(\vec{k}, s) \tag{7.21}$$

or equivalently in matrix-vector notation

$$\frac{\partial}{\partial s} \underline{\hat{g}}(s) = -K \underline{\hat{g}}(s) - NW \underline{\omega g}(s) = -K \underline{\hat{g}}(s) - NW \Omega \underline{g}(s). \tag{7.22}$$

K is a diagonal matrix with the values of $|\vec{k}|^2$ as nonzero entries and $\Omega = \mathrm{diag}(\omega(\vec{r}_0), ..., \omega(\vec{r}_{m-1}))$. The matrix-vector notation can be cast into the form

$$\frac{\partial}{\partial s}\underline{\hat{g}}(s) = -K\underline{\hat{g}}(s) - NW\Omega W^{-1}W\underline{g}(s) = \left[-K - W(N\Omega)W^{-1}\right]\underline{\hat{g}}(s), \tag{7.23}$$

and if the s-axis is discretized into intervals of length ds, the exact solution $\underline{\hat{g}}(s+ds)$ for given $\underline{\hat{g}}(s)$ reads

$$\underline{\hat{g}}(s+ds) = e^{\left[-K-W(N\Omega)W^{-1}\right]ds}\,\underline{\hat{g}}(s). \tag{7.24}$$

Rewriting the matrix exponential to

$$e^{\left[-K-W(N\Omega)W^{-1}\right]ds} = e^{-W(N\Omega)W^{-1}ds/2 - Kds - W(N\Omega)W^{-1}ds/2} \tag{7.25}$$

and a twofold application of the Baker-Hausdorff identity leads to the approximation

$$e^{-W(N\Omega)W^{-1}ds/2 - Kds - W(N\Omega)W^{-1}ds/2} = e^{-W(N\Omega)W^{-1}ds/2}e^{-Kds}e^{-W(N\Omega)W^{-1}ds/2} \tag{7.26}$$

with a truncation error $\mathcal{O}(ds^3)$ in the exponent [162]. Because the Fourier matrix W is invertible it can be extracted from the exponents to arrive at

$$\begin{aligned}\underline{\hat{g}}(s+ds) &= We^{-N\Omega ds/2}W^{-1}e^{-Kds}We^{-N\Omega ds/2}W^{-1}\,\underline{\hat{g}}(s)\\ \Leftrightarrow \underline{g}(s+ds) &= e^{-N\Omega ds/2}W^{-1}e^{-Kds}We^{-N\Omega ds/2}\,\underline{g}(s).\end{aligned} \tag{7.27}$$

Expressing the m-dimensional vectors by their corresponding fields, re-substituting W multiplications by the discrete Fourier transformation $\mathcal{F}$ and remembering that K and Ω are diagonal yields an update rule for g at every $\vec{r}_i$ and s, which is

$$g(\vec{r}_i, s+ds) = e^{-N\omega(\vec{r}_i)ds/2}\mathcal{F}^{-1}_{\vec{r}_i}\left[\left(e^{-|\vec{k}|^2 ds}\mathcal{F}_{\vec{k}}\left[\left(e^{-N\omega(\vec{r}_i)ds/2}g(\vec{r}_i, s)\right)_{i=0,...,m-1}\right]\right)_{\vec{k}\in\mathcal{K}}\right]. \tag{7.28}$$

$\mathcal{F}^{-1}_{\vec{r}_i}$ denotes the inverse discrete Fourier transform evaluated at position $\vec{r}_i$ in the coordinate space and $\mathcal{F}_{\vec{k}}$ is the discrete Fourier transform evaluated at position $\vec{k}$ in the wave number space. This scheme is also used to update g' with the corresponding adaptation of ω (cp. equation 7.6).

Integrals in equations 7.7 – 7.9 are calculated by a standard Euler method. The discretized monomer densities read

$$\phi_j(\vec{r}) = \frac{V f_P}{Q_P}\sum_{i\in\mathcal{S}_j} g(\vec{r}, i\,ds)g'(\vec{r}, 1-i\,ds)ds \text{ for } j = A, B \tag{7.29}$$

with

$$\mathcal{S}_A = \{i : 0 < i\,ds < c_A\} \subset \mathbb{N},\ \mathcal{S}_B = \{i : c_A < i\,ds < 1\} \subset \mathbb{N},\ ds = 1/N. \tag{7.30}$$

The discretized partition functions are

$$Q_P = \sum_i g(\vec{r}_i, 1)\Delta l^d \text{ and } Q_S = \sum_i e^{-\omega_S(\vec{r}_i)}\Delta l^d, \tag{7.31}$$

where the sum over i covers all lattice points of the spatial grid. Therefore, it is

$$\phi_j(\vec{r}) = \frac{f_P m}{\sum_i g(\vec{r}_i)} \sum_{i \in \mathcal{S}_j} g(\vec{r}, i\,ds) g'(\vec{r}, 1 - i\,ds) ds \text{ for } j = A, B \tag{7.32}$$

and

$$\phi_S(\vec{r}) = \frac{f_S m}{\sum_i e^{-\omega_S(\vec{r}_i)}} e^{-\omega_S(\vec{r})} \tag{7.33}$$

at all grid point positions $\vec{r}$.

Equation 7.10 is solved with a pseudo spectral method similar to the evolution equations from model I and II. If the variational derivatives of the free energy are cast into the form

$$\frac{1}{\rho_0} \frac{\delta \beta F[\phi_A, \phi_B, \phi_S]}{\delta \phi_i} = \widetilde{F}_i - \omega_i \text{ for } i \in \mathcal{C} \tag{7.34}$$

the evolution equations for the potential fields become

$$\frac{\partial \omega_i}{\partial t} = -D_i \Delta (\widetilde{F}_i + \eta_i) + D_i \Delta \omega_i, \tag{7.35}$$

and insertion of trigonometric interpolation polynomials for ω_i and $\widetilde{F}_i + \eta_i$ immediately yields

$$\frac{\partial \hat{\omega}_i}{\partial t}(\vec{k}, t) = D_i |\vec{k}|^2 \mathcal{F}_{\vec{k}} \left[\left(\widetilde{F}_i(\vec{r}_j, t) + \eta_i(\vec{r}_j, t) \right)_{j=0,\ldots,m-1} \right] - D_i |\vec{k}|^2 \hat{\omega}_i(\vec{k}, t). \tag{7.36}$$

Integrating in time and approximating the integral of the last term on the right hand side by an implicit Euler formula and the integral of the first with an explicit one yields the first order time accurate update scheme

$$\hat{\omega}_i^{(n+1)}(\vec{k}) = \frac{\hat{\omega}_i^{(n)}(\vec{k})}{1 + h D_i |\vec{k}|^2} + \frac{h D_i |\vec{k}|^2}{1 + h D_i |\vec{k}|^2} \mathcal{F}_{\vec{k}} \left[\left(\widetilde{F}_i^{(n)}(\vec{r}_j) + \eta_i^{(n)}(\vec{r}_j) \right)_{j=0,\ldots,m-1} \right] \tag{7.37}$$

with

$$\omega_i^{(n+1)}(\vec{r}_j) = \mathcal{F}_{\vec{r}_j}^{-1} \left[\left(\hat{\omega}_i^{(n+1)}(\vec{k}) \right)_{\vec{k} \in \mathcal{K}} \right], \tag{7.38}$$

where h is the with of a time step and $x^{(n)}$ the numerical approximation to $x(\cdot, t_n)$ for $x \in \left\{ \omega, \hat{\omega}, \widetilde{F}_i, \eta_i \right\}$. Equations 7.28, 7.32, 7.33, and 7.38 constitute the conventional scheme. If the time integral of the first term on the right hand side in equation 7.36 is approximated with an Adams-Bashforth method and the integral over the second summand by an Adams-Moulton method (cp. equations 5.39 and 5.40), the corresponding second order time accurate integrator in Fourier space reads

$$\hat{\omega}_i^{(n+1)}(\vec{k}) = \frac{2 - D_i |\vec{k}|^2 h}{2 + D_i |\vec{k}|^2 h} \hat{\omega}_i^{(n)}(\vec{k})$$

$$+ \frac{D_i |\vec{k}|^2 h}{2 + D_i |\vec{k}|^2 h} \mathcal{F}_{\vec{k}} \left[\left(3(\widetilde{F}_i^{(n)}(\vec{r}_j) + \eta_i^{(n)}(\vec{r}_j)) - (\widetilde{F}_i^{(n-1)}(\vec{r}_j) + \eta_i^{(n-1)}(\vec{r}_j)) \right)_{j=0,\ldots,m-1} \right]. \tag{7.39}$$

This update rule is not part of the conventional scheme. But as a second order time accurate pseudo spectral method it possesses the lowest truncation errors of all integrators in the present chapter and will be used as a reference when we discuss numerical approximation

errors in subsection 7.3.3.

7.2.2 Characterization of numerical instabilities

The conventional scheme has been used for extensive parameter studies by He and Schmid [88, 89]. Their choices of physical parameters prove sufficient to simulate a variety of particle morphologies and both pathways of vesicle formation, but restrict to rather low solvent-phobic interactions χ_{BS} and low compressive moduli κ_H. In this context, 'low' refers to χ-parameters close to their spinodal values and κ_H not being much larger than 1. As polymer solutions typically possess extremely high compressive moduli, it would be preferable to perform simulations with a κ_H-value that is large enough to keep the sum $\phi_A(\vec{r},t)+\phi_B(\vec{r},t)+\phi_S(\vec{r},t)$ very close to 1 at any $(\vec{r},t)$. In the simulations from reference [88], for example, this is clearly not the case as already normalized densities of the solvent-phobic block alone peak at values of approximately 1.3. Additionally, an implementation of solvent mixing requires at least the interaction of the solvent-phobic block to increase. Due to the analogous implementation of solvent mixing to model I we already know that the size of particles in the limit of infinitely fast solvent mixing corresponds to the size of particles at a constant interaction parameter $\chi_{BS}(t) = \chi_{BS}^{(max)}$. So to allow a satisfactory evaluation of rate-size relations, $\chi_{BS}^{(max)}$ should be large enough for the non-asymptotic regime to extend over several decades of quench rates.

Applying sufficiently large compressive moduli or solvent-phobic interactions, however, creates complications with the conventional scheme. Given an arbitrary parameter set from He and Schmid [88, 89] as a reference, the sole increase of *either* χ_{BS} *or* κ_H produces a different respective numerical artifact with distinctive features. In the present subsection these features are exemplarily characterized using the set of physical parameters in table 7.1 as the reference. For this parameter set, the conventional scheme is numerically stable on a two-dimensional spatial grid of size $m = 256 \times 256$ with a lattice constant $\Delta l = 0.25$, a polymer chain discretization step $ds = 1/N$, and a time step $h = 0.005$. In the following, instabilities are provoked by variation of κ_H and χ_{BS} at constant step and lattice sizes. Since a qualitative analysis will be sufficient to identify the source of instabilities and to enable their compensation, we consider a mathematically rigorous stability analysis to go beyond the scope of the present work.

The numerical artifact that appears if the compressive modulus in the reference set is increased to $\kappa_H = 5$, for instance, is illustrated in figure 7.1. Figure 7.1 shows only density profiles ϕ_B, but ϕ_A, ϕ_S, and ω_i for $i \in \mathcal{C}$ look practically identical: the numerical artifact develops rapidly within 10 time steps and is characterized by the global appearance of a 'chessboard pattern' as depicted in the magnification at $n = 10$. It amplifies quickly and the simulation run aborts at $n = 14$ because density values exceed double precision limits. The unphysical alternation of densities and potential fields from grid point to grid point (a grid point corresponds to a pixel in the rightmost snapshot of 7.1) implies the artifact to

Parameter	f_P	N_A	N_B	χ_{AB}	χ_{AS}	χ_{BS}	κ_H	D_P	D_S
Value	0.1	2	15	1.05	0.0375	1.2	1.176	$1/N$	1

Table 7.1: *Reference set of physical parameters for the SCF-EPD model taken from [88].*

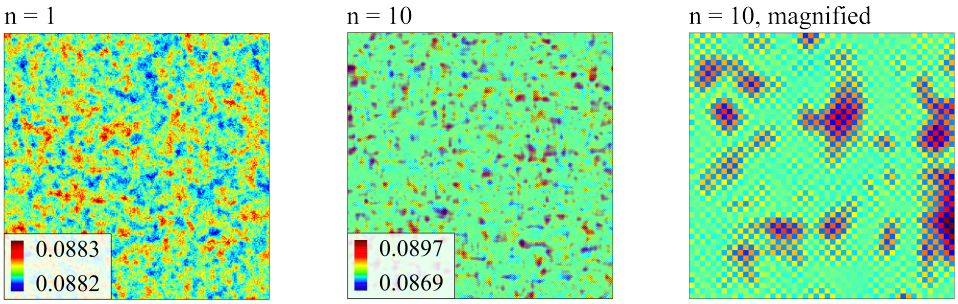

Figure 7.1: *Color coded density profile $\phi_B^{(n)}$ at two different time steps $n = 1$ and $n = 10$, simulated with the conventional scheme for the SCF-EPD equations to illustrate κ-instabilities. The compressive modulus is $\kappa_H = 5$ and the remaining physical parameters were taken from table 7.1. The snapshot on the right hand side is a magnification of a section with size 50×50 at $n = 10$.*

be caused by the modes with the largest wave numbers. Since κ_H is only present in the evolution equation for the potential fields as a prefactor of a Laplacian and since modes with the largest wave numbers are typically the most rapidly varying ones in diffusion type problems, the chessboard pattern is clearly a manifestation of a stiffness instability originating from the update scheme for the potential fields given by equation 7.37. Because the instability was triggered by an increase of κ_H, we term it *κ-instability*. The same stiffness instabilities also appear if the resolution is increased by decreasing the lattice constant Δl. Conveniently avoiding κ-instabilities by restriction to low κ_H-values was reasonable in references [88] and [89], but if controlled assembly is considered, such a workaround can become problematic due to a second instability that appears when low compressive moduli are combined with moderate interaction parameters.

The characterization of this second instability type also starts from the parameter set in table 7.1. The corresponding value of the spinodal solvent-phobic interaction reads $\chi_{BS}^{(Spin)} = 1.081$ according to equation 7.17. Thus, $\chi_{BS} = 1.2$ in table 7.1 is quite close to the spinodal line, rendering the particular quench depth $\chi_{BS} - \chi_{BS}^{(Spin)} = 0.119$ to be rather low. Ideally, a maximum quench depth of 1 as employed in model I would be desirable because it already proved to produce sufficiently large extensions of the non-asymptotic regime. But if only the solvent-phobic interaction in table 7.1 is increased to $\chi_{BS} = 1.4$, numerical instabilities appear in a simulation run. Consequently, the conventional scheme allows only a maximum quench depth of roughly $1.3 - 1.08 = 0.22$, which is four to five times smaller than the desired value 1. The development of the second instability fundamentally differs from κ-instabilities and is shown in figure 7.2. In contrast to the artifact associated with κ-instabilities, this one appears much later, when polymer aggregates with well defined interfaces have already formed. It is also not characterized by a the appearance of a global chessboard pattern but a local one restricted to the white-framed regions in figure 7.2. Figure 7.2 does not only illustrate the numerical artifact but it also provides necessary information to track its origin. First, the artifact is very pronounced at $n = 61935$ for $\phi_S^{(n)}$ in (b), while it is not visible for $\phi_B^{(n)}$ at the same time step. If we looked into the density profile for $\phi_A^{(n)}$ (not shown) there is also no visible artifact. The fact that the numerical artifact first appears in the density profile of the solvent indicates that it is not generated by the iteration along a polymer chain

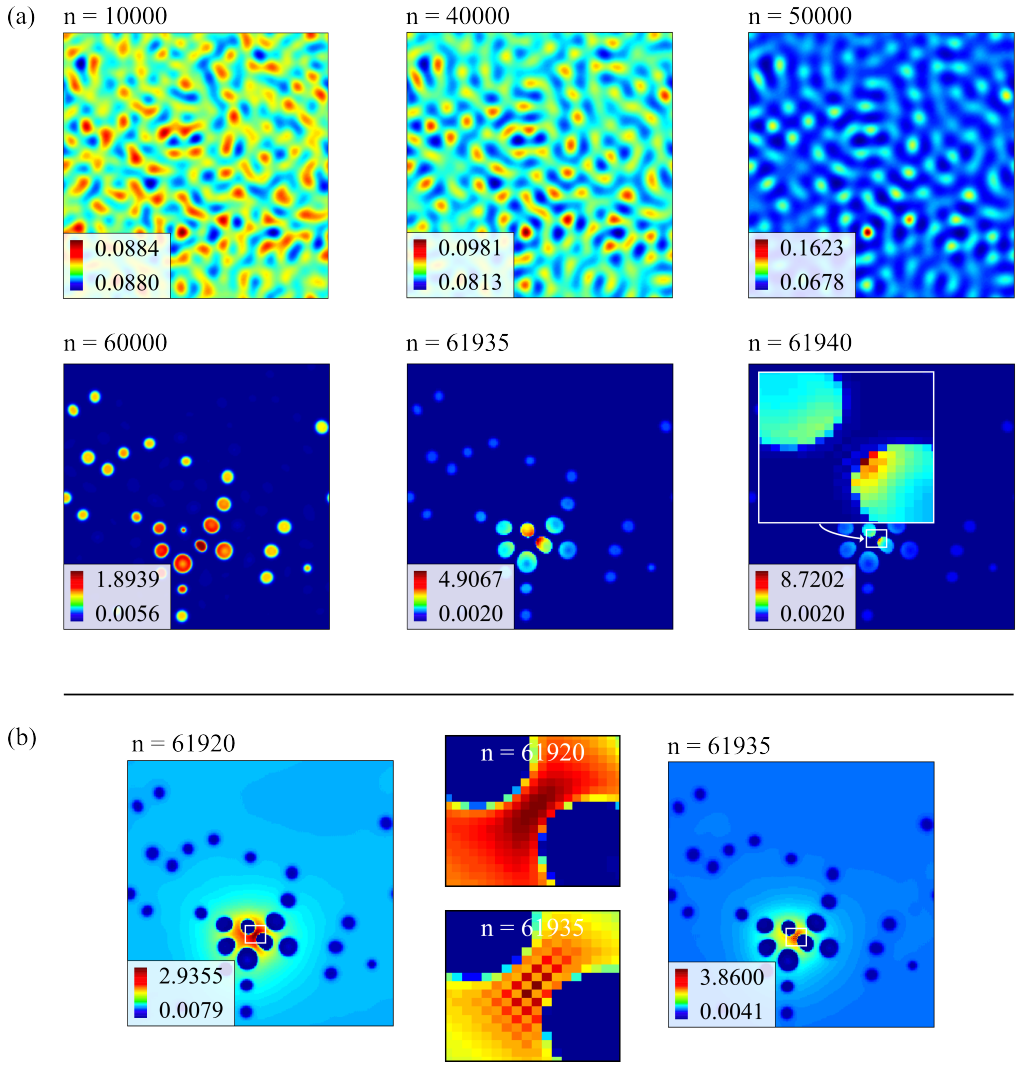

Figure 7.2: *Color coded density profiles simulated with the conventional scheme for the SCF-EPD equations to illustrate ϕ-instabilities. Physical parameters are given in table 7.1 except that $\chi_{BS} = 1.4$. (a) shows the density profile of the solvent-phobic block $\phi_B^{(n)}$ at different time steps n. At $n = 61940$ there is a weak local chessboard-patterned numerical artifact between two regions of high polymer density, which is magnified in the inset. One time step later (not shown) it is amplified to ϕ_B-values of over 4000 and two time steps later it exceeds double precision limits. The numerical artifact is not visible at earlier time steps. (b) shows the solvent density profile $\phi_S^{(n)}$ at $n = 61920$ on the left and $n = 61935$ on the right. The white framed regions are magnified in between and it is evident that a numerical artifact appears in regions of high solvent densities.*

in equation 7.28, but has to be caused by the numerical scheme for the evolution equation of the potential fields as well – most probably by the update scheme for ω_S because due to the larger diffusion coefficient, $D_S = ND_P$, the evolution equation for ω_S requires the lowest step widths to be stable and thus sets the stability constraint for the whole system. Second, the numerical artifact is characterized by alternating colors in each pixel, which is a clear indication for stiffness instabilities as discussed in the context of κ-instabilities. Third, the artifact appears exactly in the region with the highest solvent density, which is seen by a

comparison of the magnified parts in figure 7.2 (b). Due to the correlation to high densities we are going to refer to it as a *ϕ-instability*. Compendiously, a ϕ-instability is a stiffness instability that is coupled to locally high densities and caused by the update scheme from equation 7.37. The connection of this instability to large local densities of a component is also supported by its behavior observed in several other simulation runs. If the system size is decreased sufficiently enough, it vanishes and simulations are stable. In this case, it does not matter if the number of grid points or the lattice constant is reduced (as long as the reduction of Δl does not lead to another stiffness instability). Keeping the overall volume fraction of components constant results in a diminishing amount of molecules in the system when its size is decreased, and decreasing the total amount of molecules results in lower peak values of ϕ_i, which do not trigger the instability. Vice versa, an increase of the system size favors ϕ-instabilities. For example, by decreasing the lattice constant to $\Delta l = 1/3$, which is the original value in references [88] and [89], the ϕ-instability already appears at $\chi_{BS} = 1.3$.

The current subsection demonstrates that the conventional scheme is not well suited to deal with large compressive moduli due to κ-instabilities or large interaction parameters due to ϕ-instabilities. We should emphasize though that the time step was fixed at $h = 0.005$. It was not discussed how much it has to be decreased to perform stable simulations and how long they take. Such a discussion is provided in subsection 7.3.2 where the new scheme developed in the next section is directly compared to the conventional one.

7.3 A SEMI-IMPLICIT INTEGRATOR FOR THE POTENTIAL FIELD EQUATIONS

7.3.1 UPDATE RULE AND IMPLEMENTATION

Because both κ- and ϕ-instabilities are caused by the update rule for the potential fields, the aim of the present subsection is to find a numerically robust alternative for equation 7.37. The dynamical equations 7.10 can be written as

$$\omega_i(t_{n+1}) - \omega_i(t_n) = -D_i \int_{t_n}^{t_{n+1}} \left(\sum_{j \in \mathcal{C}_i} \left[(\chi_{ij} + \kappa_H)\, \Delta\phi_j \right] + \kappa_H \Delta\phi_i - \Delta\omega_i + \Delta\eta_i \right) dt, \quad (7.40)$$

where $\mathcal{C}_i \coloneqq \mathcal{C} \setminus \{i\}$ for $i = A, B, S$. As mentioned in section 5.2, a procedure to deal with stiffness in diffusion-type equations is to apply a numerical scheme where Laplacian-terms are approximated by implicit quadrature rules. In the simple example from equation 5.23 both the explicit and the implicit method can be algebraically inverted to obtain an expression for $\hat{\phi}^{(n+1)}$. As a result, the implicit scheme extends the stability region without significant additional computational cost when the integrator is implemented into a computer program. This is also true for the solvers of model I and II as well as the conventional scheme, where only $\Delta\omega_i$ is treated implicitly.

To gain a stabilization against κ- and ϕ-instabilities, implicit quadrature rules for terms involving a χ-parameter or κ_H on the right hand side of equation 7.40 are necessary. A direct implicit quadrature without further modification of equation 7.40 is of course possible, e.g. by an Euler Backward or a Crank-Nicholson method, but would introduce $\phi_A(t_{n+1})$ and $\phi_B(t_{n+1})$. As ϕ_A and ϕ_B are integrals of g and g', which are in turn solutions to a diffusion equation with an inhomogeneity $Ng\omega$ (cp. equation 7.5), the resulting equations for the numerical approximations to $g(\vec{r}_j, s, t_{n+1})$, $g'(\vec{r}_j, s, t_{n+1})$, $\phi_i(\vec{r}_j, t_{n+1})$ and $\omega_i(\vec{r}_j, t_{n+1})$ could not

be solved independently from one another. Since an algebraic inversion of a large nonlinear system of discretized integro-differential equations is not possible in general, one had to perform a numerical inversion with an iterative solver like Newton's method at any time step. Iterative methods add another layer of complexity to the problem, because implicit treatments might improve stability and allow faster simulations by virtue of larger step sizes on the one hand, but on the other hand their costly implementation also increases computation times per step. As a new numerical scheme would be useless if the additional computational cost outweighs the speedup of simulations gained by increasing step sizes within a desired accuracy for truncation errors, we do not only need to extend the stability region of the integrator for the potential fields but we also need find one with a possibly efficient implementation. Since the computational cost of iterative methods decreases with diminishing dimension of the system of equations they are applied to and since we cannot exclude the possibility to use such a method from the outset (it will actually turn out that we need one), a good starting point to find an efficient scheme should be trying to handle the stiffness of the potential field equations without touching the other integrators in the conventional scheme. By doing so, an iterative scheme is used to find only the $3m$ unknowns $\omega_i^{(n+1)}(\vec{r}_j)$ for all $i \in \mathcal{C}$ and $j = 0, ..., m-1$ instead of the $(6+2N)m$ unknowns $g^{(n+1)}(\vec{r}_j, s)$, $g'^{(n+1)}(\vec{r}_j, s)$, $\phi_i^{(n+1)}(\vec{r}_j)$ and $\omega_i^{(n+1)}(\vec{r}_j)$ for all $i \in \mathcal{C}$, $j = 0, ..., m-1$ and discretized positions s along the polymer chain with N monomers of distance $ds = 1/N$. This strategy involves a slight modification of equation 7.40 to prepare it for a semi-implicit integrator.

To this end, explicit ω-dependencies are extracted from all $\Delta\phi_i$. $\Delta\phi_S$ can be expressed exactly in terms of ω_S by means of equation 7.9. This leads to

$$\Delta\phi_S(\vec{r}) = \sum_{i=1}^{3} \frac{\partial^2}{\partial r_i^2}\left[\frac{Vf_S}{Q_S}e^{-\omega_S(\vec{r})}\right] = \frac{Vf_S}{Q_S}e^{-\omega_S(\vec{r})}\left[\sum_{i=1}^{3}\left(\frac{\partial\omega_S}{\partial r_i}(\vec{r})\right)^2 - \sum_{i=1}^{3}\frac{\partial^2\omega_S}{\partial r_i^2}(\vec{r})\right]$$

$$= \phi_S(\vec{r})\left[\nabla\omega_S(\vec{r})\right]^2 - \phi_S(\vec{r})\Delta\omega_S(\vec{r}), \tag{7.41}$$

which shows that $\kappa_H\Delta\phi_S$, for instance, contributes a term $\kappa_H\phi_S\Delta\omega_S$ to the right hand side of equation 7.40. The mathematical structure of this term matches the phenomenological characterization of the numerical artifacts associated with ϕ- and κ-instabilities. If the Laplacian is discretized, it becomes

$$\kappa_H\phi_S(\vec{r})\Delta\omega_S(\vec{r}) \mapsto \frac{\kappa_H\phi_S(\vec{r}_j)}{\Delta l^2}\delta\omega_S(\vec{r}_j), \tag{7.42}$$

where $\delta\omega_S(\vec{r}_j)$ is a short hand notation for the sum over nearest neighbors in the discrete Laplacian operator. As both κ_H and $\phi_S(\vec{r}_j)$ are prefactors of $\delta\omega_S$, their enhancement directly shrinks stability regions in the same manner as a decrease of Δl does. Because κ_H is independent from the position $\vec{r}_j$ it induces global instabilities, while $\phi_S(\vec{r}_j)$ provokes local instabilities only at positions where the solvent density is high. The same argumentation also holds for the first term on the right hand side of equation 7.41, $\kappa_H\phi_S(\nabla\omega_S)^2$. The similarity between the mathematical structure of its explicit ω-dependence and the exemplary characterization of numerical artifacts from subsection 7.3.3 leads to the conclusion that $\Delta\phi_S$ is a leading stiffness contribution, which is responsible for κ- and ϕ-instabilities.

To extract analogous explicit ω-dependencies from $\Delta\phi_A$ and $\Delta\phi_B$, the Feynman-Kac for-

mula is applied. It states that the solution g of the inhomogeneous diffusion equation

$$\frac{\partial g}{\partial s}(\vec{r},s) = \Delta g(\vec{r},s) - N\omega(\vec{r})g(\vec{r},s) \tag{7.43}$$

can be recursively defined by

$$g[\omega](\vec{r},s) = e^{-dsN\omega(\vec{r})} \int R_g \Phi(R_g\,(\vec{r}-\vec{r}\,'))g[\omega](\vec{r}\,',s-ds)d\vec{r}\,', \tag{7.44}$$

where $\Phi(\vec{r})$ is the normalized bond transition probability for a Gaussian chain [103]. In the following considerations neither the functional form of Φ nor the integral play a role and thus, the short hand notation

$$I(\vec{r},s) \coloneqq \int R_g \Phi(R_g\,(\vec{r}-\vec{r}\,'))g[\omega](\vec{r}\,',s-ds)d\vec{r}\,' \Rightarrow g[\omega](\vec{r},s) = e^{-dsN\omega(\vec{r})}I(\vec{r},s) \tag{7.45}$$

is used. Because

$$\Delta\phi_i(\vec{r}) = \frac{Vf_P}{Q_P}\Delta \int g(\vec{r},s)g'(\vec{r},1-s)ds$$

$$= \frac{Vf_P}{Q_P} \int g'(\vec{r},1-s)\Delta g(\vec{r},s) + 2\nabla g(\vec{r},s)\cdot\nabla g'(\vec{r},1-s) + g(\vec{r},s)\Delta g'(\vec{r},1-s)\,ds \tag{7.46}$$

with proper integration limits for $i = A, B$ like in equations 7.7 and 7.8, the first two derivatives of g and g' need to be calculated. They read

$$\frac{\partial g}{\partial r_i}(\vec{r}) = -e^{-dsN\omega(\vec{r})}I(\vec{r},s)dsN\frac{\partial\omega}{\partial r_i}(\vec{r}) + e^{-dsN\omega(\vec{r})}\frac{\partial I}{\partial r_i}(\vec{r},s)$$

$$=: g(\vec{r},s)\left[-dsN\frac{\partial\omega}{\partial r_i}(\vec{r}) + R_i^{(1)}(\vec{r},s)\right] \tag{7.47}$$

and

$$\frac{\partial^2 g}{\partial r_i^2}(\vec{r},s) = e^{-dsN\omega(\vec{r})}I(\vec{r},s)\left[\left(dsN\frac{\partial\omega}{\partial r_i}(\vec{r})\right)^2 - dsN\frac{\partial^2\omega}{\partial r_i^2}(\vec{r})\right]$$

$$-e^{-dsN\omega(\vec{r})}\left[2dsN\frac{\partial\omega}{\partial r_i}(\vec{r})\frac{\partial I}{\partial r_i}(\vec{r},s) - \frac{\partial^2 I}{\partial r_i^2}(\vec{r},s)\right]$$

$$=: g(\vec{r},s)\left[\left(dsN\frac{\partial\omega}{\partial r_i}(\vec{r})\right)^2 - dsN\frac{\partial^2\omega}{\partial r_i^2}(\vec{r})\right] + R_i^{(2)}(\vec{r},s). \tag{7.48}$$

The functions $R_i^{(1)}$ and $R_i^{(2)}$ for $i = 1,2,3$ are defined to include all the partial derivatives of I with respect to r_i. The above equations are also valid if g is substituted by $g' = e^{-dsN\omega}I'$, and the derivatives of the corresponding integral I' are then contained in $R_i^{(1)'}$ and $R_i^{(2)'}$. Summation of equation 7.48 over coordinate indices i leads to

$$\Delta g(\vec{r},s) = \sum_{i=1}^{3}\frac{\partial^2 g}{\partial r_i^2}(\vec{r},s) = g(\vec{r},s)\left[(dsN\nabla\omega(\vec{r}))^2 - dsN\Delta\omega(\vec{r})\right] + R^{(2)} \tag{7.49}$$

with $R^{(2)} \coloneqq \sum_{i=1}^{3} R_i^{(2)}$. Defining $R^{(1)} = (R_1^{(1)}, R_2^{(1)}, R_3^{(1)})^T$ and analogously introducing $R^{(1)'}$

and $R^{(2)'}$, insertion of Δg, $\Delta g'$, ∇g, and $\nabla g'$ into equation 7.46 yields

$$\Delta\phi_A(\vec{r}) = \frac{Vf_P}{Q_P}\Big\{ \int_0^{c_A} \left[(dsN\nabla\omega_A(\vec{r}))^2 - dsN\Delta\omega_A(\vec{r})\right] g(\vec{r},s)g'(\vec{r},1-s) + R^{(2)}g'(\vec{r},1-s)\,ds$$
$$+ \int_0^{c_A} 2g(\vec{r},s)g'(\vec{r},1-s)\left[-dsN\nabla\omega_A + R^{(1)}(\vec{r},s)\right]\cdot\left[-dsN\nabla\omega_A + R^{(1)'}(\vec{r},s)\right] ds$$
$$+ \int_0^{c_A} g(\vec{r},s)g'(\vec{r},1-s)\left[(dsN\nabla\omega_A(\vec{r}))^2 - dsN\Delta\omega_A(\vec{r})\right] + g(\vec{r},s)R^{(2)'}(\vec{r},s)\,ds\Big\}. \quad (7.50)$$

If all terms containing any $R^{(1)}$, $R^{(2)}$ or corresponding primed expressions are summarized in one single remainder R_A and s-independent terms are pulled out of the integrals, the Laplacian of ϕ_A can be cast into the form

$$\Delta\phi_A = \phi_A\left[4\left(dsN\nabla\omega_A\right)^2 - 2dsN\Delta\omega_A\right] + R_A. \quad (7.51)$$

With analogous calculations $\Delta\phi_B$ can be expressed as

$$\Delta\phi_B = \phi_B\left[4\left(dsN\nabla\omega_B\right)^2 - 2dsN\Delta\omega_B\right] + R_B. \quad (7.52)$$

Equations 7.51 and 7.52 reveal explicit ω-dependencies that affect the dynamical equations in the same manner as $\kappa_H\phi_S\Delta\omega_S$ or $\kappa_H\phi_S(\nabla\omega_S)^2$ from equation 7.41. Therefore, we have extracted additional stiffness terms that cause κ- and ϕ-instabilities.

The knowledge of explicit ω-dependencies is now used to construct a semi-implicit integrator for the potential field equations without implicit treatments of ϕ_A and ϕ_B. In the process, the right hand side of equation 7.40 is abbreviated by $-D_i\int_{t_n}^{t_{n+1}}\Delta\mu_i\,dt$ and as we always set $ds = 1/N$, $dsN = 1$ is assumed in the following for the sake of notational convenience. To prepare the dynamical equations for a semi-implicit integrator we zero pad the right hand side of equation 7.40 according to

$$\omega_A(t_{n+1}) - \omega_A(t_n) = -D_P\int_{t_n}^{t_{n+1}}\left[\Delta\mu_A + \Delta\omega_A + \tilde{c}_{AB}\phi_B X_B + \tilde{c}_{AS}\phi_S X_S + \tilde{\kappa}_H\phi_A X_A\right] dt$$
$$+D_P\int_{t_n}^{t_{n+1}}\left[\Delta\omega_A + \tilde{c}_{AB}\phi_B X_B + \tilde{c}_{AS}\phi_S X_S + \tilde{\kappa}_H\phi_A X_A\right] dt \quad (7.53)$$
$$\omega_B(t_{n+1}) - \omega_B(t_n) = -D_P\int_{t_n}^{t_{n+1}}\left[\Delta\mu_B + \Delta\omega_B + \tilde{c}_{AB}\phi_A X_A + \tilde{c}_{BS}\phi_S X_S + \tilde{\kappa}_H\phi_B X_B\right] dt$$
$$+D_P\int_{t_n}^{t_{n+1}}\left[\Delta\omega_B + \tilde{c}_{AB}\phi_A X_A + \tilde{c}_{BS}\phi_S X_S + \tilde{\kappa}_H\phi_B X_B\right] dt \quad (7.54)$$
$$\omega_S(t_{n+1}) - \omega_S(t_n) = -D_S\int_{t_n}^{t_{n+1}}\left[\Delta\mu_S + \Delta\omega_S + \tilde{c}_{AS}\phi_A X_A + \tilde{c}_{BS}\phi_B X_B + \tilde{\kappa}_H\phi_S X_S\right] dt$$
$$+D_S\int_{t_n}^{t_{n+1}}\left[\Delta\omega_S + \tilde{c}_{AS}\phi_A X_A + \tilde{c}_{BS}\phi_B X_B + \tilde{\kappa}_H\phi_S X_S\right] dt, \quad (7.55)$$

where the short hand notations

$$X_i = 2\Delta\omega_i - \beta_i 4(\nabla\omega_i)^2 \text{ for } i = A, B, \quad (7.56)$$
$$X_S = \Delta\omega_S - \beta_S(\nabla\omega_S)^2, \quad (7.57)$$

and $\tilde{c}_{ij} := \alpha_\kappa \kappa_H + \alpha_{ij}\chi_{ij}$ are applied. We call $\alpha_{ij}, \beta_i, \alpha_\kappa \in [0,1]$ damping-constants, which can later be used to adjust the 'degree' of the implicit treatment and to regulate truncation errors. $\tilde{\kappa}_H$ is defined by $\tilde{\kappa}_H = \alpha_\kappa \kappa_H$.

The numerical scheme is obtained by approximating the integrals in equations 7.53 – 7.55 by quadrature rules. As the first integral on the respective right hand side contains the chemical potential subtracted by the leading stiffness terms it is treated explicitly with an Euler Forward formula. In the following, its explicit approximation at time step n is abbreviated as $E_i^{(n)}$ with $i = A, B, S$. To approximate the second integral, we apply quadrature rules for the products $\phi_i X_i$ that do not involve $\phi_i^{(n+1)}$. Given two scalar functions f and g it is

$$\begin{aligned}
\int_{t_n}^{t_{n+1}} f(t)g(t)dt &= f(t_{n+1})g(t_{n+1})h + \mathcal{O}(h^2) \\
&= \left[f(t_n) + \frac{\partial f}{\partial t}(t_n)h + \mathcal{O}(h^2)\right] g(t_{n+1})h + \mathcal{O}(h^2) \\
&= f(t_n)g(t_{n+1})h + \frac{\partial f}{\partial t}(t_n)g(t_{n+1})h^2 + \mathcal{O}(h^2)g(t_{n+1})h + \mathcal{O}(h^2) \\
&= f(t_n)g(t_{n+1})h + \mathcal{O}(h^2),
\end{aligned} \tag{7.58}$$

so

$$\int_{t_n}^{t_{n+1}} \phi_i \Delta\omega_i \, dt \approx \phi^{(n)} \Delta\omega_i^{(n+1)} h \tag{7.59}$$

and

$$\int_{t_n}^{t_{n+1}} \phi_i \left(\nabla\omega_i\right)^2 \, dt \approx \phi_i^{(n)} \nabla\omega_i^{(n)} \cdot \nabla\omega_i^{(n+1)} h \tag{7.60}$$

are first order time accurate. As usual, the superscript $^{(n)}$ denotes the numerical approximation to a function evaluated at t_n. The reason why the first gradient of the scalar product in equation 7.60 is treated explicitly is because we want the resulting equations to be linear in $\omega_i^{(n+1)}$. This enables the application of different solvers for linear systems, which typically are more efficiently to implement than non-linear solvers. Insertion of the above quadrature rules into equations 7.53 – 7.55 leads to the new semi-implicit update rule in its most general form:

$$\begin{aligned}
&\left[1 - hD_P\left((1 + 2\tilde{\kappa}_H\phi_A^{(n)})\Delta - 4\beta_A\tilde{\kappa}_H\phi_A^{(n)}\nabla\omega_A^{(n)}\cdot\nabla\right)\right]\omega_A^{(n+1)} \\
&\qquad - \left[hD_P\tilde{c}_{AB}2\phi_B^{(n)}\left(\Delta - 2\beta_B\nabla\omega_B^{(n)}\cdot\nabla\right)\right]\omega_B^{(n+1)} \\
&- \left[hD_P\tilde{c}_{AS}\phi_S^{(n)}(\Delta - \beta_S\nabla\omega_S^{(n)}\cdot\nabla)\right]\omega_S^{(n+1)} = \omega_A^{(n)} - hD_P E_A^{(n)},
\end{aligned} \tag{7.61}$$

$$\begin{aligned}
&\qquad - \left[hD_P\tilde{c}_{AB}2\phi_A^{(n)}\left(\Delta - 2\beta_A\nabla\omega_A^{(n)}\cdot\nabla\right)\right]\omega_A^{(n+1)} \\
&+ \left[1 - hD_P\left((1 + 2\tilde{\kappa}_H\phi_B^{(n)})\Delta - 4\beta_B\tilde{\kappa}_H\phi_B^{(n)}\nabla\omega_B^{(n)}\cdot\nabla\right)\right]\omega_B^{(n+1)} \\
&- \left[hD_P\tilde{c}_{BS}\phi_S^{(n)}\left(\Delta - \beta_S\nabla\omega_S^{(n)}\cdot\nabla\right)\right]\omega_S^{(n+1)} = \omega_B^{(n)} - hD_P E_B^{(n)},
\end{aligned} \tag{7.62}$$

$$\begin{aligned}
&- \left[hD_S\tilde{c}_{AS}2\phi_A^{(n)}\left(\Delta - 2\beta_A\nabla\omega_A^{(n)}\cdot\nabla\right)\right]\omega_A^{(n+1)} \\
&- \left[hD_S\tilde{c}_{BS}2\phi_B^{(n)}\left(\Delta - 2\beta_B\nabla\omega_B^{(n)}\cdot\nabla\right)\right]\omega_B^{(n+1)}
\end{aligned}$$

$$+\left[1-hD_S\left((1+\tilde{\kappa}_H\phi_S^{(n)})\Delta-\beta_S\tilde{\kappa}_H\phi_S^{(n)}\nabla\omega_S^{(n)}\cdot\nabla\right)\right]\omega_S^{(n+1)}=\omega_S^{(n)}-hD_SE_S^{(n)}. \quad (7.63)$$

In Fourier space, products of numerical approximations $x^{(n)}(\vec{r})y^{(n+1)}(\vec{r})$ can be calculated via a convolution matrix. However, this matrix is dense while the products in the coordinate space can be expressed by diagonal and thus sparse matrices. Therefore, calculations are performed in the coordinate space and spatial derivatives are approximated by second order central finite difference schemes with periodic boundary conditions instead of using a pseudo spectral method. If equations 7.61, 7.62, and 7.63 are discretized on a grid with m grid points at positions $\vec{r}_i$, $i=0,...,m-1$, they constitute a $3m$-dimensional linear system for the vector

$$\omega^{(n+1)} :=$$

$$\left(\omega_A^{(n+1)}(\vec{r}_0),...,\omega_A^{(n+1)}(\vec{r}_{m-1}),\omega_B^{(n+1)}(\vec{r}_0),...,\omega_B^{(n+1)}(\vec{r}_{m-1}),\omega_S^{(n+1)}(\vec{r}_0),...,\omega_S^{(n+1)}(\vec{r}_{m-1})\right)^T.$$

Due to the complex structure of this system we did not write down its inversion by hand but inverted it numerically.

The remainder of this subsection deals with the implementation of the update rule. At every time step the set of equations is numerically solved with a generalized minimal residual (GMRES) method [163], which is known to be efficient and robust. It is a Krylow subspace iteration for linear systems with semi positive definite matrices and it is also especially convenient to implement because it does not explicitly require the matrix A of a linear system $Ax=b$, but only matrix vector products, whose entries are formally given by the left hand sides of equations 7.61 – 7.63. The entries $\omega_i^{(n+1,0)}(\vec{r}_j)$ of the starting vector for the Krylow iteration at time step $n+1$ are set to

$$\omega_i^{(n+1,0)}(\vec{r}_j)=\omega_i^{(n)}(\vec{r}_j)+\frac{\omega_i^{(n)}(\vec{r}_j)-\omega_i^{(n-1)}(\vec{r}_j)}{h}h=2\omega_i^{(n)}(\vec{r}_j)-\omega_i^{(n-1)}(\vec{r}_j) \quad (7.64)$$

for all $i=A,B,S$ and $j=0,...,m-1$. With this choice, the iteration turns out to converge a little bit faster than for $\omega_i^{(n+1,0)}(\vec{r}_j)=\omega_i^{(n)}(\vec{r}_j)$, but approximations by higher order Taylor polynomials with backwards discretized temporal derivatives do not show any improvement. Residuals decrease monotonically and if there were no round-off errors, the GMRES method would yield the exact solution after $3m$ iterations. However, performing all $3m$ iterations in each time step is computationally not feasible. In our particular implementation a Krylow iteration is considered to have converged once the residual falls below 10^{-10} or the maximum number of 50 iterative steps is reached. In case the residual is not below 10^{-8} after 50 steps, we decrease the width of subsequent time steps by multiplication with $1/1.5$. This adaptive time stepping is introduced because the distance between the starting vector $\omega^{(n+1,0)}$ and the solution $\omega^{(n+1)}$, i.e. the number of iterative steps in the Krylow space required to arrive at a specific threshold for the residual, increases with the width of the time step h. As both an increase in Krylow iterations and a decrease of step sizes enhance simulation times we decided to prefer a decrease of h at fixed maximum iterative steps over an increase of iterative steps at fixed h due to the additional reduction of truncation errors for diminishing h. The number of Krylow iterations per time step at fixed h is also influenced by the variation of the 'demixing speed' during the phase separation. This variation is, for example, illustrated in figure 7.2 (a). It is evident that the maximum value of ϕ_B changes from 0.0884 to 0.1623 within the first three pictures, which corresponds to a span of 40000 time steps and an increase in maximum

densities of $0.1623 - 0.0884 = 0.0739$. From time step 50000 to 60000, the maximum density increases by an approximately 23 times larger amount of $1.8939 - 0.1623 = 1.7316$ within 10000 time steps. When densities change more rapidly, the potential fields also do. If time steps were fixed the number of iterative steps in the GMRES method would grow significantly between 50000 and 60000. So the adaptive time stepping usually reduces the width of time steps when dynamics become fast at the end of spinodal decomposition. The performance increase gained from ILU(0) preconditioning was also tested but it was found that the time spent with the construction of precondition matrices typically outweighs the accompanied (slight) performance gain by far.

Similar to section 5.2, the semi-implicit integrator introduces truncation errors that scale with damping-constants. The added zeroes in equations 7.53 – 7.55 are still exact, e.g. $\tilde{c}_{ij} \int \phi_i X_i \, dt - \tilde{c}_{ij} \int \phi_i X_i \, dt = 0$ for all $i, j \in \mathcal{C}$. But after using different quadrature formulas for subtrahend and minuend, they differ by a $\mathcal{O}(h^2)$-term, and then it is

$$\begin{aligned} 0 &= \tilde{c}_{ij} \int_{t_n}^{t_{n+1}} \phi_i X_i \, dt - \tilde{c}_{ij} \int_{t_n}^{t_{n+1}} \phi_i X_i \, dt \\ &= \tilde{c}_{ij} \left(\phi_i^{(n)} X_i^{(n)} h + \mathcal{O}(h^2) - \phi_i^{(n)} X_i^{(n+1)} h - \mathcal{O}(h^2) \right) \end{aligned} \tag{7.65}$$

with the short hand notations

$$X_i^{(n+1)} \coloneqq 2\Delta\omega_i^{(n+1)} - \beta_i 4 \nabla\omega_i^{(n)} \cdot \nabla\omega_i^{(n+1)} \text{ for } i = A, B \tag{7.66}$$

and

$$X_S^{(n+1)} \coloneqq \Delta\omega_S^{(n+1)} - \beta_S \nabla\omega_S^{(n)} \cdot \nabla\omega_S^{(n+1)}. \tag{7.67}$$

Both truncation errors in equation 7.65 are of order h^2 but they do not necessarily cancel, so

$$0 = \tilde{c}_{ij} \left(\phi_i^{(n)} X_i^{(n)} - \phi_i^{(n)} X_i^{(n+1)} \right) h + \tilde{c}_{ij} \mathcal{O}(h^2). \tag{7.68}$$

To reduce contributions from $\tilde{c}_{ij}\mathcal{O}(h^2)$-terms, it is best to keep the constants α_{ij}, β_i and α_κ as low as possible. Equations 7.53 – 7.55 are the most general formulation of the semi-implicit scheme. But because we aim to simulate systems with much higher compressive moduli than interaction parameters only κ_H-terms are treated implicitly, i.e. we set $\alpha_{ij} = \beta_i = 0$ and $\alpha_\kappa = 0.5$. If α_κ is increased in steps of 0.1, $\alpha_\kappa = 0.5$ is the lowest value yielding a good stability in test simulations with typical physical parameters we are going to apply. The next subsection compares computation times of the particular implementation described above and the conventional scheme.

We should note though that we used an implementation that worked well for all simulations we have tested. This does not necessarily mean that the implementation is optimized. So there might exist different values for α_{ij}, β_i, and maximum Krylow iterations as well as starting vectors, preconditioning techniques or even completely different methods to solve the linear system of equations that could lead to larger simulation speedups.

7.3.2 Computation times

Replacing the update rule for the potential fields in the conventional scheme (equation 7.37) by equations 7.61 – 7.63 extends stability regions for moderate χ-parameters at moderate

compressive moduli and for high κ_H, meaning the semi-implicit integrator is more robust against both ϕ- and κ-instabilities. In the following the resulting speedup of simulations is demonstrated by means of representative examples. All simulations are performed on a two dimensional grid of size 256×256 with a lattice constant $\Delta l = 1/3$ and $ds = 1/N$. These numerical parameters are taken from reference [88] except that the number of grid points is increased from $m = 220 \times 220$ to $m = 256 \times 256$. Applied physical parameters are slight modifications of table 7.1.

At first, the compressive modulus and the solvent-phobic interaction in table 7.1 are replaced by moderate values $\kappa_H = 5$ and $\chi_{BS} = 2$ to investigate the stabilization against ϕ-instabilities. If simulations are performed with the conventional scheme, a step size of $h = 0.002$ will not produce a κ-instability but there eventually appears a ϕ-instability. This instability is not eliminated even if time steps are decreased by a factor of 20 to $h = 0.0001$. The actual value of h where the ϕ-instability disappears with the conventional scheme is unknown. Because it takes excessive simulation time to arrive at ϕ-instabilities (cp. figure 7.2) with $h < 0.0001$, $h = 0.0001$ is used as an upper bound in the following considerations. The semi-implicit integrator generates no instability at $h = 0.002$, and at that particular h its GMRES implementation described in subsection 7.3.1 takes practically the same computation time per step as the conventional one. Thus, it allows a minimum speedup of a factor 20. In fact, the semi-implicit integrator develops neither a κ- nor a ϕ-instability even for step sizes as large as $h = 0.1$. Compared to the conventional scheme, this does not necessarily translate into 1000 times faster computation times though because the GMRES loses efficiency with increasing step sizes. The two reasons for this non-ideal speedup behavior are the already mentioned increasing amount of required Krylow iteration steps with increasing h and the adaptive time stepping, which might decrease h during the simulation run. Hence, to compare computation times a complete test simulation up to a dimensionless time $t_{end} = 683$ is performed with both schemes. The semi-implicit scheme starts with a step width $h = 0.1$ that is reduced to $h = 0.1/1.5$ at $t = 51$ by the adaptive time stepping. It takes 2978 seconds ≈ 50 minutes to arrive at t_{end} with 4 threads on an Intel Core i5 2500K at a clock rate of 4.6 GHz. Since the conventional scheme takes the same computation time for every step and keeps h fixed, the total time required for a complete simulation run can be obtained by a rule of three. The same CPU as above spends $t_{ts} = 19$ seconds at $n_{ts} = 200$ time steps leading to an extrapolated simulation time of

$$\frac{t_{end}}{h}\frac{t_{ts}}{n_{ts}} = \frac{683}{0.0001}\frac{19}{200}\ \text{sec} = 648850\ \text{sec} \approx 7.5\ \text{days}, \tag{7.69}$$

if the conventional scheme is assumed to be stable at $h = 0.0001$. Therefore, the semi-implicit scheme finishes the same simulation at least

$$\frac{648850}{2978} = 217$$

times faster. As already mentioned in subsection 7.3.1, its implementation is not optimized and slightly better speedups can be achieved. If the maximum number of Krylow iterations is increased to 100, the time step would not decrease during a simulation and the computation time until $t_{end} = 683$ was 2627 seconds ≈ 44 minutes with a resulting acceleration of factor $648850/2627 = 247$.

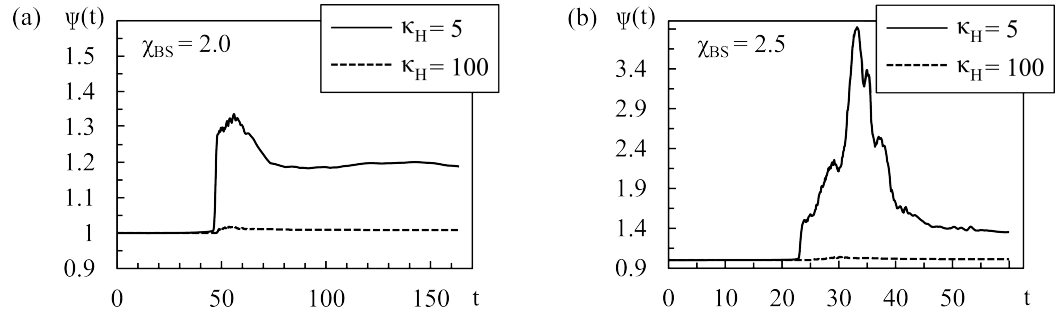

Figure 7.3: *Times series of $\Psi(t)$ from equation 7.70 for two compressive moduli $\kappa_H = 5$ and $\kappa_H = 100$ at $\chi_{BS} = 2.0$ (a) and $\chi_{BS} = 2.5$ (b). Remaining physical and numerical parameters are described in the first paragraph of subsection 7.3.2. At $(\kappa_H, \chi_{BS}) = (5, 2.5)$ the damping-constants were for once set to $\alpha_\kappa = \alpha_{ij} = 1$ and $\beta_i = -1$ with $i, j \in \mathcal{C}$ to stabilize the simulation.*

The semi-implicit scheme is not unconditionally stable. If χ_{BS} is just large enough, ϕ-instabilities return at any κ_H. At which χ_{BS} they return, depends on the damping-constants α_{ij}, β_i, and α_κ. If the step size is set to $h = 0.002$, the conventional scheme becomes unstable once χ_{BS} exceeds 1.6 when χ_{BS} is increased by 0.2 in successive simulation runs with parameters from table 7.1 and $\kappa_H = 5$. The semi-implicit integrator with the implementation from subsection 7.3.1 is stable at $\chi_{BS} = 2$, but there appear numerical artifacts similar to a ϕ-instability at $\chi_{BS} = 3$, for example. If the damping-constants are changed to $\alpha_\kappa = \alpha_{AB} = \alpha_{AS} = \alpha_{BS} = 1$ and $\beta_A = \beta_B = \beta_S = -1$ the semi-implicit integrator remains stable even if $\chi_{BS} = 3$. Consequently, it is possible to stabilize the scheme against ϕ-instabilities over an even wider range of solvent-phobic interactions. Nevertheless, we just restrain to mentioning that possibility. Avoiding ϕ-instabilities with an appropriate choice of damping-constants is not further investigated because this topic is rather technical in nature as moderate κ_H in combination with moderate χ_{BS} correspond to the unrealistic case of highly compressible polymer solutions where maximum normalized densities peak at values significantly larger than 1. This means that different choices of the damping-constants would allow us to simulate rather unphysical situations.

As polymer solutions are hardly compressible, the stabilization at large compressive moduli against the associated κ-instabilities is physically more relevant. The relating investigation of simulation speedups requires to prepend the specification of a typical value κ_H should have to enforce $\phi_A(\vec{r}, t) + \phi_B(\vec{r}, t) + \phi_S(\vec{r}, t) \approx 1$. To this end the quantity

$$\Psi(t) \coloneqq \max_{j \in \{0,\ldots,m-1\}} \left(\sum_{i \in \mathcal{C}} \phi_i(\vec{r}_j, t) \right) \tag{7.70}$$

is defined, which should be 1 at any time in the limit of an incompressible system. Figure 7.3 shows the time series of Ψ for two different compressive moduli $\kappa_H = 5$ and $\kappa_H = 100$, once for $\chi_{BS} = 2.0$ and once for $\chi_{BS} = 2.5$. It is evident that it peaks considerably above 1 for $\kappa_H = 5$, namely at 1.337 and 3.921, which constitutes relative deviations from 1 of about 34 % and 292 %. If the compressive modulus is set to $\kappa_H = 100$, the maximum value of $\Psi(t)$ is 1.018 with a relative deviation below 2 % at $\chi_{BS} = 2.0$ and 1.041 with a relative deviation of 4.1 % at $\chi_{BS} = 2.5$, demonstrating that Ψ being close to 1 requires compressive

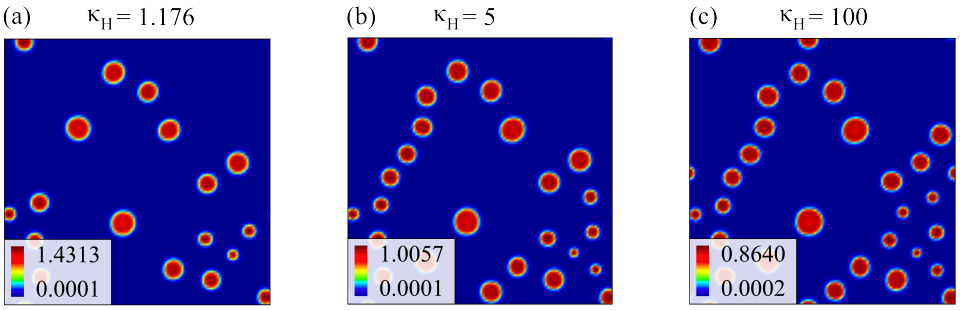

Figure 7.4: *Color coded solvent-phobic density profiles ϕ_B of stable micelles for different compressive moduli. In (a) it is $\kappa_H = 1.176$, in (b) $\kappa_H = 5$ and in (c) $\kappa_H = 100$. Simulations were performed with the semi-implicit scheme on a 128×128 grid with a lattice constant $\Delta l = 1/3$ and a temporal step size $h = 0.002$. The solvent-phobic interaction is set to $\chi_{BS} = 1.6$ and the remaining physical parameters are listed table 7.1. Every snapshot is taken at time step $n = 200000$.*

moduli with magnitudes of 100 at solvent-phobic interactions between $\chi_{BS} = 2$ and 2.5. Figure 7.4 shows that different compressive moduli potentially change the size distribution of polymer particles and heavily affect their polymer content, which indicates the importance of large κ_H for obtaining realistic results. Increasing κ_H decreases the maximum value of ϕ_B and in turn increases the number of micelles. The suppression of high densities by large κ_H automatically prevents ϕ-instabilities, i.e. ϕ-instabilities are a trait of strongly compressible dynamics at moderate or low κ_H and are no issue if κ_H is sufficiently large with respect to the χ-parameters.

To compare performances for high compressive moduli, we set $\kappa_H = 100$ and $\chi_{BS} = 2.0$ in table 7.1, which is also the κ_H-value used for the simulations in chapter 8 together with a $\chi_{BS}^{(max)}$ close to 2. Calculating to $t_{end} = 163$ with an initial step size $h = 0.1$ takes the semi-implicit scheme 6745 sec = 112.4 min. The conventional scheme requires a time step of $h = 0.0001$ to be stable against κ-instabilities, and the extrapolated run time is

$$\frac{163}{0.0001}\frac{19}{200}\ \text{sec} = 154850\ \text{sec} \approx 1.8\ \text{days}, \tag{7.71}$$

meaning the semi-implicit scheme is

$$\frac{154850}{6745} \approx 23$$

times faster. The main reason why the speed up drops an order of magnitude from the previous 217 to a still significant factor of 23 is the adaptive time stepping, which results in step sizes of $h = 0.005853$ at approximately $t = 50$ and above with the specific parameters at hand. Additionally, high κ_H require typically more Krylow iteration steps.

In the hitherto discussed examples the computation times with the conventional scheme are below seven days and thus, feasible. So up to this point significant speedups of factors 20-250 are nice to have as performing costly 3D calculations, for example, could benefit from the acceleration, and as they enable extensive parameter studies without access to a high performance cluster because simulations can be done sequentially within a reasonable time. However, the relatively short simulation times of seven days and below are owed

to the choice of χ_{BS}: using $\chi_{BS} = 1.6$ or 2.0, phase separation dynamics are fast and simulated dimensionless time spans t_{end} are rather short. When low quench rates, i.e. low interaction parameters and slow dynamics, are combined with large compressive moduli, the semi-implicit scheme becomes mandatory. To illustrate that matter, we specifically consider computation times of a system used for evaluation in chapter 8. With $\kappa_H = 100$, one needs to simulate dimensionless times t_{end} of up to 40000 for low quench rates in the range of 10^{-6} to obtain stable polymer particles. Applying an initial time step $h = 0.05$, which eventually reduces to about $h = 0.0148$, such a simulation takes about 10 days = 864000 sec on the parallel cluster Mogon. Due to a slightly higher resolution of $\Delta l = 0.25$, κ-instabilities in the conventional scheme do not vanish until step sizes fall below $h = 0.000075$. As the CPUs in the cluster are operated at a lower clock rate than the one we used in our previous comparisons, the conventional scheme takes ≈ 30 seconds for 200 time steps. Therefore, simulating to $t_{end} = 40000$ would take at least

$$\frac{40000}{0.000075}\frac{30}{200}\ \text{sec} \approx 8 \times 10^7\ \text{sec} = 926\ \text{days} = 2.54\ \text{years}. \tag{7.72}$$

The corresponding speedup factor is approximately

$$\frac{9.7 \times 10^7}{864000} = 92.6.$$

To make matters worse, $t_{end} = 40000$ is just a typical time span to *observe* stable polymer particles. *Checking* if certain polymer particles are truly stable demands to simulate until $t_{end} = 120000$, which would correspond to a computation time of above 7.5 years with the conventional scheme. With the semi-implicit scheme we performed these simulations in about 3 to 5 weeks depending on t_{end}. Since run times of 2.5 or 7.5 years are unbearable, the construction of the new scheme was essential because it basically 'unlocks' the possibility to perform SCF-EPD simulations of approximately incompressible dynamics at low quench rates.

As already mentioned in the beginning of subsection 7.2.2, switching to compressible dynamics by choosing low κ_H is no option in the present work since it provokes ϕ-instabilities at large quench rates for desired maximum quench depths. Even at $\kappa_H = 100$ sufficiently large χ_{BS} provoke ϕ-instabilities. An incompressibility constraint would eliminate them for good, but we preferred the compressible case to give the semi-implicit scheme a more general scope as investigating the response of polymer solutions to pressure variations may also be of interest [90]. If incompressibility is incorporated by a position dependent $\kappa_H(\vec{r})$ that takes the role of a Lagrange parameter similar to the work of Uneyama [81], the semi-implicit scheme should still be practical because potentially high local $\kappa_H(\vec{r})$ should provoke instabilities just like constant κ_H.

The present subsection demonstrates by exemplary simulations that the semi-implicit scheme allows up to 1000 times larger step sizes than the conventional one, which translates into significant speedups of a factor 20-250 with the implementation described in subsection 7.3.1. For high κ_H speedup factors close to the lower value of 20 typically appear at moderate to large χ_{BS} when phase separation is fast and t_{end} is rather low anyways, while factors up to 100 are achieved at slower dynamics where t_{end} is large and simulations require long computation times.

7.3.3 Relevance of approximation errors

Up to this point we discussed speedups of simulations by enlarging the width of time steps without considering the concomitant increase of truncation errors. Estimating these errors and their effect on particle size distributions is subject to the current subsection. In doing so it is also checked whether the substitution of the conventional integrator by the semi-implicit one introduces any additional relevant approximation errors. Possible sources of such errors

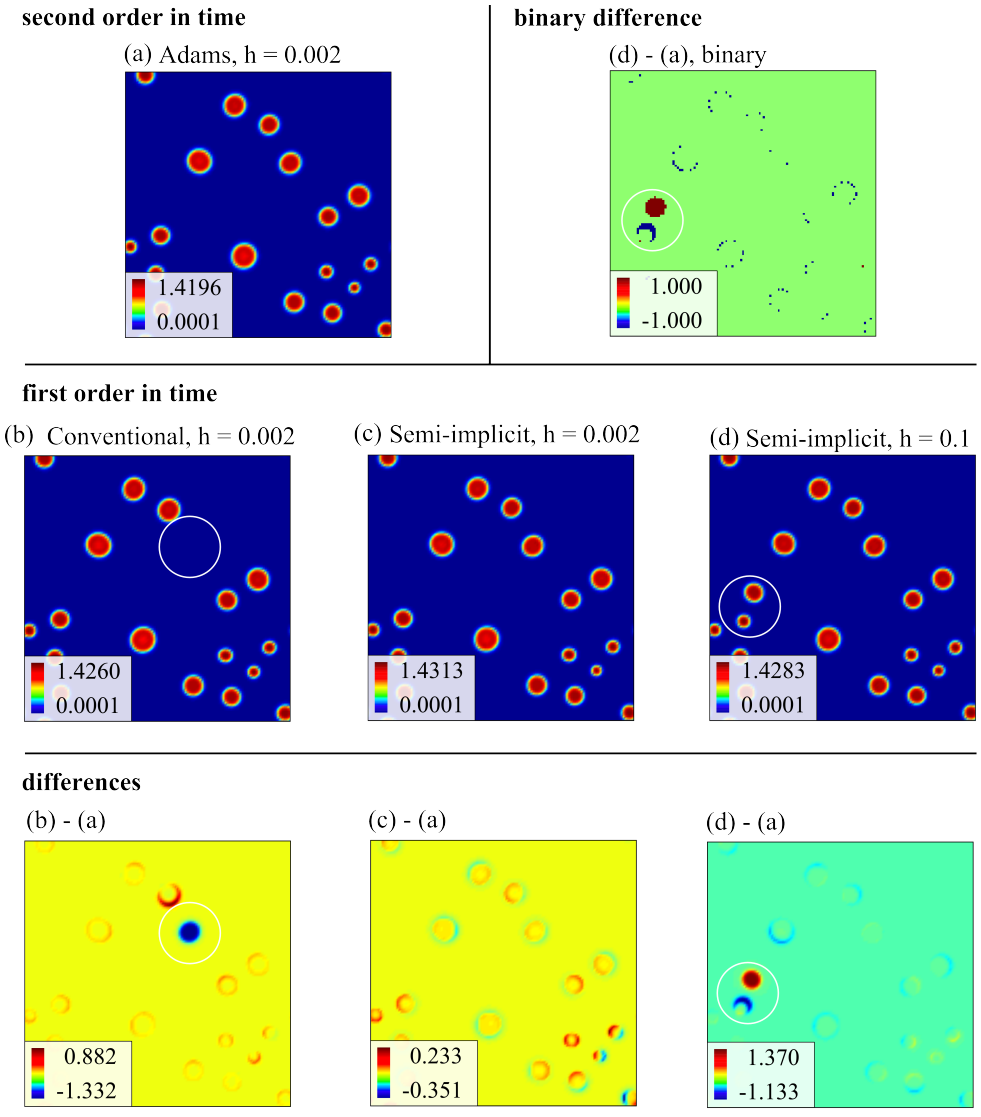

Figure 7.5: *Color coded density profiles of the solvent-phobic block ϕ_B, simulated with different update rules for the potential fields. 'Adams' in (a) denotes the second order update rule from equation 7.39, 'Conventional' in (b) the one from equation 7.37, and 'Semi-implicit' in (c) and (d) refers to equations 7.61 – 7.63. Every snapshot is taken at the same time and depicts stable micelles for identical initial conditions. Except for the step size h, which is given above each diagram, physical and numerical parameters correspond to figure 7.4 with $\kappa_H = 1.176$. Discrepancies from (a) that are visible to the eye are marked by white circles and the diagrams at the bottom show differences of density profiles as indicated by their labeling. The diagram on the top right presents the difference of (d) and (a) after conversion to binary images with a threshold value $\phi_B^{(th)} = 0.3$.*

are the formulas for product quadrature (equations 7.59 and 7.60), the discretization of derivatives by a second order accurate central finite difference instead of using a spectral method, or the termination of Krylow iterations at non-vanishing values of the residual. The reference constitute simulations with the method from equation 7.39. It is a second order time accurate pseudo spectral method and possesses the smallest temporal and spatial truncation errors of all schemes presented in this chapter. Once again simulations with a slight modification of the physical parameter set in table 7.1 are considered as a representative example. This time the solvent-phobic interaction is changed to $\chi_{BS} = 1.6$, where the polymer assembles into stable micelles.

Figure 7.5 shows simulated solvent-phobic density profiles ϕ_B of these micelles. (a) depicts the reference simulation at $h = 0.002$, while (b) and (c) show the results of the conventional and the semi-implicit scheme at the same step size. A superficial comparison between (a) and (b) reveals a visual discrepancy in the density profiles, namely a missing micelle whose location is framed by a white circle in (b), implying size distributions are potentially influenced by temporal truncation errors, but only slightly. (c) lacks that discrepancy. So despite the semi-implicit integrator being first order time accurate, too, its density profile matches the reference. This indicates that the error constant of the semi-implicit scheme is likely to be smaller than the error constant of the conventional one. It further proves that the termination of Krylow iterations and the discretization scheme of derivatives introduce no significant errors, which is also confirmed by the similarity of the difference profiles (b)-(a) and (c)-(a) outside the white framed region. The relatively large deviations in these profiles, ranging from -0.351 up to 0.233 in (c)-(a), mainly appear at the edge of solvent-phobic micelle cores, and most of the time an orange or red region is accompanied by an opposite approximately equally large green or blue region, so micelles are just shifted in a certain direction without changing their size. Increasing step widths to $h = 0.1$ provokes visual discrepancies for the semi-implicit scheme as well. The corresponding density profile is shown in figure 7.5 (d) and the white circle frames an additional micelle not present in (a). The difference between the density profiles in (d) and (a) is shown in the diagram labeled by (d)-(a) and resembles (b)-(a). To check in how far the truncation errors affect particle sizes in simulations, (a) and

PARAMETER SET 2

Physical parameter	f_P	N_A	N_B	χ_{AB}	χ_{AS}	χ_{BS}	κ_H	D_P	D_S
Value	0.1	2	15	1.05	0.0375	1.6	5	$1/N$	1
Numerical parameter	grid size		Δl	h (Adams)		h (GMRES)		ds	
Value	128×128		$1/3$	0.0002		0.0002/0.01		$1/N$	

PARAMETER SET 3

Physical parameter	f_P	N_A	N_B	χ_{AB}	χ_{AS}	χ_{BS}	κ_H	D_P	D_S
Value	0.1	2	15	1.05	0.0375	1.2	1.176	$1/N$	1
Numerical parameter	grid size		Δl	h (Adams)		h (GMRES)		ds	
Value	128×128		$1/3$	0.002		0.002		$1/N$	

Table 7.2: *Two additional parameter sets that were used to compare differences between the numerical integrators for the potential fields. Parameter set 1 is the set used for simulations in figure 7.5.*

(d) are converted into binary images with a threshold value of $\phi_B^{(th)} = 0.3$ and subtracted. The result is seen on the second diagram in the first line. The absolute majority of the pixels have zero-value, expect for the white framed region. As there appears only one new droplet at $h = 0.1$, it does also not alter the mean particle size significantly.

Although their density profiles are not shown, such comparisons were also performed for the parameters sets listed in table 7.2 for the sake of completeness. They look very similar to figure 7.5 and consequently, the current subsection indicates that the implementation of the semi-implicit scheme with the GMERS method does not introduce any errors that outweigh the usual truncation errors and that the latter do not significantly distort particle size distributions. There are minor differences, but we consider them to be small enough not to justify an increase of computation times by choosing $h = 0.002$ over $h = 0.1$.

7.4 Chapter summary and main conclusions

In the present chapter we developed a semi-implicit numerical integration scheme to approach the stiffness of the SCF-EPD equations at large compressive moduli κ_H and/or high χ-parameters. The semi-implicit scheme is obtained from the 'conventional' one used in previous studies about spontaneous self-assembly [88, 89], if the update rule for the potential fields $\{\omega\}$ is replaced by equations 7.61, 7.62, and 7.63.

As we avoid introducing implicit expressions for the end-segment distribution functions g and g', the growth of computational complexity with increasing numbers of monomers per polymer chain N is identical to the explicit conventional scheme. This is an appealing characteristic of our semi-implicit integrator because the iteration along a polymer backbone to calculate $g(\vec{r}, s)$ and $g'(\vec{r}, s)$ for all $s \in [0, N]$ and $\vec{r}$ typically consumes the most part of computation times per time step. Compared to the conventional scheme, larger stability regions allow using up to 1000 times larger step sizes h and our particular implementation with a GMRES method performs simulations up to 100 or even 200 times faster as discussed in subsection 7.3.2. Subsection 7.3.3 indicates that temporal truncation errors do not significantly affect simulation results even if the width of time steps is as large as $h = 0.1$.

Since the GMRES implementation tends to throttle simulation speedups (the number of Krylow steps increases with h), future work could address the implementation of our new scheme or slight variations of it. Because real polymer solutions typically possess high compressive moduli and because κ_H affects particle size distributions (cp. figure 7.4), the stabilization against κ-instabilities is particularly important – especially since high κ_H also suppress ϕ-instabilities. In this regard, one approach could be zero-padding the right hand side of equation 7.40 only by the terms $-D_i \int \Delta\omega_i + c_i\kappa_H\phi_i\Delta\omega_i dt + D_i \int \Delta\omega_i + c_i\kappa_H\phi_i\Delta\omega_i dt$ with damping-constants c_i. After application of the quadrature rule from equation 7.59 to the last integral and an Euler forward to the remaining terms, one would obtain a linear system of equations for every $\omega_i^{(n+1)}$ with a tridiagonal matrix that could be solved directly (i.e. without a Krylow iteration) by the tridiagonal matrix algorithm, also known as Thomas algorithm, for periodic boundary conditions.

The semi-implicit scheme is of course not only applicable for time-dependent interaction parameters, but also for constant interaction parameters. As a consequence, it allows to extend the studies about spontaneous self-assembly of He and Schmid [89] to larger parameter spaces. If an incompressibility constraint is introduced by position dependent compressive

moduli $\kappa_H(\vec{r})$ in a similar manner as in Uneyama's Density Functional Theory approach [81] or described in the review article [91], the evolution equations for $\{\omega\}$ should not change except for the substitution $\kappa_H \mapsto \kappa_H(\vec{r})$. This means that descriptions of incompressible dynamics should benefit from the semi-implicit integrator as well.

Chapter 8

Time dependent interaction parameters in the SCF-EPD equations

Thiermann et al. [22, 23] report a depletion of vesicles and an enrichment of micelles with increasing flow rates in their experiments, as it is illustrated by the Transmission Electron Microscopy (TEM) images in figure 8.1. The morphology of drug delivery systems is another one of their key properties because it affects loading possibilities during fabrication with the co-solvent method. Vesicles allow both hydrophilic and hydrophobic loading, which makes them appealing candidates for multifunctional drug delivery systems: hydrophilic substances can be enclosed in their solvent containing core, while the hydrophobic part of the bilayer shell can be loaded with hydrophobic substances [11]. These loading possibilities are important because some therapeutic substances are hydrophilic while others are hydrophobic. An example for a hydrophilic substance is the toxic anti-cancer drug camptothecin [164]. Hydrophilic materials are, for instance, the anti-cancer drug doxorubicin [165] or the dye pholoxine B, which can be used to trace particles at in vitro cell binding studies or studies about (hydrophilic) loading efficiencies [166]. Although vesicles are more versatile when it comes to loading possibilities, micelles have the advantage that due to the smaller size com-

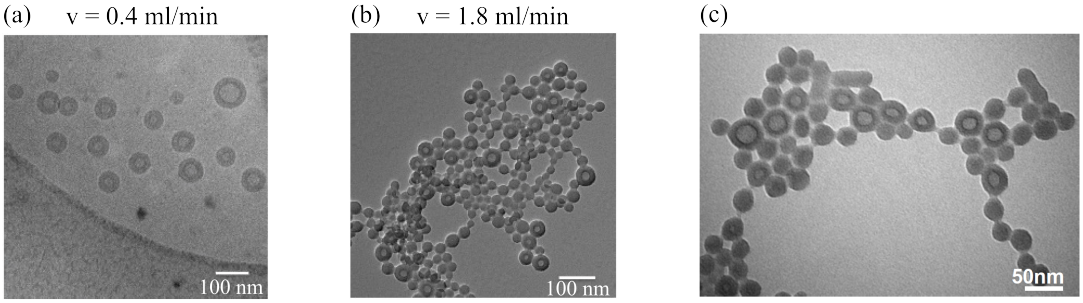

Figure 8.1: *TEM images of cross-linked nanoparticles made of PB-PEO diblock-copolymers. (a) and (b) directly contrast particle sizes and morphologies for two different flow rates v at symmetric flow conditions in the Caterpillar Micromixer with identical remaining experimental parameters. (a) refers to v = 0.4 ml/min and (b) to v = 1.8 ml/min. The pictures are taken from Thiermann [22] and correspond to his samples Cd10 (in b) and Cd11 (in a). (c) shows figure 6.24 from Mueller [36]. It cannot be directly compared to (a) or (b) because it refers to a measurement for asymmetric flow conditions but it implies that also cylindrical micelles may appear in addition to the spherical ones. The samples Cd10 and Cd11 were prepared identically to the ones that were used for the diamonds in figure 1.3 (f).*

pared to vesicles they may also enable ways of cellular uptake that bypass the drug efflux mechanism of cancer cells in order to treat multiresistant cancer [11, 167].

The SCF-EPD model is able to describe a variety of particle morphologies [89]. Depending on the physical input parameters amphiphilic diblock-copolymers spontaneously self-assemble not only to vesicles or spherical micelles, but also to rod-like, ring-like or toroidal structures. An extensive parameter study about the general impact of different continuous quench processes onto particle shapes could be interesting, but the present chapter aims to selectively continue part II. Therefore, we focus on the questions if time dependent interaction parameters in the SCF-EPD equations reproduce the experimentally observed effects of flow rates on particle morphologies and how the formation of morphologies in copolymer solutions affects rate-size relations in comparison to model I.

8.1 Rate-size relations for linear mixing profiles

We start with inserting linear mixing profiles into equation 7.18. Like in model I linear mixing profiles

$$\varphi_{SS}(t) = \begin{cases} \varphi_0 + st & \text{for } t \leq t_{max} \\ \varphi_{max} & \text{for } t > t_{max} \end{cases} \tag{8.1}$$

allow to reduce solvent mixing parameters to $\chi_i^{(0)}$, $\chi_i^{(max)}$ and $s_{\chi,i}$ for $i = A, B$ by writing

$$\chi_{iS}(t) = \left\{ \begin{array}{l} \left(\chi_{iGS} + \dfrac{\chi_{iSS} - \chi_{iGS}}{1 - f_P} \varphi_0 \right) + \dfrac{\chi_{iSS} - \chi_{iGS}}{1 - f_P} s\, t \\ \chi_{iGS} + \dfrac{\chi_{iSS} - \chi_{iGS}}{1 - f_P} \varphi_{max} \end{array} \right\} =: \begin{cases} \chi_i^{(0)} + s_{\chi,i} t & \text{for } t \leq t_{max} \\ \chi_{iS}^{(max)} & \text{for } t > t_{max} \end{cases}$$

with $t_{max} = {}^{(\chi_i^{(max)} - \chi_i^{(0)})}/_{s_{\chi,i}}$. Note that in contrast to model I there currently may be two time dependent interaction parameters, namely the solvent-philic one χ_{AS} and the solvent-phobic one χ_{BS}. In the following, the term 'rate-size relation' refers to the particle size dependence on the quench rate $s_{\chi,B}$ when χ_{AS} is fixed. When χ_{AS} depends on time and $s_{\chi,A}$ differs from $s_{\chi,B}$, it refers to the particle size dependence on s.

8.1.1 Simulation setup

The physical parameters in the SCF-EPD model with time dependent interactions are

- the mean polymer volume fraction f_P,
- the number of A-monomers per polymer chain N_A,
- the number of B-monomers per polymer chain N_B,
- the interaction parameter between A- and B-type monomers χ_{AB},
- the segment diffusion coefficient D_0,
- the compressive modulus κ_H,
- the initial value of the solvent-philic interaction $\chi_{AS}^{(0)}$,

- the maximum value of the solvent-philic interaction $\chi_{AS}^{(max)}$,
- the initial value of the solvent-phobic interaction $\chi_{BS}^{(0)}$,
- the maximum value of the solvent-phobic interaction $\chi_{BS}^{(max)}$, and
- the quench rates $s_{\chi,A}$ and $s_{\chi,B}$.

The numerical parameters are

- the number of grid points on the spatial lattice $m = n_1 \times ... \times n_d$,
- the lattice constant Δl,
- the initial width of a time step h, and
- the discretization level of a polymer chain ds.

In the present section we consider a volume fraction $f_P = 0.1$ of a model polymer with a solvent-philic block length $N_A = 3$ and an incompatible solvent-phobic block containing $N_B = 14$ monomers. The incompatibility is described by an interaction parameter $\chi_{AB} = 1.05$, and to mimic approximately incompressible dynamics the compressive modulus is set to $\kappa_H = 100$ (cp. figure 7.3). The diffusion coefficient D_0 in equation 7.10 is substituted by 1 without loss of generality as lengths are given in units of the polymer's radius of gyration $l_0 = R_g$ and times in units of $t_0 = {}^{R_g^2}/_{D_0}$.

In subsection 8.1.2 the solvent-philic interaction is kept constant, i.e. $\chi_{AS} \equiv \chi_{AS}^{(0)} = \chi_{AS}^{(max)} = -0.15$, and the solvent-phobic one is varied from its spinodal value $\chi_{BS}^{(0)} = \chi_{BS}^{(Spin)} = 1.249$ to $\chi_{BS}^{(max)} = 2.25$, which corresponds to a maximum quench depth of approximately 1 like in chapter 5. This parameter choice extends the polymer from part II by a solvent-philic block of 3 monomers and constitutes a slight modification of a set from He and Schmid [88]. The solvent-phobic interaction in the original set from reference [88] with $\chi_{BS} = 1.2$, $N_A = 2$, $N_B = 15$, and $\kappa_H = 1.176$ is quite close to the corresponding spinodal line and generates vesicles, so we considered this set a good starting point to investigate a potential depletion of vesicles and the enrichment of micelles with increasing flow rates during controlled assembly. The large compressive modulus $\kappa_H = 100$, however, tends to impede vesicle formation by suppressing solvent diffusion into droplet centers, so block lengths are adapted to $N_A = 3$ and $N_B = 14$ in order increase the solvent-philicity of the A-block and to favor the formation of vesicles at quench depths comparable to He and Schmid [88]. In subsection 8.1.3 the solvent-philic interaction χ_{AS} is varied simultaneously to χ_{BS} from $\chi_{AS}^{(0)} = 0.5$ to $\chi_{AS}^{(max)} = -0.15$ as solvent mixing might also change solvent-philic interactions. Like in part II, the random noise is turned off, i.e. $\eta_i = 0$.

The number of spatial grid points is set to $m = 256 \times 256$ with a lattice constant $\Delta l = 0.25$. In the present chapter we restrict to 2D simulations since we focus on a discussion about characteristics of rate-size relations that we found to be independent of the spatial dimension in part II (cp. figure 5.3). The initial time step reads $h = 0.05$ and the segment length in a polymer chain is $ds = {}^1/_N$.

8.1.2 Time dependent solvent-phobic interaction only

A) Morphological transition and evaluation method

In the early stages of phase separation density profiles ϕ_B of the solvent-phobic block resemble ϕ_P from model I, which can already be seen by a comparison of the first three pictures in figure 7.2 (a) to figure 5.2. Qualitatively, the response of ϕ_B to changing quench rates looks also practically identical to ϕ_P in figure 5.2. So for the sake of convenience we renounce showing snapshots of ϕ_B in the early stages. The time series of the Minkowski perimeter C are very similar as well and time series for the SCF-EPD model are shown in figure 8.2. There are again two regimes where the variation of C is fast or slow, respectively, and they are again separated by a distinct maximum, which enables an analogous definition of a transition time t_{tr}. In Cahn-Hilliard models the equilibrium state is always a macroscopic phase separation, and $C(t)$ decreases until there is only one single homopolymer particle left. At the plateau of constant C that appears at large t in figure 8.2, however, there exist multiple stable particles due to a steric stabilization that prevents Ostwald ripening [88].

The density profiles corresponding to these particles, ϕ_B at t_{end}, are shown in figure 8.3 (b), (d), and (f). Strictly speaking, figure 8.3 depicts only the density solvent-phobic B-monomers. But since the solvent-philic A-monomers accumulate approximately at green to yellow ϕ_B-values, these colors roughly illustrate the A-blocks. Like in figure 5.2 structure sizes decrease with increasing quench rates, but this time the structures are no droplets but stable particles. The left and the center column in figure 8.3 show an enrichment of micelles and a depletion of vesicles for an increasing quench rate, much like figure 8.1 (a) and (b) – except that the simulated density profiles show cylindrical micelles which are not present in figure 8.1 (b). But since figure 8.1 (c) shows that cylindrical micelles can also appear along with spherical ones, we consider our simulations to be in qualitative agreement with experiments. Further taking into account the rightmost column in figure 8.3, our simulations indicate that the experimentally observed enrichment of micelles is likely to be only the beginning of a complete morphological transition from vesicles to micelles. This implies that, theoretically, the co-solvent method should allow to fabricate particle populations of controllable uniform

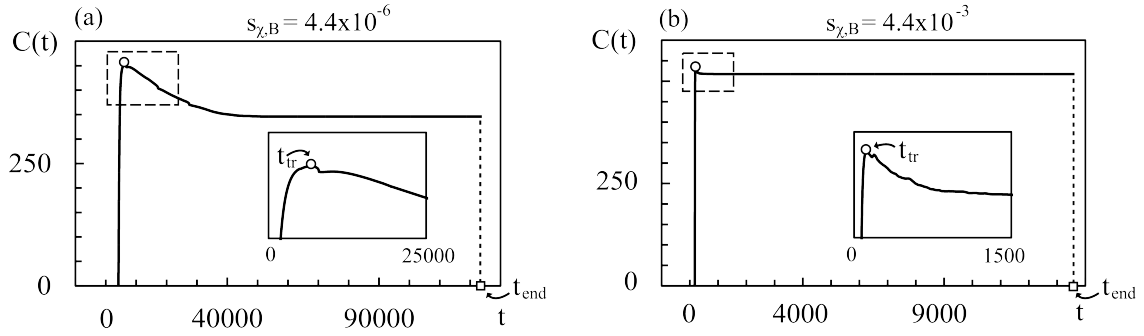

Figure 8.2: *Temporal evolution of the Minkowski perimeter C during two SCF-EPD simulations. In (a) the quench rate is set to $s_{\chi,B} = 4.4 \times 10^{-6}$ and in (b) it is $s_{\chi,B} = 4.4 \times 10^{-3}$, while χ_{AS} is kept constant. t_{tr} denotes the transition time, which is marked by a circle, and the rectangle represents the simulated time span t_{end}. C is calculated from solvent-phobic density profiles ϕ_B analogously to section 5.3.2 with a threshold value $\phi_B^{(th)} = 0.3$. The inset shows a magnification of the section inside the dashed rectangle.*

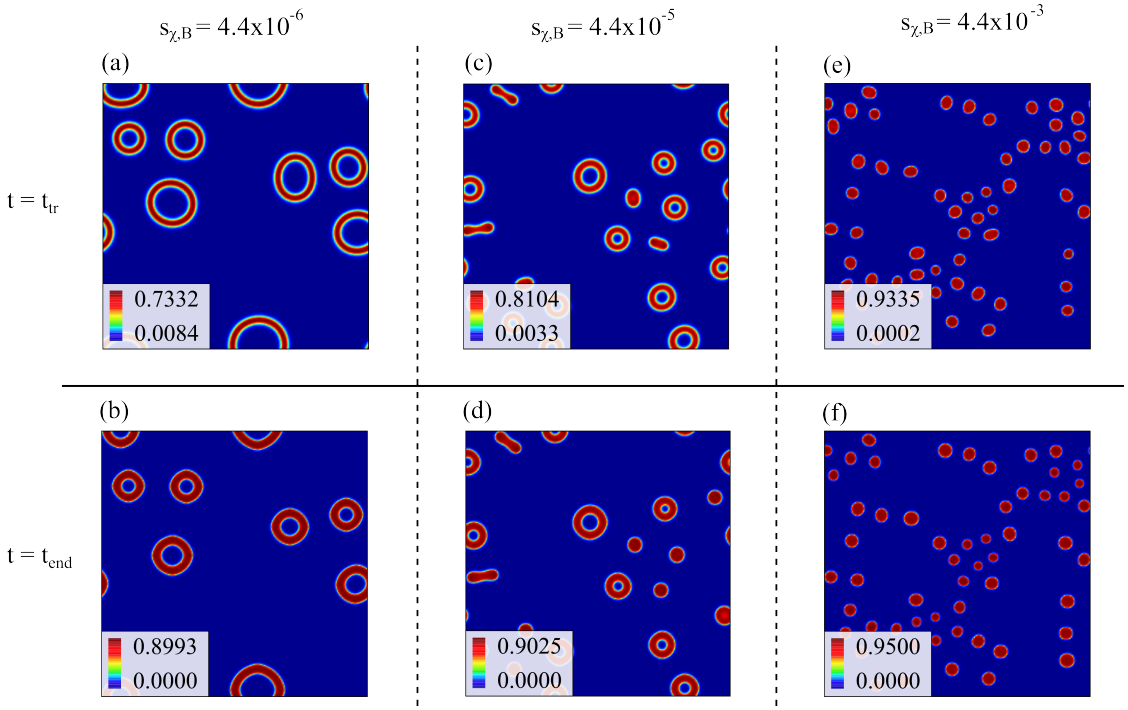

Figure 8.3: *Solvent-phobic density profiles ϕ_B for three different quench rates $s_{\chi,B}$. All profiles are calculated with the semi-implicit SCF-EPD scheme and identical initial conditions. (a) and (b) depict ϕ_B for $s_{\chi,B} = 4.4 \times 10^{-6}$ at transition time $t = t_{tr}$ and at $t = t_{end}$, respectively. Likewise, (c) and (d) display the density profiles for the quench rate $s_{\chi,B} = 4.4 \times 10^{-5}$, and (e) and (f) for $s_{\chi,B} = 4.4 \times 10^{-3}$.*

morphology. Like particle sizes the morphology can be controlled by mixing speeds: slow mixing exclusively produces large vesicles while very fast mixing produces only small micelles.

Figure 8.3 (a), (c), and (e) depict particles at transition time. Although their size does slightly change between t_{tr} and t_{end}, which is also indicated by the drop of C behind its maximum in figure 8.2, we evaluate particle sizes at transition time to keep the analogy to model I and because the convention to sample a maximum of C is more precisely definable than a time 'when C becomes almost constant' (a plateau might still exhibit a very slight descent at t_{end} if C is described by double precision numbers). Geometric particle sizes are determined from solvent-phobic density profiles after binary conversion with a threshold value $\phi_B^{(th)} = 0.3$. Identically to subsection 5.3.2, particles are labeled by a standard recursively defined image labeling algorithm with $i = 1, ..., p$, and for every single particle the total perimeter U_i and the total area A_i are determined in 2D. In 3D the perimeter and the area are replaced by the surface area S_i and the volume V_i, respectively. The sphere equivalent radius $R_{s,i}$ of particle i is defined by

$$R_{s,i} = \sqrt{\frac{A_i}{\pi}} \text{ in 2D and } R_{s,i} = \sqrt[3]{\frac{3V}{4\pi}} \text{ in 3D.} \tag{8.2}$$

In addition we introduce the vesicle equivalent radius $R_{i,v}$, which is the outer radius of a spherical shell with equal surface area and volume as a particle. In two spatial dimensions

the inner radius r_i and the outer radius R_i are given by

$$A_i = \pi(R_i^2 - r_i^2) \Leftrightarrow r_i^2 = R_i^2 - \frac{A_i}{\pi} \text{ and } U_i = 2\pi(R_i + r_i) \Leftrightarrow R_i = \frac{U_i}{2\pi} - r_i. \tag{8.3}$$

Insertion of r_i into R_i yields

$$R_{v,i} \coloneqq R_i = \frac{A_i}{U_i} + \frac{U_i}{4\pi}. \tag{8.4}$$

The vesicle equivalent radius of a spherical micelle is its radius R because

$$R_{v,i} = \frac{A_i}{U_i} + \frac{U_i}{4\pi} = \frac{\pi R^2}{2\pi R} + \frac{2\pi R}{4\pi} = \frac{R}{2} + \frac{R}{2} = R. \tag{8.5}$$

In three spatial dimensions it is

$$V_i = \frac{4}{3}\pi(R_i^3 - r_i^3) \text{ and } S_i = 4\pi(R_i^2 + r_i^2) \Leftrightarrow r_i = \sqrt{\frac{S_i}{4\pi} - R_i^2} \tag{8.6}$$

and insertion of r_i into V_i leads to the polynomial

$$-2\left(\frac{4}{3}\pi\right)^2 R_i^6 + \frac{4}{3}\pi S_i R_i^4 + \frac{8}{3}\pi V_i R_i^3 - \frac{1}{3}S_i^2 R_i^2 + \frac{S_i^3}{36\pi} - V_i^2 = 0, \tag{8.7}$$

which may be solved for R_i numerically with a bisection method to obtain $R_{v,i}$. Inserting $V_i = {}^{4\pi}/_{3}R_i^3$ and $S_i = 4\pi R_i^2$ verifies that in case a spherical micelle is processed, the above polynomial is solved by its radius. R_s and R_v denote the mean values of the sphere and vesicle equivalent radii, i.e.

$$R_v = \frac{1}{p}\sum_{i=1}^{p} R_{v,i} \text{ and } R_s = \frac{1}{p}\sum_{i=1}^{p} R_{s,i}, \tag{8.8}$$

while l_1 and l_{max} are defined analogously to equation 5.52. We note that we only performed 2D simulations but included the 3D case into the description of the evaluation method for the sake of completeness.

B) Rate-size relations and transition times

Rate-size relations and transition times are shown in figure 8.4. Data point progressions in (a), (b), and (d) are very similar to figure 5.3: there is an asymptotic regime and a non-asymptotic regime, where data points can be approximated by scaling laws. As in part II, the beginning of the asymptotic regime is labeled by the intersection of t_{tr} and t_{max} in figure 8.4 (d). The exponents -0.198 and -0.160 of the regression lines for R_s and R_v in figure 8.4 (a) agree well with ${}^{-1}/_{6}$ from the Cahn-Hilliard theory. The exponent of l_1 in 8.4 (b) takes the comparatively high value -0.09 but is still relatively close, while l_{max} in (c) looks entirely different.

Of all four measures for particle sizes, R_v and R_s should be the most reliable ones as they are the 'real' geometric particle radii. The resemblance of their characteristic attribution to simulation results from section 5.3 implies that the formation of particle morphologies and the steric stabilization do not significantly affect the fundamental behavior of rate-size relations. Since the early stage development of ϕ_B-profiles is also very similar to ϕ_P for homopolymers

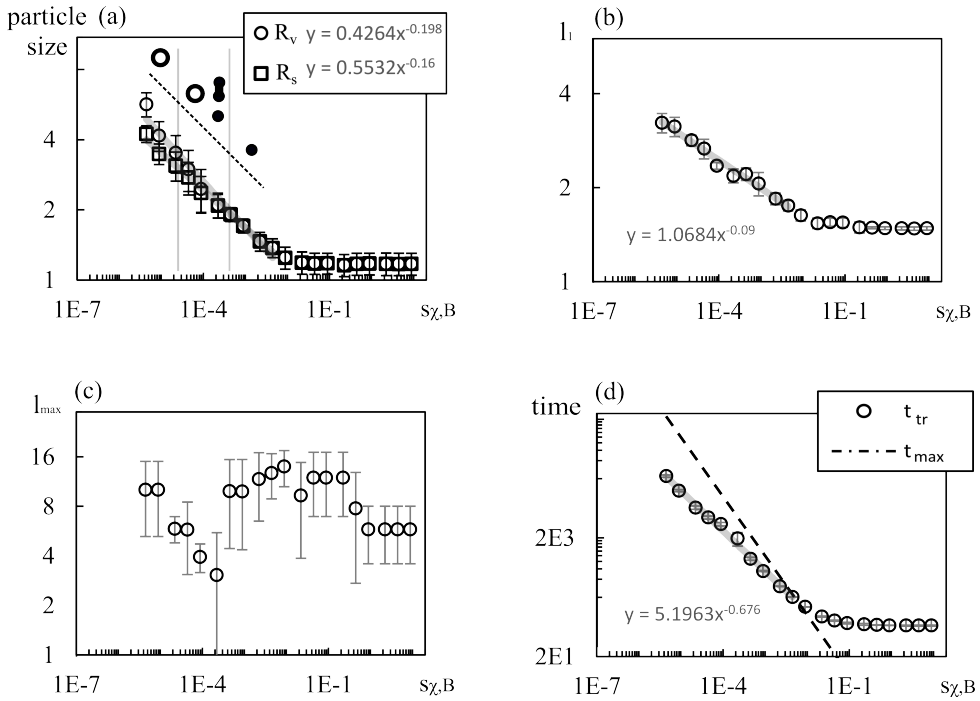

Figure 8.4: *Rate-size relations and transition times, simulated with the SCF-EPD model in 2D for linearly time-dependent χ_{BS} at fixed χ_{AS}. (a) shows the mean sphere and vesicle equivalent radii R_s and R_v, (b) depicts l_1, and (c) l_{max} (cp. equation 5.52). Data points in (d) represent the transition time t_{tr} and the dash-dotted line is t_{max}. All data are averaged over five simulation runs with different random initial conditions. Error bars in (a) represent a polydispersity ΔR_s or ΔR_v defined analogously to equation 5.48. In (b), (c), and (d) error bars indicate the statistical standard deviation over the five simulation runs. Vertical grey lines in (a) label characteristic transition quench rates that separate three morphological regimes. In each regime there appear particle morphologies as illustrated by the symbols above the dotted line. Black dots symbolize micelles, open circles vesicles, and the dumbbell shape cylindrical micelles. Each column in figure 8.3 shows exemplary snapshots for one respective morphological regime. Trend line equations $y = \beta\, x^{\alpha}$ to data points in the non-asymptotic regime are displayed in the corresponding diagrams, and the physical parameters applied in the simulations are specified in subsection 8.1.1.*

from figure 5.2 as stated in paragraph A), particle sizes in copolymer systems are likely determined during the very early stages of phase separation as well – mainly by the dynamics of solvent-phobic block. The combined content of the last two sentences leads to the conclusion that the fundamental interpretation to the working principle of size-controlled assembly from model I is directly transferable to amphiphilic copolymer solutions. Thus, model I and the SCF-EPD model combine to form a consistent overall picture of size-controlled assembly. While the SCF-EPD model describes the formation of structured nanoparticles in amphiphilic copolymer solutions in a physically more accurate manner, model I provides an analytical explanation for the characteristic and fundamental scaling behavior $R \propto s^{\alpha}$.

The deviating or even abnormal behavior of l_1 or l_{max} with respect to R_s and R_v is most likely caused by 'non-unimodal' ϕ_B-profiles. In the Cahn-Hilliard model, the arrangement of polymer droplets at transition time looks nearly equidistant as depicted, for example, in figure 5.2 (e) and (d). Equidistant patterns can be described by merely one single complex

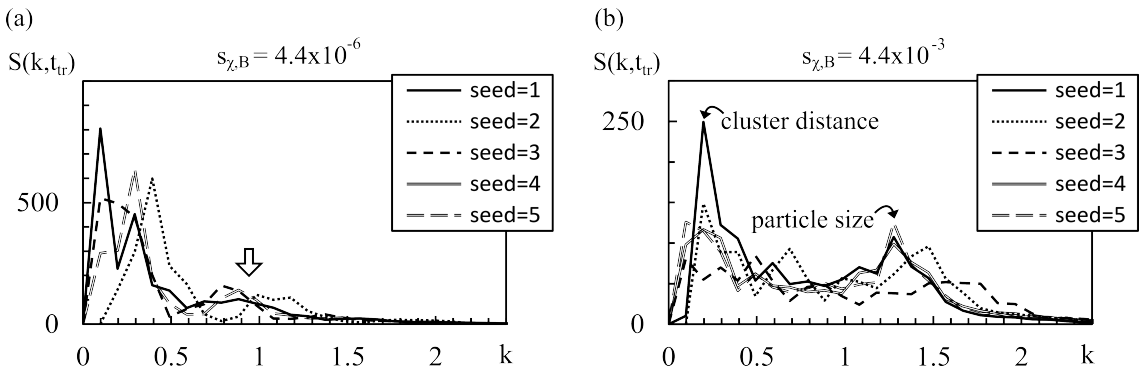

Figure 8.5: *Normalized radially averaged structure factors $S(k, t_{tr})$ of ϕ_B in the SCF-EPD model (S is defined analogously to equation 5.49). (a) shows the structure factors at $s_{\chi,B} = 4.4 \times 10^{-6}$ for initial conditions that are generated by different random seeds from 1 to 5. (b) depicts the same for $s_{\chi,B} = 4.4 \times 10^{-3}$. The solid lines (seed=1) correspond to diagrams (a) and (e) in figure 8.3. The arrow in (a) indicates secondary peaks originating from vesicle structures.*

exponential function leading to a distinct peak of the radially averaged structure factor as a function in wave numbers k. In the SCF-EPD model spatial distributions of polymer particles are far more irregular. There are regions that contain many particles and there are regions that contain none, as for example seen in figure 8.3 (e). Such a distribution possesses multiple significant Fourier coefficients that may interfere with the identification of maxima or first moments of S as inverse particle sizes.

To demonstrate that interference, structure factors at $s_{\chi,B} = 4.4 \times 10^{-6}$ and $s_{\chi,B} = 4.4 \times 10^{-3}$ are depicted in figure 8.5 for different random initial conditions. Figure 8.5 (a) shows structure factors for the low quench rate $s_{\chi,B} = 4.4 \times 10^{-6}$. The solid line labeled 'seed = 1' corresponds to the composition profile in figure 8.3 (a). The main wave number contributions between $k = 0$ and $k \approx 0.5$ characterize a typical distance between the particles and the small secondary peaks at larger k (indicated by the white arrow) can be attributed to the vesicle structure [88]. Therefore, primary peaks can be used to estimate particle sizes. However, at a higher quench rate such as $s_{\chi,B} = 4.4 \times 10^{-3}$ in figure 8.5 (b) the structure factor is either bimodal (seed = 1,4,5), trimodal (seed=2), or it extends at an approximate constant level plus minus some variations up to $k = 2$ (seed=3). Thus, the solvent-phobic density profiles are highly modulated. The impossibility to extract a meaningful particle size from the latter (almost constant S-values) is clear. The problem about bimodal structure factors can be rationalized by looking at the solid line in figure 8.5 (b), which corresponds to the ϕ_B-profile shown in figure 8.3 (e). If one compares figure 8.3 (e) and (a), the typical extension of micelle clusters, as they can be seen at the top right or at the center in figure 8.3 (e), is similar to the extension of a vesicle in (a). Comparing the structure factors (solid lines) in figure 8.5 shows that the primary peak is at almost equal positions. Thus, the main peak in figure 8.5 (b) does not correspond to typical micelle distances but distances between micelle clusters. The wave numbers corresponding to particle sizes are most probably the k-values at the secondary peak. Consequently, l_{max} completely fails to predict particle sizes. The bimodal structure, of course, also shifts l_1 and thus, particle size measures from the structure factor are not reliable in the SCF-EPD model and one should use the geometric ones. The

vesicle equivalent radius possesses a more negative exponent than the sphere equivalent radius because it grows as droplets transform into vesicles while the sphere equivalent radius does not.

8.1.3 Time dependent solvent-phobic and solvent-philic interactions

Simultaneously decreasing χ_{AS} from 0.5 to -0.15 to mimic an increasing solvent quality for the solvent-philic block may induce a slight increase of exponents and particle sizes in the non-asymptotic regime as demonstrated by a comparison between the trend line equations in figure 8.4 (a) and figure 8.6 (a) or (b). This is because in the very early stages of spinodal decomposition, a larger χ_{AS} should accelerate the termination of early stage coarsening. Consequently, in contrast to part II, the SCF-EDP model contains degrees of freedom that can regulate exponents of rate-size relations even for linearly time dependent interaction parameters without an implementation of solvent mixing via chemical potentials. The shift of particle sizes is, however, relatively weak, which is consistent with the idea that spinodal decomposition (of the model polymer with a short solvent-philic block of $N_A = 3$ monomers) is mainly driven by the unfavorable interaction of the solvent-phobic block as mentioned in the introduction of part II.

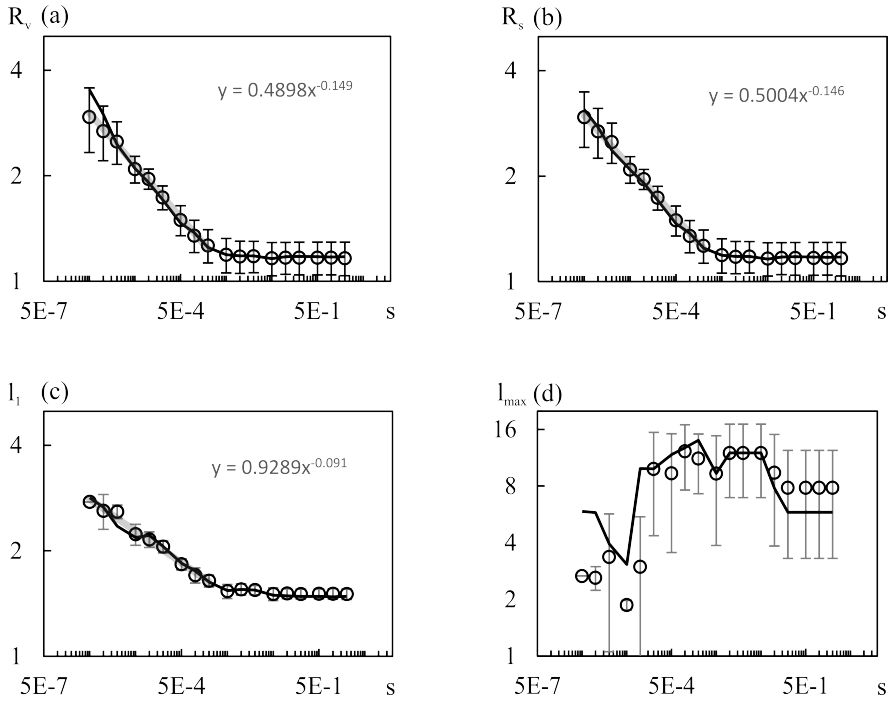

Figure 8.6: *Rate-size relations for linearly time-dependent χ_{BS} and χ_{AS} from the SCF-EPD model. (a), (b), (c), and (d) show R_v, R_s, l_1, and l_{max}, respectively. Data points are simulation results, grey lines regression lines in the non-asymptotic regime, and black lines the simulation results from figure 8.4 for constant χ_{AS}.*

8.2 Rate-size relations for the SFIMM- and CPMM-profiles

Rate-size relations for SFIMM- and CPMM-profiles with constant χ_{AS} are displayed in figure 8.7. The physical and numerical parameters are identical to subsection 8.1.1 except for an increased initial time step of $h = 0.1$. The corresponding spinodal composition is $\varphi_{SS}^{(Spin)} = 0.5$, and the additional parameters introduced by the two mixing profiles (cp. figure 5.14) are set to $\varphi_{SS}^{(1)} = 0.45$, $\varphi_{max} = 0.725$, and $t_0 = 10^{-6}$ seconds. x_l is fixed to the center of a polymer lamella, i.e. $x_l = 0$ in the SFIMM and $x_l = 1/4$ in the CPMM.

Simulation results for the CPMM in figure 8.7 (c) again agree with both linear mixing profiles and experimental results as they exhibit a scaling behavior with exponents close to

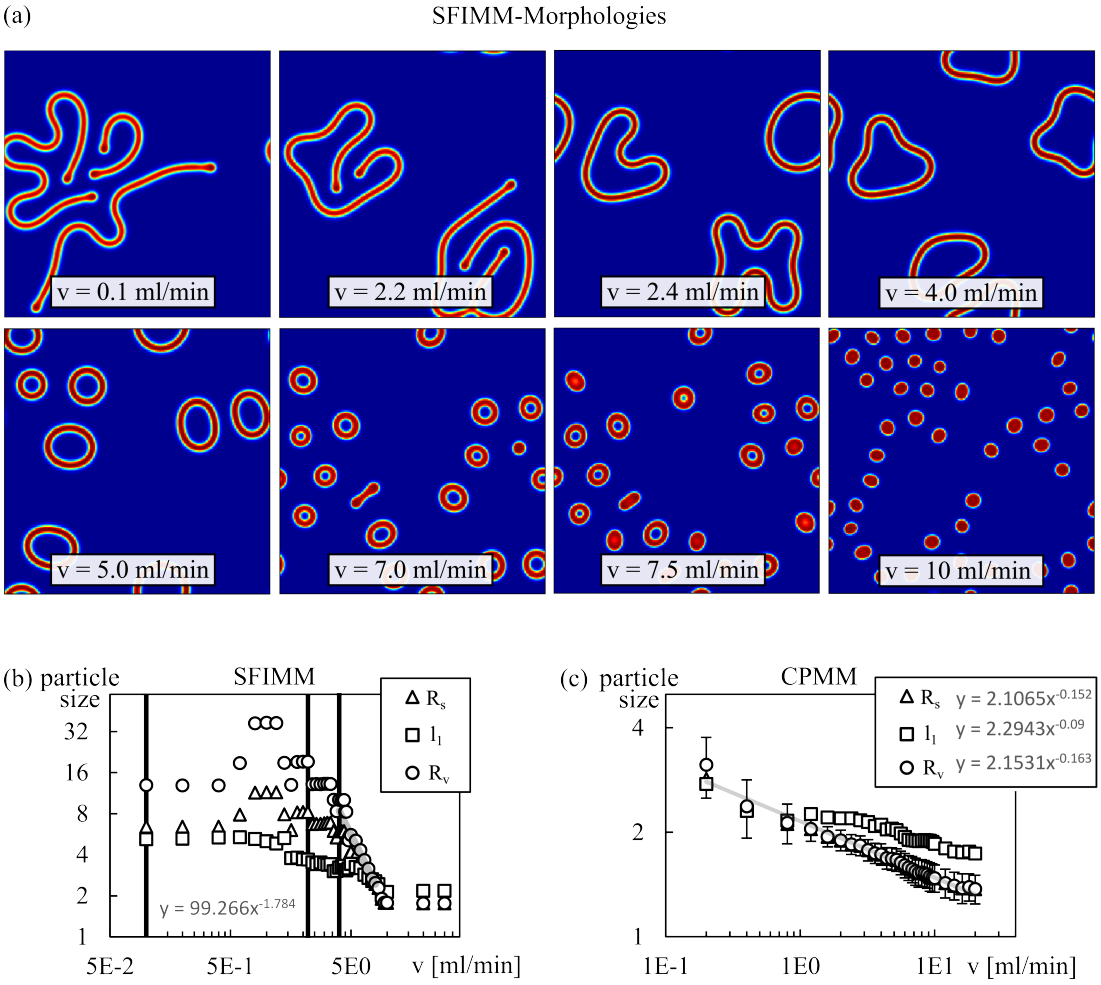

Figure 8.7: *Morphological transition in the SFIMM (a) and rate-size relations for both the SFIMM- (b) and the CPMM-mixing profile (c). (a) shows color coded densities $\phi_B(\vec{r}, t_{tr})$ in the SFIMM. Flow rates below $v = 2.2$ ml/min produce coils, and completely spherical vesicles are obtained at approximately $v = 4.8$ ml/min. Increasing v beyond 4.8 ml/min generates a transition from vesicles to micelles similar to figure 8.3. The vertical lines in (b) are placed at $v = 0.1$, 2.2, and 4.0 ml/min to draw a connection to (a). The equation between the first two lines is associated with the trend line (grey) to R_v in the straight section at $v > 4.0$ ml/min. Error bars in (c) represent the polydispersity ΔR_v, and trend line equations are given in the legend. For the sake of clarity only the trend line to R_v is shown.*

$-1/6$ and reproduce particle sizes between 20 and 40 nm if $R_g \approx 10$ nm. The morphological transition for increasing flow rates resembles figure 8.3. Vesicles are found at $v = 0.2$ ml/min, and at $v > 0.8$ ml/min only micelles are present. This indicates that the complete morphological transition is possible within the experimentally applied range of flow rates from 0.1 ml/min to 5 ml/min.

In the SFIMM a comparable morphological transition occurs at much higher values of $v > 4.8$ ml/min. At $v \leq 4.8$ ml/min vesicles are deformed with decreasing flow rates and eventually become coils as illustrated by 8.7 (a). The switch from deformed vesicles to coils happens between 2.2 and 2.4 ml/min, and conclusively, at $v < 2.4$ ml/min the measures to estimate particle sizes produce undefined results, which makes an evaluation of rate-size relations in the SFIMM very problematic. The sole purpose of figure 8.7 (b) is to demonstrate that the extension to copolymers does not bring rate-size relations from the SFIMM to an agreement with experimental data point progressions. At $v > 4$ ml/min they show a scaling behavior but with a much too low exponent of -1.784.

In summary, rate-size relations for the CPMM-profile in section 8.2 show an agreement with experimental results once more, while the results for the SFIMM still disagree as stated in subsection 5.4.2. Therefore, the distortion of rate-size relations in part II was not caused by the restriction to homopolymers.

8.3 Interpretation as an effective two-component system

Like model I, the SCF-EPD model with time dependent interaction parameters can also be interpreted as an effective two-component system with a position independent solvent composition. The proof is subject of the current section. In the process we start from equation 2.29 for a three-component ensemble containing n_P diblock-copolymers, n_{S1} particles of a solvent 1, and n_{S2} particles of a solvent 2. Using an interaction potential and nomenclature of variables analogous to section 7.1 with $n = Nn_P + n_{S1} + n_{S2}$, the free energy is given by

$$\begin{aligned}\frac{1}{n}\beta F_0[\phi_A, \phi_B, \phi_{S1}, \phi_{S2}] = &-f_{S1} \ln\left(\frac{Q_{S1}}{V f_{S1}}\right) - f_{S2} \ln\left(\frac{Q_{S2}}{V f_{S2}}\right) - \frac{f_P}{N} \ln\left(\frac{Q_P N}{V f_P}\right) \\ &+\frac{1}{V}\int_V \Big[\chi_{AB}\phi_A\phi_B + \chi_{AS1}\phi_A\phi_{S1} + \chi_{AS2}\phi_A\phi_{S2} + \chi_{BS1}\phi_B\phi_{S1} + \chi_{BS2}\phi_B\phi_{S2} \\ &+\frac{\kappa_H}{2}\left(\phi_A + \phi_B + \phi_{S1} + \phi_{S2} - 1\right)^2 - \omega_A\phi_A - \omega_B\phi_B - \omega_{S1}\phi_{S1} - \omega_{S2}\phi_{S2}\Big] d\vec{r} \end{aligned} \tag{8.9}$$

where the potential field ω_i depends on the density ϕ_i only. The relations $\phi_A[\omega_A]$ and $\phi_B[\omega_B]$ are identical to equations 7.7 and 7.8, and

$$\phi_{Si}[\omega_{Si}] = \frac{V f_{Si}}{Q_{Si}} e^{-\omega_{Si}} \text{ with } Q_{Si}[\omega_{Si}] = \int_V e^{-\omega_{Si}} d\vec{r} \text{ for } i = 1, 2. \tag{8.10}$$

Replacing ϕ_{S1} and ϕ_{S2} in the free energy by the density of total solvent ϕ_S and the solvent compositions α through the relations $\phi_S = \phi_{S1} + \phi_{S2}$ and $\phi_{S2} = \alpha\phi_S$ with a $\vec{r}$-independent α yields

$$\frac{1}{n}\beta F[\phi_A, \phi_B, \phi_S](\alpha) = -(1-\alpha) f_S \ln\left(\frac{Q_{S1}}{V(1-\alpha) f_S}\right) - \alpha f_S \ln\left(\frac{Q_{S2}}{V\alpha f_S}\right) - \frac{f_P}{N} \ln\left(\frac{Q_P N}{V f_p}\right)$$

$$+\frac{1}{V}\int_V \Big[\chi_{AB}\phi_A\phi_B + \chi_{AS}\phi_A\phi_S + \chi_{BS}\phi_B\phi_S$$
$$+\frac{\kappa_H}{2}(\phi_A+\phi_B+\phi_S-1)^2 - \omega_A\phi_A - \omega_B\phi_B - ((1-\alpha)\omega_{S1}+\alpha\omega_{S2})\,\phi_S\Big]d\vec{r} \tag{8.11}$$

with the short hand notations

$$\chi_{AS} \coloneqq \chi_{AS1} + \alpha(\chi_{AS2}-\chi_{AS1}) \text{ and } \chi_{BS} \coloneqq \chi_{BS1} + \alpha(\chi_{BS2}-\chi_{BS1}). \tag{8.12}$$

The connection between the potential fields ω_{S1} and ω_{S2} can be established by

$$(1-\alpha)\phi_S(\vec{r}) = \phi_{S1}(\vec{r}) = \frac{V(1-\alpha)f_S}{Q_{S1}}e^{-\omega_{S1}(\vec{r})} \Leftrightarrow \phi_S(\vec{r}) = \frac{Vf_S}{Q_{S1}}e^{-\omega_{S1}(\vec{r})} \tag{8.13}$$

and

$$\alpha\phi_S(\vec{r}) = \phi_{S2}(\vec{r}) = \frac{V\alpha f_S}{Q_{S2}}e^{-\omega_{S2}(\vec{r})} \Leftrightarrow \phi_S(\vec{r}) = \frac{Vf_S}{Q_{S2}}e^{-\omega_{S2}(\vec{r})}. \tag{8.14}$$

Equalizing the respective expression for ϕ_S from equations 8.13 and 8.14 leads to

$$\frac{e^{\omega_{S1}(\vec{r})}}{Q_{S1}} = \frac{e^{\omega_{S2}(\vec{r})}}{Q_{S2}} \Leftrightarrow \omega_{S2}(\vec{r}) = \omega_{S1}(\vec{r}) + \ln\left(\frac{Q_{S1}}{Q_{S2}}\right) \forall\,\vec{r}. \tag{8.15}$$

As the ln-term is independent of $\vec{r}$, it contains the reference states of the potential fields. Because the reference states are arbitrary, one can set $Q_S \coloneqq Q_{S1} = Q_{S2}$ without loss of generality and define $\omega_S \coloneqq \omega_{S1} = \omega_{S2}$. Insertion of ω_S into equation 8.11 and calculating the variational derivatives at fixed segment numbers (implying fixed α) leads to the chemical potentials

$$\frac{1}{\rho_0}\frac{\delta\beta F}{\delta\phi_A} = \chi_{AB}\phi_B + \chi_{AS}\phi_S + \kappa_H(\phi_A+\phi_B+\phi_S-1) - \omega_A, \tag{8.16}$$

$$\frac{1}{\rho_0}\frac{\delta\beta F}{\delta\phi_B} = \chi_{AB}\phi_A + \chi_{BS}\phi_S + \kappa_H(\phi_A+\phi_B+\phi_S-1) - \omega_B, \tag{8.17}$$

$$\frac{1}{\rho_0}\frac{\delta\beta F}{\delta\phi_S} = \chi_{AS}\phi_A + \chi_{BS}\phi_B + \kappa_H(\phi_A+\phi_B+\phi_S-1) - \omega_S. \tag{8.18}$$

Because it also follows from equation 8.14 that $\phi_S(\vec{r}) = \frac{Vf_S}{Q_S}e^{-\omega_S(\vec{r})}$, the relation of potential fields to densities is completely analogous to a system containing only one solvent with time dependent interaction parameters. So far we have shown that under the constraint of $\vec{r}$-independent solvent compositions α, the SCF relations $\phi_i[\omega_i]$ for $i = A, B, S1, S2$ and the variational derivatives of the free energy for a conventional three-component canonical ensemble collapse to expressions for a two-component canonical ensemble ($i = A, B, S$) with interaction parameters given by equation 8.12.

Now we consider the dynamical equations. Rewriting the dynamical equations 2.20 in terms of normalized densities $\phi_i = \rho_i/\rho_0$ yields

$$\frac{\partial\phi_i}{\partial t}(\vec{r}) = \frac{D_0}{N}\sum_{\gamma\in\{A,B\}}\nabla_{\vec{r}}\cdot\int_V\left(\frac{1}{\rho_0}P^{(1)}_{i\gamma}(\vec{r},\vec{r}\,')\right)\nabla_{\vec{r}\,'}\left(\frac{1}{\rho_0}\frac{\delta\beta F_0[\phi_A,\phi_B,\phi_{S1},\phi_{S2}]}{\delta\phi_i(\vec{r}\,')}\right)d\vec{r}\,' \tag{8.19}$$

for $i \in \{A, B\}$. Since

$$F_0[\phi_A,\phi_B,\phi_{S1}[\phi_S,\alpha],\phi_{S2}[\phi_S,\alpha]] = F[\phi_A,\phi_B,\phi_S,\alpha], \tag{8.20}$$

one can directly substitute

$$\frac{\delta F_0[\phi_A, \phi_B, \phi_{S1}, \phi_{S2}]}{\delta \phi_i} \mapsto \frac{\delta F[\phi_A, \phi_B, \phi_S, \alpha]}{\delta \phi_i} \tag{8.21}$$

for $i \in \{A, B\}$ if variables are changed from $(\phi_A, \phi_B, \phi_{S1}, \phi_{S2})$ to $(\phi_A, \phi_B, \phi_S, \alpha)$. Consequently, the chemical potentials from equations 8.16 and 8.17 can be simply inserted into equation 8.19. Considering large system volumes and remembering equation 2.67, the dynamical equation 2.20 for the two solvents can be cast into the form

$$\frac{\partial \phi_{Sj}}{\partial t}(\vec{r}) = D_0 \nabla_{\vec{r}} \cdot \left[\phi_{Sj}(\vec{r}) \nabla_{\vec{r}} \left(\frac{1}{\rho_0} \frac{\delta \beta F_0[\phi_A, \phi_B, \phi_{S1}, \phi_{S2}]}{\delta \phi_{Sj}(\vec{r})} \right) \right] \tag{8.22}$$

with $j = 1, 2$ if we assume both solvents to share a common diffusion coefficient D_0. Adding the temporal derivatives of ϕ_{S1} and ϕ_{S2} and introducing the constraint of spatially constant solvent composition $(\phi_{S1}(\vec{r}), \phi_{S2}(\vec{r})) = ((1-\alpha)\phi_S(\vec{r}), \alpha\phi_S(\vec{r}))$ gives

$$\frac{\partial \phi_S}{\partial t}(\vec{r}) = D_0 \nabla_{\vec{r}} \cdot \left[\phi_S \nabla_{\vec{r}} \frac{1}{\rho_0} \left((1-\alpha) \left. \frac{\delta \beta F_0}{\delta \phi_{S1}(\vec{r})} \right|_\alpha + \alpha \left. \frac{\delta \beta F_0}{\delta \phi_{S2}(\vec{r})} \right|_\alpha \right) \right]. \tag{8.23}$$

with

$$\left. \frac{\delta \beta F_0}{\delta \phi_{Sj}} \right|_\alpha := \frac{\delta \beta F_0[\phi_A, \phi_B, (1-\alpha)\phi_S, \alpha\phi_S]}{\delta \phi_{Sj}}. \tag{8.24}$$

Applying the chain rule to equation 8.20 yields

$$\frac{\delta F}{\delta \phi_S} = (1-\alpha) \left. \frac{\delta F_0}{\delta \phi_{S1}} \right|_\alpha + \alpha \left. \frac{\delta F_0}{\delta \phi_{S2}} \right|_\alpha \tag{8.25}$$

and insertion of the derivative into equation 8.23 leads to

$$\frac{\partial \phi_S}{\partial t}(\vec{r}) = D_0 \nabla_{\vec{r}} \cdot \left[\phi_S \nabla_{\vec{r}} \frac{1}{\rho_0} \frac{\delta \beta F}{\delta \phi_S(\vec{r})} \right]. \tag{8.26}$$

As a result, equations 8.19 and 8.26 are consistent with conventional canonical three-component dynamics under the constraint of $\vec{r}$-independent solvent compositions α. The time dependence of α in equation 8.12 specifies the solvent mixing.

8.4 Chapter summary and main conclusions

In this chapter we inserted time dependent interaction parameters into the SCF-EPD model from He and Schmid [88] to describe size-controlled assembly of amphiphilic diblock-copolymers. In contrast to model I and II, rate-size relations do not refer to droplets but stable particles since amphiphilic diblock-copolymers introduce a steric stabilization that prevents Ostwald Ripening [88]. The SCF-EPD model with time dependent interaction parameters reproduces the experimentally observed depletion of vesicles and the enrichment of micelles for increasing mixing speeds [22, 23]. Our simulations further indicate that this enrichment is only the beginning of a complete vesicle-to-micelle transition, which implies that the co-solvent method theoretically offers the possibility to produce nanoparticle populations with a controllable uniform morphology.

The qualitative match of simulated rate-size relations for *homopolymer droplets* and experimental data for *copolymer particles* in part II has already raised the following two expectations. First, one expects the size-control in experiments to be mainly caused by the interaction between solvent molecules and the monomers of the hydrophobic block during the early stages of phase separation and second, the fundamental characteristics of particle size dependencies on flow rates should be unaffected by the specific particle morphology – at least as far as the distinction between vesicles and micelles to homopolymer droplets is concerned. The SCF-EPD simulations directly confirm both expectations from a theoretical perspective since density profiles ϕ_B of the solvent-phobic block look similar to figure 5.2 in the very early stages of phase separation and since the characteristics of rate-size relations for structured particles from the present chapter (cp. figure 8.4 (a)) closely resemble the ones from model I (cp. figure 5.3). The similarity to figure 5.2 implies that the interpretation to the working principle of size-controlled assembly from model I is qualitatively transferable to amphiphilic copolymer-solutions, which in turn means that the interaction between the solvent and the solvent-phobic block determines the size of unstructured predecessors of polymer particles (that are similar to droplets) by competing with interfacial tension of diffuse interfaces in the very early stages of phase separation. The SCF-EPD simulations further show that once the polymer content inside such a droplet is sufficiently large, it internally arranges – depending on its size – to either a vesicular or a micellar particle due to block-incompatibility without significantly changing the characteristic scaling behavior of rate-size relations. The explicit confirmation that the fundamental working principle of the co-solvent method transfers from homopolymer solutions to copolymer solutions and its consistency with the experimentally observed effect of mixing speeds on particle morphologies are the central results of the present chapter.

It should be noted though that in our simulations we observed only pathway II of vesicle formation, where vesicles are formed by solvent diffusion into the center of droplets. This happens for every single droplet separately and therefore, it preserves droplet sizes to some degree. It may be a topic for future work to adapt input parameters of the SCF-EPD model in order to study mechanism I, where vesicles form via coagulation of multiple droplets and subsequent bilayer folding.[1] The two mechanisms are discussed, for instance, by Uneyama [81] and He and Schmid [89]. If mechanism I would produce fundamentally different characteristics of rate-size relations, one could draw the conclusion that mechanism II occurred in the experiments from figure 1.3. However, we believe that mechanism I is likely to produce a similar scaling behavior, too: if there is a characteristic number n of droplets that merge to each single bilayer and the size R of droplets scales with the mixing speed s as $R \propto s^{\alpha}$, an approximate characteristic size of the vesicle that originates after folding of the bilayer could very well be proportional to $n\, s^{\alpha}$. Pathway I of vesicle formation can only be observed in 3D, because line tension driven bilayer folding requires a spatial dimension perpendicular to the bilayer plane [89]. One could think that the coils in figure 8.7 (a) are 2D-analogues to the bilayers, which cannot fold because of the missing third dimension and the lack of line tension. In this case, the pictures for $v = 0.1$ ml/min and $v = 2.2$ ml/min in figure 8.7 (a)

[1] Since the SCF-EPD model is still a mean field description, it does not capture Brownian motion of droplets and the concomitant collision-induced coagulation. But if the density of stationary droplets is sufficiently high, several droplets may coagulate due to their short distances among each other and merge to a bilayer in the process.

would show an unfinished pathway I. However, this is not the case. For both flow rates, there are vesicles that form via pathway II. But they eventually deform and break up into the coils seen in the pictures.

Chapter 9

Semi-grand canonical effective two-component SCF dynamics

The apparent drawback from time dependent chemical potentials (model II) to time dependent interaction parameters in part III is owed to the fact that model II has chronologically been developed after the SCF-EPD model. Originally, the SCF-EPD model was the direct follow-up to model I before we established the concept of effective two-component systems. In the present chapter we derive semi-grand canonical effective two-component SCF dynamics similarly to model II for the sake of completeness. The effective two-component SCF dynamics model was not implemented and we performed no simulations with it. It is still presented for two reasons. First, it shows that the concept of effective two-component systems can also be applied to a more elaborate description of particle formation than just a phase field model and second, it might be a promising starting point for potential future work according to the conclusions from chapter 6. In that context, the present chapter can be understood as a detailed part of the outlook to part III. The derivation considers a copolymer and two solvents, but the transfer to homopolymers is trivial. Such a transfer could be used to get rid of the Flory-Huggins-de Gennes approximation for the free energy functional in model II.

The construction of the effective two-component SCF dynamics model is analogous to the derivation of model II in section 6.2 and starts from the free energy F_0 given by equation 8.9. Upon substituting ϕ_{S1} by $\phi_{S1}[\phi_S, \phi_{S2}] = \phi_S - \phi_{S2}$ the free energy becomes

$$\frac{1}{n}\beta\widetilde{F}[\phi_A,\phi_B,\phi_S,\phi_{S2}] = E[\phi_A,\phi_B,\phi_S,\phi_{S2}] + \frac{1}{V}\int \Big[\chi_{AB}\phi_A(\vec{r})\phi_B(\vec{r}) + \chi_{AS1}\phi_A(\vec{r})\phi_S(\vec{r})$$

$$+\chi_{BS1}\phi_B(\vec{r})\phi_S(\vec{r})+\Delta\chi_{AS}\phi_A(\vec{r})\phi_{S2}(\vec{r})+\Delta\chi_{BS}\phi_B(\vec{r})\phi_{S2}(\vec{r})+\frac{\kappa_H}{2}(\phi_A(\vec{r})+\phi_B(\vec{r})+\phi_S(\vec{r})-1)^2\Big]\,d\vec{r}$$

$$-\frac{1}{V}\int \Big[\omega_A(\vec{r})\phi_A(\vec{r}) + \omega_B(\vec{r})\phi_B(\vec{r}) + \omega_{S1}(\vec{r})\phi_S(\vec{r}) + (\omega_{S2}(\vec{r}) - \omega_{S1}(\vec{r}))\phi_{S2}(\vec{r})\Big]\,d\vec{r} \qquad (9.1)$$

with $F_0[\phi_A,\phi_B,\phi_{S1},\phi_{S2}] = \widetilde{F}[\phi_A,\phi_B,\phi_S[\phi_{S1},\phi_{S2}],\phi_{S2}]$,

$$E[\phi_A,\phi_B,\phi_S,\phi_{S2}] = -(f_S - f_{S2})\ln\left(\frac{Q_{S1}[\omega_{S1}]}{V(f_S - f_{S2})}\right) - f_{S2}\ln\left(\frac{Q_{S2}[\omega_{S2}]}{V f_{S2}}\right)$$

$$-\frac{f_P}{N}\ln\left(\frac{NQ_P[\omega_A,\omega_B]}{V f_P}\right), \qquad (9.2)$$

$\Delta\chi_{AS} = \chi_{AS2} - \chi_{AS1}$, $\Delta\chi_{BS} = \chi_{BS2} - \chi_{BS1}$, and $f_i = \frac{1}{V}\int \phi_i\,d\vec{r}$. The original formulation, equation 8.9, makes use of the short hand notation $\omega_i = \omega_i[\phi_i]$ with $i = A, B, S_1, S_2$. Ex-

pressing ϕ_{S1} as a function of ϕ_S and ϕ_{S2} coherently renders ω_{S1} a functional of the latter two, i.e. in equations 9.1 and 9.2 it is

$$\omega_{S1} = \omega_{S1}[\phi_{S1}[\phi_S, \phi_{S2}]]. \tag{9.3}$$

The composition variable is the relative chemical potential of solvents μ_s that is calculated from the variation of ${}^{\beta\widetilde{F}}/_{n}$ with respect to ϕ_{S2} at fixed f_S and f_P. Dropping all functional dependencies except for ϕ_{S2} for the sake of notational simplicity, the variation of E reads

$$\begin{aligned}\frac{d}{d\epsilon}\Big|_{\epsilon=0} E[\phi_{S2}+\epsilon\eta] = -\sum_{i=1}^{2}\Big[\ln\left(\frac{Q_{Si}[\phi_{S2}]}{V f_{Si}[\phi_{S2}]}\right)\frac{d}{d\epsilon}\Big|_{\epsilon=0} f_{Si}[\phi_{S2}+\epsilon\eta] \\ + f_{Si}[\phi_{S2}]\,\frac{d}{d\epsilon}\Big|_{\epsilon=0}\ln\left(\frac{Q_{Si}[\phi_{S2}+\epsilon\eta]}{V f_{Si}[\phi_{S2}+\epsilon\eta]}\right)\Big],\end{aligned} \tag{9.4}$$

which becomes

$$\begin{aligned}\frac{d}{d\epsilon}\Big|_{\epsilon=0} E[\phi_{S2}+\epsilon\eta] = \frac{1}{V}\int \ln\left(\frac{Q_{S1}f_{S2}V}{Q_{S2}f_{S1}V}\right)\eta(\vec{r})\,d\vec{r} + \frac{1}{V}\int \phi_S(\vec{r})\,\frac{d}{d\epsilon}\Big|_{\epsilon=0}\omega_{S1}(\vec{r})[\phi_{S2}+\epsilon\eta]\,d\vec{r} \\ + \frac{1}{V}\int \phi_{S2}(\vec{r})\,\frac{d}{d\epsilon}\Big|_{\epsilon=0}\Big(\omega_{S2}(\vec{r})[\phi_{S2}+\epsilon\eta] - \omega_{S1}(\vec{r})[\phi_{S2}+\epsilon\eta]\Big)\,d\vec{r}\end{aligned} \tag{9.5}$$

upon inserting

$$f_{S1}[\phi_{S2}] = \frac{1}{V}\int \phi_S(\vec{r}) - \phi_{S2}(\vec{r})\,d\vec{r} \text{ and } f_{S2}[\phi_{S2}] = \frac{1}{V}\int \phi_{S2}(\vec{r})\,d\vec{r}.$$

The variation of the interaction terms is given by

$$\begin{aligned}\frac{d}{d\epsilon}\Big|_{\epsilon=0}\left(\frac{1}{n}\beta\widetilde{F}[\phi_{S2}+\epsilon\eta] - E[\phi_{S2}+\epsilon\eta]\right) = \frac{1}{V}\int\Big[\Delta\chi_{AS}\phi_A(\vec{r}) + \Delta\chi_{BS}\phi_B(\vec{r}) \\ -\Big(\omega_{S2}(\vec{r})[\phi_{S2}] - \omega_{S1}(\vec{r})[\phi_{S2}]\Big)\Big]\eta(\vec{r})\,d\vec{r} - \frac{1}{V}\int \phi_S(\vec{r})\,\frac{d}{d\epsilon}\Big|_{\epsilon=0}\omega_{S1}(\vec{r})[\phi_{S2}+\epsilon\eta]\,d\vec{r} \\ - \frac{1}{V}\int \phi_{S2}(\vec{r})\,\frac{d}{d\epsilon}\Big|_{\epsilon=0}\Big(\omega_{S2}(\vec{r})[\phi_{S2}+\epsilon\eta] - \omega_{S1}(\vec{r})[\phi_{S2}+\epsilon\eta]\Big)\,d\vec{r}.\end{aligned} \tag{9.6}$$

Adding equations 9.5 and 9.6 directly leads to

$$\begin{aligned}\frac{1}{n}\,\frac{d}{d\epsilon}\Big|_{\epsilon=0}\beta\widetilde{F}[\phi_{S2}+\epsilon\eta] = \frac{1}{V}\int \ln\left(\frac{Q_{S1}f_{S2}V}{Q_{S2}f_{S1}V}\right)\eta(\vec{r})\,d\vec{r} \\ + \frac{1}{V}\int\Big[\Delta\chi_{AS}\phi_A(\vec{r}) + \Delta\chi_{BS}\phi_B(\vec{r}) - \big(\omega_{S2}(\vec{r})[\phi_{S2}] - \omega_{S1}(\vec{r})[\phi_{S2}]\big)\Big]\eta(\vec{r})\,d\vec{r},\end{aligned} \tag{9.7}$$

implying

$$\mu_s = \frac{1}{n}\frac{\delta\beta\widetilde{F}}{\delta\phi_{S2}} = \frac{1}{V}\left[\ln\left(\frac{Q_{S1}f_{S2}V}{Q_{S2}f_{S1}V}\right) + \Delta\chi_{AS}\phi_A + \Delta\chi_{BS}\phi_B - \big(\omega_{S2}(\vec{r}) - \omega_{S1}(\vec{r})\big)\right]. \tag{9.8}$$

Rearranging equation 9.8 by means of equation 8.10 to

$$\mu_s = \frac{1}{V}\left[\ln\left(\frac{Q_{S1}f_{S2}Ve^{-\omega_{S2}}}{Q_{S2}f_{S1}Ve^{-\omega_{S1}}}\right) + \Delta\chi_{AS}\phi_A + \Delta\chi_{BS}\phi_B\right]$$

$$= \frac{1}{V}\left[\ln\left(\frac{\phi_{S2}}{\phi_{S1}}\right) + \Delta\chi_{AS}\phi_A + \Delta\chi_{BS}\phi_B\right] \tag{9.9}$$

immediately yields

$$\phi_{S2}[\phi_A, \phi_B, \phi_S, \mu_s] = \frac{1}{1 + e^{-V\mu_s + \Delta\chi_{AS}\phi_A(\vec{r}) + \Delta\chi_{BS}\phi_B(\vec{r})}}\phi_S(\vec{r}) =: \phi_{S2}(\vec{r}, \mu_s), \tag{9.10}$$

which is the direct analogue to equation 6.26 from model II. The Legendre transform F of $\widetilde{F}$ with respect to ϕ_{S2} reads

$$\begin{aligned}
\frac{1}{n}\beta F[\phi_A, \phi_B, \phi_S, \mu_s] &\coloneqq \frac{1}{n}\beta\widetilde{F}[\phi_A, \phi_B, \phi_S, \phi_{S2}(\mu_s)] - \int \mu_s\phi_{S2}(\mu_s)\, d\vec{r} \\
&= E[\phi_A, \phi_B, \phi_S, \phi_{S2}(\mu_s)] + \frac{1}{V}\int \Big[\chi_{AB}\phi_A\phi_B + \chi_{AS1}\phi_A\phi_S + \chi_{BS1}\phi_B\phi_S \\
&\quad + \frac{\kappa_H}{2}(\phi_A + \phi_B + \phi_S - 1)^2 - \omega_A\phi_A - \omega_B\phi_B - \omega_{S1}\phi_S\Big]\, d\vec{r} \\
&\quad + \frac{1}{V}\int \Big[\Delta\chi_{AS}\phi_A\phi_{S2}(\mu_s) + \Delta\chi_{BS}\phi_B\phi_{S2}(\mu_s) - (\omega_{S2} - \omega_{S1})\phi_{S2}(\mu_s)\Big]\, d\vec{r} \\
&\quad - \int \mu_s\phi_{S2}(\mu_s)\, d\vec{r}.
\end{aligned} \tag{9.11}$$

As the second to last line in equation 9.11 is identical to

$$\frac{1}{V}\int \left(V\mu_s - \ln\left(\frac{Q_{S1}f_{S2}V}{Q_{S2}f_{S1}V}\right)\right)\phi_{S2}(\mu_s)\, d\vec{r} = \int \mu_s\phi_{S2}(\mu_s)\, d\vec{r} - f_{S2}\ln\left(\frac{Q_{S1}f_{S2}V}{Q_{S2}f_{S1}V}\right) \tag{9.12}$$

(cp. equation 9.8), the semi-grand canonical thermodynamic potential can be expressed as

$$\begin{aligned}
\frac{1}{n}\beta F[\phi_A, \phi_B, \phi_S](\mu_s) &= -f_S\ln\left(\frac{Q_{S1}[\omega_{S1}]}{f_{S1}[\phi_S, \phi_{S2}(\mu_s)[\phi_A, \phi_B]]V}\right) - \frac{f_P}{N}\ln\left(\frac{NQ_P[\omega_A, \omega_B]}{f_P V}\right) \\
&\quad + \frac{1}{V}\beta U[\phi_A, \phi_B, \phi_S] - \frac{1}{V}\int \omega_A\phi_A + \omega_B\phi_B + \omega_{S1}\phi_S\, d\vec{r}
\end{aligned} \tag{9.13}$$

with

$$\beta U[\phi_A, \phi_B, \phi_S] = \int \chi_{AB}\phi_A\phi_B + \chi_{AS1}\phi_A\phi_S + \chi_{BS1}\phi_B\phi_S + \frac{\kappa_H}{2}(\phi_A + \phi_B + \phi_S - 1)^2\, d\vec{r} \tag{9.14}$$

if μ_s is assumed to be $\vec{r}$-independent. μ_s may be determined analogously to model II by equation 9.10 with $\phi_A = \phi_B = 0$. Due to the replacement of ϕ_{S2} by μ_s (i.e. insertion of equation 9.10) it is

$$\omega_{S1} = \omega_{S1}[\phi_{S1}[\phi_S, \phi_{S2}(\mu_s)[\phi_A, \phi_B, \phi_S]]]. \tag{9.15}$$

Taking into account that nesting, the variation of the semi-grand potential F with respect to ϕ_α at fixed f_S and f_P becomes

$$\begin{aligned}
&\frac{1}{n}\left.\frac{d}{d\epsilon}\right|_{\epsilon=0}\beta F[\phi_\alpha + \epsilon\eta](\mu_s) \\
&= -f_S\left(\frac{1}{Q_{S1}}\int \frac{\delta Q_{S1}}{\delta\omega_{S1}(\vec{r})}\left.\frac{d}{d\epsilon}\right|_{\epsilon=0}\omega_{S1}(\vec{r})[\phi_\alpha + \epsilon\eta]\, d\vec{r} - \frac{1}{f_{S1}}\left.\frac{d}{d\epsilon}\right|_{\epsilon=0}f_{S1}[\phi_\alpha + \epsilon\eta]\right)
\end{aligned}$$

$$+\frac{1}{V}\int\left(\frac{\delta\beta U}{\delta\phi_\alpha(\vec{r})}-\omega_\alpha(\vec{r})\right)\eta(\vec{r})\,d\vec{r}-\frac{1}{V}\int\phi_S(\vec{r})\,\frac{d}{d\epsilon}\Big|_{\epsilon=0}\omega_{S1}(\vec{r})[\phi_\alpha+\epsilon\eta]\,d\vec{r}$$

$$=-\frac{1}{V}\int\left[-\frac{f_S}{f_{S1}}\phi_{S1}(\vec{r})+\phi_S(\vec{r})\right]\,\frac{d}{d\epsilon}\Big|_{\epsilon=0}\omega_{S1}(\vec{r})[\phi_\alpha+\epsilon\eta]\,d\vec{r}+\frac{f_S}{f_{S1}}\,\frac{d}{d\epsilon}\Big|_{\epsilon=0}f_{S1}[\phi_\alpha+\epsilon\eta]$$

$$+\frac{1}{V}\int\left(\frac{\delta\beta U}{\delta\phi_\alpha(\vec{r})}-\omega_\alpha(\vec{r})\right)\eta(\vec{r})\,d\vec{r} \tag{9.16}$$

for $\alpha = A, B, S$. At $\alpha = S$ the notation $\omega_\alpha = \omega_{S1}$ is applied for conciseness of equation 9.16. According to equation 9.15 the variation of ω_{S1} can be expressed by the chain rule

$$\frac{d}{d\epsilon}\Big|_{\epsilon=0}\omega_{S1}(\vec{r})[\phi_i+\epsilon\eta]=\int\int\frac{\delta\omega_{S1}(\vec{r})}{\delta\phi_{S1}(\vec{r}\,')}\frac{\delta\phi_{S1}(\vec{r}\,')}{\delta\phi_i(\vec{r}\,'')}\,d\vec{r}\,'\eta(\vec{r}\,'')\,d\vec{r}\,'', \tag{9.17}$$

where the first functional derivative, $\frac{\delta\omega_{S1}(\vec{r})}{\delta\phi_{S1}(\vec{r}\,')}[\phi_{S1}]$, is evaluated at

$$\phi_{S1}=\phi_{S1}[\phi_S,\phi_{S2}(\mu_s)[\phi_A,\phi_B,\phi_S]].$$

The second one, $\frac{\delta\phi_{S1}(\vec{r}\,')}{\delta\phi_i(\vec{r}\,'')}$, is known as it can be directly calculated from $\phi_{S1}=\phi_S-\phi_{S2}(\mu_s)$ with $\phi_{S2}(\mu_s)$ from equation 9.10. To obtain $\frac{\delta\omega_{S1}(\vec{r})}{\delta\phi_{S1}(\vec{r}\,')}[\phi_{S1}]$, the inversion rule of variational calculus,

$$\delta(\vec{r}_0-\vec{r})=\int\frac{\delta\phi_{S1}(\vec{r}\,')}{\delta\omega_{S1}(\vec{r}_0)}\frac{\delta\omega_{S1}(\vec{r})}{\delta\phi_{S1}(\vec{r}\,')}\,d\vec{r}\,', \tag{9.18}$$

is applied. Remembering equations 2.67 and 7.2 with $n_{S1}/\rho_0 = f_{S1}V$, the inversion rule can be cast into the form

$$\delta(\vec{r}_0-\vec{r})=-f_{S1}V\int\left\langle\hat{\rho}_{S1}^{(c,S1)}(\vec{r}_0)\hat{\rho}_{S1}^{(c,S1)}(\vec{r}\,')\right\rangle_c\frac{\delta\omega_{S1}(\vec{r})}{\delta\phi_{S1}(\vec{r}\,')}\,d\vec{r}\,', \tag{9.19}$$

where $\langle ...\rangle_c$ is the single 'chain' average for a solvent molecule in an external field ω_{S1}, i.e.

$$f_{S1}V\left\langle\hat{\rho}_{S1}^{(c,S1)}(\vec{r}_0)\hat{\rho}_{S1}^{(c,S1)}(\vec{r}\,')\right\rangle_c=\frac{f_{S1}V}{Q_{S1}}\int\delta(\vec{r}_0-\vec{R})\delta(\vec{r}\,'-\vec{R})e^{-\omega_{S1}(\vec{R})}\,d\vec{R}$$

$$=\frac{f_{S1}V}{Q_{S1}}\int\delta(\vec{r}_0-\vec{r}\,')\delta(\vec{r}\,'-\vec{R})e^{-\omega_{S1}(\vec{R})}\,d\vec{R}$$

$$=\delta(\vec{r}_0-\vec{r}\,')\phi_{S1}(\vec{r}\,'). \tag{9.20}$$

Consequently, equation 9.19 is equivalent to

$$\delta(\vec{r}_0-\vec{r})=-\phi_{S1}(\vec{r}_0)\frac{\delta\omega_{S1}(\vec{r})}{\delta\phi_{S1}(\vec{r}_0)}\Leftrightarrow\frac{\delta\omega_{S1}(\vec{r})}{\delta\phi_{S1}(\vec{r}_0)}=-\frac{\delta(\vec{r}_0-\vec{r})}{\phi_{S1}(\vec{r}_0)}. \tag{9.21}$$

Inserting equation 9.17 with $\frac{\delta\omega_{S1}}{\delta\phi_{S1}}$ from equation 9.21 into equation 9.16 finally yields

$$\frac{1}{\rho_0}\,\frac{d}{d\epsilon}\Big|_{\epsilon=0}\beta F[\phi_\alpha+\epsilon\eta](\mu_s)=\int\Big[\int\left(\frac{\phi_S(\vec{r}\,')}{\phi_{S1}(\vec{r}\,')}-\frac{f_S}{f_{S1}}\right)\frac{\delta\phi_{S1}(\vec{r}\,')}{\delta\phi_i(\vec{r})}\,d\vec{r}\,'+\int\frac{f_S}{f_{S1}}\frac{\delta\phi_{S1}(\vec{r}\,')}{\delta\phi_i(\vec{r})}\,d\vec{r}\,'$$

$$+\frac{\delta\beta U}{\delta\phi_i(\vec{r})}-\omega_\alpha\Big]\eta(\vec{r})\,d\vec{r}, \tag{9.22}$$

so it is

$$\frac{1}{\rho_0}\frac{\delta\beta F}{\delta\phi_\alpha(\vec{r})} = \int \frac{\phi_S(\vec{r}\,')}{\phi_{S1}(\vec{r}\,')}\frac{\delta\phi_{S1}(\vec{r}\,')}{\delta\phi_\alpha(\vec{r})}\,d\vec{r}\,' + \frac{\delta\beta U}{\delta\phi_\alpha(\vec{r})} - \omega_\alpha \tag{9.23}$$

with

$$\phi_{S1}(\vec{r}) = \left(1 - \frac{1}{1 + e^{-V\mu_s + \Delta\chi_{AS}\phi_A(\vec{r}) + \Delta\chi_{BS}\phi_B(\vec{r})}}\right)\phi_S(\vec{r}) \tag{9.24}$$

and βU from equation 9.14. Except for the integral term, equation 9.23 is formally identical to equations 7.14 – 7.16. Since $\phi_{S1}(\vec{r})$ depends only on the densities ϕ_A, ϕ_B, and ϕ_S at the same position $\vec{r}$, the variational derivative $\frac{\delta\phi_{S1}(\vec{r}\,')}{\delta\phi_\alpha(\vec{r})}$ is proportional to $\delta(\vec{r} - \vec{r}\,')$ and the integral in equation 9.23 collapses. So as far as the implementation of solvent mixing into the free energy derivatives is concerned, the effective two-component SCF-model does not introduce any significant additional computational cost compared to time-dependent interaction parameters.

$\phi_A[\omega_A]$ and $\phi_B[\omega_B]$ are still given by equations 7.7 and 7.8, respectively, because none of the preceding variable transformations affect ω_A, ω_B, or Q_P. The relation between ϕ_S and the potential fields reads

$$\begin{aligned}\phi_S(\vec{r}) &= \left(1 + e^{V\mu_s - \Delta\chi_{AS}\phi_A(\vec{r})[\omega_A] - \Delta\chi_{BS}\phi_B(\vec{r})[\omega_B]}\right)\phi_{S1}(\vec{r}) \\ &= \left(1 + e^{V\mu_s - \Delta\chi_{AS}\phi_A(\vec{r})[\omega_A] - \Delta\chi_{BS}\phi_B(\vec{r})[\omega_B]}\right)\frac{f_{S1}V}{Q_{S1}[\omega_{S1}]}e^{-\omega_{S1}(\vec{r})}.\end{aligned} \tag{9.25}$$

Since

$$f_{S1} = \frac{1}{V}\int \phi_{S1}(\vec{r})\,d\vec{r} = \frac{1}{V}\int \left(1 + e^{V\mu_s - \Delta\chi_{AS}\phi_A(\vec{r})[\omega_A] - \Delta\chi_{BS}\phi_B(\vec{r})[\omega_B]}\right)\phi_S(\vec{r})\,d\vec{r}, \tag{9.26}$$

equation 9.25 is implicit in ϕ_S as its right hand side contains a ϕ_S-dependence. Instead of directly inverting equation 9.25 to calculate the explicit ω-dependence of ϕ_S, it is more convenient to determine the $\vec{r}$-independent constant ${}^{f_{S1}V}/_{Q_{S1}[\omega_{S1}]}$ by the normalization constraint

$$\begin{aligned}1 - f_P = \frac{1}{V}\int \phi_S(\vec{r})\,d\vec{r} &= \frac{f_{S1}V}{Q_{S1}[\omega_{S1}]}\frac{1}{V}\int \left(1 + e^{V\mu_s - \Delta\chi_{AS}\phi_A(\vec{r})[\omega_A] - \Delta\chi_{BS}\phi_B(\vec{r})[\omega_B]}\right)e^{-\omega_{S1}(\vec{r})}\,d\vec{r} \\ \Leftrightarrow \frac{f_{S1}V}{Q_{S1}[\omega_{S1}]} &= \frac{V(1 - f_P)}{\int \left(1 + e^{V\mu_s - \Delta\chi_{AS}\phi_A(\vec{r})[\omega_A] - \Delta\chi_{BS}\phi_B(\vec{r})[\omega_B]}\right)e^{-\omega_{S1}(\vec{r})}\,d\vec{r}}\end{aligned} \tag{9.27}$$

at any time step, leading to

$$\phi_S(\vec{r}) = (1 - f_P)V\frac{\left(1 + e^{V\mu_s - \Delta\chi_{AS}\phi_A(\vec{r})[\omega_A] - \Delta\chi_{BS}\phi_B(\vec{r})[\omega_B]}\right)e^{-\omega_{S1}(\vec{r})}}{\int \left(1 + e^{V\mu_s - \Delta\chi_{AS}\phi_A(\vec{r}\,')[\omega_A] - \Delta\chi_{BS}\phi_B(\vec{r}\,')[\omega_B]}\right)e^{-\omega_{S1}(\vec{r}\,')}\,d\vec{r}\,'}, \tag{9.28}$$

which replaces equation 7.9.

The variational derivatives of ϕ_S at fixed f_P in the limit of large system volumes V can be calculated to

$$\frac{\delta\phi_S(\vec{r})}{\delta\omega_A(\vec{r}\,')} = -\Delta\chi_{AS}\,\phi_{S2}(\vec{r},\mu_s)\frac{\delta\phi_A(\vec{r})}{\delta\omega_A(\vec{r}\,')} =: \Delta\chi_{AS}\phi_{S2}(\vec{r},\mu_s)p_{AA}(\vec{r},\vec{r}\,'), \tag{9.29}$$

$$\frac{\delta\phi_S(\vec{r})}{\delta\omega_B(\vec{r}\,')} = -\Delta\chi_{BS}\,\phi_{S2}(\vec{r},\mu_s)\frac{\delta\phi_B(\vec{r})}{\delta\omega_B(\vec{r}\,')} =: \Delta\chi_{BS}\phi_{S2}(\vec{r},\mu_s)p_{BB}(\vec{r},\vec{r}\,'), \tag{9.30}$$

and

$$\frac{\delta\phi_S(\vec{r})}{\delta\omega_{S1}(\vec{r}\,')} = -\phi_S(\vec{r})\delta(\vec{r}-\vec{r}\,') =: -p_{SS}(\vec{r},\vec{r}\,'), \tag{9.31}$$

where $p = {}^{P}\!/_{\rho_0}$ with the pair correlators P from equation 2.63. The non-vanishing right hand sides in equations 9.29 and 9.30 hint at a kinetic coupling between monomers and solvent molecules. Unlike the (non-local) kinetic coupling between different monomers of a polymer chain, the coupling between ϕ_S and ω_A, ω_B is not directly caused by covalent bonds but by the constraint of instantaneous solvent-equilibration, i.e. $\vec{r}$-independent μ_s.

Neglecting thermal fluctuations, the corresponding effective two-component[1] dynamical equations for large system volumes V may be written as (cp. equation 2.20)

$$\frac{\partial\phi_\alpha}{\partial t}(\vec{r},t) = \frac{D_0}{N}\sum_{\gamma\in\{A,B\}}\nabla_{\vec{r}}\cdot\int p_{\alpha\gamma}(\vec{r},\vec{r}\,')\nabla_{\vec{r}\,'}\left(\frac{1}{\rho_0}\frac{\delta\beta F[\{\phi_i(\cdot,t)\}](\mu_s)}{\delta\phi_\alpha(\vec{r}\,')}\right)d\vec{r}\,' \tag{9.32}$$

for $\alpha = A$, B and

$$\begin{aligned}\frac{\partial\phi_S}{\partial t}(\vec{r},t) &= D_0\nabla_{\vec{r}}\cdot\int p_{SS}(\vec{r},\vec{r}\,')\nabla_{\vec{r}\,'}\left(\frac{1}{\rho_0}\frac{\delta\beta F[\{\phi_i(\cdot,t)\}](\mu_s)}{\delta\phi_S(\vec{r}\,')}\right)d\vec{r}\,' \\ &-\frac{D_0}{N}\nabla_{\vec{r}}\cdot\sum_{\gamma=A,B}\Delta\chi_{\gamma S}\,\phi_{S2}(\vec{r},\mu_s,t)\int p_{\gamma\gamma}(\vec{r},\vec{r}\,')\nabla_{\vec{r}\,'}\left(\frac{1}{\rho_0}\frac{\delta\beta F[\{\phi_i(\cdot,t)\}](\mu_s)}{\delta\phi_\gamma(\vec{r}\,')}\right)d\vec{r}\,'\end{aligned} \tag{9.33}$$

with the short hand notation $\{\phi_i\} = \{\phi_i\}_{i=A,B,S}$. Since

$$\frac{1}{n}\beta F[\phi_A,\phi_B,\phi_S,\mu_s] = \frac{1}{n}\beta\widetilde{F}[\phi_A,\phi_B,\phi_S,\phi_{S2}[\phi_A,\phi_B,\phi_S,\mu_s]] - \int\mu_s\phi_{S2}[\phi_A,\phi_B,\phi_S,\mu_s]\,d\vec{r}$$

and $\widetilde{F}[\phi_A,\phi_B,\phi_S,\phi_{S2}] = F_0[\phi_A,\phi_B,\phi_{S1}[\phi_S,\phi_{S2}],\phi_{S2}]$, analogous considerations like the ones that led to equation 6.31 result in

$$\begin{aligned}&\frac{\delta\beta F[\phi_A,\phi_B,\phi_S,\mu_s]}{\delta\phi_i} \\ &= \frac{\delta\beta F_0[\phi_A,\phi_B,\phi_{S1}[\phi_S,\phi_{S2}[\phi_A,\phi_B,\phi_S,\mu_s]],\phi_{S2}[\phi_A,\phi_B,\phi_S,\mu_s]]}{\delta\phi_i} =: \left.\frac{\delta\beta F_0}{\delta\phi_i}\right|_{\mu_s}\end{aligned} \tag{9.34}$$

for $i = A$, B. This means that equation 9.32 describes the motion of A- and B-monomers in a canonical three-component ensemble under the constraint of solvent compositions set by μ_s just like equation 6.32 from model II. The evolution of the solvent density ϕ_S is again described by a phenomenological equation. The second line in equation 9.33 accounts for the kinetic coupling between solvent molecules and monomers that is caused by the constraint of homogeneous μ_s.

According to equations 9.10 and 9.24, the constraint 'attaches' a certain amount of good and selective solvent molecules to monomers. Since the contribution of that attachment to solvent-exchange between lattice cells is driven by the motion of polymer chains, we use the diffusion coefficient ${}^{D_0}\!/_N$ in the second line of equation 9.33. In case N is large (in figure 1.3 it is $N \approx 190$), the right hand side in the first line of equation 9.33 contributes much more to $\frac{\partial\phi_S}{\partial t}$ than the second line ($p_{\gamma\gamma} = {}^{P_{\gamma\gamma}}\!/_{\rho_0} = P_{\gamma\gamma}V/n$ does not grow with N since $n = Nn_P + n_{S1} + n_{S2}$),

[1] We count the AB-diblock-copolymer as one component.

meaning that the evolution of ϕ_S can be approximated by the first line only. Equations 9.32 and the first line of equation 9.33 formally correspond to the dynamical equations from He and Schmid [88] for a two-component diblock-copolymer solution. As a consequence, one can also apply the EPD formalism to solve the dynamics. The corresponding evolution equations for the potential fields are identical to equation 7.10, except that the variational derivatives of the free energy are given by equation 9.23 (ω_S corresponds to ω_{S1}). The model is completed by the relations between the densities and the potential fields: ϕ_A and ϕ_B can still be calculated by equations 7.7 and 7.8, while the connection between $\omega_{S1} \equiv \omega_S$ and ϕ_S is given by equation 9.28. Comparing the effective two-component SCF-EPD model to conventional three-component dynamics similar to section 6.5 could be addressed in future work. The advantage of the effective two-component SCF dynamics over the conventional three component dynamics is again the implementation of solvent mixing. If we used source terms or Neumann boundary conditions, the application of the EPD formalism, for instance, would not work.

Note that in contrast to model II, where we applied local kinetic coupling, the diffusion coefficient for the polymers in equation 9.32 reads D_0/N. So at large N, solvent diffuses much faster than polymer chains and thus, the assumption of fast solvent relaxation compared to polymer phase separation receives a similar character like an adiabatic approximation. Therefore, it might be possible that in contrast to model II the validity of the current model in the limit of large N is not restricted to dilute polymer solutions.

Chapter 10

Conclusion and Outlook

The present work deals with modeling the co-solvent method or representatively, size-controlled assembly, which denotes particle formation from a homogeneous solution during solvent mixing. Our primary focus is on developing a fundamental understanding of the nanoparticle size dependence on mixing speeds or more specifically, on flow rates in interdigital micromixers (cp. figure 1.3). Since a direct numerical simulation of complete mixer geometries with nanometer resolutions is not possible, testing any eligible model against experiments also poses a spatial multiscale problem. We approach this problem by viewing particle formation from a Lagrangian perspective of fluid elements that follow stream lines and in doing so, constructing a suitable description for solvent mixing in such nanoscale fluid elements is automatically another focal point. Roughly formulated, we address the fundamental understanding of particle size dependencies in chapters 5 and 8 by applying deliberately simplified implementations of solvent mixing, while more realistic implementations are subject to chapters 6 and 9. As far as the classification into the available theoretical literature is concerend, this thesis complements the publications from Nikoubashman et al. [35] and Spaeth et al. [38], which are, to our knowledge, the only prior modeling approaches to investigate size-control with the co-solvent method.

In part II we model size-controlled assembly of homopolymer nanoparticles by spinodal decomposition, where phase separation dynamics are described by a Cahn-Hilliard equation with a Flory-Huggins-de Gennes free energy functional. In chapter 5 solvent mixing is implemented simply by temporally increasing Flory-Huggins interaction parameters and the combination of the Cahn-Hilliard equation with time dependent interaction parameters is called model I.

Other than in the present work the theoretical investigation of size-controlled homopolymer assembly is addressed in the recent publication by Nikoubashman et al. [35]. They implement solvent mixing into Molecular Dynamics similarly to model I by time dependent repulsive forces between one single solvent and polymer beads. A comparison between results from the Molecular Dynamics simulations and from model I indicates that the phase field model is on par with much more complex particle models as far as non-asymptotic regimes of rate-size relations are concerned. In general, Molecular Dynamics describes particle growth of course more accurately than any mean field continuum theory but model I provides exclusive advantages with respect to size-controlled assembly. One such advantage of model I is its mathematical structure. It enables a perturbation theory that takes a central role as it leads to a theoretical scaling law $R \propto s^{-1/6}$ (R is a typical polymer aggregate size and s characterizes the solvent mixing speed that may be simplistically considered to represent flow rates in

interdigital micromixers), which is in very good agreement with simulation results from both model I (cp. figure 5.3) and the Molecular dynamics model (cp. figure 5.4). This agreement implies that the perturbation theory provides an analytical explanation of the homopolymer particle size dependence on mixing speeds: the scaling law originates from a competition between the time dependent repulsion of chemical components and interfacial tension of diffuse interfaces during the very early stages of phase separation when single polymer chains aggregate. The analytical explanation to trends in recently published Molecular Dynamics data constitutes a novelty of the present work. In contrast to simulations, the perturbation theory directly shows that the scaling behavior is independent from the input parameters and constitutes an universal characteristic as long as quench processes are linearly time dependent. To break the scaling law, specific non-linear mixing profiles such as the SFIMM-profile have to be applied.

A very similar scaling is also reflected in the experimental data for diblock-copolymers from figure 1.3 (the exponents in figure 1.3 scatter around an average of -0.158 with a standard deviation 0.058) and in the results from Dissipative Particle Dynamics simulations by Spaeth et al. [38], who simulated size-controlled assembly of polymer-protected nanoparticles in a ternary mixture of a solvent-phobic solute, an amphiphilic block-copolymer, and one solvent with time dependent interactions. This resemblance shows that a scaling behavior $R \propto s^{\alpha}$ seems to occur regardless of the polymer architecture.[1] The minor importance of polymer architecture is further supported by the fact that the response of rate-size relations from model I to variations in temperature and mean polymer volume fraction qualitatively agrees with experimental observations for copolymers in figure 1.3 as well. The results from the Molecular Dynamics simulations reproduce such qualitative tendencies from the experimental data, too. These qualitative similarities motivate the hypothesis that the principle physical mechanism behind the size-control is identical in both homo- and copolymer solutions, which may be attributed to the fact that phase separation in the early stages is mainly driven by the solvent-phobic blocks.[2] For this reason, model I provides a fundamental qualitative explanation to much more general applications than just homopolymers.

At the level of a more quantitative comparison with experiments, a second advantage of model I, its computational efficiency, comes into play. While Molecular Dynamics does not allow simulations up to realistic mixing times due to its computational complexity, model I does and hence, it enables the direct comparison of its simulation results to experimental data (cp. figures 5.10 and 5.15). The resulting match of length and time scales eventually complements the qualitative similarities from the previous paragraph and completes the evidence leading to one of the most important conclusions of the present work, namely that the response of molecular assembly to solvent mixing, i.e. coupling mechanism (i) from page 50, is probably the dominating determinant for particle sizes in the co-solvent method. This in turn implicates that the analytical perturbation theory for model I provides a fundamental (qualitative) explanation to the experimental observations in figure 1.3.

The dominance of mechanism (i) implies that mean field continuum descriptions should

[1] Deviations of exponents α from $-1/6$ are not captured by model I but we have found in chapters 6 and 8 that, within model II or the SCF-EPD model, the values of Flory-Huggins interaction parameters between solvents and polymer beads may cause these deviations without violating the explanation to particle size dependencies.

[2] One major result of the SCF-EPD simulations in chapter 8 is the explicit confirmation of this hypothesis from a theoretical point of view.

be promising frameworks to simulate size-controlled assembly at experimental conditions, since they represent the computationally most efficient descriptions of molecular organization (but do not capture Brownian motion of droplets or particles and the concomitant collision-induced coagulation in the late stages or particle growth). Although model I provides a clear interpretation to size-controlled assembly and reproduces experimental trends surprisingly well,[3] the description of solvent mixing by time dependent quench processes is oversimplified since it cannot account for an independent motion of good and poor solvent. To approach that matter we refine the description of solvent mixing in chapter 6. In the process, we introduce the phenomenological concept of effective two-component systems and propose model II, which assumes an instantaneous equilibration of solvent compositions. In contrast to model I, model II does not only show a qualitative agreement with experimental results, but its canonical version is also quantitatively consistent with a conventional three-component model in incompressible dilute polymer solutions. Since incompressible dilute polymer solutions correspond to experimental conditions, model II could possibly be indeed a promising starting point to develop computationally efficient, quantitatively accurate descriptions of co-solvent method for homopolymers. This possibility is the final conclusion of chapter 6, as due to a lack of material data we have to leave a detailed check to future work.

The reason to choose model II (or more generally, effective two-component models) over conventional three-component dynamics is the 'coupling interface' to solvent mixing. While a conventional three-component model required source terms or Neumann conditions at the boundaries of a fluid element, solvent mixing (including mixer geometries and flow rates) in model II is implemented as an algebraic relation for the interaction term in a free energy. Since effective two-component systems differ from spontaneous self-assembly only in that relation, the mathematical framework – e.g. numerical integrators, a perturbation theory, and even the EPD formalism if copolymers are considered like in chapter 9 – can be directly transferred. The description of solvent mixing by source terms or Neumann boundary conditions, in contrast, would break the direct mathematical analogy to spontaneous self-assembly. As the derivation of model II relies on concepts from phenomenological equilibrium thermodynamics (the analytical calculation of solvent compositions from a constant relative chemical potential μ_s), such a computationally efficient refinement of solvent mixing should be exclusive to continuum theories and therefore, it constitutes another advantage over particle models. The algebraic relation in the free energy represents a spatial multiscale approach, which completely avoids any numerical and computational difficulties associated with the different length scales of particle sizes and mixer geometries. The consideration of mixer geometries and the implementation of more realistic solvent quality distributions than just globally increasing repulsions is another novelty of the present work with respect to references [35] and [38]. The multiscale approach works really well for the CPMM (cp. figures 5.15 and 6.5). The deviations from experimentally observed trends in the SFIMM have been discussed to be caused most likely by the SFIMM-profile itself and not our coupling interfaces for solvent mixing (cp. the end of subsection 5.4.2, A).

In part III we consider controlled assembly of copolymers based on the SCF-EPD equations from He and Schmid [88] and the primary outcome of chapter 7 is the new numerical integration scheme. In chapter 8 we apply time dependent interaction parameters like in model I and besides the direct confirmation that the characteristics of rate-size relations and their expla-

[3]The reason for that qualitative reproduction is discussed in the beginning of section 6.6.

nation transfer from homopolymer solutions (model I) to copolymer solutions (SCF-EPD), a main result is the vesicle-to-micelle transition that also agrees with experiments. The main point of chapter 9 is the effective two-component SCF model with a monomer concentration dependent solvent quality distribution analogously to model II.

Since the current chapter is only meant to recapitulate the intentions of the work at hand and to put its most general results into an overall context, we refer to the chapter summaries (sections 5.5 [model I], 6.6 [model II], 7.4 [integration scheme for SFC-EPD], and 8.4 [results from SCF-EPD]) for more detailed discussions. Based on the previous recapitulation, the questions from the end of chapter 1 may be answered as follows:

- What causes the approximate scaling behavior $R_{DLS} \propto v^{\alpha}$ in figure 1.3? Is this behavior only specific to the chemical components used by references [22, 23, 36] or is it more general? How can it be broken?
  The scaling behavior originates from a competition between repulsion of chemical components and interfacial tension of diffuse interfaces during the very early stages of phase separation when single polymer chains aggregate. It may be approximately described by a Cahn-Hilliard equation with continuous time dependent quenches and appears to be a generic feature that is not specific to the chemical components. It can be broken, however, by particular non-linear time dependencies of a quench process.

- Taking into account that the polydispersity of nanoparticle populations is also important for their applications, is it theoretically possible to control the polydispersity with the co-solvent method independently of their mean size?
  The fact that any continuous quench is analogous to an effective constant interaction parameter implicates that the independent adjustment of polydispersities should not be possible.

- Assuming one wants to develop simulation tools that enable accurate predictions about particle sizes in the future, which theoretical descriptions can be used as starting points? Which physical mechanisms need to be included? And how could a computationally efficient implementation of these mechanisms look like?
  Our investigations indicate that the co-solvent method can be modeled if only spinodal decomposition and solvent mixing are taken into account. As a consequence, mean field continuum descriptions should constitute suitable starting points. This is a fortunate coincidence because detailed particle models, which capture collision-coagulation, do not allow simulations at realistic mixing times. The concept of effective two-component systems provides a computationally very efficient coupling interface of particle formation to solvent mixing, and we constructed effective two-component models that agree with conventional three-component dynamics in incompressible dilute polymer solutions.

As the present work focuses on the development of models and the explanation of general experimental observations, we extracted qualitative features from exemplary polymers with arbitrary interaction parameters. Future work could aim at investigating in how far model II or the model from chapter 9, for instance, are able to reproduce experimental results quantitatively. That the computational efficiency of our models suffices to simulate experimental conditions is indicated by subsection 5.3.5 B. So as a next step, rate-size relations could be compared to experimental data for a specific polymer with measured χ-parameters. One

may even account for temperature or density dependencies as proposed by Wolf [153]. A qualitative aspect that was not addressed at all are the two potential pathways of vesicle formation [89]. Since pathway I appears in three dimensions only and since we restricted to 2D simulations with the SFC-EPD model for the sake of simplicity, we only observed pathway II. Because the actual vesicle formation mechanism may affect hydrophilic loading of vesicles, it could be interesting to see if pathway I produces the typical progressions of rate-size relations from the present work as well or if they are exclusive to pathway II. In case the latter is true, the attribution of rate-size relations might give information about the vesicle formation mechanism that occurred in the experiments used to generate figure 1.3. As an effect of solvent mixing speed on the pathways is observed by Han et al. [168], it should also be interesting to study how the pathway depends on flow rates.

Bibliography

[1] J. F. Sargent. The National Nanotechnology Initiative: Overview, Reauthorization, and Appropriations Issues. *Congressional Research Service*, 2014.

[2] D. M. Herlach, I. Klassen, P. Wette, and D. Holland-Moritz. Colloids as model systems for metals and alloys: A case study of crystallization. *Journal of Physics: Condensed Matter*, 22(15):153101, 2010.

[3] F. Smallenburg, N. Boon, M. Kater, M. Dijkstra, and R. Roij. Phase Diagrams of Colloidal Spheres with a Constant Zeta-Potential. *Journal of Chemical Physics*, 134:074505, 2011.

[4] M. A. Bucaro, P. R. Kolodner, J. A. Taylor, A. Sidorenko, J. Aizenberg, and T. N. Krupenkin. Tunable Liquid Optics: Electrowetting-Controlled Liquid Mirrors Based on Self-Assembled Janus Tiles. *Langmuir*, 25(6):3876–3879, 2009.

[5] D. Lensen, D. M. Vriezema, and J. C. M. van Hest. Polymeric Microcapsules for Synthetic Applications. *Macromolecular Bioscience*, 8(11):991–1005, 2008.

[6] D. E. Discher and A. Eisenberg. Polymer Vesicles. *Science*, 297:967–972, 2002.

[7] L. Zhang, F. X. Gu, J. Chan, A. Z. Wang, R. S. Langer, and O. Farokhzad. Nanoparticles in Medicine: Therapeutic Applications and Developments. *Clinical Pharmacology and Therapeutics*, 83:761–769, 2008.

[8] M. E. Gindy and R. K. Prud'homme. Multifunctional nanoparticles for imaging, delivery and targeting in cancer therapy. *Expert Opinion on Drug Delivery*, 6(8):865–878, 2009.

[9] P. Vartholomeos, M. Fruchard, A. Ferreira, and C. Mavroidis. MRI-Guided Nanorobotic Systems for Therapeutic and Diagnostic Applications. *Annual Review of Biomedical Engineering*, 13(1):157–184, 2011.

[10] H. Maeda, J. Wu, T. Sawa, Y. Matsumura, and K. Hori. Tumor vascular permeability and the EPR-effect in macromolecular therapeutics: a review. *Journal of Controlled Release*, 65:271–284, 2000.

[11] R. Bleul. Herstellung, Charakterisierung und Funktionalisierung polymerer Nanopartikel und Untersuchung der Wechselwirkung mit biologischen Systemen. *Dissertation, Free University of Berlin*, 2014.

[12] S. K. Hobbs, W. L. Monsky, F. Yuan, W. G. Roberts, L. Griffith, V. P. Torchilin, and R. K. Jain. Regulation of transport pathways in tumor vessels: Role of tumor type and microenvironment. *Proceedings of the National Academy of Sciences*, 95:4607–4612, 1998.

[13] S. Sukriti, M. Tauseef, P. Yazbeck, and D. Mehta. Mechanisms regulating endothelial permeability. *Pulmonary Circulation*, 4:535–546, 2014.

[14] E. Wisse, F. Jacobs, B. Topal, P. Frederik, and B. de Geest. The size of endothelial fenestrae in human liver sinusoids: implications for hepatocyte-directed gene transfer. *Gene Therapy*, 15:1193–1199, 2008.

[15] H. J. Paek, Y. J. Lee, H. E. Chung, N. H. Yoo, J. A. Lee, M. K. Kim, J. K. Lee, J. Jeong, and S. J. Choi. Modulation of the pharmacokinetics of zinc oxide nanoparticles and their fates in vivo. *Nanoscale*, 5(23):11416, 2013.

[16] D. P. K. Lankveld, A. G. Oomen, P. Krystek, A. Neigh, A. Troost-De Jong, C. W. Noorlander, J. C. H. Van Eijkeren, R. E. Geertsma, and W. H. De Jong. The kinetics of the tissue distribution of silver nanoparticles of different sizes. *Biomaterials*, 31:8350–8361, 2010.

[17] K. Ogawara, K. Furumoto, S. Nagayama, K. Minato, K. Higaki, T. Kai, and T Kimura. Pre-coating with serum albumin reduces receptor-mediated hepatic disposition of polystyrene nanosphere: Implications for rational design of nanoparticles. *Journal of Controlled Release*, 100(3):451–455, 2004.

[18] S. Tenzer, D. Docter, S. Rosfa, A. Wlodarski, J. Kuharev, A. Rekik, S. K. Knauer, C. Bantz, T. Nawroth, C. Bier, J. Sirirattanapan, W. Mann, L. Treuel, R. Zellner, M. Maskos, H. Schild, and R. H. Stauber. Nanoparticle Size Is a Critical Physicochemical Determinant of the Human Blood Plasma Corona: A Comprehensive Quantitative Proteomic Analysis. *ACS Nano*, 5(9):7155–7167, 2011.

[19] D. E. Owens and N. A. Peppas. Opsonization, biodistribution, and pharmacokinetics of polymeric nanoparticles. *International Journal of Pharmaceutics*, 307:93–102, 2006.

[20] T. M. Allen and P. R. Cullis. Drug Delivery Systems: Entering the Mainstream. *Science*, 303:1818–1822, 2004.

[21] B. M. Discher, Y. Y. Won, D. S. Ege, J. C. M. Lee, F. S. Bates, D. E. Discher, and D. A. Hammer. Polymersomes: Tough Vesicles Made from Diblock Copolymers. *Science*, 284:1143–1146, 1999.

[22] R. Thiermann. Selbstorganisation amphiphiler Block-Copolymere in Mikromischern. *Dissertation, Berlin University of Technology*, 2014.

[23] R. Thiermann, W. Mueller, A. Montesinos-Castellanos, D. Metzke, P. Löb, V. Hessel, and M. Maskos. Size controlled polymersomes by continuous self-assembly in micromixers. *Polymer*, 53(11):2205–2210, 2012.

[24] S. Wohlfahrt, S. Gelperina, and J. Kreuter. Transport of drugs across the blood-brain barrier by nanoparticles. *Journal of Controlled Release*, 161:264–273, 2012.

[25] K. K. Jain. Nanobiotechnology-Based Strategies for Crossing the Blood-Brand Barrier. *Nanomedicine*, 7:1225–1233, 2012.

[26] C. Roney, P. Kulkarni, V. Arora, P. Antich, F. Bonte, A. Wu, N. N. Mallikarjuana, S. Manohar, H. F. Liang, A. R. Kulkarni, H. S. Sung, M. Sairam, and M. T. Aminabhavi. Targeted nanoparticles for drug delivery through the blood-brain barrier for Alzheimer's disease. *Journal of Controlled Release*, 108:193–214, 2005.

[27] S. Schubert, J. T. Delaney, and U. S. Schubert. Nanoprecipitation and nanoformulation of polymers: form histroy to powerful possibilities beyond poly(lactic acid). *Soft Matter*, 7:1581–1588, 2011.

[28] G. G. Odian. *Principles of Polymerization*. Wiley-Interscience, Hoboken, N.J., 2004.

[29] K. Tauer, R. Deckwer, I. Kühn, and C. Schellenberg. A comprehensive experimental study of surfactant-free emulsion polymerization of styrene. *Colloid and Polymer Science*, 277:607–626, 1999.

[30] J. P. Rao and K. E. Geckeler. Polymer nanoparticles: Preparation techniques and size-controlled parameters. *Progress in Polymer Science*, 36:887–913, 2011.

[31] O. Thioune, H. Fessi, J. P. Devissaguet, and F. Puisieux. Preparation of pseudolatex by nanoprecipitation: influence of the solvent nature on intrinsic viscosity and interaction constant. *International Journal or Pharmaceutics*, 146:233–238, 1997.

[32] D. Quintanar-Guerrero, E. Allemann, H. Fessi, and E. Doelker. Pseudolatex preparation using a novel emulsion-diffusion process involving direct displacement of partially water-miscible solvents by distillation. *International Journal of Pharmaceutics*, 188:155–164, 1999.

[33] N. Anton, J. P. Benoit, and P. Saulnier. Design and production of nanoparticles formulated from nano-emulsion templates - A review. *Journal of Controlled Release*, 128:185–199, 2008.

[34] C. Zhang, V. J. Pansare, R .K. Prud'homme, and R. D. Priestley. Flash nanoprecipitation of polysterene nanoparticles. *Soft Matter*, 8:86–93, 2012.

[35] A. Nikoubashman, V. E. Lee, C. Sosa, R. K. Prud'homme, R. D. Priestly, and A. Z. Panagiotopoulos. Directed Assembly of Soft Colloids through Rapid Solvent Exchange. *ACS Nano*, 10:1425–1433, 2016.

[36] W. Müller. Hydrophobe und hydrophile Beladung polymerer Vesikel. *Dissertation, Johannes Gutenberg University Mainz*, 2009.

[37] S. Hauschild, U. Lipprandt, A. Rumplecker, U. Bochert, A. Rank, R. Schubert, and S. Förster. Direct preparation and loading of lipid and polymer vesicles using inkjets. *Small*, 1:1177–1180, 2005.

[38] J. R. Spaeth, I. G. Kevrekidis, and A. Z. Panagiotopoulos. Dissipative particle dynamics simulations of poylmer-protedcted nanoparticle self-assembly. *The Journal of Chemical Physics*, 135:184903, 2011.

[39] M. O. Steinhauser and S. Hiermaier. A Review of Compuatational Methods in Materials Science: Examples from Shock-Wave and Polymer Physics. *International Journal of Molecular Sciences*, 10:5135–5216, 2009.

[40] D. Marx and J. Hutter. *Ab initio molecular dynamics: Theroy and Implementation, in Modern Methods and Algorithms of Quantum Chemistry, ed. J. Grotendorst, pp. 301-449, 2000.* NIC 2000.

[41] M. Born and R. Oppenheimer. Zur Quantentheorie der Molekeln. *Annalen der Physik*, 84:457–484, 1927.

[42] R. Car and M. Parrinello. Unified Approach for Molecular Dynamics and Density-Functional Theory. *Physical Review Letters*, 55:2471–2474, 1985.

[43] P. H. Hünenberger. Thermostat Algorithms for Molecular Dynamics Simulations. *Advances in Polymer Science*, 173:105–149, 2005.

[44] S. M. J. Rogge, L. Vanduyfhuys, A. Ghysels, M. Waroquier, T. Verstraelen, G. Maurin, and V. Van Speybroeck. A Comparison of Barostats for the Mechanical Characterization of Metal-Organic Frameworks. *Journal of Chemical Theory and Computation*, 11:5583–5597, 2015.

[45] M. A. Gonzalez. Force fields and molecular dynamics simulations. *Collection SFN*, 12:169–200, 2011.

[46] Z. Zhang, L. Lu, W. G. Noid, V. Krishna, J. Pfaendtner, and G. A. Voth. A Systematic Methodology for Defining Coarse-Grained Sites in Large Biomolecules. *Biophysical Journal*, 95:5073–5083, 2008.

[47] J. M. Drouffe, A. C. Maggs, and S. Leibler. Computer Simulations of Self-Assembled Membranes. *Science*, 254:1353–1356, 1991.

[48] M. Jorge. Molecular Dynamics Simulation of Self-Assembly of n-Decyltrimethylammonium Bromide Micelles. *Langmuir*, 24:5714–5725, 2008.

[49] S. J. Marrink, E. Lindahl, O. Edholm, and A. E. Mark. Simulation of Spontaneous Aggregation of Phospholipids into Bilayers. *Journal of the American Chemical Society*, 123:8638–8639, 2001.

[50] S. J. Marrink and A. E. Mark. Molecular Dynamics Simulation of the Formation, Structure, and Dynamics of Small Phospholipid Vesicles. *Journal of the American Chemical Society*, 125(49):15233–15242, 2003.

[51] J. C. Shelley, M. Y. Shelley, R. C. Reeder, S. Bandyopadhyay, and M. L. Klein. A Coarse Grain Model for Phospholipid Simulations. *The Journal of Physical Chemistry B*, 105:4464–4470, 2001.

[52] B. Smit, P. A. J. Hilbers, K. Esselink, L. A. M Rupert, N. M. van Os, and A. G. Schlijper. Structure of a Water/Oil Interface in the Presence of Micelles: A Computer Simulation Study. *The Journal of Physical Chemistry B*, 95:6361–6368, 1991.

[53] A. H. de Vries, A. E. Mark, and S. J. Marrink. Molecular Dynamics Simulation of the Spontaneous Formation of a Small DPPC Vesicle in Water in Atomistic Detail. *Journal of the American Chemical Society*, 126(14):4488–4489, 2004.

[54] P. M. Kasson, E. Lindahl, and V. S. Pande. Atomic-Resolution Simulations Predict a Transition State for Vesicle Fusion Defined by Contact of a Few Lipid Tails. *PLoS Computational Biology*, 6(6):e1000829, 2010.

[55] D. Mirjanian, A. N. Dickey, J. H. Hoh, T. B. Woolf, and M. J. Stevens. Splaying of Alipathic Tails Plays a Central Role in Barrier Crossing During Liposome Fusion. *The Journal of Physical Chemistry B*, 114:11061–11068, 2010.

[56] R. Goetz, G. Gompper, and R. Lipowski. Mobility and Elasticity of Self-Assembled Membranes. *Physical Review Letters*, 82(1):221–224, 1999.

[57] R. W. Pastor. Molecular dynamics and Monte Carle simulations of lipid bilayers. *Journal of Structural Biology*, 4:486–492, 1994.

[58] W. Shinoda, N. Namiki, and S. Okazaki. Molecular dynamics study of a lipid bilayer: Convergence, structure, and long-time dynamics. *The Journal of Chemical Physics*, 106(13):5731, 1997.

[59] H. W. Tieleman. A computer perspective of membranes: molecular dynamics studies of lipid bilayer systems. *Biochimica et Biophysica Acta*, 1331:235–270, 1997.

[60] C. Pastorino, T. Kreer, M. Müller, and K. Binder. Comparison of dissipative particle dynamics and langevin thermostats for out-of-equilibrium simulations of polymeric systems. *Physical Review E*, 76:026706 1 – 11, Aug 2007.

[61] T. Kinjo and S. Hyodo. Equation of motion for coarse-grained simulation based on microscopic description. *Physical Review E*, 75:051109 1–9, 2007.

[62] P. J. Hoogerbrugge and J. M. V. A. Koelman. Simulating Microscopic Hydrodynamic Phenomena with Dissipative Particle Dynamics. *Europhysics Letters*, 19(3):155–160, 1992.

[63] R. M. Füchslin, T. Maeke, and J. S. McCaskill. Spatially resolved simulations of membrane reactions and dynamics: Multipolar reaction DPD. *The European Physical Journal E*, 29(4):431–448, 2009.

[64] S. G. Wu and H. X. Guo. Dissipative particle dynamics simulation study of the bilayer-vesicle transition. *Science in China Series B: Chemistry*, 51(8):743–750, 2008.

[65] J. C. Shillcock. Spontaneous Vesicle Self-Assembly: A Mesoscopic View of Membrane Dynamics. *Langmuir*, 28:541–547, 2012.

[66] M. Venturoli and B. Smit. Simulating the self-assembly of model membranes. *PhysChemComm*, 10, 1999.

[67] S. Yamamoto, Y. Maruyama, and S. Hyodo. Dissipative particle dynamics study of spontaneous vesicle formation of amphiphilic molecules. *The Journal of Chemical Physics*, 116(13):5842, 2002.

[68] M. Laradji and P. B. Sunil Kumar. Domain growth, budding, and fission in phase-separating self-assembled fluid bilayers. *The Journal of Chemical Physics*, 123(22):224902, 2005.

[69] B. Peng, Y. Liu, Y. Zhou, L. Yang, G. Zhang, and Y. Liu. Modeling Nanoparticle Targeting to a Vascular Surface in Shear Flow Through Diffusive Particle Dynamics. *Nanoscale Research Letters*, 10(1):117, 2015.

[70] J. C. Shillcock and R. Lipowsky. Equilibrium structure and lateral stress distribution of amphiphilic bilayers from dissipative particle dynamics simulations. *The Journal of Chemical Physics*, 117(10):5048, 2002.

[71] J. C. Shillcock and R. Lipowsky. The computational route from bilayer membranes to vesicle fusion. *Journal of Physics: Condensed Matter*, 18(28):S1191–S1219, 2006.

[72] H. Noguchi and M. Takasu. Self-assembly of amphiphiles into vesicles: A Brownian dynamics simulation. *Physical Review E*, 64:041913, 2001.

[73] J. R. Spaeth, I. G. Kevrekidis, and A. Z. Panagiotopoulos. A comparison of implicit- and explicit-solvent simulations of self-assembly in block copolymer and solute systems. *The Journal of Chemical Physics*, 134(16):164902, 2011.

[74] T. Chen, S. M. D'Addio, M. T. Kennedy, A. Swietlow, I.G. Kevrekidis, A. Z. Panagiotopoulos, and R. K. Prud'homme. Protected Peptide nanoparticles: Experiments and Brownian Dynamics Simulations of the Energetics of Assembly. *9*, Nano Letters:2218–2222, 2009.

[75] K. Kawasaki and K. Sekimoto. Dynamical Theory of Polymer Melt Morphology. *Physica*, 143A:349–413, 1987.

[76] E. Wajnryb, P. Szymczak, and B. Cichocki. Brownian dynamics: divergence of mobility tensor. *Physica A*, 335:339–358, 2004.

[77] A. J. Archer and M. Rauscher. Dynamical density functional theory for interacting Brownian particles: Stochastic or deterministic? *Journal of Physics A: Mathematical and General*, 37(40):9325–9333, 2004.

[78] U. M. B. Marconi and P. Tarazona. Dynamic density functional theory of fluids. *The Journal of Chemical Physics*, 110(16):8032, 1999.

[79] B. A. C. van Vlimmeren and J. G. E. M. Fraaije. Calculation of noise distribution in mesoscopic dynamics models for phase separation of multicomponent complex fluids. *Computer Physics Communications*, 99:21–28, 1996.

[80] J. G. E. M. Fraaije, B. A. C. van Vlimmeren, N. M. Maurits, M. Postma, O. A. Evers, C. Hoffmann, P. Altevogt, and G. Goldbeck-Wood. The dynamic mean-field density functional method and its application to the mesoscopic dynamics of quenched block copolymer melts. *The Journal of Chemical Physics*, 106(10):4260, 1997.

[81] T. Uneyama. Density functional simulation of spontaneous formation of vesicle in block copolymer solutions. *The Journal of Chemical Physics*, 126(11):114920, 2007.

[82] G. J. A. Sevink and A. V. Zvelindovsky. Self-Assembly of Complex Vesicles. *Macromolecules*, 38(17):7502–7513, 2005.

[83] G. J. A. Sevink and A. V. Zvelindovsky. Mesoscopic dynamics of complex vesicle formation: Kinetic versus thermodynamic factors. *Molecular Simulation*, 33(4-5):405–415, 2007.

[84] J. G. E. M. Fraaije. Dynamic density functional theory for microphase separation kinetics of block copolymer melts. *The Journal of Chemical Physics*, 99(11):9202, 1993.

[85] N. M. Maurits, B. A. C. van Vlimmeren, and J. G. E. M. Fraaije. Mesoscopic phase separation dynamics of compressible copolymer melts. *Physical Review E*, 56(1997):816–825, 1997.

[86] N. M. Maurits and J. G. E. M. Fraaije. Mesoscopic dynamics of copolymer melts: From density dynamics to external potential dynamics using nonlocal kinetic coupling. *The Journal of Chemical Physics*, 107(15):5879, 1997.

[87] T. Kawakatsu. Effects of changes in the chain conformation on the kinetics of order-disorder transitions in block copolymer melts. *Physical Review E*, 56(3):3240–3250, 1997.

[88] X. He and F. Schmid. Dynamics of Spontaneous Vesicle Formation in Dilute Solutions of Amphiphilic Diblock Copolymers. *Macromolecules*, 39(7):2654–2662, 2006.

[89] X. He and F. Schmid. Spontaneous Formation of Complex Micelles from a Homogeneous Solution. *Physical Review Letters*, 100(13), 2008.

[90] K. F. Freed. Interrelation between density functional and self-consistent-field formulations for inhomogeneous polymer systems. *The Journal of Chemical Physics*, 103(8):3230, 1995.

[91] F. Schmid. Self-consistent-field theories for complex fluids. *Journal of Physics: Condensed Matter*, 10:8105–8138, 1998.

[92] F. Schmid. *Theory and Simulation of Multiphase Polymer Systems, in Handbook of Multiphase Polymer Systems (eds A. Boudenne, L. Ibos, Y. Candau and S. Thomas)*. John Wiley and Sons, Ltd, Chichester, UK, 2011.

[93] X. He, H. Liang, L. Huang, and C. Pan. Complex Microstructures of Amphiphilic Diblock Copolymer in Dilute Solution. *The Journal of Physical Chemistry B*, 108:1731–1735, 2004.

[94] T. Uneyama and M. Doi. Calculation of the Micellar Structure of Polymer Surfactant on the Basis of the Density Functional Theory. *Macromolecules*, 38:5817–5825, 2005.

[95] E. Helfand and Y. Tagami. Theory of the Interface between Immiscible Polymers. II. *The Journal of Chemical Physics*, 56(7):3592, 1972.

[96] M. Laradji, A. C. Shi, J. Noolandi, and R. C. Desai. Stability of Ordered Phases in Diblock Copolymer Melts. *Macromolecules*, 30:3242–3255, 1997.

[97] M. Laradji, A. C. Shi, R. C. Desai, and J. Noolandi. Stability of Ordered Phases in Weakly Segregated Diblock Copolymer Systems. *Physical Review Letters*, 78:2577–2580, 1997.

[98] A. C. Shi and J. Noolandi. Theory of Anisotropic Fluctuaions in Ordered Block Copolymer Phases. *Macromolecules*, 29:6487–6504, 1996.

[99] L. Leibler. Theory of Microphase Separation in Block Copolymers. *Macromolecules*, 13:1602–1617, 1980.

[100] M. Müller and F. Schmid. Incorporating fluctuations and dynamics in self-consistent field theories for polymer blends. 2005.

[101] P. Hohenberg and W. Kohn. Inhomogeneous Electron Gas. *Physical Review*, 136:B 864 – 871, 1964.

[102] M. Doi and S. F. Edwards. *The Theory of Polymer Dynamics*. Oxford University Press, 1986.

[103] G. H. Fredrickson. *The Equilibrium Theory of Inhomogeneous Polymers*. Oxford University Press, 2006.

[104] P. J. Flory. Thermodynamics of High Polymer Solutions. *The Journal of Chemical Physics*, 10(1):51, 1942.

[105] Y. K. Suh and S. Kang. A Review on Mixing in Microfluidics. *Micromachines*, 1(3):82–111, 2010.

[106] C. Y. Lee, C. L. Chang, Y. N. Wang, and L. M. Fu. Microfluidic Mixing: A Review. *International Journal of Molecular Sciences*, 12(12):3263–3287, 2011.

[107] N. T. Nguyen and Z. Wu. Micromixers—a review. *Journal of Micromechanics and Microengineering*, 15(2):R1–R16, 2005.

[108] S. Hardt, K. S. Drese, V. Hessel, and F. Schönfeld. Passive micromixers for applications in the microreactor and muTAS fields. *Microfluid Nanofluid*, 1:108–118, 2005.

[109] F. Schönfeld, V. Hessel, and C. Hofmann. An optimised split-and-recombine micromixer with uniform 'chaotic' mixing. *Lab on a Chip*, 4(1):65–69, 2004.

[110] V. Hessel, S. Hardt, H. Löwe, and F. Schönfeld. Laminar mixing in different interdigital micromixers: I. Experimental characterization. *AIChE Journal*, 49(3):566–577, 2003.

[111] L. Falk and J. M. Commenge. Performance comparison of micromixers. *Chemical Engineering Science*, 65(1):405–411, 2010.

[112] K. S. Drese. Optimization of interdigital micromixers via analytical modeling—exemplified with the SuperFocus mixer. *Chemical Engineering Journal*, 101(1-3):403–407, 2004.

[113] A. S. Tijani, D. Barr, and A. H. Abdol Rahim. Computational Modelling of the Flow Field of An Electrolyzer System using CFD. *Energy Procedia*, 79:195–203, 2015.

[114] J. Crank. *The mathematics of diffusion, 2nd edition.* Oxford University Press, 1999.

[115] S. Hardt and F. Schönfeld. Laminar mixing in different interdigital micromixers: II. Numerical simulations. *AIChE Journal*, 49(3):578–584, 2003.

[116] G. Taylor. Dispersion of Soluble Matter in Solvent Flowing Slowly through a Tube. *Proceedings of the Royal Society of London A: Mathematical, Physical and Engineering Sciences*, 219(1137):186–203, 1953.

[117] H. M. Srivastava, K. Y. Kung, and K. J. Wang. Analytic solutions of a two-dimensional rectangular heat equation. *Russian Journal of Mathematical Physics*, 14(1):115–119, 2007.

[118] F. Schönfeld, K. S. Drese, S. Hardt, V. Hessel, and C. Hofman. Optimized distributive μ-mixing by 'chaotic' multilamination. *NSTI-Nanotech*, 1:378–381, 2004.

[119] D. E. Smith, H. P. Babcock, and S. Chu. Single-Polymer Dynamics in Steady Shear Flow. *Science*, 283:1724 – 1727, 1999.

[120] E. L. Huston, J. W. Cahn, and J. E. Hilliard. Spinodal decomposition during continuous cooling. *Acta Metallurgica*, 14:1053 – 1062, 1966.

[121] E. Reister, M. Müller, and K. Binder. Spinodal decomposition in a binary polymer mixture: Dynamic self-consistent-field theory and Monte Carlo simulations. *Physical Review E*, 64(4), 2001.

[122] J. W. Barrett, J. F. Blowey, and H. Garcke. On fully practical finite element approximations of degenerate Cahn-Hilliard systems. *ESAIM: Mathematical Modelling and Numerical Analysis*, 35(4):713–748, 2001.

[123] J. W. Cahn and J. E. Hilliard. Free Energy of a Nonuniform System. I. Interfacial Free Energy. *The Journal of Chemical Physics*, 28(2):258, 1958.

[124] A. Novick-Cohen. *Handbook of differential equations: evolutionary equations, chapter 4.* Elsevier, 2008.

[125] M. V. Ariyapadi and E. B. Naumann. Gradient energy parameters for polymer-polymer-solvent systems and their application to spinodal decomposition in true ternary systems. *Journal of Polymer Science: Part B: Polymer Physics*, 28(12):2395–2409, 1990.

[126] C. F. Curtiss and J. O. Hirschfelder. Integration of stiff equations. *Proceedings of the National Academy of Sciences*, 38:235–243, 1952.

[127] E. Hairer and G. Wanner. Stiff differential equations solved by Radau methods. *Journal of Computational and Applied Mathematics*, 111:93–111, 1999.

[128] R. J. LeVeque. Finite Difference Methods for Differential Equations, 2005.

[129] J. H. Seinfeld, L. Lapidus, and M. Hwang. Review of Numerical Integration Techniques for Stiff Ordinary Differential Equations. *Industrial and Engineering Chemistry Fundamentals*, 9(2):266–275, 1970.

[130] G. Dahlquist. A special stability problem for linear multistep methods. *Communications of the ACM*, 14(3):176–179, 1963.

[131] C. W. Gear. The automatic integration of ordinary differential equations. *BIT*, 3:27–43, 1971.

[132] J. Zhu, L. Q. Shen, J. Shen, and V. Tikare. Coarsening kinetics from a variable-mobility Cahn-Hilliard equation: Application o fa semi-implicit Fourier spectral method. *Physical Review E*, 60(4):3564–3572, 1999.

[133] U. M. Ascher, S. J. Ruuth, and B. T. R. Wetton. Implicit-explicit methods for time-dependent partial differential equations. *SIAM Journal on Numerical Analysis*, 32(3):797–823, 1995.

[134] M. Frigo and S. G. Johnson. *The Fastest Fourier Transform in the West.* MIT: Cambridge, MA, 2000.

[135] C. Shu. *Differential Quadrature and Its Application in Engineering.* Springer, 2000.

[136] B. P. Vollmayr-Lee and A. D. Rutenberg. Fast and accurate coarsening simulation with an unconditionally stable time step. *Physical Review E*, 68:066703 1–13, 2003.

[137] M. Matsumoto and T. Nishimura. Mersenne twister: a 623-dimensionally equidistributed uniform pseudo-random number generator. *ACM Transactions on Modeling and Computer Simulation*, 8:3–30, 1998.

[138] M. Kotnis and M. Muthukumar. Entropy Induced Frozen Morphology in Unstable Polymer Blends. *Macromolecules*, 25:1716–1724, 1992.

[139] M. Fialkowski and R. Holyst. The unphysical pinning of the domain growth during the separation of homopolymer blends near the spinodal. *Journal of Chemical Physics*, 120:5802–5808, 2004.

[140] H. Tanaka. Unusual Phase Separation in a Polymer Solution Cause by Asymmetric Molecular Dynamics. *Physical Review Letters*, 71:3158–3161, 1993.

[141] D. Zhou, P. Zhang, and E. Weinan. Modified models for polymer phase separation. *Physical Review E*, 73:061801 1–9, 2006.

[142] I. M. Lifshitz and V. V. Slyozov. The kinetics of precipitation from supersaturated solid solutions. *Journal of Physics and Chemistry of Solids*, 19:35–50, 1961.

[143] C. Wagner. Theorie der Alterung von Niederschlägen durch Umlösen (Ostwald-Reifung). *Zeitschrift für Elektrochemie*, 65:581–591, 1961.

[144] V. Sofonea and K. R. Mecke. Morphological characterization of spinodal decomposition kinetics. *The European Physical Journal B*, 8(1):99–112, 1999.

[145] K. R. Mecke. Additivity, Convexity, and Beyond: Applications of Minkowski Functionals in Statistical Physics, 2000.

[146] H. Mantz, K. Jacobs, and K. Mecke. Utilizing Minkowski functionals for image analysis: A marching square algorithm. *Journal of Statistical Mechanics: Theory and Experiment*, 2008(12):P12015, 2008.

[147] T. T. Nielsen. *An Implementation Of The Connected Component Labelling Algorithm.* https://www.codeproject.com/articles/825200/an-implementation-of-the-connected-component-label, 2014.

[148] D. Legland, K. Kieu, and M. F. Devaux. Computation of Minkowski Measures on 2D and 3D binary images. *Image Analysis and Stereology*, 26:83–92, 2007.

[149] J. D. Weeks, D. Chandler, and H. C. Andersen. Role of Repulsive Forces in Determining the Equilibrium Structure of Simple Liquids. *Journal of Chemical Physics*, 54:5237–5247, 1971.

[150] M. Bishop, M. H. Kalos, and H. L. Frisch. Molecular Dynamics of Polymeric Systems. *Journal of Chemical Physics*, 70:1299–1304, 1979.

[151] G. S. Grest and K. Kremer. Molecular Dynamics Simulation for Polymers in the Presence of a Heat Bath. *Physical Review A*, 33:3628, 1986.

[152] M. E. Gindy, R. K. Prud'homme, and A. Z. Panagiotopoulos. Phase behavior and structure formation in linear multiblock copolymer solutions by Monte Carlo simulation. *The Journal of Chemical Physics*, 128(16):164906, 2008.

[153] B. A. Wolf. Making Flory-Huggins Practical: Thermodynamics of Polymer-Containing Mixtures. *Advances in Polymer Science*, 238:1–66, 2011.

[154] S. Janssen, D. Schwahn, K. Mortensen, and T. Springer. Pressure Dependence of the Flory-Huggins Interaction Parameter in Polymer Blends: A SANS Study and a Comparison to the Flory-Orwoll-Vrij Equation of State. *Marcomolecules*, 26:5587–5591, 1993.

[155] T. P. Russell, R. P. Hjelm, and P. A. Seeger. Temperature Dependence of the Interaction Parameter of Polystyrene and Poly(methyl methacrylate). *Macromolecules*, 23:890–893, 1990.

[156] N. Schuld and B. A. Wolf. Solvent Quality as Reflected in Concentration- and Temperature-Dependent Flory-Huggins Interaction Parameters. *Joural of Polymer Science: Part B: Polymer Physics*, 39:651–662, 2001.

[157] C. I. D. Bica, W. Burchard, and R. Stadler. Dilute solution properties of poybutadiene modified by 4-phenyl-1,2,4-triazoline-3,5-dione. *Macromolecular Chemistry and Physics*, 197:3407–3426, 1996.

[158] C. P. Grant. Spinodal decomposition for the Cahn-Hilliard equation. *Communications in Partial Differential Equations*, 18(3-4):453–490, 1993.

[159] C. Elliot. The Cahn-Hilliard model for the kinetics of phase separation. *International Series of Numerical Mathematics*, 88:35–71, 1989.

[160] C. Schaefer, P. van der Schoot, and J. J. Michels. Structuring of polymer solutions upon solvent evaporation. *Physical Review E*, 91:022602 1–6, 2015.

[161] J. J. van Franeker, G. H. L. Heintges, C. Schaefer, G. Portale, W. Li, M. M. Wienk, P. van der Schoot, and R. A. J. Janssen. Polymer Solar Cells: Solubility Controls Fiber Network Formation. *Journal of the American Chemical Society*, 137:11783–11794, 2015.

[162] G. Tzeremes, K. O. Rasmussen, T. Lookman, and A. Saxena. Efficient computation of the structural phase behavior of block copolymers. *Physical Review E*, 65:041806 1–5, 2002.

[163] Y. Saad and M. H. Schlutz. GMRES: A generalized minimal residual algorithm for solving nonsymmetric linear systems. *SIAM Journal on Scientific and Statistical Computing*, 7:856–869, 1986.

[164] M. E. Wall, M. C. Wani, C. E. Cook, K. H. Palmer, A. T. McPhail, and G. A. Sim. Plant Antitumor Agents. I. The Isolation and Structure of Camptothecin, a Novel Alkaloidal Leukemia and Tumor Inhibitor from Camptotheca acuminata. *Journal of American Chemical Society*, 88:3888 – 3890, 1966.

[165] V. P. Torchilin. Recent advances with liposomes as pharmaceutical carriers. *Nature Review Drug Discovery*, 4:145 – 160, 2005.

[166] W. Mueller, K. Koynov, S. Pierrat, R. Thiermann, C. Fischer, and M. Maskos. pH-change protective PB-b-PEO polymersomes. *Polymer*, 52:1263 – 1267, 2011.

[167] A. V. Kabanov, E. V. Batrakova, and V. Y. Alakhov. Pluronic((R)) block copolymers for overcoming drug resistance in cancer. *Advanced Drug Delivery Reviews*, 54:759 – 779, 2002.

[168] Y. Han, Y. Haizhou, H. Du, and W. Jiang. Effect of Selective Solvent Addition Rate on the Pathways for Spontaneous Vesicle Formation of ABA Amphiphilic Triblock Copolymers. *Jornal of American Chemical Society*, 132(3):1144–1150, 2010.

Danksagung

Besonderer Dank gilt meinen beiden Betreuern, Prof. Friederike Schmid von der Uni Mainz und Prof. Klaus Drese von Seiten des Fraunhofer ICT-IMM, für die sehr freundliche und immer hilfreiche Unterstützung. Dem Fraunhofer ICT-IMM, der Johannes Gutenberg-Universität Mainz und EFRE danke ich für die Finanzierung dieser Arbeit. Ebenfalls bedanken möchte ich mich bei allen Mitgliedern der Arbeitsgruppe KOMET 331 und Kollegen am ICT-IMM für die nette Arbeitsatmosphäre – insbesondere bei Johannes Heuser, der mir seinen Quelltext für den konventionellen SCF-EPD-Löser zur Verfügung gestellt hat, Dr. Arash Nikoubashman, der mir die Ergebnisse seiner Molekulardynamik-Simulationen gegeben und meine Fragen dazu ausführlich beantwortet hat, und Dr. Raphael Thiermann, der die experimentellen Daten bereitgestellt hat. Zum Schluss bedanke ich mich noch für die Rechenzeit auf dem Supercomputer Mogon an der Johannes Gutenberg-Universität Mainz (hpc.uni-mainz.de).